UNIVERSITY OF SOUTHAMPTON

FACULTY OF ENGINEERING, SCIENCE & MATHEMATICS

School of Engineering Sciences

POST-YIELD CHARACTERISATION OF WELDS BASED ON INSTRUMENTED HARDNESS TESTER DATA

by

Hamdi Habbab

Thesis for the degree of Doctor of Philosophy

January 2005

UNIVERSITY OF SOUTHAMPTON

ABSTRACT

SCHOOL OF ENGINEERING SCIENCES

Doctor of Philosophy

POST-YIELD CHARACTERISATION OF WELDS BASED ON INSTRUMENTED HARDNESS TESTER DATA

by Hamdi Habbab

The strength of welded joints has a vital effect on the structural response of a welded structure under severe loading conditions. The thermal nature of the weld process causes considerable changes in the microstructure across the weld regions, which leads to different material properties in these regions, namely, the parent metal, the weld fusion zone, and weld heat-affected zone.

The reliability of predicting the real behaviour of the welded structure using finite element analysis depends on the accurate determination of the material properties across these regions which are essential input data in the model. Whilst conventional tensile testing is incapable of providing these properties on such a small scale, the instrumented micro/nano-hardness test lends itself for such a task. In this non-destructive technique a small indenter, which is spherical in this study, is pressed onto the surface of the material and then unloaded while load and depth of indentation are continuously measured. Several approaches have evolved to analyse the measured load indentation data to extract various material mechanical properties corresponding to each indent location. The primary objective sought from such an analysis is the determination of the contact area, which is then used to obtain material properties. While the existing analytical approaches assume the contact edges sink-in, soft metals, however, tend to pile-up resulting in possible large errors in the derived results. The available correction formulae attempt to predict pile-up based on a prior knowledge of the strain hardening exponent of the test material. In addition, they assume a constant ratio of the pile-up lip height to indentation depth, which they defined as a function of the strain hardening exponent. Thus they do not predict pile-up based solely on the indentation data.

This study shows, based on detailed finite element modelling, that pile-up starts with a negative value (sink-in) in the early stages of an indentation experiment and then develops and builds up until it stabilises at a certain level. An empirical relation is proposed to predict the extent of pile-up of an unknown material based on the residual to total indention depth ratio. This leads to a more accurate estimate of the contact area and thus the derived stress-strain curve. In addition, a characterisation model for an indenter of imperfect geometry is also proposed in this study which identifies the characteristic strain for an imperfect sphere. An algorithm is suggested which incorporates the proposed characterisation analysis in a complex iteration technique in the frame compliance calibration routine to process the raw acquired data. The proposed characterisation technique has been verified on experimental data of test materials, and it has then been applied to indentation data on butt-welded steel spanning the distinct weld regions.

ACKNOWLEDGMENT

First of all, all praise is due to Allah (GOD) Almighty for helping me accomplish this research work.

I would like to express my sincere gratitude to my supervisors Dr BG Mellor and Dr S Syngellakis for their continuous support, fruitful discussions and patient guidance. Their close supervision was inspirational to deliver this research to its completion.

I am also grateful to the University of Southampton and School of Engineering Sciences for the fund and facilities provided to carry out this research.

Many thanks to Mr Ian Perryman in Vosper Thornycroft who helped with performing the weld work needed for this research.

I would also like to thank Prof A Walker, Dr K Williams, Dr K Kamhawi, and Dr S Mesmar for their support and constructive feedback of this thesis.

Last but not least, I am grateful to my family and all my friends for their enduring assistance and continuous encouragement.

DEDICATION

I dedicate this research work to my family, (my parents and siblings: *Manal, Lina, Hiba, Ahmad and Waseem*), to whom I am indebted and obliged for their everlasting love and support, and enduring encouragement throughout all my life. As I feel incapable of returning the favour back, I hope the fruit of this research will act as a symbolic thank in recognition to their endless love and sacrifice. Thank you father for your unlimited giving and effort in everything you have given me and worked for me. Thank you for teaching me how to learn and the patience of learning. I hope I will always be up to your expectations and follow the examples you set through yourself. Finally, I specially dedicate this work to my dear mother, the angel who has been lightening my road and feeding me with all strength and inspiration in every step I took in my life. Mother, through you the greatness is made, and under your feet the heaven is laid. God made you of unselfish love and sacrifice, yet full of wisdom and insight. You are the school who taught me the determination and that success must be in continuation. You taught me that achievements are made by us not opportunities granted to us. You taught me the power of the desire to accomplish, and the discipline of moving forward and progress. You taught me that with a real will, the fate must comply and fulfil. To you I have all love and devotion, and to Allah I pray with supreme zeal and zest to embrace you with his bless and passion. Would you accept this as a humble thank for the honour and pride of that you are my mother.

NOMENCLATURE

Subscripts	
cr	Refers to critical.
i	Refers to the indenter.
s	Refers to the specimen.
Roman Upper Case	
A	The projected contact area.
BHN	Brinell hardness number.
B_m	Material type constant, Eq. 2-67.
C	Constraint factor, Eq. 2-18.
C_1, C_2, C_3, C_{max}	Constants relating to the constraint factor C covering three stages of strain field development during indentation, Eq. 2-73.
C_f	Frame compliance, Eq. 3-2.
C_s	Specimen compliance, Eq. 3-3.
C_t	Total compliance of the specimen and the frame, Eq. 3-2.
D	Indenter diameter.
E	Young's modulus.
G	Shear modulus.
H	Hardness.
H_v	Vickers hardness number.
H_k	Knoop hardness number.
K	Material strength coefficient.
N_1 , N_2	Fitting constants in Eq. 2-82 and Eq. 2-83.
P	Load applied on the indenter.

P_{max}	Peak load in a cycle.
P_{int}	Load at an intermediate location on the unloading curve.
S	Elastic contact stiffness (initial gradient of the unloading curve).
S_l	Loading contact stiffness at peak load (gradient of the loading curve at peak load)
X_b	Constant of the ideal area function of a pyramidal indenter in Eq. 2-6.
X_m	Material constant obtained from Meyer's law.
R	Indenter radius.
R_c	Rockwell hardness number for a conical indenter.
R_b	Rockwell hardness number for a spherical indenter.
R_r	Effective radius.
U_r	Radial displacement.
UTS	Ultimate tensile strength.
X_1, X_2, X_3, X_4	Fitting constants in Eq. 2-85.

Roman Lower Case

a_0	Radius of the contact circle that lies in the plane of the original surface, which corresponds to the maximum penetration depth.
a_c	Radius of the contact circle of an indentation.
b_m	Material yield stress offset constant Eq. 2-68.
c^2	Pile-up parameter for spherical indentation, Eq. 2-57.
c_v^2	A pile-up parameter for Vickers indentation, Eq. 2-60.
d	Diameter of the contact circle of a residual impression.
d_0	Diameter of the contact circle of a residual impression that lies in the plane of the original surface, which corresponds to the maximum penetration depth.
e	Engineering strain.
h	Penetration depth.
h_e	Elastic penetration depth or elastic recovery of the contact centre.
h_r	Depth of a residual indentation.

h_c	Contact depth.
h_{raw}	Penetration depth acquired by the instrument (raw data).
h_s	Indentation depth of the indentation edges.
h_l	Maximum lip height of the pile-up.
h_t	Maximum penetration depth in a load cycle.
h_{int}	Indentation depth at an intermediate location on the unloading curve.
k	Material constant in Meyer's law.
l	Mean diagonal of the residual Vickers indentation.
l_k	The longer diagonal of the residual Knoop indentation.
m	Meyer index.
n	Strain hardening exponent.
$p(r)$	Contact pressure at radial distance r from the contact area centre.
p_0	Contact pressure at the centre of the contact area.
p_m	Mean pressure over the contact area.
q	Exponent of a simple power law function Eq. 2-17.
r	Radial distance from the contact centre.
r_2	Radius of curvature of the recovered indentation surface.
Greek	
α	Semi-included angle of the indenter tip.
α_m	Strain rate sensitivity.
β	Angle between the tangent to the indenter at the indentation edge and the original surface.
δ	Mutual approach of distant points in two spherical bodies during elastic contact, Eq. 2-13.
φ	Coefficient of a simple power law function Eq. 2-17.
ε	True strain.
σ	True stress/ flow stress.
σ_0	Engineering stress.
$\sigma_{0.2}$	Stress at plastic strain of 0.2%.

σ_e	Elastic limit.
σ_r	True stress corresponding to the characteristic/representative strain.
σ_y	Yield stress.
ε_l	Lüders strain.
ε_r	Characteristic/Representative Eq. 2-71.
γ	The correction factor to Sneddon's solution for a conical indenter, Eq. 2-35.
γ_b	Correction factor to Hertz solution for spherical indentations Eq. 2-54.
ν	Poisson's ratio.
η	Correction factor accounting for the indenter geometry Eq. 2-27.
λ	Yield shear stress Eq. 2-20.
θ	An angle related to the indenter tip included angle and used only for calculation, Eq. 2-21.
τ	Shear stress.
χ	A parameter that accounts for the indenter geometry when calculating the contact depth Eq. 2-33.

TABLE OF CONTENTS

CHAPTER 1

INTRODUCTION

Steel construction requires the assembly of structural steel components manufactured in particular dimensions that facilitate handling, transportation, and installation. The most commonly used method of connecting these components is fusion-welding, which is of interest in this study. The strength and response of the welded joints are essential design issues to ensure safe load transfer between the steel members, as if these members were continuous at the joints.

Welded joints play a major role in the design and performance of the whole structure. Hence, it is important to understand their behaviour to deliver a safe and efficient design. Many attempts [1-7] have been made to investigate the stress distribution in welds in order to estimate the joint strength. These approaches were based on the theory of strength of materials and fracture mechanics. Although different parameters were considered such as the connection geometry, the direction of the applied load, and the weld size, these approaches ignored the variation in the material properties across the weld regions. A review of different methods for evaluating the strength of welded joints was presented by Mellor *et al.* [8].

The thermal nature of the weld process causes not only residual stresses in the welded joint but also changes in the microstructure across the weld regions. Many studies on such effects have been carried out [9, 10]. The behaviour of a welded joint is influenced not only by the strength of the weld metal and the joint geometry but also by the variation in the microstructure across the weld regions, which leads to different material properties in these regions. Therefore, the metallurgical events that occur in welding should be considered.

1.1 Effect of welding on the microstructure

Welding involves complex metallurgical phenomena that take place during the course of making a weld. These phenomena occur very rapidly in comparison with those occurring in other metallurgical fields such as casting and heat treatments. The fusion welding processes involve a very intense heat source that inevitably leads to rapid local melting of the weld and base metal, which then cool again rapidly under conditions of restraint imposed by the geometry of the joint. As a result, three distinct regions are created in the weld region: the weld fusion zone (weld pool), the heat weld affected zone (HAZ) and the base metal, as shown in Fig. 1-1.

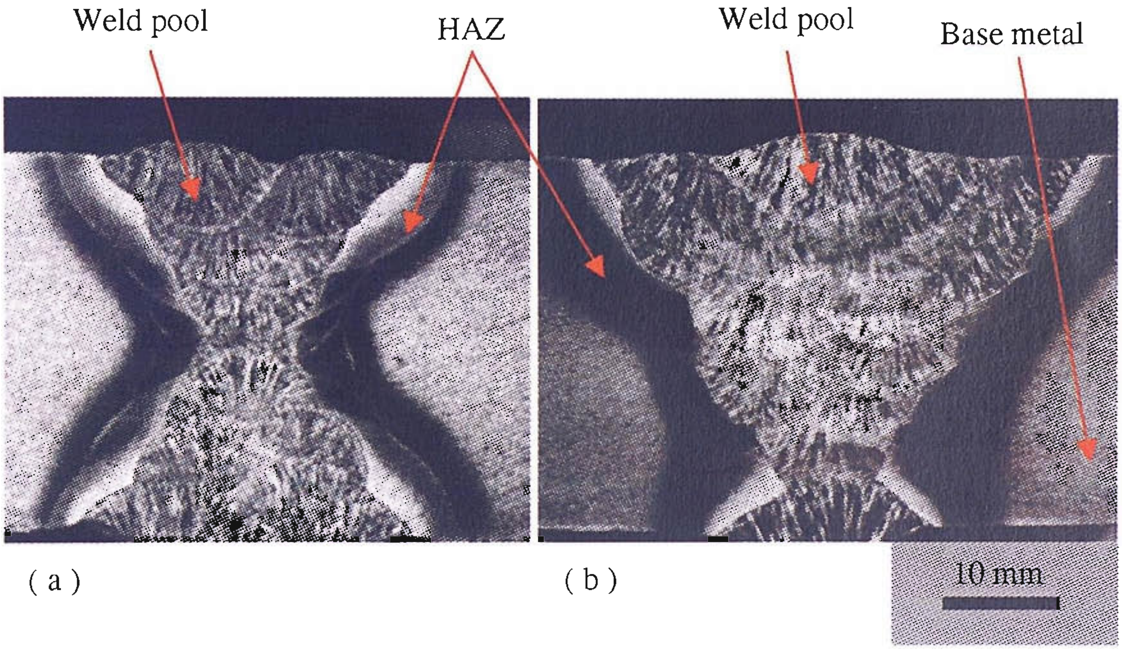

Fig. 1-1 Manual metal arc welds of (a) a double V-butt weld and (b) a single V-butt weld in a constructional steel. The weld pool, HAZ, and the base metal are identified.[9].

The different microstructures observed in Fig. 1-1 result from the reaction of the alloy to the various welding variables. Columnar grains appear in the weld fusion zone as a result of epitaxial growth from the fusion line under a high temperature gradient, while the microstructural changes in a steel weldment result from the solid state phase transformations that occur on heating and cooling steel [11]. This results in the changes in grain structures across the weld regions shown schematically in Fig. 1-2, which can considerably influence the mechanical properties.

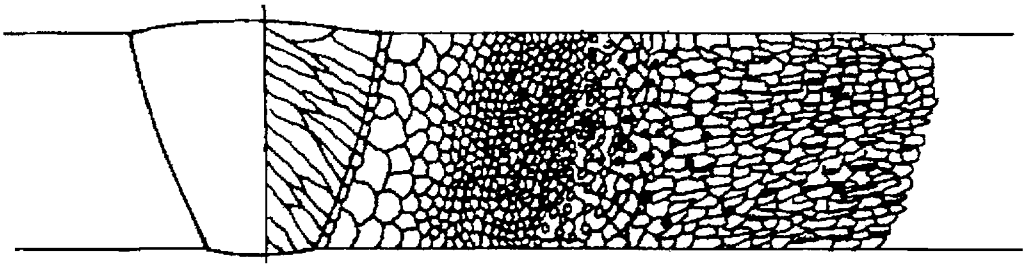

Fig. 1-2 A schematic diagram of the various grain structures across the weld regions of a constructional steel.

1.2 Evaluation of the strength of welded joints by the finite element method

Determining the strength and behaviour of welded joints is essential when analysing the whole structure. Due to the complexity of this problem, the analytical design approaches neglect various important factors as a result of the approximations and assumptions made. Whilst this gives rise to uncertainty in the analysis prediction, especially when plastic strains are present, it is essential to identify a more rigorous means of analysing the structure. With the advances of the computing capabilities and high data storage capacity, the Finite Element Method (FEM) can effectively be employed for such a task. In fact, elasto-plastic finite element analysis is a powerful tool that can be used for analysing structures under various loading conditions. However, the effectiveness of the FEM simulation to predict the response of a structure relies largely on the accuracy of the material data input into the model. This is particularly essential when modelling welded joints since the material properties across the weld regions are not uniform and vary as a consequence of the microstructural changes induced by the welding process. This necessitates utilising an accurate means to probe the surface on a micrometre scale given that the weld regions stretch over a few millimetres. On this requirement, the conventional tensile testing, which is a destructive testing method, is incapable of providing the material properties on such a scale. On the other hand, the hardness test, as a localised non-destructive method, can lend itself for such a task.

1.3 Instrumented micro-indentation technique

Conventional hardness tests are attractive as they are cheap, non-destructive, simple, quick, and can be used to estimate the strain-hardening exponent. They were first used to qualitatively compare the quality of steel products. In a hardness test, an indenter, which can be conical, pyramidal, or spherical is pressed onto the surface of the material under a pre-specified load and then fully unloaded forming a residual indent. The load applied divided by the surface area of the residual indent, which is determined from optical measurement, defines the hardness number of the material.

Whilst pyramidal indenters have the advantage of the hardness being independent of the load applied since the strain pattern imposed by the indenter is similar for all load values, the hardness number derived from a spherical indenter increases with penetration depth to a degree dependent on the strain hardening capability of the material. This allows the stress-strain curve to be determined by carrying out a series of hardness tests at different loads.

The development of high-resolution measurement instruments that have the capability of continuous measurement of force and displacement has made it possible to obtain load-depth indentation data during a hardness test. This facilitates probing the material surface on the micrometre scale using a very small indenter. Many approaches [12-14] have been introduced to extract the material properties from analysing cyclic load-indentation data based on the unloading deformation being considered elastic. Hence, the indentation unloading curve can be correlated with the elastic properties by implementing the elastic contact solution to describe the elastic recovery of the material. The key quantities measured from this analysis are the contact area and contact stiffness at full loading, leading to the determination of hardness and the elastic modulus [13, 15]. Meyer hardness and the indent size, in conjunction with the indenter geometry, at different load levels, could then be correlated with the stress-strain curve derived from the uniaxial tensile test. The effectiveness of this correlation relies particularly on the accuracy of the estimated contact area, which is derived based on the assumption that the contact edges deform in the direction of the indenter movement. Whilst this represents the behaviour of hard material, soft metals act differently in that the contact perimeter tends to rise above the level of the original surface (piling-up). Ignoring the pile-up effect results in an error in estimating the contact area, which can amount to 40% [16]. Empirical correction formulae were then proposed [17-19] to account for the pile-up effect assuming a prior knowledge of the strain hardening of the material, which is clearly not applicable to unknown materials. Assessing the performance of these formulae on test materials, whose properties are known, showed the weakness of these formulae in predicting the correct stress-strain curve in the case of a spherical indenter. To day, there is no a general method to derive the stress-strain curve of any unknown metal based solely on the indentation data from a spherical indenter. The knowledge of the strain hardening exponent or yield stress is required a priori.

1.4 Objectives

The outcomes sought from this research are:

1. The assessment of the reliability and the performance of an instrumented microindentation tester, and the development of a characterisation model that represents the geometry of the available spherical indenter.
2. The assessment of the analysis approaches for deducing elasto-plastic material properties from load-indentation data and the highlighting of their limitations.
3. The development of a reliable finite element model, based on a general purpose software package, for simulating spherical indentations.
4. The investigation, through finite element simulations, of the pile-up phenomenon and the effectiveness of the existing methods that aim to account for the pile-up effect.
5. The development of a new technique to account for the pile-up effect, in the case of indentations with an almost spherical, axisymmetric indenter, relying exclusively on the load-indentation data in a scheme to predict the stress-strain curve of an unknown material.
6. The assessment of the effectiveness of the new technique to predict accurately the stress-strain curve through its extensive application on different test materials.
7. The implementation of the new technique to the analysis of indentation data produced from hardness testing across the distinct weld regions of a butt-welded joint, in order to assess the elasto-plastic material properties variation across these regions.

1.5 Methodology

The methods adopted to achieve the aforementioned objectives are divided into two classes as follows:

- Experimental procedures
    1. Reference specimens are prepared for indentation testing from various steel grades whose stress-strain curves are determined through tensile testing. Indentations are also performed on reference hardness test blocks (Vickers Hardness=303 and 700).
    2. Indentation testing is performed on the reference specimens using the instrumented microindentation and Vickers microhardness testers to evaluate the performance of the instrument and compare its result with those from the conventional hardness testing. A diamond spherical indenter, of nominal radius R=150 μm, and the Berkovich indenter are used with the instrumented tester. The Berkovich residual indents are imaged to measure their contact area to be compared with the corresponding derived value from analysing the load-indentation data. In addition, the hardness from both the Berkovich and the Vickers indenters are compared.
    3. Scanning Electron Microscopy (SEM) is used to image the spherical indenter at various angles of rotation about its nominal axis of symmetry, and these profiles are digitised in a scheme to characterise the actual indenter geometry.
    4. Test specimens are prepared from constructional steel and stainless steel plates, 8 mm thick, for indentation testing. The surface of these specimens are ground and polished to a mirror finish. In addition, tensile test samples, of a circular cross-section, are machined from the as-received plates and pulled until rupture to extract the stress strain curve, thus the true-stress-logarithmic strain curves. These curves are regarded as the material properties sought to re-produce from indentation testing.
    5. A butt-welded joint is formed from an 8-mm thick steel plate using submerged arc welding. The joint is then sectioned transverse to the weld line and indentation testing is carried out on the cross section to span the three distinct regions of the weld, which are the parent metal, HAZ, and weld fusion zone.
- Modelling and analysis procedures

1. A reliable Finite Element (FE) model is developed using ANSYS and the meshing facilities in PATRAN to simulate the indentation process with the spherical indenter for different cases as follows:
   - » Rigid perfectly spherical indenter, R=150 μm, on virtual materials, whose stress-strain curves are described by a single power law function as an approximation to those of the test materials.
   - » The actual geometry measured for the imperfect spherical indenter used pressed on the test materials using their stress-train curves from tensile testing as input data to the FE model

   Resulting from the FE simulation are the load-indentation data, which serve as simulated experiment output, as well as the indent profile geometry at various load levels.
2. A computer program is developed using MATLAB, benefiting from its statistical toolbox to analyse the load-indentation data and thus deduce the contact area and initial contact stiffness, which lead to hardness and reduced elastic modulus. The program implements the existing approaches of analysis including a correction formula to account for the pile-up effect. The analysis is applied to the simulated load-indentation data resulting from the two aforementioned cases above.
3. Based on the FE output, a fitting procedure is employed aiming at relating indent geometry to load-indentation data for different material properties. This is a scheme to develop an improved empirical relation accounting for the pile-up effect relying exclusively on the load-indentation data, and hence deduce the stress-strain curve for a new material.
4. The new characterisation analysis with the empirical relation developed is applied to the indentation data from the spherical indenter on the various weld regions of a butt-welded joint.

1.6 Layout of this thesis

- The second chapter includes the literature review on the subject of this thesis.
- The third chapter presents a detailed description of the instrumented indentation tester and the mechanism of performing indentation including all calibration routines. Validation of the instrument performance and reliability tests are carried

out. In addition, a characterisation model of the spherical indenter available is presented.

- In the fourth chapter, tensile testing is performed on the test steel plates to obtain their stress-strain curves. In addition, an FE model that simulates the indentation process is developed and validated. Finally, the effect of the creep phenomenon exhibited by the constructional steel is investigated.
- The fifth chapter investigates the correlation of the stress-strain curve with the indentation parameters. The effectiveness of the applicable analysis approaches and existing correction formulae to account for the pile-up effect are assessed based on FE simulated data. A new analysis technique is proposed to predict the pile-up from the load-indentation data, which involves a new iterative mechanism that facilitates the prediction of the strain hardening exponent.
- In the sixth chapter, the proposed characterisation analysis is applied to the experimental data of the test materials. A method to incorporate the new technique into the frame compliance calibration of the instrumented hardness tester is suggested, and its capability of predicting the stress-strain curve is assessed. Finally, it is applied to the indentation data from the indents performed across the weld regions in a butt-welded joint.
- The seventh chapter summarises and discusses the findings of this research, and introduces future work.
- Appendix 1 includes some background on welding process and metallurgy.
- Appendix 2 contains description of the MATLAB program developed for this research to analyse the load indentation data incorporating the new characterisation analysis and the frame compliance calibration.
- Appendix 3 is a brief description of the ANSYS PROGRAMMING LANGUAGE (APDL) script built to extract various output quantities of the FE simulation.

CHAPTER 2

LITERATURE REVIEW

2.1 Overview of conventional hardness testing

There are several types of hardness measurements: indentation hardness, scratch hardness, and dynamic hardness. Indentation hardness is the one considered in this study. Quantitative indentation hardness techniques have been developed over the past 50 years which involve a small indenter pressed into the surface of the test material under controlled conditions of load application. In these conventional hardness tests, the hardness number is determined from the knowledge of the maximum applied load and from the depth and size measurement of the resulting residual indent. There are different conventional indentation hardness tests used to estimate materials hardness and the values from those tests are conventionally presented in kg/mm^2.

- **Brimley hardness test**

In Brinell tests, a hardened steel (or tungsten carbide) spherical indenter is used. The diameters used are 1, 2, 2.5, 5, 10 mm. Standard load ranges are between 500 and 3000 kg in 500 kg increments. During a test, the load is maintained constant, and the diameter of residual impression is averaged from its measurements in two orthogonal directions. Assuming that the radius of the impression curved surface area is equal to the indenter diameter, Brinell hardness number, *B.H.N*, is then defined as the ratio of the applied load to the curved surface area of the resulting indentation:

$$B.H.N = \frac{2P}{\pi\left(D^2 - D\sqrt{D^2 - d^2}\right)} \qquad \text{Eq. 2-1}$$

where P is the applied load, D is the ball diameter, and d is the chordal diameter of the residual indentation. Brinell hardness is load dependent. Hence, both the load and the ball size should be mentioned when reporting the hardness of a material. For steel ball indenters, the Brinell hardness test is not recommended for testing materials whose hardness is in excess of 400. A spherical indentation can also yield Meyer's hardness [20], or the mean pressure p_m, which is ratio of the load applied to the projected area of the residual indentation:

$$p_m = \frac{4P}{\pi d^2} \qquad \text{Eq. 2-2}$$

- **Rockwell hardness test**

The indenters in Rockwell tests include hardened steel balls with diameters of 1/16, 1/8, 1/4, 1/2 in., and a conical diamond indenter, which is used for harder materials. With this system a hardness number is determined by the difference in depth of penetration resulting from the application of an initial minor load and followed by a larger major load. Several different scales may be used. The hardness number used is designated R_b for spherical indenters and R_c for a conical indenter. Both hardness number and scale symbol must be indicated. On the basis of the magnitude of both major and minor loads, there are two types of tests: Rockwell and superficial Rockwell.

- **Vickers hardness test**

This test employs a square-base diamond pyramidal indenter. The angle between opposite faces of the pyramid is 136° and this was chosen so that close correlation can be obtained between Vickers and Brinell hardness. The two diagonal measurements of the residual impression are averaged and the pyramidal surface area of contact is then calculated assuming that the residual impression is of an included angle equal to that of the pyramidal indenter. Vickers hardness, H_v, is defined as the ratio of the applied load to the pyramidal surface area of the indent, and is calculated from the following expression

$$H_v = 1.854\frac{P}{l^2} \qquad \text{Eq. 2-3}$$

where l is the mean diagonal of the pyramidal indentation. The standard loads used in this test are 1, 2.5, 5, 10, 20, 30, 50, and 100 kg. In a Vickers test, there is geometrical similarity between impressions under different indenter loads, and the hardness number is independent of the load, except for very low loads at which there is often a higher hardness owing to a *skin* effect on the test piece. Another advantage of the Vickers test is that it can be used to test hard materials that are far in excess of that possible with the steel ball in the Brinell test.

- **Knoop and Vickers micro-hardness tests**

These tests are different from the previous ones as they are on the micro scale for which the applied load is of the order of grams. For each test of Knoop and Vickers micro-hardness, a very small diamond indenter having a pyramidal geometry is forced into the surface of the specimen. The difference between the two is in the geometry of the pyramidal indenter. The Vickers indenter is a square based pyramidal diamond while the Knoop indenter is a rhombic based pyramidal diamond that produces a diamond shaped indenter with a ratio between long and short diagonals of 7:1. The applied loads are much smaller than for Rockwell and Brinell, ranging between 1 and 1000 g and the hardness numbers are denoted by H_k and H_v, respectively. The mean diagonal of the indentation is measured, thus the corresponding surface area of the indentation is calculated based on the assumption that it has the same geometry as the indenter. For a Vickers micro-hardness test, the hardness is calculated using Eq. 2-3. For a Knoop test, the hardness number is calculated using the following equation

$$H_k = 14.2\frac{P}{l_k^2} \qquad \text{Eq. 2-4}$$

where l_k is the measured long diagonal of the residual indent.

2.2 Instrumented micro-indentation technique

In hardness measurements, plastic deformation is incorporated in the indentation. A closed form solution for the plastic stage of indentation is a very complex problem since the constitutive equations are non-linear and a number of material parameters must be included to describe the material behaviour. Analytical solutions are not easily obtained. As a result, more insight on the plastic behaviour of materials during indentation has been gained through load and depth sensing experiments and finite element simulation.

The development of the instrumented hardness technique with the capability of continuous high-resolution measurement of forces and displacements has made it possible to probe the mechanical properties of a surface at localised positions and map its properties on the micrometre scale. The outcome of an experiment using an instrumented micro-hardness tester is the load-depth indentation data. The testing pattern at each location is either in one cycle or in multiple cycles in which partial unloading takes place at the end of each cycle then the load is applied progressively in the succeeding cycle involving load increase.

The two mechanical properties measured most frequently using this technique are the elastic modulus E and the hardness H. Methods for determining the post-yield stress-strain relationship have also been applied. The latter can be expressed as a power law in the form

$$\sigma = K\varepsilon^n \qquad \text{Eq. 2-5}$$

where σ is the true stress or flow stress, ε the logarithmic strain, K is the material strength coefficient and n the strain hardening exponent. Interest in load and displacement sensing during indentation as a means of measuring the elastic modulus of the indented material began in the early 1970's with the work of Bulychev *et al.*[21] on instrumented micro-hardness testing machines.

The direct measurement of the residual impression in the case of a micrometre indentation is difficult and tedious. Hence there was a great need to estimate the contact area at a peak load through the load-displacement data. This should be based on the knowledge of the contact depth, h_c, at the peak load in conjunction with the indenter area function, X_b, which relates the projected area at certain distance from the tip to this distance, and is ideally given by

$$A = X_b h_c^2 \qquad \text{Eq. 2-6}$$

where X_b is equal to 24.5 for the Vickers indenter. Since with the Vickers indenter it is inevitable to form a line tip where four planes intersect, an equilateral triangle-base pyramidal indenter known as the Berkovich indenter has been more frequently used and favoured over Vickers as it can have a pointed tip. The Berkovich indenter has an included half angle of 65.3° between a face and the vertical axis so as to give the same area function as Vickers, but with X_b equal to 24.56. However, hardness measurements using the Berkovich indenter were reported to be slightly larger than those with Vickers [22]. It should be noted that the original Berkovich indenter [23] had a slightly different angle, that of 65.03°, which gives the same surface area to depth ratio as a Vickers indenter.

Several approaches were developed that aim to analyse the load-depth indentation data in order to evaluate the material mechanical properties. These data are the outcome of the interaction between the indented material and the indenter itself. Both the material and the geometry of the indenter have an influence on the resulting indentation data, and should be taken into account when analysing the indentation curve. As a result, analytical approaches were developed accordingly.

2.3 Theoretical studies on contact

2.3.1 Elastic contact

The hardness problem was first addressed in terms of elastic contact in the 19th century by Hertz [24] and Boussinesq [25]. Boussinesq developed a method to compute the stresses and displacements in a semi infinite elastic body loaded by a rigid, axisymmetric flat punch. Hertz analysed the problem of the elastic contact between two spherical surfaces with different radii and elastic constants. His solutions comprise the basis of theoretical work in the field of contact mechanics [26]. In the Hertzian theory, several assumptions were made:

- The surfaces of the bodies in contact are continuous.
- The strains are small: $a_c \ll R$, where a_c is the contact area radius and R is the indenter radius.
- Each solid can be considered as an elastic half space.
- The surfaces are frictionless.

Contact deformations and stresses are calculated assuming a pressure distribution over the area of contact that obeys the equation

$$p(r) = p_0 \left(\frac{a_c^2 - r^2}{a_c^2} \right)^{0.5} \qquad \text{Eq. 2-7}$$

where r is the radial distance from the contact centre, and p_o is the pressure at the centre of the contact area, which is the maximum value for the contact pressure. The contact area radius and p_0 are calculated from

$$p_0 = \frac{3}{2} p_m = \frac{3P}{2\pi a_c^2} = \left[\frac{6P}{\pi^3} \left(\frac{E_r}{R} \right)^2 \right]^{\frac{1}{3}} \qquad \text{Eq. 2-8}$$

$$a_c = \left(\frac{3PR}{4E_r} \right)^{\frac{1}{3}} \qquad \text{Eq. 2-9}$$

where p_m is the mean pressure, and E_r is the reduced modulus, or composite modulus, which accounts for the case of a deformable indenter and is determined by

$$\frac{1}{E_r} = \frac{1-\nu_s^2}{E_s} + \frac{1-\nu_i^2}{E_i} \qquad \text{Eq. 2-10}$$

and in the case of a rigid indenter Eq. 2-10 reduces to

$$\frac{1}{E_r} = \frac{1-\nu_s^2}{E_s} \qquad \text{Eq. 2-11}$$

where ν is Poisson's ratio, and the subscripts i and s refer to the indenter and the specimen, respectively. The penetration depth at the centre can be calculated using the following expression:

$$h_e = \frac{1-\nu_s^2}{E_s} \frac{3P}{4a_c} = \frac{1-\nu_s^2}{E_s} \sqrt[3]{\frac{9E_r P^2}{16R}} \qquad \text{Eq. 2-12}$$

The mutual approach of distant points in two bodies during contact is obtained from

$$\delta = \frac{a_c^2}{R} = \left(\frac{9P^2}{16RE_r^2} \right)^{\frac{1}{3}} \qquad \text{Eq. 2-13}$$

For ν=0.3 the maximum shear stress, τ_{max}, occurs at $0.48a_c$ below the centre of the contact area, and is determined from

$$\tau_{\max} = 0.31 p_0 = 0.47 p_m \qquad \text{Eq. 2-14}$$

The condition for plasticity is reached at that point of maximum shear when the shear stress becomes equal to half the yield stress σ_y

$$\tau_{\max} = 0.5\sigma_y \qquad \text{Eq. 2-15}$$

At this stage of first plasticity, the mean pressure, defined in Eq. 2-8, is

$$p_m \cong 1.1\sigma_y \qquad \text{Eq. 2-16}$$

Sneddon [13] derived a general relationship between the load, displacement, and contact area for a punch that can be described as a solid of revolution of a smooth function. His results show that the load-displacement, *(P-h)*, relationship for many simple punch geometries can be written as

$$P = \varphi h_e^q \qquad \text{Eq. 2-17}$$

where h_e is the elastic penetration depth, φ and q are constants. Values of the exponent q for some geometries are: q = 1 for flat cylinder, q = 2 for cones, q = 1.5 for spheres in the limit of small displacements, and paraboloids of revolution. For q greater than 1, elastic deformation is thus linear with load.

2.3.2 Plastic deformation - spherical indentations

As pointed out in the previous section, when the spherical indenter is loaded into the surface, the metal surface will deform elastically according to the classical equations of Hertz [24]. This stage continues until plasticity commences at maximum shear stresses and the mean pressure $p_m \cong 1.1\sigma_y$. As the applied load increases, the plastic zone beneath the indenter grows and the mean pressure increases until the plastic zone surrounds the whole indentation and reaches the surface comprising the onset of the full plastic stage. Between the point of the first yield and fully plastic flow there is a range of behaviour where both elastic and plastic strains influence the deformation and the indentation pressure. It is noteworthy that these stages are clearly distinguished when indenting with blunt indenters, such as the spherical indenters. In contrast, indenting using pointed indenters produces plastic flow when the indenter touches the surface at low loads. Once penetration has commenced the flow pattern is unchanged.

For an ideal plastic material, Tabor [14] has correlated the mean pressure p_m to the yield stress in simple compression σ_y , for an ideal plastic material, through the constraint factor C. The relation has the form

$$p_m = C\sigma_y \qquad \text{Eq. 2-18}$$

For strain hardening materials, the yield stress is replaced by the true stress σ_r corresponding to the representative strain (see Section 2.6.1), and Eq. 2-18 will become

$$p_m = C\sigma_r \qquad \text{Eq. 2-19}$$

The condition of reaching the fully plastic stage has no close form solution for spherical indentations. Ishlinsky's analysis [27] showed that, over a wide range of experimental conditions, $p_m = 2.6\sigma_y$ -$2.9\sigma_y$. A value of $3\sigma_y$ was a good approximation. Experimental work by Tabor [14, 28] has found that the constraint factor, C, varies from 2.8 for mild steel and copper to 2.9 for aluminium.

Johnson [29] through his experimental work on shallow indentations using spherical indenters, proposed that the indentation pressure induced is governed by the single parameter $(E/\sigma_r)\tan\beta$, where β is the angle between the tangent to the indenter at the indentation edge and the original surface. This parameter can be interpreted as the ratio of the characteristic strain imposed by the indenter to the maximum strain that can be accommodated by the material before yielding. With strain-hardening materials, σ_r was taken to be the true stress at a representative strain of 0.2 $\tan\beta$. This parameter can also be used to identify the development of plastic deformation during the indentation process, which consists of three stages: (i) a reversible, elastic deformation at which $(E/\sigma_r)\tan\beta<2$; (ii) a permanent, plastic deformation when $(E/\sigma_r)\tan\beta>50$; or (iii) both plastic and elastic deformation when $2<(E/\sigma_r)\tan\beta<50$.

2.3.3 Ideal plastic solid indented by a flat punch

This problem has been solved using the slip line method by Prandtl [30, 31]. For a flat punch the fully plastic stage will be achieved when the normal pressure of the punch satisfies the condition:

$$p_m = 2\lambda(1 + 0.5\pi) \qquad \text{Eq. 2-20}$$

According to Tresca yield criterion, $2\lambda = \sigma_y$, while the von Mises criterion requires $2\lambda = 1.15\sigma_y$. Hence, the yield pressure, which is the mean pressure at the fully plastic stage, will vary between $p_m = 2.6\sigma_y$ and $3\sigma_y$. Hencky [31] and Ishlinsky [27] have shown theoretically that the fully plastic stage will be achieved when the mean pressure of the punch satisfies the condition: $p_m = 2.84\sigma_y$. As a result, the constraint factors in the case of the circular flat punch and the spherical indenter are similar.

2.3.4 Plastic deformation by pyramidal indentation

The hardness obtained by using pointed indenters is practically independent of the load but it depends on the included angle of the indenter. The smaller the angle is, the larger the mean pressure.

A theoretical relation between the mean pressure and yield stress for ideal plastic material has been found based on a two-dimensional model for a wedge and adopting von Mises criterion (Hill *et al* [32])

$$p_m = 1.15\sigma_y(1+\theta) \qquad \text{Eq. 2-21}$$

where θ is related to α, the semi-included angle of the indenter, through the relation

$$\cos(2\alpha-\theta)=\frac{\cos\theta}{1+\sin\theta} \qquad \text{Eq. 2-22}$$

Hence for a wedge with a semi-included angle between 70° and 90°, the mean pressure is of the order $3\,\sigma_y$. The solution for the two-dimensional wedge is roughly valid for the three-dimensional indenter, particularly if the semi-angle is not too small. This is supported by the observations of Tabor [14] who reported that for conical indenters of semi-angle greater than 60° and for a square pyramidal indenter of semi-angles of 68° the theoretical value for the mean pressure is also $3\sigma_y$. However, Tabor found experimentally that the corresponding mean pressure is about $3.2\sigma_y$ to $3.3\sigma_y$. The discrepancy was attributed to the fact that the flow pattern for three-dimensional deformation is different from that which is obtained in two-dimensional deformation. The discrepancy becomes more marked for indenters of small included angles. The mean pressure was noticed to increase as the semi angle decreases unlike the two-dimensional model.

2.3.5 Expansion of a spherical cavity in an elastic-plastic half space

Johnson [29] has proposed a simplified theoretical model for indentation by extending Hill's theory [33] on expanding a cylindrical or spherical cavity in an elastic-plastic material. This model considers the surface of the indenter to be encased in a semi-cylindrical or hemispherical 'core' of radius a, which is the contact radius, and the mode of deformation was assumed to be radial expansion caused by the hydrostatic stress beneath the indenter within the core.

The elastic-plastic boundary in the model coincides with the boundary of the core ($c_r/a=1$) at $p_m/\sigma_y = 1.1$. At the fully plastic pressure, the elastic boundary moves out to make $c_r/a \approx 2.5$. For a pyramidal indenter, as it is not a solid of revolution, β was taken to be the equivalent angle for a cone, which displaces the same volume of material as the pyramidal indenter for the same indentation depth. Considering the equivalent cone angle enables the use of the cone indenter, as it is a solid of revolution, in modelling indentation produced by pyramidal indenters. For a Vickers diamond pyramid, β was taken as 19.7°. Johnson [29] showed that the dependence upon the single parameter $((E/\sigma_r)\tan\beta$ appears to correlate with the experimental results reasonably well up to values of $\beta = 30°$. With sharper indenters, the work of Hirst and Howse [34] with cones, showed that the deformation mode was different and correlation of indentation pressures on the basis of $(E/\sigma_r)\tan\beta$ is no longer appropriate.

Marsh [35] likened the mode of deformation of Vickers indentation to that of a spherical cavity in an elastic-plastic material. He found that the indentation pressure for a variety of materials, measured with a Vickers indenter, followed the relation

$$\frac{p_m}{\sigma_y} \approx 0.07 + 0.6\ln\left(\frac{E}{\sigma_y}\right) \qquad \text{Eq. 2-23}$$

which is similar in form to the theoretical expression derived by Hill [33] for the pressure necessary to expand a spherical cavity in an elastic-plastic infinite solid, viz.

$$\frac{p_m}{\sigma_y} = 0.40 + \frac{2}{3}\ln\left(\frac{E}{\sigma_y}\right) \qquad \text{Eq. 2-24}$$

2.4 Determination of elastic modulus and hardness

Hardness and elastic modulus are determined from direct analysis of the unloading indentation curve. All approaches rely on the following observations in their analysis:

- The recovered deformations on unloading are considered elastic so that the elastic solution of contact can be applied.
- During unloading, there is appreciable recovery in depth whilst there is practically negligible change in the diameter of the indentation, less than 3%.
- During indentation, the contact perimeter is depressed downwards elastically, and regains its original position upon unloading.

When indenting a material using a spherical indenter, the residual contact impression was found by Tabor [14] to be still spherical but with a slightly larger radius than that of the indenter. The elastic loading and unloading of such an impression can thus be described as a spherical ball of one size elastically deforming in a spherical hole of another, which is a problem of Hertzian contact. When indenting a material using a conical indenter, as observed by Stilwell *et al.* [36], the residual impression is still conical but with a larger included tip angle than that of the indenter.

2.4.1 Approach based on pyramidal indentations

Analysing the unloading curve to determine hardness and elastic modulus was based on Sneddon's solution [13] of an elastic half space indented by an elastic punch that can be described as a solid of revolution. The important feature of his solution was that it related the elastic modulus to the slope of the unloading curve at the initial stage, namely the contact stiffness. The basic assumption is that during the initial withdrawal of the indenter, the contact area between the indenter and the specimen remains constant. This was the basic framework of all approaches that analyse the unloading curve to determine hardness and elastic modulus.

Sneddon's analysis on indenting an elastic half space with a flat rigid cylindrical punch leads to a simple relation between P and h_e of the form [13]

$$P = \frac{4a_c G_s}{1 - \nu_s} h_e \qquad \text{Eq. 2-25}$$

where a_c is also the radius of the cylinder and G_s is the shear modulus. Oliver and Pharr proposed a method [15, 37] based on the above solution and Tabor's observations [14]. Rewriting Eq. 2-25 in terms of E and the area of the contact circle, A, and then differentiating it with respect to h_e in order to obtain the contact stiffness gives

$$S=\frac{dP}{dh_e}=\frac{2}{\sqrt{\pi}}E_r\sqrt{A} \qquad \text{Eq. 2-26}$$

where S is the stiffness of the upper portion of the unloading data. Hence, by measuring the initial unloading stiffness and assuming that the contact area is equal to the measured area of the residual impression, Eq. 2-26 can be used to calculate the reduced elastic modulus. However, applying Eq. 2-26 to the unloading indentation data, assuming the recovery is elastic, is questionable as it was derived based on the following two assumptions:

- The surface of the indented material is flat.
- The indenter is a cylindrical punch so that the contact area is constant during indentation.

Oliver and Pharr [37] showed that Eq. 2-26 is still valid for describing the elastic behaviour of a material when unloading the indenter, and the fact that the indented surface is not flat does not appear to impose severe restrictions on the application. They also showed that the equation is independent of the indenter geometry which means that methods for determining contact area and elastic modulus from the initial unloading slope of load-depth sensing indentation data can be used even when the contact area between the indenter and the specimen changes continuously as the indenter is withdrawn and the indenter does not behave like a flat punch.

Although Berkovich and Vickers indenters are not bodies of revolution, Eq. 2-26 can still be used with negligible error. This follows from finite element calculations of the load-displacement characteristics of elastic half spaces deformed by flat-ended punches with circular, triangular and square cross sections performed by King [38]. The latter two geometries are equivalent to the Berkovich and Vickers indenters. King found that for all three geometries, the unloading stiffness is given by

$$\frac{dP}{dh_e}=\eta\frac{2}{\sqrt{\pi}}\sqrt{A}E_r \qquad \text{Eq. 2-27}$$

where the values of the constant η are 1.0, 1.034, and 1.012 for circular, triangular, and square cross-sections, respectively. This means that the value for η for triangular and square indenters will deviate from the circular one by only 3.4% and 1.2%, respectively.

Doerner and Nix [12] suggested that the unloading stiffness can be determined by fitting a straight line to the upper one-third of the unloading curve. This was justified by the experimental observations they carried out which suggested that the initial portion of the unloading curve is linear. This means that the contact area between the indenter and the specimen remains constant and the relationship between the contact stiffness, the contact area, and the elastic modulus is not dependent on the geometry of the punch. Hence, Sneddon's analysis for the indentation of an elastic half space by a flat cylindrical punch is considered to approximate the real behaviour.

Oliver and Pharr [37] subsequently carried out nano-indentation experiments using the Berkovich indenter on different materials that span a range of hardness and elastic modulus. They suggested that a specimen should be loaded and unloaded three times in succession to ensure the reversibility of the deformation, and the peak load should be held for 100 s to allow for any creep effect to diminish. They plotted the unloading curves on logarithmic axes and proved that none of the curves were linear. In fact they were slightly concave upwards. They fitted the unloading curve to a simple power law function in the form of Eq. 2-17. By substituting h_e with $(h-h_r)$ where h_r is the residual depth, Eq. 2-17 becomes

$$P = \varphi(h-h_r)^q \qquad \text{Eq. 2-28}$$

The parameters φ, q, and h_r are determined by the fitting procedure. It was observed that the power law exponents for the test materials varied from 1.25 to 1.51 with a mean value of 1.40. This means that none of the data is consistent with flat punch behaviour.

The value obtained for the unloading stiffness together with the indentation projected area are substituted in Eq. 2-26 to calculate the elastic modulus. Hence there was a great need to estimate the contact area at peak load through the load-displacement data. This should be based on the knowledge of the contact depth h_c at the peak load in conjunction with the indenter area function. Doerner and Nix [12] suggested that the contact depth,

h_c, is obtained by extrapolating the initial linear portion of the unloading curve to zero load.

In the indentation of electro-polished tungsten, a continuous measurement of the contact stiffness, which is a measure of the contact area as well, proved that the contact stiffness changes immediately and continuously as the specimen was unloaded. Thus, the contact area is not constant during unloading even during the initial stages of unloading. This means that the flat punch is not an adequate approximation. Oliver *et al.* [37] proposed a procedure to account for the curvature in the unloading data in determining the contact depth, which is used in conjunction with the indenter shape function to establish the contact area at peak load. It was assumed that the behaviour of the indenters that can be described as a body of revolution would give a better description for a Berkovich indenter. Hence, in this solution a conical indenter, equivalent to the Berkovich indenter, was chosen for modelling the indentation. The included angle of the cone was taken to give the same area function as the Berkovich indenter. At any time during indentation, the total displacement h_t is written as

$$h_t = h_c + h_s \qquad \text{Eq. 2-29}$$

where h_s is the deflection of the surface at the contact perimeter, which depends on the indenter geometry, as illustrated below in Fig. 2-1 that shows the indentation profile assumed by the Oliver and Pharr approach when loading and unloading.

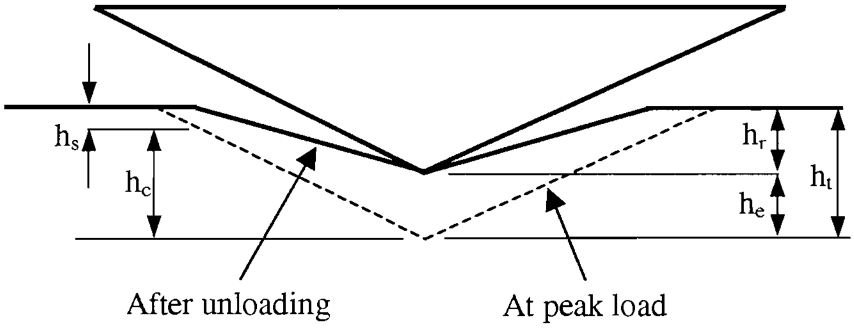

Fig. 2-1 The profile of an indentation at peak load and after unloading for a pyramidal indenter.

For a conical indenter, h_s is given by [13]

$$h_s = \frac{\pi - 2}{\pi}(h_t - h_r) \quad \text{Eq. 2-30}$$

where $(h_t - h_r)$ is the elastic displacement at the indenter tip. Sneddon's force-displacement relationship (Eq. 2-28) for a conical indenter $(q = 2)$ yields

$$(h - h_r) = 2\frac{P}{S} \quad \text{Eq. 2-31}$$

Substituting Eq. 2-31 into Eq. 2-30 gives

$$h_s = \chi \frac{P_{\max}}{S} \quad \text{Eq. 2-32}$$

where the geometry constant χ for the conical indenter is given by

$$\chi = \frac{2}{\pi}(\pi - 2) = 0.72 \quad \text{Eq. 2-33}$$

For a flat punch, $\chi = 1.0$, and for paraboloids of revolution, $\chi = 0.75$. It can be seen now why Doerner and Nix in their analysis used the value 1.0 for χ, which is the case for flat punch as their analysis was based on flat punch behaviour. Having found the contact area at the peak load, the hardness can be determined through the equation

$$H = \frac{P_{\max}}{A} \quad \text{Eq. 2-34}$$

The reduced modulus can then be calculated from Eq. 2-27. Oliver *et al.* [37] compared the measured residual contact areas using Scanning Electron Microscopy (SEM) with the calculated ones and reported a good agreement except for aluminium whose calculated areas were smaller than the imaged ones, which was attributed to the pile up around the indentation. It was suggested that a paraboloid geometry for the indenter can best describe the unloading behaviour and matches well the predicted mean value for the power law exponent, which was found equal to 1.40 that is very close to that predicted by Sneddon's analysis for paraboloid.

Oliver and Pharr [37] reported that the power law method for fitting is less sensitive to creep and that the stiffness measured from the first unloading data was slightly greater than that from the last unloading curve. However, when linear fitting was used to measure the initial unloading stiffness, the fraction size of the unloading curve used for the fit affected significantly the contact stiffness. The modulus values predicted by their method were compared with the values measured by different methods. The difference was within 4% except for sapphire and quartz whose measured modulus was higher by about 9% for sapphire and 30% for quartz. This was attributed to the anisotropy, the influence of which was not fully investigated, and it was suggested that the measured value should be some average quantity. Fischer-Cripps [39-41] verified the approach of Oliver and Pharr on experimental and simulation indentation data.

Hay *et al.* [42] investigated the applicability of Sneddon's solution that assumes a rigid conical indenter penetrating an elastic half-space. They compared Sneddon's analytical solution with the finite element simulations, under the same boundary conditions. FE results showed that Sneddon's solution deviates from the physical interpretation of a rigid conical indenter in that the deformed surface of an indent does not conform to the indenter profile. Rather, the radial displacement within the contact radius is inwards virtually penetrating the indenter surface. The severity of this deviation depends on both the semi-included angle of the indenter tip and the Poisson's ratio of the material being indented. Sneddon's solution was found to underestimate the actual contact radius by up to 9% and 27% for rigid conical indenters with half-included angles of 70.32° and 42.28°, respectively. Hay *et al.* proposed an aproximate analytical correction to the Sneddon relationships for the case of a right circular cone of arbitrary included angle. This was presented by the factor γ, which accounts for the effect of the indenter angle and Poisson's ratio, given by

$$\gamma = 1 + \frac{(1-2\nu)}{4(1-\nu)\tan\alpha} \qquad \text{Eq. 2-35}$$

The correction factor is implemented in determining the contact area from the instrumented hardness experimental data. Hence, Eq. 2-27 is modified to

$$S = \frac{dP}{dh_e} = \gamma(\eta\frac{2}{\sqrt{\pi}}\sqrt{A}E_r) \qquad \text{Eq. 2-36}$$

A new technique, called the slope technique, was later proposed by Oliver [43] to measure the elastic modulus and hardness from the analysis of the indentation data with the Berkovich indenter. In this technique the initial contact stiffness at the cycle peak on both the loading and the unloading curves are utilised. The determination of the loading curve was based on the work by Malzbender and Toonder [44] who proposed that the loading curve produced with a perfect Berkovich indenter is given by

$$P = E_r \left(\frac{1}{\sqrt{X_b}} \sqrt{\frac{E_r}{H}} + 0.75 \sqrt{\frac{\pi}{4}} \sqrt{\frac{H}{E_r}} \right) h^2 \qquad \text{Eq. 2-37}$$

Combining the initial contact stiffness from the loading curve at the cycle peak with that from the unloading curve, Oliver proposed the following equations to obtain the reduced modulus and hardness.

$$E_r = \sqrt{\frac{\pi}{X_b}} \frac{1}{2\eta P_{\max}} \left(\frac{S^2 S_l}{2S - 0.75 S_l} \right) \qquad \text{Eq. 2-38}$$

where S_l is initial contact stiffness from the loading curve at the cycle peak. The contact area is given by

$$A = X_b P_{\max}^2 \left(\frac{2S - 0.75 S_1}{S S_l} \right)^2 \qquad \text{Eq. 2-39}$$

and hardness can be computed from

$$H = \frac{1}{X_b P_{\max}} \left(\frac{2S - 0.75 S_l}{S S_l} \right)^{-2} \qquad \text{Eq. 2-40}$$

Results from this technique agree well with those from the original one that is based on Eq. 2-26 for deep indentations. However, this technique was shown to be less sensitive to the tip roundings thus more accurate estimation of the hardness measurement at shallow indentation can be obtained. On the other hand, it assumes that the peak of the loading curve coincides with the start of the unloading curve with no presence of creep, time dependent deformation.

2.4.2 Approach based on spherical indentations

Field and Swain [45, 46] proposed a method based on a cyclic loading routine with multiple partial unloading, which allows an estimate to be made of the impression depth for all load steps by employing the Hertzian elastic solution during unloading. The basis of their approach is Eq. 2-13, which they rewrote in the form

$$h_e = QT = \frac{a_c^2}{R} \text{ (for rigid indenter)}$$

$$Q = \sqrt[3]{\frac{9}{16}\left(\frac{P}{E_r}\right)^2}\ , T = \sqrt[3]{\frac{1}{R}} \qquad \text{Eq. 2-41}$$

where $1/R$ is the curvature of the contact surface. It is worth remembering that Eq. 2-13 assumes indenting a flat surface with a sphere. However, partially unloading an indentation from the peak load P_{max} to an intermediate value P_{int} is elastic and is equivalent to reloading a residual impression into reconformation with the indenter. The total penetration is the sum of the depth of the residual impression and the elastic displacement associated with its reloading. The problem of loading a residual spherical impression was analysed by Goodman *et al.* [47]. In order to make the above equation valid to describe the unloading behaviour in which the indented surface is not flat, the curvature of the indented surface should be considered. This was done by introducing the effective radius R_r defined through

$$\frac{1}{R_r} = \frac{1}{R} - \frac{1}{r_2} \qquad \text{Eq. 2-42}$$

where r_2 is the radius of curvature of the residual impression. Field and Swain's approach is only concerned with the fully plastic stage of indentation, which was assumed to start when C approaches 3.0.

When partially unloading an indentation, Field and Swain assume that the elastic recovery h_e is known as well as the contact radius a_c. Hence

$$T = \sqrt[3]{\frac{h_e}{a_c^2}} \qquad \text{Eq. 2-43}$$

The contact depth can then be determined from

$$h_c = R - \sqrt{R^2 - a_c^2} \qquad \text{Eq. 2-44}$$

The depth of the loaded indentation below the original surface is

$$h_t = h_r + h_e = h_c + \frac{h_e}{2} \Rightarrow h_r = h_c - \frac{h_e}{2} \qquad \text{Eq. 2-45}$$

Fig. 2-2 shows the geometry of the profile of an indentation when it is fully unloaded.

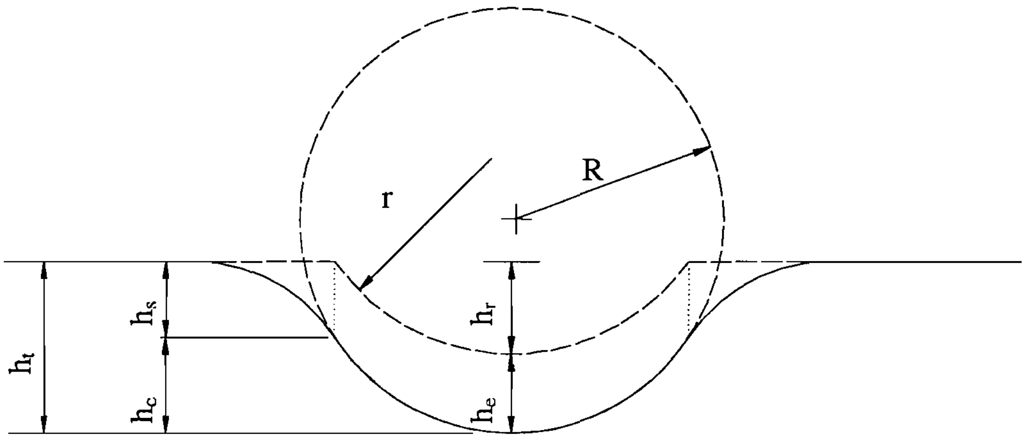

Fig. 2-2 Schematic relationship between the depth of loaded and unloaded indentation

Field and Swain's approach assumes that the unloading curve can be described by Eq. 2-28 with q=1.5, which is a short form of Eq. 2-41. It was suggested that only two points on the unloading curve are required to determine this equation. The first point is the one at peak load and the second is at any intermediate position of the unloading curve. The direct aim of this is to determine the residual depth h_r that follows from

$$h_r = \frac{h_{\text{int}}\left(\dfrac{P_{\max}}{P_{\text{int}}}\right)^{2/3} - h_t}{\left(\dfrac{P_{\max}}{P_{\text{int}}}\right)^{2/3} - 1} \qquad \text{Eq. 2-46}$$

where P_{int} is an arbitrary intermediate load value on the unloading curve. The contact depth in this case is found from Eq. 2-45 as

$$h_c = \frac{h_t + h_r}{2} \qquad \text{Eq. 2-47}$$

From the contact depth, the contact radius of the circle of contact is given by

$$a_c = \sqrt{2Rh_c - h_c^2} \qquad \text{Eq. 2-48}$$

The reduced modulus can then be determined directly from

$$E_r = \frac{3}{4}\frac{Ph_e}{a_c} \qquad \text{Eq. 2-49}$$

Field and Swain applied their approach to different materials and found that the material response under indentation was underestimated. They managed to achieve a good agreement when they assume a larger value for the indenter radius in their calculations by 30% and 44% for the 50 μm and 5 μm radius indenters, respectively. They justified this from their observations of interferograms of the tip which showed a slight flattening to the spherical shape at the tip as if material was missing. Their prediction of the elastic modulus of aluminium ranged between 70 and 150 GPa whilst the calculated hardness varied between 0.9 and 1.1 GPa [46]. This approach was reviewed and verified by others, e.g. Fischer-Cripps [40, 41, 48-51].

Hay *et al.* [52] also proposed a correction to Eq. 2-49. Their idea was based on the discrepancy between the boundary conditions for the elastic contact problem (in which the deformed surface within the contact radius must fall on the indenter profile) and the inward radial displacement resulting from analysing the indentation data using Hertzian analysis. Hertzian radial displacement within the area of contact is given by

$$U_r = -\frac{(1-2\nu_s)(1+\nu_s)}{3E_s}\frac{a_c^2}{r}p_0\left[1-\left(1-\frac{r^2}{a_c^2}\right)^{3/2}\right] \quad : r \le a_c \qquad \text{Eq. 2-50}$$

hence the contact radius can be calculated from the radial displacement added to the original radial coordinate of the contact edge as follows

$$a_c = r + U_r \qquad \text{Eq. 2-51}$$

Based on the approach of Hay et al. [52] the corrected Hertzian relation can be written in the form

$$P = \gamma_b \frac{4}{3} E_r \sqrt{R_r}\, h_e^{1.5} \qquad \text{Eq. 2-52}$$

thus

$$E_r = \frac{3}{4}\left(\frac{P}{\gamma_b}\right)\frac{1}{\sqrt{R_r}\, h_e^{1.5}} \qquad \text{Eq. 2-53}$$

where the correction factor γ_b is defined by

$$\gamma_b = 1 + \frac{2}{3\pi}\frac{E_r}{E_s}\frac{(1-2\nu_s)}{(1-2\nu_s)}\frac{a_c}{R_r} \qquad \text{Eq. 2-54}$$

Whilst this correction assumed an infinitely rigid indenter, a similar equation was also proposed to consider a deformable indenter. However, the elastic deformation accommodated during the elasto-plastic indentation is small enough to make the contribution of this correction negligible especially for soft metals, the focus of this research.

2.4.3 Effects of sinking-in and piling-up on estimating the contact area

During indentation, material is displaced around the vicinity of the indenter. It either deforms downwards sinking-in or deforms upwards forming a raised lip surrounding the impression, i.e. piling-up. For a work-hardened material the displaced metal tends to pile-up, whilst with annealed and hard metals, the initial displacement of the metal produces appreciable work-hardening and the metal immediately adjacent to the indentation is depressed, sinking in. For materials exhibiting piling-up during indentation, applying the elastic solution to the unloading curve, which always assumes the contact edges deform downwards, would include an error resulting in underestimating the contact area, which is supposed to lie in a plane above the original surface.

Cheng *et al.* [53] studied the phenomena of piling-up and sinking-in of the surface profiles in conical indentation in elastic-plastic metals that work-harden. Their study was carried out using dimensional and finite element analysis. A rigid conical indenter equivalent to Berkovich indenter was modelled. The contact depth was assumed as a function of the form

$$h_c = h_t \Pi\left(\frac{\sigma_y}{E_r}, n, \alpha\right) \qquad \text{Eq. 2-55}$$

The ratio h_c/h_t can be either greater or smaller than one, corresponding to piling-up and sinking-in, respectively. Based on dimensional analysis, the contact depth, h_c, was shown to be proportional to the indenter displacement, h_t, that is the ratio h_c/h_t is independent of indenter displacement.

The finite element simulation was applied assuming $\nu = 0.3$, $\alpha = 68°$. This meant that h_c/h_t was considered only a function of σ_y / E and n. In each calculation using E, σ_y, and n as input parameters, the loading and unloading curves were obtained together with the contact depth as a function of the indenter displacement. For large σ_y / E sinking-in was predicted for all values of n. For small σ_y / E both sinking-in and piling-up may occur depending on the degree of work hardening.

The Oliver-Pharr procedure for estimating the contact depth under load was found to be valid when the ratio σ_y / E is large (e.g. greater than 0.05 independently of the value of n) or for most σ_y / E values if $n \approx 0.3$. This is expected since this procedure is based on Sneddon's analysis of the surface profiles for elastic contacts. In fact, h_c/h_t estimated using the procedure of Oliver-Pharr is always less than unity. Thus, the procedure may be used with confidence for materials that can accommodate high elastic deformation. For materials with low σ_y / E such as soft metals, the Oliver-Pharr procedure should be used with caution as it could underestimate the contact area by up to 40%. Hence it would lead to an error in estimating the hardness and the reduced modulus.

Bolshakov *et al.* [54] also used finite element analysis to simulate indentations formed by a rigid cone, equivalent to Berkovich. They investigated the influence of the pile-up on the measurement of the contact area and tried to define the condition under which pile-up is significant. Two separate cases of strain hardening were simulated, one with no strain hardening, and the other with a work hardening rate of $d\sigma/d\varepsilon = 10\sigma_y$, based on a bilinear plasticity model. The Poisson's ratio was taken as $\nu = 0.25$ for all materials tested. A measurable material parameter, h_r/h_t was used to identify the expected behaviour of a given material. A parametric study was carried out to investigate the dependence of different material properties on this parameter. The dependence of H/E on h_r/h_t was studied for both extreme cases. The contact area was obtained at peak load, and E was the input value in the modelling. The modelling results of the simulated material showed the following

$$\lim_{h_r/h_t \to 1} (H/E) = 0$$

$$\lim_{h_r/h_t \to 0} (H/E) = 0.207 \qquad \text{Eq. 2-56}$$

A value of 0.191 was expected from Sneddon's analysis for H/E instead of the value of 0.207. This was attributed to the fact that Sneddon's analysis applies to small deformation while the finite element code accounts for finite deformation. The implied error in estimating H/E from h_r/h_t was within 15% for $0.8 < h_r/h_t < 1$ and less than 7% for $0.0 < h_r/h_t < 0.8$. Bolshakov *et al.* showed that the amount of piling-up or sinking-in depends on the amount of work hardening as well as on the value of h_r/h_t. It was noticed that for $h_r/h_t < 0.7$, very little pile-up was found no matter what the work hardening behaviour of the material is, which was supported by the FE simulation carried out by Pharr [55]. As a consequence, the contact areas given by the Oliver-Pharr method match very well the contact areas obtained from the finite element analysis, independent of the amount of work hardening. However, when $h_r/h_t > 0.7$, the pile-up depends on the degree of the work hardening, thus the accuracy of the Oliver-Pharr method depends significantly on the amount of work hardening in the material. If the material is elastic-perfect plastic, the Oliver-Pharr method underestimates the contact area by more than 40% at $h_r/h_t = 0.9735$. It was also observed that for $h_r/h_t > 0.7$, the effective modulus is overestimated by 10 to 16% even if the correct contact area is used.

Bolshakov *et al.* attributed this overestimation to the plastic properties of the material affecting the unloading curves in such a way that the analysis can no longer be done by means of elastic solutions only. It was not possible for them to predict if a material work hardens based solely on the load-displacement data. Therefore, they recommended more care to be taken when $h_r/h_t > 0.7$. However, they reported that for materials with very low h_r/h_t, the method of Oliver-Pharr overestimates the effective modulus by 2 to 9%. This was attributed to the fact that Sneddon's solution needs correction. The geometry of a spherical indentation with piling-up and sinking-in is illustrated in Fig. 2-3.

Norbury and Samuel [56] investigated the pile-up and sink-in effect on the measurement of contact area and how that can be related to the material strain hardening exponent. They measured the contact circle diameter and its elevation on recovered indentations and calculated the contact depth of penetration of the loaded indenter below the circle of contact. They found that the lower n is, the more the tendency for pile-up. The profile characteristics: the contact depth h_c, the displacement of the contact circle relative to the original surface h_l, and the radius of the circle in the plane of the original surface a_0 are related through the parameter c^2

$$c^2 = \frac{h_c}{h_t} = 1 + \frac{h_l}{h_t} \cong \frac{a_c^2}{a_0^2} \text{ or } a_c = ca_0 \qquad \text{Eq. 2-57}$$

where a_0 is given by

$$a_0 = \sqrt{2Rh_t - h_t^2} \qquad \text{Eq. 2-58}$$

The data published by Norbury and Samuel [56] comprised the framework for subsequent research to relate the pile-up extent to the strain hardening exponent through empirical equations that fit these data, which are examined in Section 5.2.2. Matthews [18] extended the Hertzian elastic contact solution to nonlinear viscoelastic materials including materials that work harden according to Meyer's law, and proposed an expression for c^2 that would fit Norbury's data. Richmond *et al.* [57] considered an approach through nonlinear elasticity theory and obtained values for h_l/h_t which lay close to Norbury's data for two materials. Hill *et al.*[58] determined the ratio a_c^2/Dh_t and verified their results by finite element analysis. They based their work on the framework by Hill [17]. They validated Meyer's law and proposed an alternative relation for c^2, which gives better fit to the experimental data than Matthews's expression.

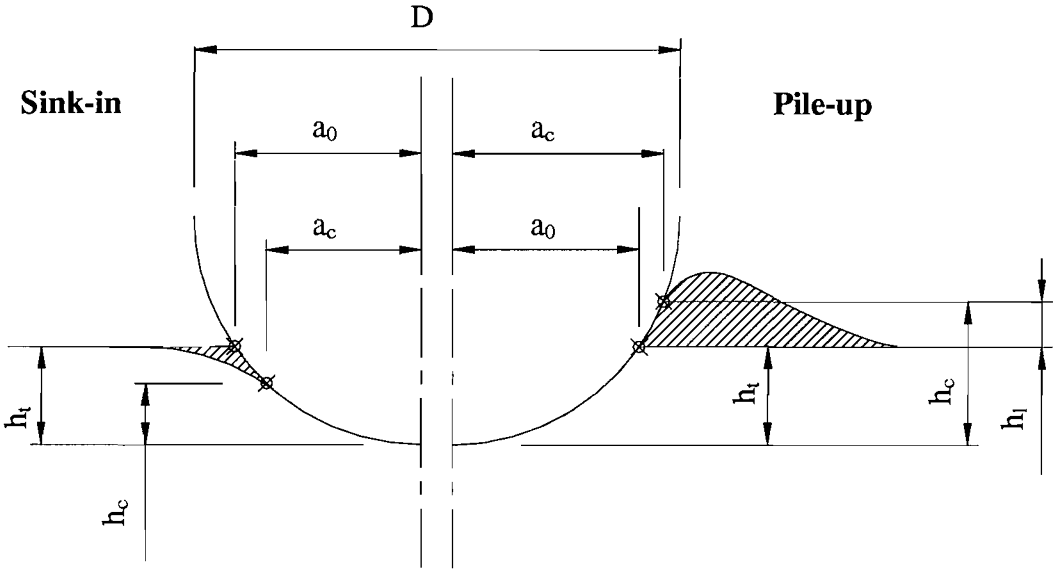

Fig. 2-3 A schematic illustration of spherical indentation with piling-up and sinking-in.

In order to account for the effect of pile-up, Field and Swain proposed in their approach to consider the measurement relative to the original surface and not to take into account any pile-up or sink-in. This would result in calculating the contact radius, a_0, that lies in the plane of the original surface. Hence, the correction is possible provided c can be determined.

Taljat *et al.* [19] produced different c^2 expressions for loaded and unloaded indentations from FE analysis. The pile-up effect was found dependent on n for E/σ_y=500, and two relationships were proposed for both cases. Alcala *et al.* [59] performed indentations with the Vickers indenter and a spherical indenter on ceramics, copper and stainless steel materials. They examined the profile of the residual indents and attempted to relate the surface deformation at the contact edges (i.e. pile-up or sink-in) to the strain hardening exponent for each type of indentation. They carried out a polynomial fitting and came up with the following empirical relations for both types of indenter, namely spherical and Vickers, respectively:

$$c^2 = 1.276 - 1.748n + 2.451n^2 - 1.469n^3 \quad \text{(spherical indenter)} \qquad \text{Eq. 2-59}$$

$$c_V^2 = 1.202 - 0.857n + 0.302n^2 \quad \text{(Vickers indenter)} \qquad \text{Eq. 2-60}$$

2.5 Relation of hardness to plastic flow

2.5.1 Meyer's Law

The relation between load and size of indentation produced by spherical indenters can be expressed by Meyer's law [20]. For a ball of fixed diameter:

$$P = kd^m \qquad \text{Eq. 2-61}$$

where k is a constant, m is Meyer index, which gradually decreases with the development of plastic deformation around the indenter. It ranges from a value of 3 in the elastic stage to a value between 2 for fully work-hardened metals and 2.5 for fully annealed metals at the full plastic stage of indentation at which the total deformation of the material around the indenter is plastic. When balls of different diameters, D_1, D_2, D_3,..., are used, the value of k changes according to:

$$P = k_1 d_1^m = k_2 d_2^m = k_3 d_3^m ..... \qquad \text{Eq. 2-62}$$

Meyer found experimentally that the index m was almost independent of D but that k decreases with increasing D in such a way that

$$X_m = k_1 D_1^{m-2} = k_2 D_2^{m-2} = k_3 D_3^{m-2} ..... \qquad \text{Eq. 2-63}$$

where X_m is a constant. Thus the most general relation involving d and D is

$$P = \frac{X_m d_1^m}{D_1^{m-2}} = \frac{X_m d_2^m}{D_2^{m-2}} = \frac{X_m d_3^m}{D_3^{m-2}} = ... \qquad \text{Eq. 2-64}$$

This can lead to the following:

$$\frac{P}{d^2} = X_m \left(\frac{d}{D}\right)^{m-2} \Leftrightarrow \frac{P}{D^2} = X_m \left(\frac{d}{D}\right)^m \qquad \text{Eq. 2-65}$$

The Meyer index and the strain-hardening exponent are related by $m = n + 2$. By performing a series of spherical indentations at different loads, Meyer law expressed in Eq. 2-65 can be a means of measuring the strain hardening exponent of a material. However, the strain-hardening exponent can also be obtained in two other ways: (i) from the uniaxial engineering strain-strain curve, as n is the true logarithmic strain at the ultimate tensile strength, UTS, Dieter [60], (ii) from fitting the true stress-true strain curve by the power law function in the form of Eq. 2-5.

2.5.2 Correlation between hardness data and yield stress

There have been attempts, Atkins *et al.* [61], to correlate the 0.2% offset yield stress of metals to Vickers hardness. Devenpeck and Weinstein [62] indicated the possibility of obtaining the proportional limit from hardness measurements but did not derive a specific relationship. Cahoon *et al.* [63] attempted to derive an expression which correlated the 0.2% offset yield stress with Vickers hardness for various materials which included the strain hardening exponent. They studied materials strengthened by heat treatment and by cold working. They selected two alloy systems, 65S, age hardening aluminium alloy, and 1040 steel and found that the strain hardening exponent determined from hardness measurements generally agreed within 25% of that obtained from stress-strain curves. For the 65S aluminium alloy, the yield stress could not be correlated directly with hardness but was dependent on the strengthening mechanism. They reported that in a 1040 steel, the strain-hardening exponent was dependent only on hardness and not on the strengthening mechanism. The results showed that the yield stress varies from $H/6$ for an alloy with a high strain hardening exponent to $H/3$ for an alloy with low strain hardening exponent. Cahoon *et al.* [63] came up with the following equation for correlating Vickers hardness with 0.2% offset yield stress:

$$\sigma_y = \frac{H_v}{3}(0.1)^n \qquad \text{Eq. 2-66}$$

This equation was derived from the power law relation between plastic stress and plastic strain, assuming the stress at 8% strain for a Vickers indenter, is $H/3$ for an ideal plastic material. The constant 0.1 was an approximation for $\varepsilon_y/0.08$, which was obtained for steel and aluminium. Comparing the calculated 0.2% offset yield stress with the experimental one, the error was about 16% for steel.

George *et al.* [64] attempted to estimate the 0.2% offset yield strength of hot and cold rolled sheet steel from hardness data using the Rockwell ball indenter. The ball diameter was 1/16 in. Their work was based on Meyer's law, Eq. 2-64 and Eq. 2-65. For each loading cycle, the total penetration depth, h_t, is measured and the corresponding diameter $2a_0$ which lies on the original surface is calculated from Eq. 2-58. Meyer's hardness law, Eq. 2-65, is then applied to determine the material parameter X_m and the strain hardening exponent *n*. Haggag *et al.* [65-67] confirmed the findings of Cahoon *et al.* [63] in that the material parameter X_m can be related to the yield stress by

$$\sigma_y = B_m X_m \qquad \text{Eq. 2-67}$$

where B_m, the material-type constant, has a single value for each type of material. B_m = 0.2285 is applicable to all carbon steels whether cold rolled, hot rolled, or irradiated, and a value of B_m = 0.191 is used for stainless steel materials [66]. For a better fit, Eq. 2-67 can be written in a more general form

$$\sigma_y = b_m + B_m X_m \qquad \text{Eq. 2-68}$$

where b_m is the material yield stress offset constant. Haggag tested different kinds of hard steel and the heat-affected zone of welding [68-72] and reported gradients in hardness and mechanical properties, which could not be correlated using his technique. He attributed this to the paucity of the data.

2.5.3 Correlation between hardness data and ultimate stress

Tabor [28] also correlated the engineering ultimate tensile strength *UTS* with Brinell hardness and with Vickers hardness by the following two equations

$$\frac{UTS}{B.H.N} = \frac{1-n}{2.62}\left(\frac{10n}{1-n}\right)^n \qquad \text{Eq. 2-69}$$

$$\frac{UTS}{H_V} = \frac{1-n}{2.9}\left(\frac{12.5n}{1-n}\right)^n \qquad \text{Eq. 2-70}$$

However, Eq. 2-69 and Eq. 2-70 are only valid for a limited range of alloys.

2.6 Stress-strain curve from indentation data

2.6.1 Representative strain and constraint factor

Tabor reported that the strain at the edge of the Vickers indentation is equal to 8% on the uni-axial stress-strain curve. He also proposed that the strain at the edge of a spherical indentation is proportional to the ratio of the contact area diameter to the indenter diameter, *d/D*. This strain was called the representative strain, ε_r, and is calculated from

$$\varepsilon_r = 0.2\sin\beta = 0.2\frac{a_c}{R} \qquad \text{Eq. 2-71}$$

The corresponding true stress is related to the hardness measurement through the constraint factor, defined in Eq. 2-19. The coefficient 0.2 was obtained by Tabor from measuring Vickers hardness of metals that have been compressed uni-axially by various amounts in order to obtain a relation between hardness number, the amount of deformation or strain at the indentation edges and the true stress. Eq. 2-71 was verified later by Hill *et al.* [58] and Sinclair *et al.* [73] using FE analysis.

In general, the value of the strain at the indentation perimeter depends on the angle between the indenter surface, at the contact edge, and the original surface plane. Therefore, the strain produced by sharp indenters is of a constant value that is related to the included angle of the indenter tip and is independent of the indentation depth. However, in the case of indentation using a spherical indenter, the angle between the indenter surface, at the contact edge, and the original surface increases with indentation depth, as would the corresponding representative strain. Hence, the strain produced by spherical indenters depends on depth of penetration. This is the main advantage of spherical indenters as it should be possible to obtain the stress-strain curve provided the contact area is measured over a range of depth values.

Using Tabor's Eq. 2-71, Au *et al.* [74] proposed the following equation to determine the contact radius from direct measurement of ball indentation depth

$$a_c = 0.5\sqrt{\frac{5.47P_{\max}}{2}D\left(\frac{1}{E_s}+\frac{1}{E_i}\right)\left(\frac{h_r^2+a_c^2}{h_r^2+a_c^2-Dh_r}\right)} \qquad \text{Eq. 2-72}$$

This equation was implemented together with Tabor's equations in order to obtain the stress-strain curve. FE results by Taljat *et al* [19] showed that values of the contact radius obtained by Eq. 2-72 are almost identical to the radius at the original surface plane a_0, meaning that this equation does not consider the pile-up effect on the measured contact area. This is because Eq. 2-72 was developed with the assumption of an ideal spherical depression in which the diameter before and after load application is the same. Hence, the radius it calculates is essentially identical to a_0 if one neglects the change of indentation diameter caused by the elastic deformation of the indenter.

Taljat *et al.* [19] verified Tabor's equation Eq. 2-71 using FE analysis by checking the distribution of the equivalent plastic strain across an indentation profile for three values of *n*, that is, 0, 0.25, 0.5, at a penetration depth corresponding to $a/R = 0.5$. The curves corresponding to the three different *n* values intersected the predicted strain value obtained by Tabor between 0.97*d* and 1.03*d*. As Tabor's equation Eq. 2-71 can cover up to 20% strain, they proposed in their method two extreme values for the representative strain at which the corresponding stress can be calculated. For each strain value, they proposed a set of equations for calculating the constraint factor.

For materials that strain-harden, Eq. 2-19 is still valid if the true stress corresponding to the representative strain was considered. Hence, the mean pressure can be correlated with the true stress, for all indenter geometries, according to the general equation Eq. 2-19. In the case of spherical indentation, the constraint factor *C* equals 2.8-3.0 according to Tabor [14] when full plasticity is reached for an ideal plastic steel. Tabor's equations for correlating hardness with the true stress are valid only during the stage of full plastic indentation; hence the onset of this stage needs to be identified.

Au *et al.* [74] also determined the process of development of the plastic zone beneath the indenter. This was based on the work of Francis [75] who tried to find the value of the constraint factor during the elastic-plastic transition. The set of equations that describe the constraint factor has the form

$$C = \begin{cases} C_1 & \Phi \le 1 \\ C_1 + C_2 \ln \Phi & 1 < \Phi \le C_3 \\ C_{\max} & \Phi > C_3 \end{cases} \qquad \text{Eq. 2-73}$$

where

$$\Phi = \frac{\varepsilon_r E_s}{0.43\sigma_r}$$

Eq. 2-73 predicts C during three mechanical stages: elastic, when C has a constant value; transition, which is a combination of elastic and plastic deformation when C is a linear function of ln(Φ); and fully plastic, when C has a constant value. Francis [75] adopted the following values from his studies: $C_1 = 1.11$, $C_2 = 0.534$, $C_3 = 27.3$ and $C_{max} = 2.87$, whilst the values for these constant by Au *et al* [74] were $C_1 = 1.07$, $C_2 = 0.759$, $C_3 = 24$ and $C_{max} = 3.48$. Nonlinear regression analysis was used to obtain a set of equations, applied iteratively, to predict the homogeneous plastic flow part of the true stress-true strain curve. The large value of $C_{max} = 3.48$ was attributed to the strain rate effect on the flow properties of 1015 steel samples. Low carbon steels generally have higher strain rate sensitivity values than most other common metals. Lucas and Haggag [76] suggested that some materials have their constraint factor dependent on the strain rate and that can affect the derived stress-strain curve.

A group of investigations [63, 65-67, 69-72, 77-82] attempted to determine flow properties of a material including welds and their heat affected zone using indentation data. They utilised tungsten carbide spherical indenters of diameter ranging from 0.1 to 0.62 inch in performing instrumented hardness indentation, and proposed a set of equations similar to those of Au *et al.* [74] Eq. 2-73 but with $C_1 = 1.12$, $C_3 = 27$, $C_2 = (C_{\max} - 1.12)/\ln 27$, and $C_{\max} = 2.87\alpha_m$ where α_m is the material strain sensitivity parameter usually taken equal to unity for most mild steels. The residual depth was determined by linearly extrapolating the upper portion of the unloading curve to zero load axis. Eq. 2-72, and Eq. 2-73 are solved iteratively to yield the contact diameter and the stress-strain curve.

Taljat *et al.* [19] adopted the values of Francis [75], and they defined the parameter Φ through

$$\Phi = \tan(\beta)\frac{E_s}{\sigma_r} = \frac{2Eh_t}{a_0\sigma_r} \qquad \text{Eq. 2-74}$$

The set of equations Eq. 2-73 that define the constraint factor do not predict its dependency on the strain hardening exponent, n. Matthews [18] and Tirupataiah and Sundararajan [83] presented approximations for this dependency. Matthews's equation

$$C = \frac{6}{2+n}\left(\frac{40}{9\pi}\right)^{n} \qquad \text{Eq. 2-75}$$

gives the values C=3, 2.85, for n=0, 0.5, respectively. The experimental results of Tirupataiah showed the same trend and the C values ranging between 2.4 and 3.1. The FE results of Taljat *et al.* [19] showed good agreement between the values of C presented by Francis [75] and Johnson [29]. The calculated C_{max} is equal to 3 and decreases for materials with higher n. This agrees with the results of Matthews [18] and Tirupataiah and Sundararajan [83]. They found that materials with low n show a high C_{max} value, and vice versa. The values of C_{max} range from 1.5 to 4.0 for n=0.5 to n=0.0, respectively.

The FE results of Taljat *et al.* [19] showed the equivalent plastic strain has a small value at the edge but it increases towards the indentation centre. It reaches the maximum at a distance around $2a_0/3$ from the indentation centre and then decreases with a smaller gradient to the centre. This location was exploited, as a reference point, to determine stresses at higher strain values that might be over 100%, and the strain at that location was taken as a maximum representative strain defined by

$$\varepsilon_{r,\max} = \left(0.5n + \frac{1.44}{\sqrt{n+0.1}} - 1.6\right)\left(\frac{d_0}{D}\right)^2 \qquad \text{Eq. 2-76}$$

where $d_0=2a_0$. The corresponding C value for calculating the corresponding stresses can be obtained from the following

$$C = \begin{cases} -0.65 + \ln(\Phi) \\ C_{\max} = -0.81 + \dfrac{2}{\sqrt{n+0.2}} \end{cases} \qquad \text{Eq. 2-77}$$

where Φ is calculated from Eq. 2-74. Similarly, the point at a distance $a_0/5$ from the indentation edge was chosen as the reference point for determining a low strain value that can be below 1%. The minimum representative strain is given by

$$\varepsilon_{r,\min} = \left(-2 + 0.87n + \frac{1.47}{\sqrt{n+0.36}}\right)\left(\frac{d_0}{D}\right)^{2.45-0.85n} \qquad \text{Eq. 2-78}$$

The corresponding C can be approximated as

$$C = \left(3.65 - 4.3n^2 + 4.36n^3\right)\left(\frac{d_0}{D}\right)^{-3.18n^2+2.89n^3} \qquad \text{Eq. 2-79}$$

The above equations are strongly dependent on n to account for the difference between a_0 and the actual contact diameter in order to determine the stress-strain curve from the indentation data.

Herbert *et al.* [84] attempted to predict the yield stress from spherical indentations, and compared the stress-strain curves derived from the spherical indentation data based on Tabor's equations with those from uniaxial tension. In their measurement of the yield stress, they explored 3 different methods, all of which relied on a deviation from the Hertzian solution. This includes: (i) Identifying initial yielding at the end of the elastic stage of indentation, which is the mean pressure divided by 1.1. However, they reported that the first evidence of yielding did not occur until $p_m/\sigma_y \cong 1.6$, which agreed with the FE investigation of Mesarovic and Fleck [85]. (ii) when $h_c/h_t = 0.5$, and (iii) when the ratio of the loading slope/unloading slope=1. Noticeable uncertainty was observed in measuring the yield stress from these methods. On the other hand, the stress-strain curve derived from the indentation data underestimated stresses at strains smaller than 12% and overestimated stresses thereafter, resulting in a considerable overestimate of the strain hardening exponent. That was due to the pile-up effect.

2.6.2 Procedures for data analysis

Tabor [14, 28] was able to correlate hardness to material mechanical properties by carrying out measurements of the residual indentations profile at different depth values. In his research on indentation with a spherical indenter, he considered Meyer hardness because, in comparison with Brinell hardness, the former has a more fundamental physical concept as geometrically similar indentations give the same hardness, and can be correlated directly with the true stress of the metal.

In spherical indentations for extracting the stress-strain curve, according to the approaches of Haggag *et al.* [82] and Field and Swain [45, 46], the indentation routine is performed in cycles in a pattern of loading with partial unloading followed by further loading to progressively higher loads. The purpose of performing multiple cycles, whose peak loads are incremented successively, is to apply incremental plastic strain as the indenter penetrates the material. Hence, the corresponding true stress at each cycle can be determined. The stress and strain values obtained from each cycle constitute one point on the stress-strain curve meaning that the number of data points for plotting this curve is equal to the number of the loading cycles. The power law has been used to fit the derived true stress-logarithmic strain to determine the strain hardening exponent *n*, and the strength coefficient *K*. The elastic modulus of the materials was obtained from the unloading curves, and hardness was determined from the maximum applied load divided by the corresponding contact area.

Jayaraman *et al.* [86] proposed a method to extract two points on the stress-strain curve from pyramidal indentation data. Their method was based on utilising two different sharp indenters: Berkovich and cube corner which has a nominal angle of 35.3 between the face and the vertical axis. Based on FE simulation, they suggested the empirical equation Eq. 2-80

$$\frac{H}{E} = 1.7\left(\frac{\sigma_y}{E}\right)^{0.92} \qquad \text{Eq. 2-80}$$

that enables the determination of two points on the stress-strain curve with the hardness measurements with these two indenters. They defined the characteristic plastic strain values corresponding to the two indenters being 0.07 and 0.225, respectively, which they obtained from best fitting as well to their FE results. However, their proposed relation is only applicable over the range $H/E<0.16$. Similar work was carried out [87-92] to relate the material flow properties with the loading indentation data produced using pyramidal indenters, i.e. Vickers and Berkovich. The relation was made through empirical equations whose forms were assumed a priori and their constants were obtained from best fitting to the finite element simulations of various materials. This approach of empirical equation was also adopted by Xu *et al.* [93] who attempted to relate the yield stress with the ratio of the elastic recovery to the total penetration depth of the Berkovich indenter.

Taljat *et al.* [19] proposed a new method to determine the stress-strain curve from spherical indentation data based on the loading part of the loading curve. Their analytical approach related the indentation data continuously measured during loading to the stress-strain curve in contrast to previous approaches, where the unloading curve is required to determine a point on the stress-strain curve. However, either n or σ_y was required for determining the full stress-strain curve. The representative strain calculated by this method is in the range from yield strain to a strain between 0.3 and 1.6, depending on material's strain hardening properties. In addition, they used the measurement of a_0, and they studied its influence on the resulting stress-strain curve. Their results were based on FE simulation of indenting materials with $E/\sigma_y = 500$ and the Poisson's ratio of 0.3. They developed a new set of equations that relates the material flow properties to the indentation parameters. The advantage of the equations developed was that a significant extension of strain range over which the curve can be determined, whilst Tabor's Eq. 2-71 allows calculating the stress and strain up to 20% strain. Also, a continuous stress-strain curve is calculated during loading of the indenter. The behaviour of materials with extreme properties may be different, see Bolshakov *el al.*[54]. They reported that friction affects the *P-h* curves when the friction coefficient considered is less than 0.2, above which no further effect was observed. In their material simulations, a set of uniaxial true stress-strain curves was obtained by varying the strain hardening exponent, *n,* in the range from 0.0 to 0.5. The strength coefficient, *K,* for each of these curves was calculated with the assumption that the power law constitutive behaviour starts at the point defined by a 0.2% offset of the yield strain, so that

$$K = \left(\frac{\sigma_y}{\frac{\sigma_y}{E} + 0.002} \right)^n \qquad \text{Eq. 2-81}$$

Taljat reported in previous work [94] that the loading part of the *P-h* curve could correlate with σ_y and *n.*

Nayebi *et al.* [95] performed FE simulation of a deformable spherical indenter, D=1.587 mm, on materials of various plastic properties. They suggested that the loading curve is a function of the yield stress and strain hardening exponent, as expressed in the form

$$h_t = N_1(\sigma_y, n)P^{N_2(\sigma_y, n)}. \qquad \text{Eq. 2-82}$$

Based on the fitting procedures of the FE results, they proposed the values of the variables N_1 and N_2 as

$$N_2 = \left[n(-0.151\sigma_y + 0.609) + 0.09\sigma_y + 0.975\right]^{-1}.$$
$$N_1 = \left[(-3294 + 22170\sigma_y^{0.8})e^{2.9n\sigma_y^{-0.323}}\right]^{-N_2} \qquad \text{Eq. 2-83}$$

They proposed that using an optimisation procedure to minimise the error between the theoretical curve in Eq. 2-82 and the experimental indentation curve will yield the parameters σ_y and n.

Recently, Cao and Lu [96] performed dimensional analysis on extracting materials plastic properties from simulated spherical indentation data assuming that the elastic modulus is known a priori. They extended the definition of the characteristic strain of sharp indenters, by Dao *et al.*[97], being independent of the strain hardening exponent, and suggested an empirical relation based on the fitting procedure that defines the characteristic strain as a function of h_t/R given by

$$\varepsilon_r\left(\frac{h_t}{R}\right) = 0.00939 + 0.435\left(\frac{h_t}{R}\right) - 1.106\left(\frac{h_t}{R}\right)^2 : \left(0.01 \le \frac{h_t}{R} \le 0.1\right) \qquad \text{Eq. 2-84}$$

For h_t/R=0.06 the characteristic strain was identified to be 0.0316. Their extraction to the material properties was based on the idea that the loading curve can be described as a dimensional function of various parameters given by

$$P = \sigma_r h_t^2\left[X_1 \ln^3\left(\frac{E_r}{\sigma_r}\right) + X_2 \ln^2\left(\frac{E_r}{\sigma_r}\right) + X_3 \ln\left(\frac{E_r}{\sigma_r}\right) + X_4\right] \qquad \text{Eq. 2-85}$$

The constant values X_1 to X_4 were determined from best fitting of the FE results and were expressed in tabular format as a function of h_t/R. Although they normalised the indentation depth relative to the indenter radius, they used a fixed radius of 5 mm in their simulations which assumed frictionless contact.

Most recently Taljat and Pharr [98] carried out extensive FE simulations investigating the development of the pile-up during spherical indentation. By examining the simulated indentation profiles and relating the deformation behaviour to the material and indentation parameters, they identified a unified material parameter $\frac{E_r}{\sigma_y}\frac{2h_c}{a_c}$ that can relate directly to the pile-up extent, which makes it applicable to any indenter radius, indentation depth, and material properties. They reported that pile-up is not a function of *n* only as assumed in previous research e.g. [17-19]. Rather, the indentation perimeter was observed lying below the original surface in the early stages of indentation then it increases with depth even beyond the limit of the fully plastic regime. Then it levels off at a value that can be predicted from various expressions [17-19]. Taljat and Pharr [98] observed that friction has a noticeable effect on the amount of the pile-up especially when it predominates. Interestingly, these two facts tie up with some of the findings in this present study. They proposed a curve to determine the pile-up extent given $\frac{E_r}{\sigma_y}\frac{2h_c}{a_c}$, which is not known from the load indentation data. Hence they suggested using $2h_t/a_0$ instead for an estimate of the pile-up.

2.7 Summary

Several analytical approaches have been proposed to deduce the Young's modulus and the hardness from the experimental instrumented indentation data. Central to these approaches are the methods by which measurable quantities such as the peak indentation load, the maximum penetration depth of the indenter tip and the contact stiffness are related to the contact area and Young's modulus. The idea of correlating the indentation pressure and geometry with the tensile stress-strain curve for the tested material was first proposed by Tabor [14]. The major step of the load-depth indentation data analysis in all approaches is determining the actual contact area without the need for direct measurement.

The approach of Oliver and Pharr [37] is aimed at deriving Young's modulus and the hardness using a pyramidal indenter. Their approach is based on Sneddon's solution. The deduced properties were in good agreement with the real ones for hard materials, but the error was about 40% when testing soft materials that pile-up.

Field and Swain [46] proposed an analysis of the load-depth indentation data produced by the spherical indenter in order to measure Young's modulus and the hardness. They adopted an existing correction expression to the contact area provided the strain-hardening exponent of the material is known a priori.

A group of researchers led by Haggag [63, 65-67, 69-72, 77-82] attempted to derive the stress-strain curve from analysing the indentation data produced by the spherical indenter. Their theory was based on the work by Au *et al.*[74], which does not appear rational in two ways: First, the determination of the contact radius was based only on E and no other material properties. Second, the contact depth value was obtained by extrapolating the upper third portion of the unloading curve linearly to the zero-load axis. Further, his determination of the yield stress was empirical.

The approach of Taljat *et al.* [19] was also aimed at determining the stress-strain curve of the test material. The proposed method was based on the total measured displacement rather than the actual contact depth and the actual contact area. As Tabor's Eq. 2-71 can cover up to 20% strain, Taljat *et al.* proposed two new bound values for the representative strain at which the corresponding stress can be calculated over a wide strain range extending from 1 to 100%. However, knowledge of the strain-hardening exponent of the material is essentially required to apply their approach.

Alcala *et al.* [59] did some work similar to that of Norbury and Samuel [56] and proposed two equations, corresponding to Vickers and spherical indenters, that relate pile-up level to the strain hardening exponent. Other approaches, such as by Cao and Nayebi [96], suggested extracting the material plastic properties from the loading curve whose equation was determined from fitting procedures. Recent work by Taljat and Pharr [98] examined the development of pile-up and correlated its extent with material properties and the true contact area, which cannot be determined from the load indentation data.

CHAPTER 3

EVALUATING THE RELIABILITY OF THE INSTRUMENTED MICROHARDNESS TESTER

The instrumented microhardness technique is an attractive non-destructive method to measure the mechanical properties of minimal volumes of material. In an indentation experiment, the indenter is pressed into the test material at a low load, and the applied load and the resultant penetration depth are acquired and measured continuously. A typical set of load-displacement data obtained from an experiment is presented in Fig. 3-1.

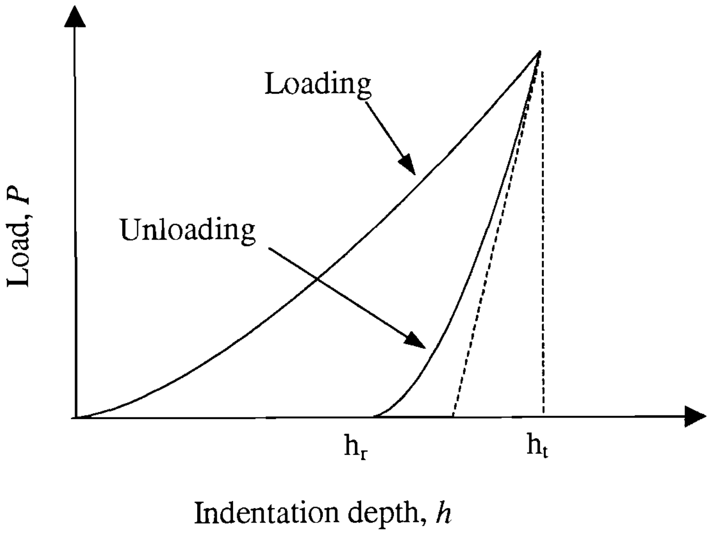

Fig. 3-1 Typical indentation load-displacement curve.

The small indents formed at the nano/micro scale renders conventional hardness techniques difficult and inaccurate since conventional hardness testing requires direct imaging and measurement of the residual contact area. This is a tedious task and lacks sufficient accuracy at the nano scale. Since the contact area is a key parameter in calculating material properties, it is essential to devise other means to measure it more accurately. Advances in the technology of instrumented indentation hardness testing facilitates high resolution measurement of load and displacement that can be in the order of mN and nm, respectively. This data can then be analysed to estimate the contact depth, which is used in conjunction with the known indenter geometry to establish the contact area at peak loads.

To verify the experimental data obtained from the instrumented indentation tester, the reliability and robustness of the instrument and its analytical procedures have to be validated. This chapter thus includes a description of the investigation carried out to assess the performance of all parts of the instrument and the analysis technique used to estimate contact area.

3.1 Description of the instrumented nano/micro indentation facility

The instrumented nano/micro indentation tester used in this study is manufactured by MicroMaterials Ltd. Its resolution of load and displacement measurement is 100 nN and 0.1 nm, respectively. It includes two separate instruments, Microtest-200 and Nanotest-600 for indentation on the micrometer and nanometre scale, respectively. Both instruments are positioned on the same base adjacent to each other. The instruments are enclosed in a temperature controlled cabinet to provide a thermally stable environment and to isolate the internal environment from any air current effect. The temperature inside the cabinet is maintained at 25°C using two internal heaters while the temperature outside the cabinet is maintained at approximately 20°C using a thermal system that consists of an air conditioner and a heater. The two instruments, Microtest-200 and Nanotest-600 sit on a self-adjustable table that keeps its level by an automatic air pumping mechanism underneath the table. The above precautions are to protect the indentation process both from any thermal disturbance and from any normal external vibrations and so minimise noise and thermal effects on the indentation data acquired.

Operating both instruments is almost the same in principle. The manual provided by MicroMaterials [99], although designed specifically for operating the Nanotest-600, was also relevant for the Microtest-200. However, slight differences between the two instruments were highlighted in a training programme provided by MicroMaterials. The instrumented micro-indentation tester, Microtest-200, is the one used to carry out all the indentation experiments in this study. It has the capability of performing indentation under loads up to 20 N, and the maximum indentation depth achievable is about 30 μm. Load and indentation depth are measured continuously during an indentation experiment, and the data acquired are transferred to a PC connected to the instrument through an IEEE port.

3.2 Operating principles

The instrumented micro-indentation tester Microtest-200 utilises a pendulum mechanism for indentation as shown in Fig. 3-2 and Fig. 3-3.

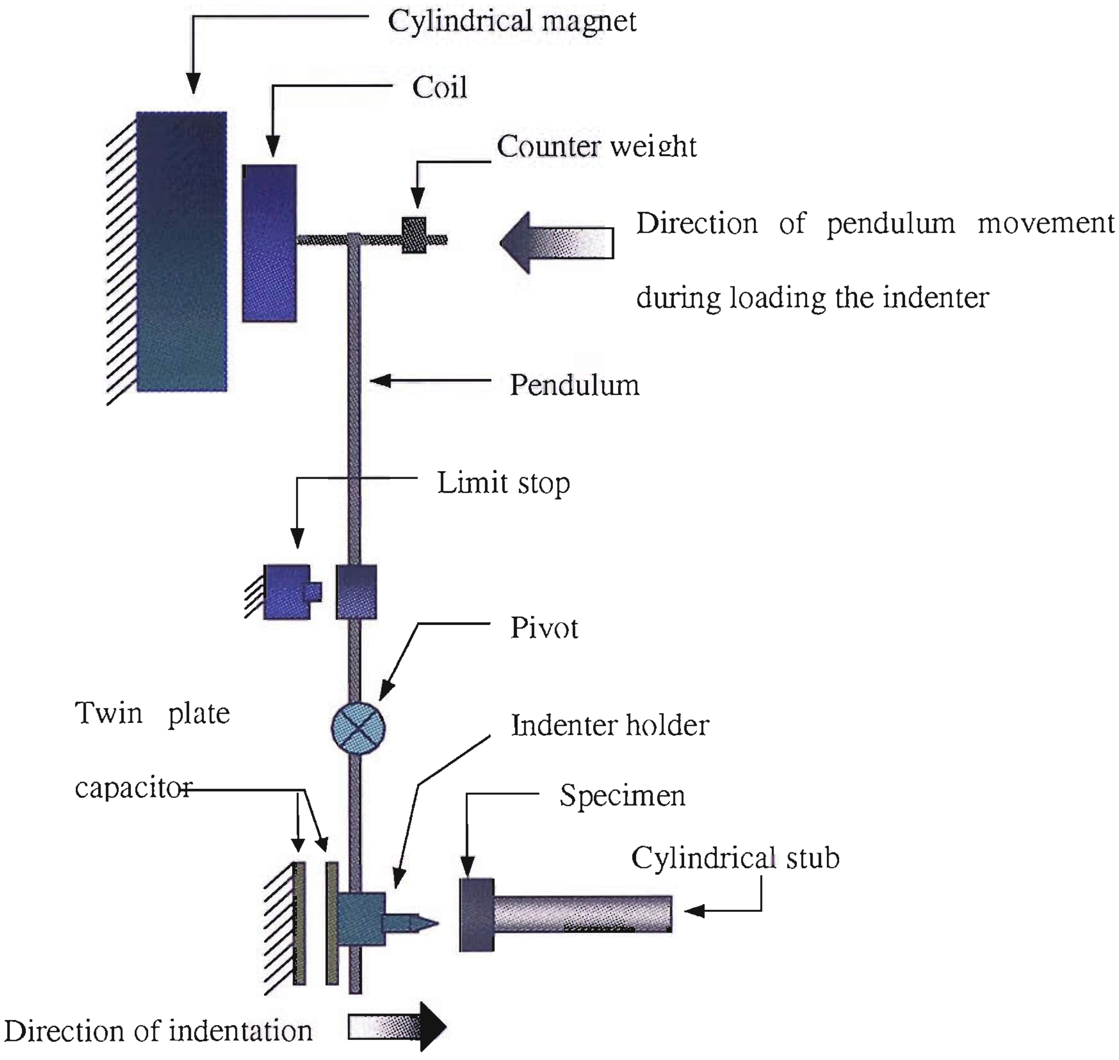

Fig. 3-2 Schematic drawing showing the main components of the Microtest-200.

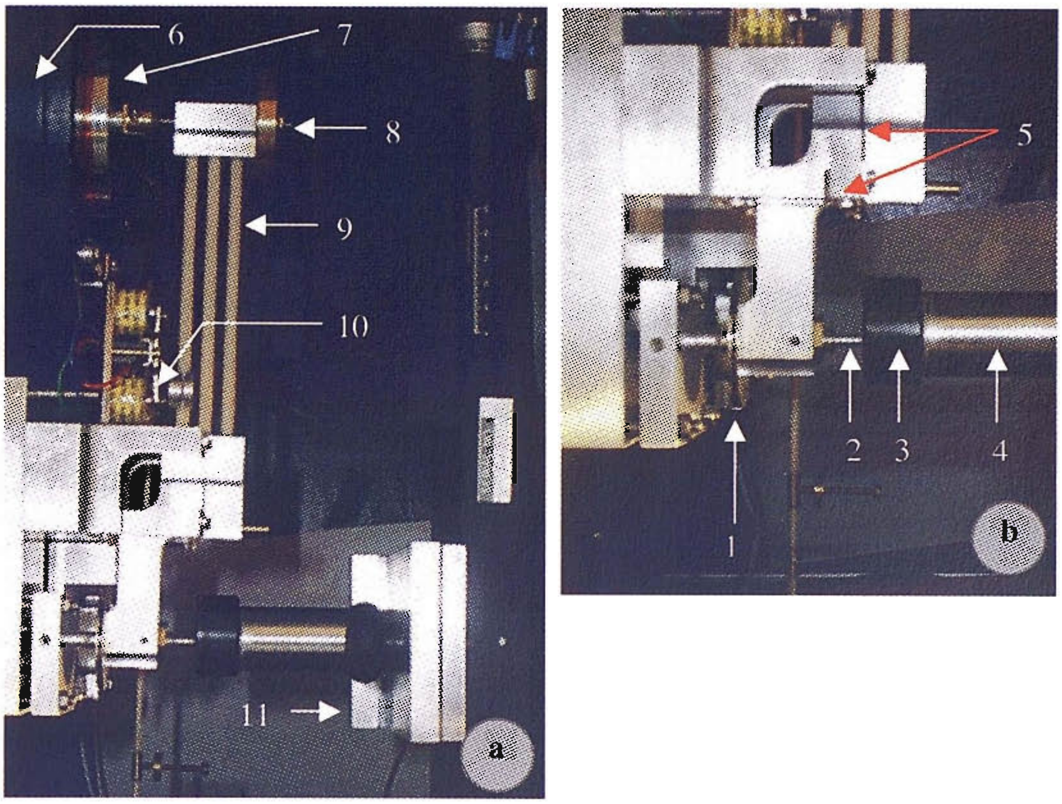

Fig. 3-3 Details of Microtest-200, (1) capacitor plates, (2) indenter holder, (3) specimen, (4) aluminium stub, (5) plates constituting the pendulum pivot, (6) permanent magnet, (7) coil, (8) counter weight, (9) 3-bar ceramic pendulum, (10) limit stop, (11) travelling stage.

A counter weight and a coil are mounted at the top of the pendulum. The coil can move freely through a central annulus surrounded by a cylindrical permanent magnet. The indenter holder, to which an indenter is fastened, is located at the bottom of the pendulum. The pendulum is pivoted using a plate mechanism located between the indenter holder and the limit stop. The motion of the indenter towards the specimen and into the specimen surface occurs when the coil is attracted towards a permanent magnet in response to the presence of a DC current in the coil. The voltage of this current is used to measure the applied force on the indenter. The limit stop, located above the pivot, is to define the vertical position of the pendulum, and its position can be manually adjusted with a micrometer. The pendulum is vertical when it is touching the limit stop at which point the coil cannot move any further towards the magnet, hence the indenter cannot move any further towards the specimen. The counter weight is for fine adjustment of the pendulum so as to ensure that it is vertical against the limit stop.

The displacement of the indenter is measured by means of a two-parallel plate capacitor situated at the back of the indenter. One plate is attached to the indenter holder and moves with it while the second plate is fixed. When the indenter is pressing into the test specimen, the spacing between the parallel plates changes, hence the capacitance changes. By measuring this change by means of a capacitance bridge, the indenter movement can be measured. Data from the capacitance bridge are transferred as signals to the main electronic control unit, which contains a ramp generator that supplies the coil current. The data received from the capacitance bridge is then amplified, rectified, digitised and transferred via the IEEE bus to a computer.

3.2.1 Indentation experiment process

The test specimen is glued (with superglue LOCTITE) at its base to a cylindrical aluminium stub that is fastened to the drive stage. Attached to this stage are three DC motors that electromechanically drive the specimen in three directions X, Y, and Z. The X-direction coincides with the axis of symmetry of the cylindrical stub, while the Y and Z directions coincide with the horizontal and vertical axis of the plane of the specimen surface. The travelling range of each motor is up to 50 mm. The X-motor brings the specimen towards or away from the indenter, while the Y and Z motors enable the specimen to be moved across its surface plane so that the indenter can indent different areas on the surface. The velocity of motion of each motor ranges from 1 to 250 μm/s. Using the X-motor, the specimen is brought into contact with the indenter. Once the specimen touches the indenter, the indenter retracts backwards away from the specimen by a distance controlled by the operating software, which is within the range of the pendulum movement. The specimen then moves half way towards the indenter and then moves in the Z-direction by 75 μm in order to move the area of first contact away from the indenter, so that the coming indent will be on a virgin area. The indenter is then brought into contact with the specimen, and it contacts the specimen at a very small load, a few mN. This stage is called initial contact and only the load and the indentation depth corresponding to the end of this stage are measured. After this stage the following load cycle(s) starts. The indenter is pressed into the surface of the specimen by a load which increases at a pre-defined rate. Loading continues until a pre-defined maximum value of load or depth is reached, then the indenter is held for a certain pre-defined time called the dwell time. Next, unloading starts and the load drops gradually at a pre-defined rate and the penetration depth decreases due to the elastic recovery of the deformed material. Load and displacement of the probe into the surface are monitored continuously and recorded.

Indentation can be carried out at each position in two patterns: a) a complete load cycle that includes loading to a maximum load, dwell time, and complete unloading. b) loading-partial unloading in which the loading mode is performed in more than one cycle, as illustrated in Fig. 3-4. The first cycle is exactly the same as explained previously in (a). However, unloading is not complete. The load drops to a previously defined minimum value before the indenter is reloaded to start the following load cycle. During partial unloading the indenter is still in contact with the indent and the minimum load can be held for a pre-defined time. Successive loading/unloading cycles are formed by increasing the peak load progressively. In the last cycle, unloading is complete.

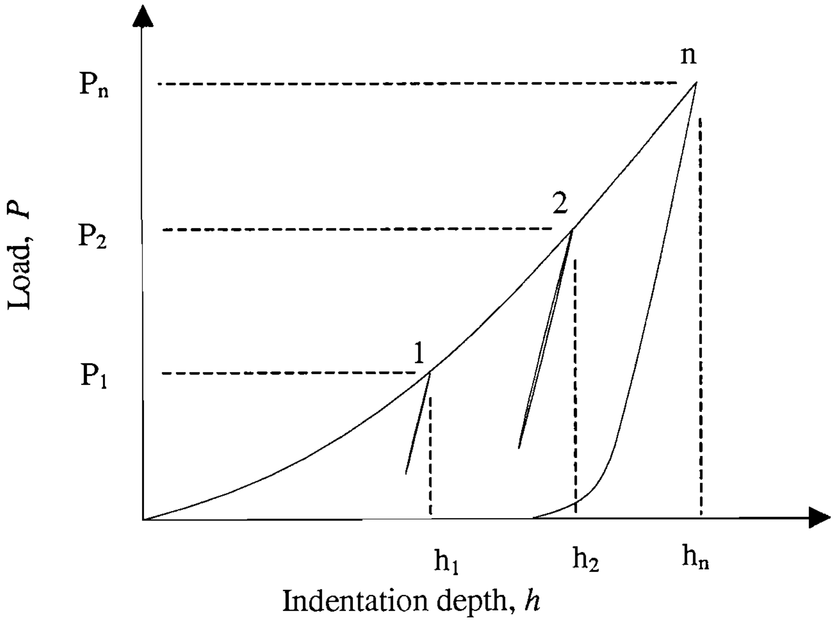

Fig. 3-4 Multi-cycle loading pattern with partial unloading.

3.2.2 Description of the built-in software in the instrument

The built-in software has the task of fully operating the instrument and analysing the indentation data. Its tasks are divided into three main parts:

a) Defining the schedule to perform an indentation experiment, which includes determining the experiment parameters setup, namely:

  - Type of the indenter used (pyramidal or spherical) and indenter radius if spherical.
  - Loading pattern for indentation (one cycle at each position or multiple cycles with partial unloading).
  - The grid of indent positions. This includes the number of lines in the grid, the number of indents in every line, the spacing between indents in the grid in two directions, and also number of cycles at each indent position if applicable.
  - Maximum load or depth to reach in a cycle, minimum load for partial unloading in cyclic loading mode, and loading and unloading rate with the dwell time at maximum and minimum load.
  - Load of initial contact.

b) Carrying out the required calibrations, discussed in more detail in Section 3.3, including load calibration, depth calibration, frame compliance, bridge box and pendulum test, and zero load calibration.

c) Analysing the acquired indentation data to determine two main quantities:

  - Hardness H, which is the mean pressure over the projected area of contact.
  - Reduced modulus E_r which is computed using the analysis based on the approach of Oliver and Pharr [15, 37] for the Berkovich indenter and that of Field and Swain [45, 46] for spherical indenters. The software also calculates for each indentation curve the maximum contact depth, the recovery in depth, and the contact stiffness. Export facility to a text file is also available. This covers the analysis parameters and results, experiment set-up parameters, and calibration parameters.

In both the Oliver and Pharr, and Field and Swain approaches, the part of the unloading curve considered for fitting extends from the peak load to the minimum load or 20% of the peak load, whichever is larger, and the geometry of both types of indenters, Berkovich or spherical, is assumed perfect.

3.3 Calibration procedures

Indentation testing, as for any experimental testing, is accompanied by three types of error: random, systematic, and gross errors. Gross errors can occur due to any accidents such as a complete instrument breakdown. Such errors are normally very easily recognised. Random error is when the results fall on both sides of the average. It can be viewed as the irreproducibility of making replicate measurements and affects the precision of a result, which is described by statistical quantities such as the standard deviation. Systematic errors are errors that produce a result that differs from the true value by a fixed amount. Examples of causes are instrument calibration, or human factors. Such errors affect the accuracy of the results. Systematic errors can be minimised by a careful check on experimental set up and the equipment used for testing. In contrast to random errors, systematic errors cannot be revealed merely by making repeated measurements. In the case of instrumented hardness testing they can be revealed by carrying out measurements on materials whose hardness and Young's modulus are already known. One important step to avoid, or minimise, instrument systematic errors is to perform careful calibration prior to any experiment. The Microtest-200 requires five calibrations.

3.3.1 Load calibration

The load calibration establishes the magnitude of the forces applied at the indenter tip during a measurement. The calibration consists of hanging three different masses, one at a time, ranging from 10-100 g, which covers the range of load applied by the instrument. Each mass has a hook which is used to hang it at a set point near the end of a cantilever attached to the pendulum close to the pivot as shown in Fig. 3-5.

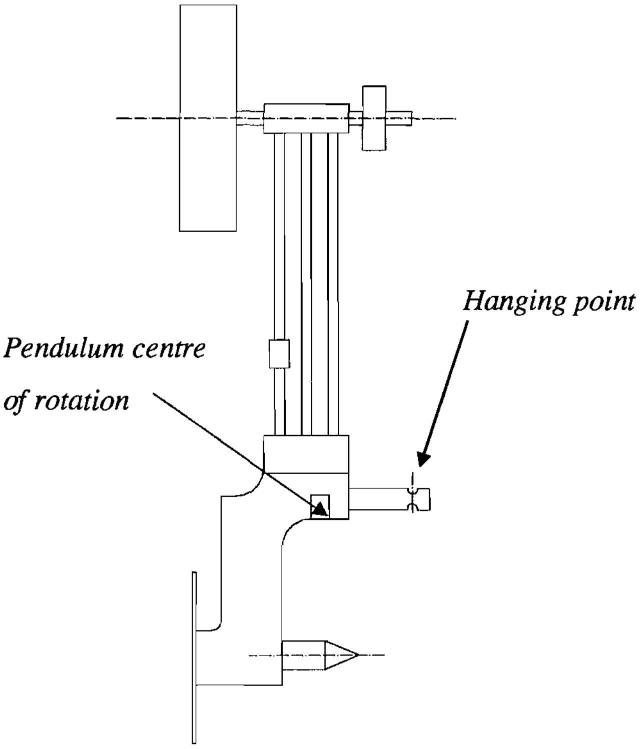

Fig. 3-5 Schematic drawing showing the lever arms involved in load calibration.

Under the weight of each mass, the pendulum will rotate slightly about its pivot clockwise so the coil will move away from the magnet. The load calibration routine built in the instrument software forces the coil to generate a current that applies a countering force corresponding to the force caused by the mass applied, in order to maintain pendulum equilibrium. The voltage measured is correlated to the load applied from the mass hung. By hanging three different masses, one at a time, three points of load versus voltage can be plotted, and then these points fitted to a straight line. The load applied to the indenter is determined by multiplying the slope of this fitting line by the voltage in the coil.

3.3.2 Depth calibration

A parallel plate capacitor is used to measure displacement. The outcome of this calibration is known as the 'Depth Calibration Factor', which relates the change of spacing between the twin plates to the indenter movement. For this calibration, a Brinell ball indenter 1 mm in radius, made of hardened steel, is used together with a fused silica sample. Selecting a rather big ball and a fused silica sample, as a hard material, is to ensure that contact during calibration is elastic. The depth calibration is performed as follows: First, the fused silica sample is brought into contact with the indenter. Then, the X-motor pushes the sample against the indenter causing the indenter to move backwards, hence the spacing between the two parallel plates decreases. The resulting change in capacitance is measured by means of the bridge box. From the known sample movement, which is determined directly from the X-motor movement, and from the solution of the elastic contact problem, the movement of the indenter can be computed. By taking at least five depth measurements, the indenter movement is related to the change in capacitance incurred so producing the mean depth calibration factor.

3.3.3 Frame compliance calibration

In any indentation experiment, the measured indentation depth is not merely the penetration depth of the indenter into the test specimen, it also includes deformation of the Bakelite used to mount specimens and deformation of the instrument parts such as the stub, the pendulum, and the indenter holder. This extraneous deformation per unit force is called the frame compliance. The frame compliance value is not negligible, hence it is essential that this is known so as to produce a more precise measurement of the indentation depth. For any acquired raw depth measurement, h_{raw}, the corresponding penetration depth h_t is calculated using the following equation:

$$h_t = h_{raw} - PC_f \qquad \text{Eq. 3-1}$$

where C_f is the frame compliance, which is expected to lie between 0.3-0.5 µm/N according to the MicroTest-200 manual.

The frame compliance calibration procedure involves performing indentations on a hard steel sample of 700 H_V 1 whose Young's modulus and Poisson's ratio are known. Hence, the reduced modulus, which is the target value for calibration, is determined a priori. The frame compliance of the instrument is initially set to zero before performing any indentation. For each indentation curve, the frame compliance is calculated to be the factor by which the depth values of the indentation curve are modified according to Eq. 3-1, so that the target reduced modulus can be derived, within any pre-defined accuracy, from the unloading indentation curve.

3.3.4 Bridge box calibration and pendulum test

This calibration ensures that all the electronics are functioning correctly and are set for taking measurement. It also tests whether or not the pendulum is properly mobile. During the test, the pendulum has to reach the limits of its range of movement. At the limit stop, the voltage should read 4 volts and when the pendulum is furthest from the limit stop, the voltage should measure zero volt. Operations such as sample contact and calibrations depend on the user being able to obtain an acceptable pendulum test.

3.3.5 Zero load calibration

The zero load calibration provides a minimum coil voltage necessary to hold the pendulum on the limit-stop. The pendulum is made to touch the limit stop at a minimum voltage at which the load is considered to be zero.

3.4 Description of the frame compliance calibration software used for a spherical indenter.

The instrumented microindentation tester is run by built-in software that controls its operation and functionality, including calibration, analysis, and plotting and extracting various results and indentation data. During the process of an experiment, the recorded acquired raw displacement data include the equipment frame deformation in addition to the material deformation, which is needed for the analysis. Since the accuracy of the analysis results largely depends on the analysed data being a true representation of the material deformation, it is essential to remove the frame compliance. Any error in estimating the frame compliance will lead to erroneous analysis results.

The built-in software that operates the Microtest -200 is capable of performing the frame compliance calibration for experiments with the Berkovich indenter only. It requires performing indentations on a reference specimen whose Young's modulus and Poisson's ratio are known a priori. Since the elastic properties of the indenter, which is made of diamond, are known, the reduced modulus of the specimen can be calculated. Indentation is performed in a cyclic loading-partial unloading pattern with an increasing cycle peak load, as shown in Fig. 3-4.

The software first calculates the reduced modulus from each unloading curve. An average value of the reduced modulus is then generated and compared with the target value which is the true reduced modulus of the specimen. The frame compliance is then calculated using Eq. 3-4 until the average value of the reduced modulus calculated equals the target value.

However, when using the frame compliance obtained using the Berkovich indenter to analyse the indentation data from a spherical indenter, the results were erroneous. The holder of both indenters, the Berkovich and the spherical (R=150 μm), are made of different materials. Also, the part of the holder to which the spherical indenter tip is brazed is longer. Such differences are expected to result in different values for frame compliance. Hence, it was considered essential to build a program that can determine the frame compliance calibration for the data produced by a spherical indenter. Using Matlab, a program presented in Appendix B, was developed to carry out this calibration in a similar way as in the case of the Berkovich indenter. It was based on the concept that the elastic modulus is a property of the material that should be constant with indentation depth. Hence, analysing the indentation cycles should yield the reduced modulus of the specimen. This method models the frame compliance and the specimen deformation as two springs in series, as proposed by Oliver and Pharr [15, 37], in which case the total measured compliance C_t is given by

$$C_t = C_f + C_s \qquad \text{Eq. 3-2}$$

where C_s is the compliance of the specimen. Based on the stiffness method, C_s can be calculated from

$$C_s = \frac{1}{S} = \frac{1}{2a_c E_r} \qquad \text{Eq. 3-3}$$

Hence, the frame compliance is determined from

$$C_f = C_t - \frac{1}{2a_c E_r} \qquad \text{Eq. 3-4}$$

The iterative procedure for calculating C_f can be summarised as follows:

(1) Having indented the reference specimen by a spherical indenter, the raw data are initially analysed with the frame compliance taken as zero leading to a value of reduced modulus, which is much smaller than the true material reduced modulus.

(2) Then the indentation data are modified according to Eq. 3-1 using a chosen value for compliance, calculated from Eq. 3-4, and

(3) the new indentation data are analysed to calculate the new value of reduced modulus. If this new value of the reduced modulus is the not same as the material modulus within a pre-defined tolerance then the total compliance is calculated from the indentation data and then steps (2) and (3) are repeated.

The iteration process terminates once the resulting value for reduced modulus is within a pre-defined tolerance of the material modulus. The corresponding value for frame compliance is considered as the calibration factor and the new data are considered to reflect the pure material deformation.

3.5 Characterisation of the spherical indenter geometry

The indenter used was supplied via MicroMaterials. It is conical with a polished diamond tip which is almost a hemisphere. Its nominal radius was 150 μm with an included apex angle of the cone of 90°. This should allow a maximum vertical distance from the the hemispherical tip of approximately 44 μm before reaching the conical part of the indenter. In order to confirm these data and also to obtain more precise information on the geometry of the indenter, the indenter was examined using a FEG-SEM 6500F, Field Emission-Gun Scanning Electron Microscope. The indenter was attached to a microscope stub, positioned with 0° tilt so that the axis of the indenter was at right angles to the electron beam. Images were taken at seven positions, each obtained by a 26° rotation of the indenter about its axis of symmetry. The SEM micrographs of the seven profiles are shown in Fig. 3-6.

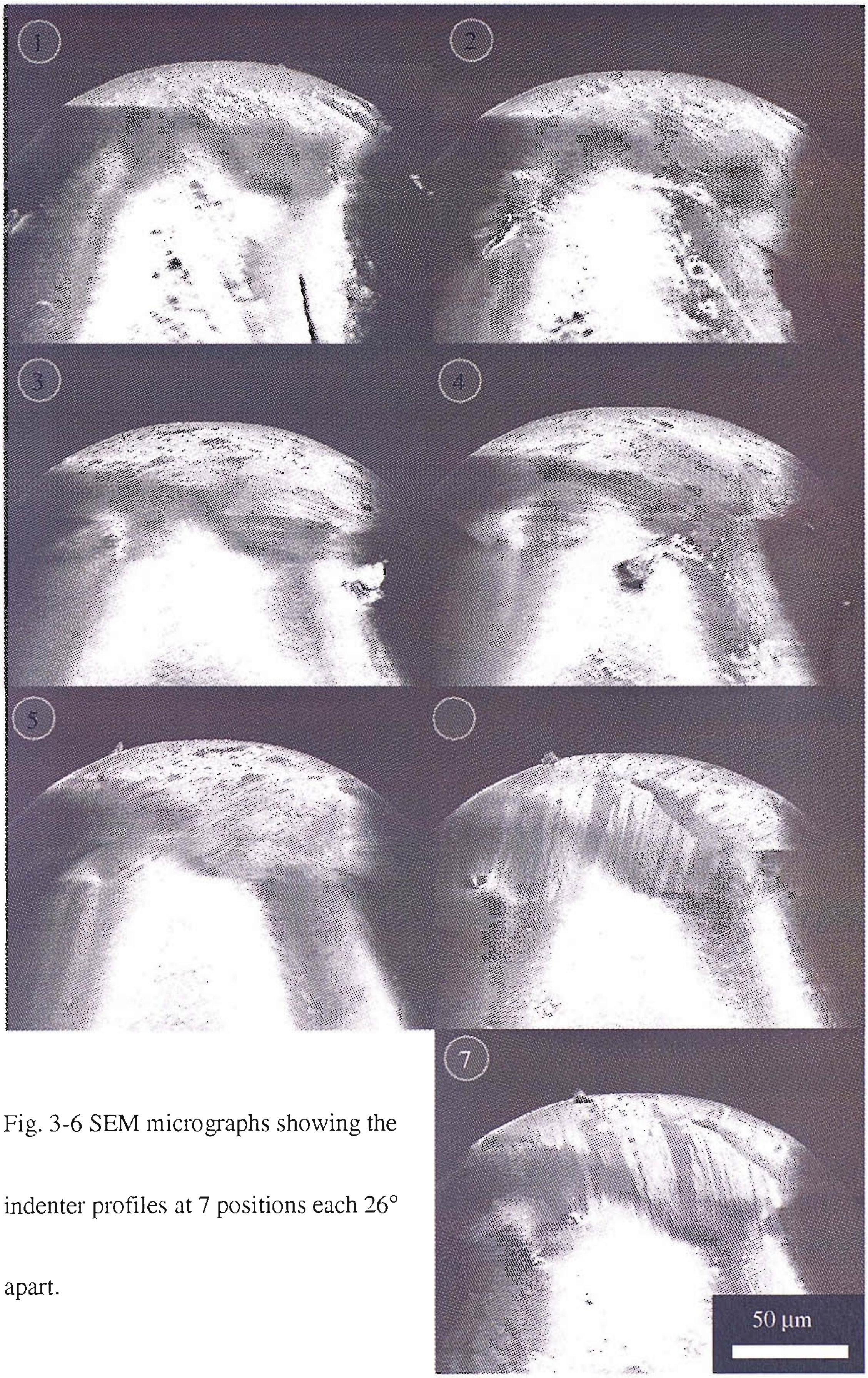

Fig. 3-6 SEM micrographs showing the indenter profiles at 7 positions each 26° apart.

Measurements shown on Fig. 3-7 and Fig. 3-8 confirmed that the cone included angle is about 95°-95.5° which is slightly larger than the nominal value, 90°. However, the vertical distance from the tip to the conical section ranges from 18-25 µm, which is less than the expected nominal value of 44 µm.

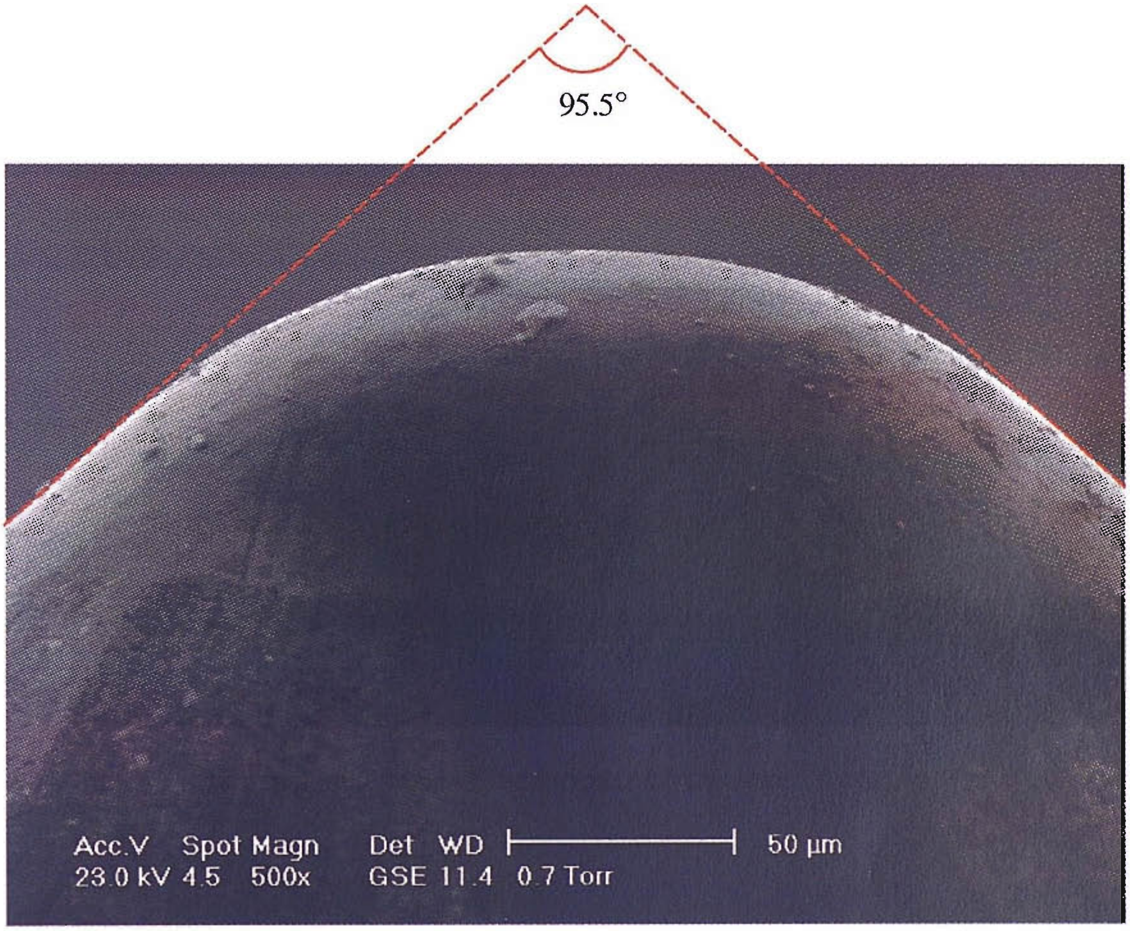

Fig. 3-7 Cone included angle of the indenter tip measured for one of the profiles imaged by SEM.

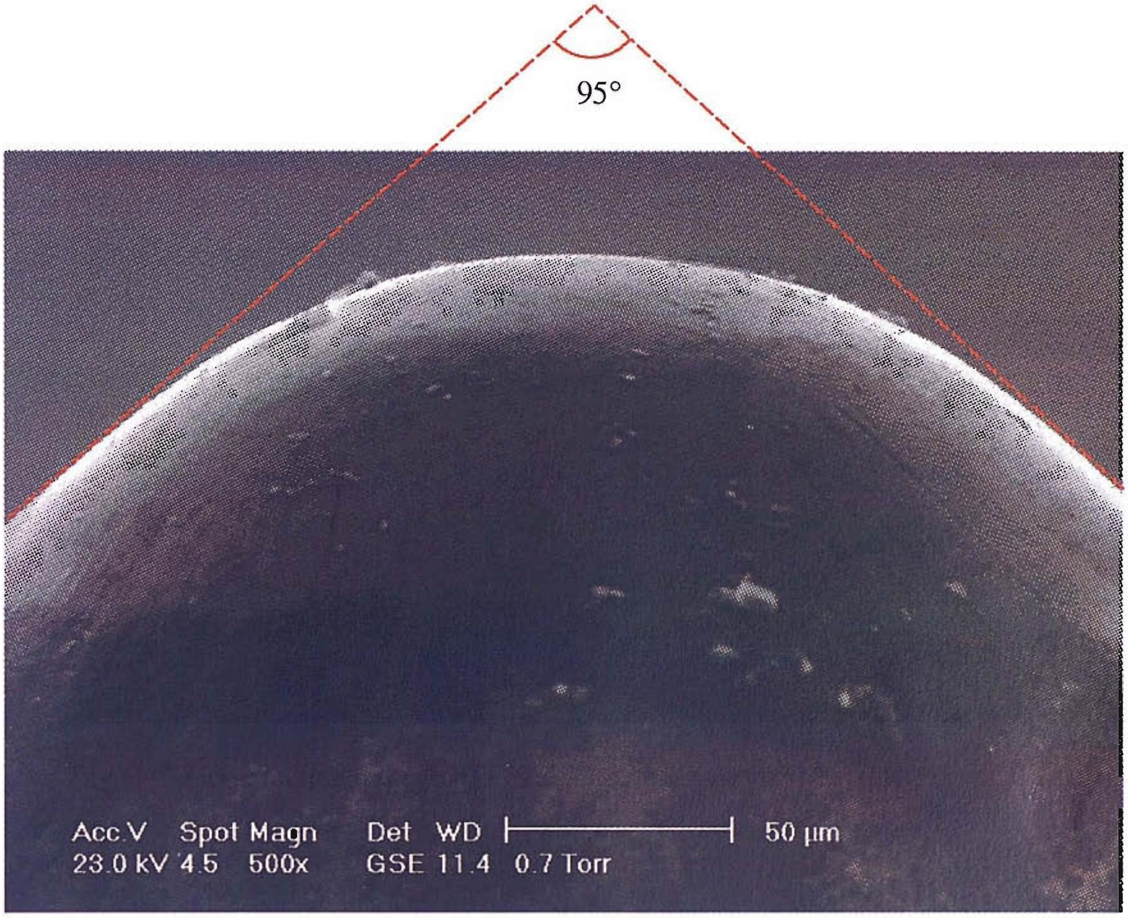

Fig. 3-8 Cone included angle of the indenter tip measured for another profile imaged by SEM.

3.5.1 Determination of the average profile of the indenter

In order to determine the tip profile, the profile in each SEM micrograph was digitised, then split into two halves and one half was mirrored so the two halves for each image could be re-plotted as shown in Fig. 3-9. The fourteen curves are then averaged.

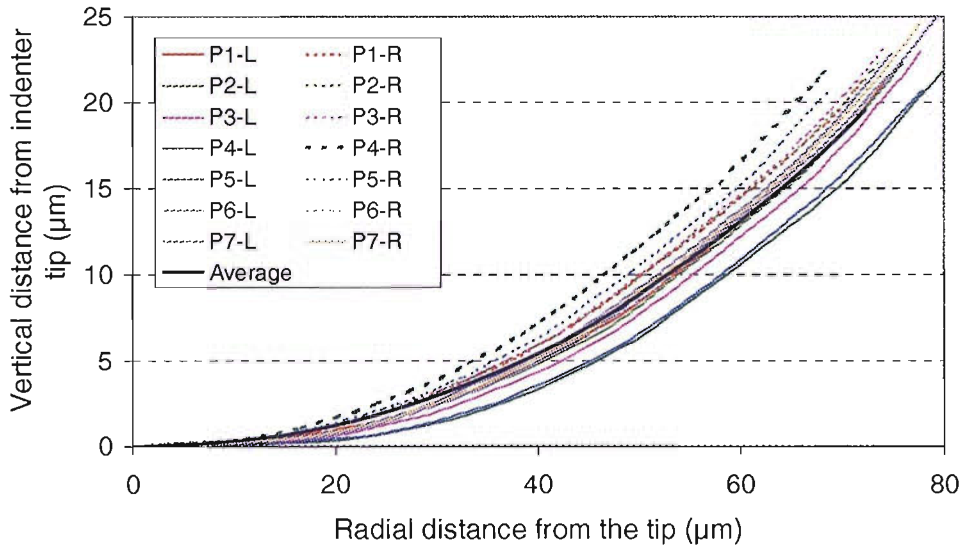

Fig. 3-9 Seven profiles split into halves, left(L) and right(R). The average profile is also given.

The average profile is then plotted and compared with the nominal spherical profile of 150 µm radius in Fig. 3-10. It can be noticed that for the first 5 µm of vertical distance from the indenter tip the average indenter profile has a slightly larger radius than the nominal sphere. At vertical distances from the indenter tip of greater than 5 µm the average indenter profile has a smaller radius than the nominal sphere. This results in a variation in curvature with vertical distance from the indenter tip.

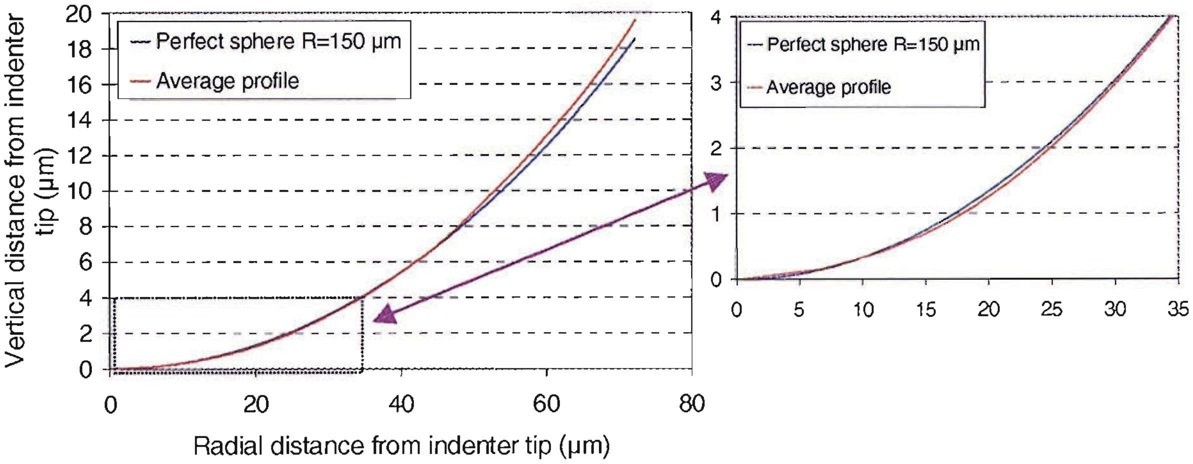

Fig. 3-10 Profile comparison with a perfect sphere of 150 µm radius.

The indents made by the spherical indenter were also examined by optical microscopy. The residual indents on a stainless steel grade 316L are shown in Fig. 3-11.

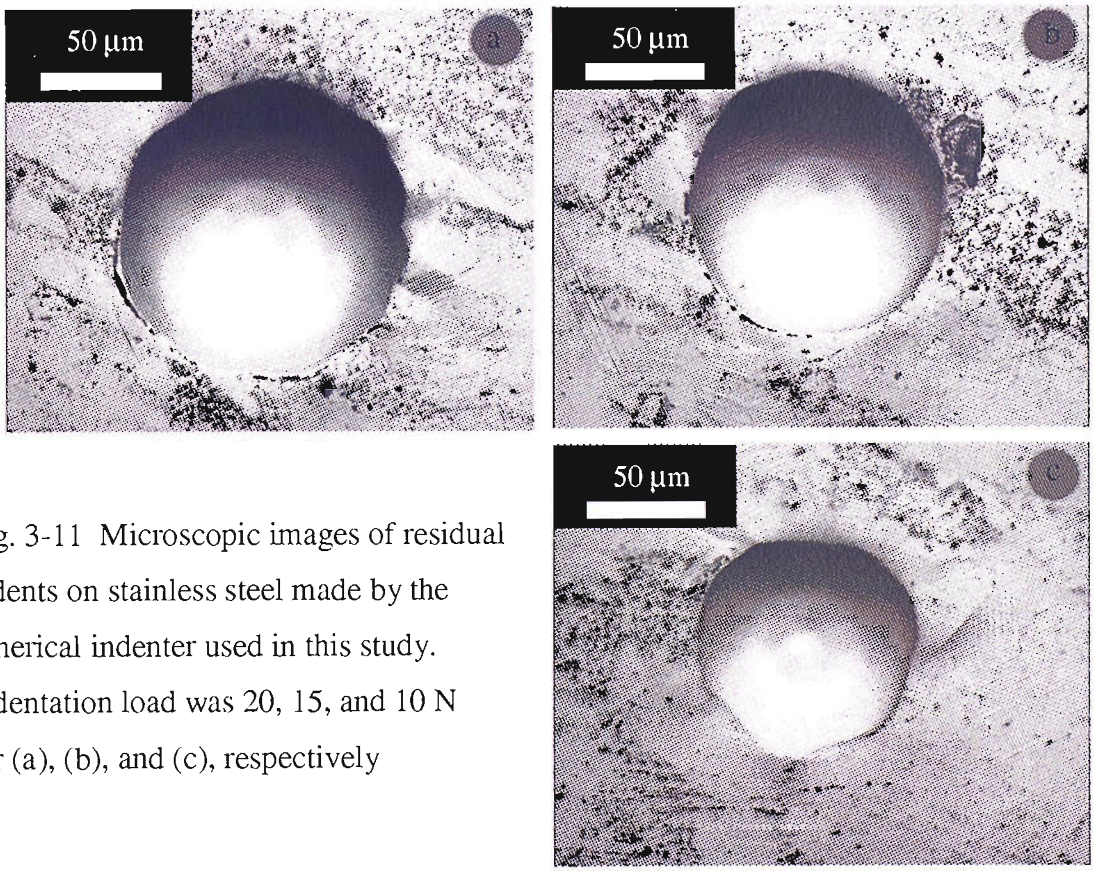

Fig. 3-11 Microscopic images of residual indents on stainless steel made by the spherical indenter used in this study. Indentation load was 20, 15, and 10 N for (a), (b), and (c), respectively

As can be observed from the residual indents, the perimeter deviates from a perfect circle especially for small indents. The indenter profile cannot be described by a constant radius of curvature. This necessitates a more accurate characterisation of the indenter geometry in order to define the variation of effective radius and gradient that can subsequently be used to represent the indenter profile geometry at a certain vertical distance from the tip for analysis purposes.

3.5.2 Gradient and radius calculation of the indenter profile

As described in Section 2.3, the uni-axial stress-strain curve of a material can be related to the measurements of the mean pressure and a representative strain value at different loads. The characteristic strain imposed is related to the gradient of the indenter surface at the edge of the contact area. Since the indenter used deviates from its nominal perfect spherical geometry, it is essential to measure the radius and gradient variation along the average profile. Three methods were attempted for this purpose:

1. Linear fitting: in this method the points making up the average profile, some 130 points, are put in adjacent groups in such a way that each two adjacent groups have overlap between each other but with a shift of 2 points to cover the whole profile. The group size was taken to range from 3 to 12 points to check the effect of group size on fitting. Each group of points is then linearly fitted and the slope of the fitting line is assigned as the local gradient of the profile at the centre of the corresponding group. The local gradient as a function of vertical distance from the indenter tip for various group sizes used is plotted in Fig. 3-12.

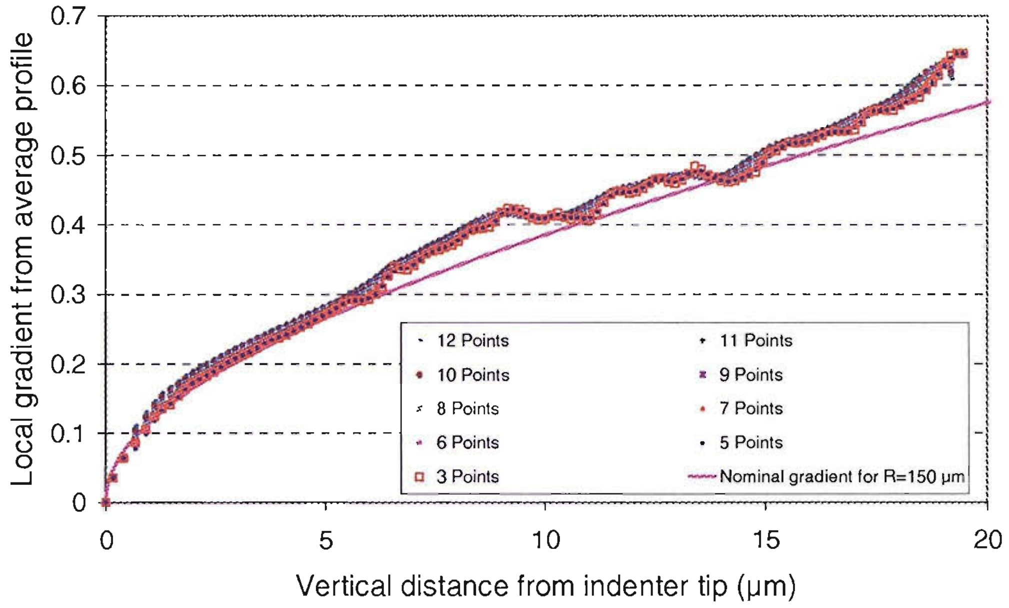

Fig. 3-12 Local gradient of the indenter profile obtained from linear fitting using different group sizes from 3-12 points.

2. Local arc fitting: This method is similar to the linear fitting method as regards methodology. However, the group size was taken to range from 12-20 points to check the effect of group size on fitting. Each group is then fitted by an arc whose centre and radius of curvature are calculated from arc fitting, a fitting routine developed using Matlab based on the least squares method. Having obtained the arc equation, it is then differentiated and the tangent at the midpoint of its length is calculated. Radius and tangent of the arc are assigned to its midpoint. The variation of gradient and radius with depth are plotted in Fig. 3-13 and Fig. 3-14, respectively.

3. Axi-symmetric circle fitting: In this method an axi-symmetric part of the indenter tip up to a certain vertical distance from the tip is fitted by an arc sharing the same axis of symmetry. The fitting procedure is started by fitting a region close to the indenter tip then gradually increasing the vertical distance of the fitted part around the tip centre until it covers the whole spherical tip. The radius value of the fitting arc is assigned to the point furthest from the tip considered for fitting. Gradient values are also taken at this point. Gradient and radius as a function of

vertical distance from the indenter tip are shown in Fig. 3-13 and Fig. 3-14, respectively.

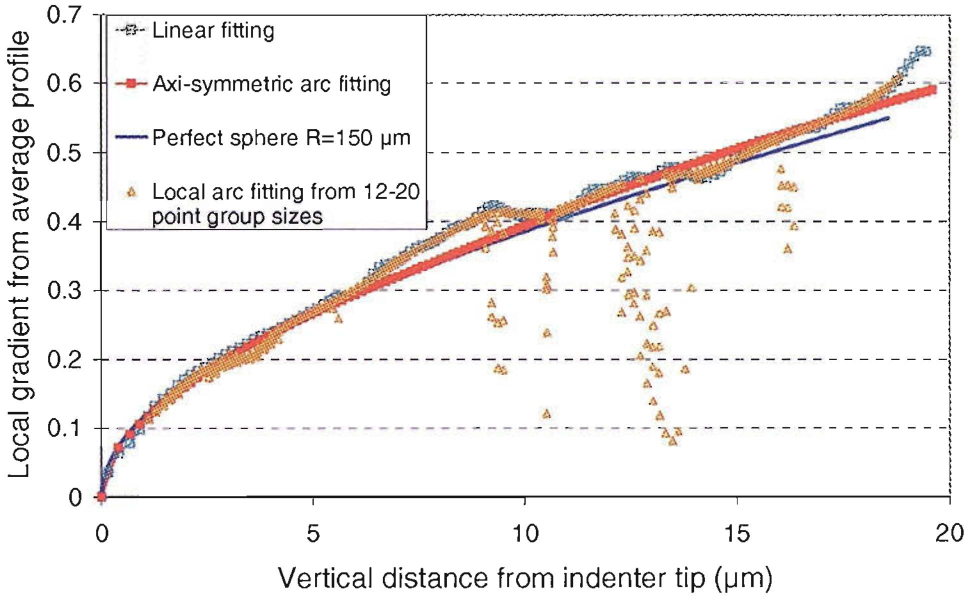

Fig. 3-13 Comparison of profile gradient calculated from local arc fitting, local linear fitting, axi-symmetric arc fitting, and that of perfect sphere of 150 μm radius.

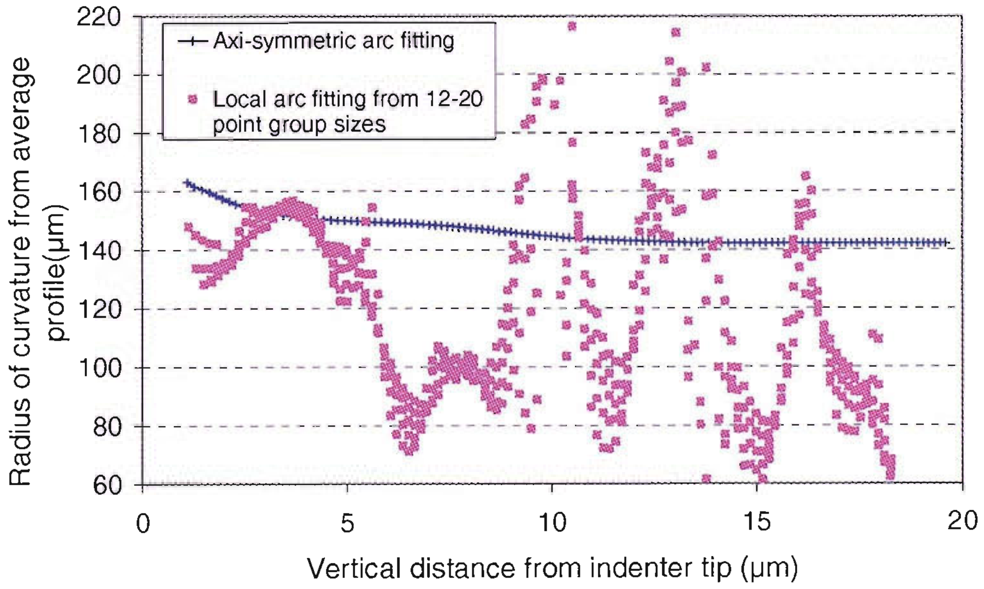

Fig. 3-14 Radius obtained from local arc fitting and axi-symmetric arc fitting.

As observed from Fig. 3-13 and Fig. 3-14, the results from local arc fitting are very sensitive to the number of points in the group size. An abrupt change in gradient and large scatter in radius is observed. On the other hand, the linear fitting method gives a rather smooth variation of gradient with vertical distance from the indenter tip and is insensitive to the number of points in the group size but it is incapable of measuring local radius. However, better performance can be observed from the axi-symmetric arc fitting method. It gives a smooth change of radius and gradient with vertical distance from the indenter tip. In addition, the radius obtained by this method is close to the nominal value provided by the manufacturer of 150 μm, and the gradient is close to that obtained from linear fitting.

The results from the various profile measurements and curve fitting applications presented above are used in Chapter 6 for material characterisation using a non spherical indenter.

3.6 Validation of instrumented hardness measurement with conventional Vickers microhardness values

Since the Berkovich indenter was designed to give approximately the same area function as the Vickers indenter, the hardness values resulting from both indenters should be almost identical. To confirm that the instrument results are reliable, the following validation procedures were adopted:

- Conventional Vickers micro hardness testing was carried out on two reference samples named REF-700 and REF-303, which are the reference hardness blocks allocated to calibrate the conventional Vickers microhardness tester. The nominal Vickers hardness values for the two blocks, as printed on the blocks, are 303 and 700 Vickers. Vickers micro hardness testing was carried at loads of 200, 300, 500, and 1000g. For each load, 3 to 5 indentations at different locations were performed.

- Using the instrumented microhardness tester, indentation testing using the Berkovich indenter was performed at different locations on each reference sample. The impressions on the surface comprised a rectangular grid at a regular spacing. Each row of the grid consists of a series of impressions, 13 indents, performed at loads ranging from 3 to 15 N. Each row of indents was repeated three times to form the columns of the grid. This was to ensure the reproducibility of the force-indentation data curves at each load value at different locations. The spacing of impressions was about 4 times the impression diameter. The resulting indentation data were then analysed by the instrument built-in software to determine hardness.

- Indentation testing is load-controlled. The loading rate used was 40 mN/s. An experiment was set up to reach a pre-specified load value, and then held for 180 s at the maximum load before commencing unloading. This allows creep to take place. Unloading was performed at the same rate as for loading.

- Residual impressions formed using both indenters, Vickers (by micro Vickers testing) and Berkovich (by instrumented microhardness tester), were imaged and captured using a microscope instrumented with a camera. The indent images were then viewed and their dimensions were measured optically using image analysis software. The contact area was then calculated for each indent and the hardness was determined.

3.6.1 Preliminary results of instrument performance

Having performed the hardness assessment on the reference samples REF-700 and REF-303, the three hardness values obtained are compared in Fig. 3-15 and Fig. 3-16.

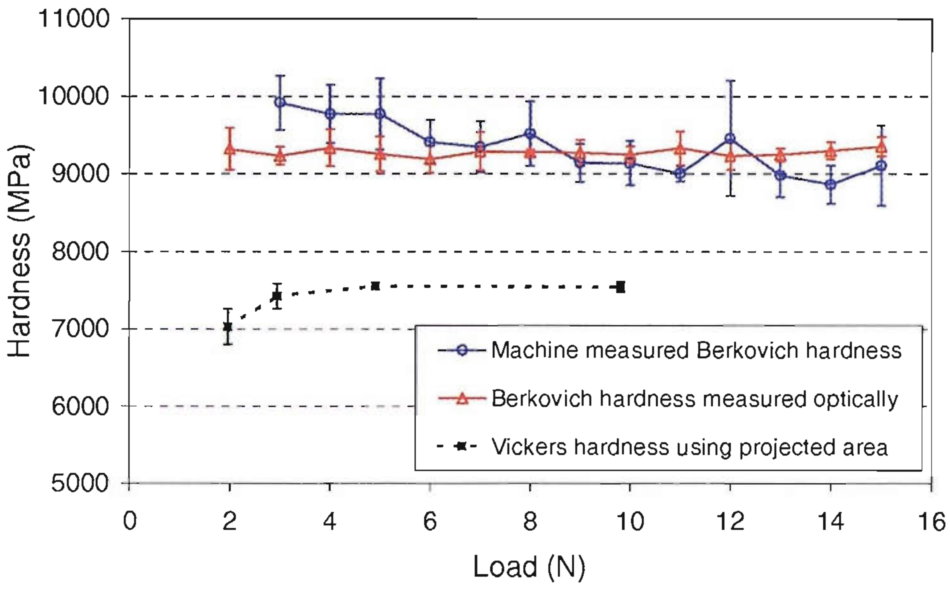

Fig. 3-15 Berkovich hardness of REF-700 measured by the instrumented hardness tester compared with the corresponding optically measured values and Vickers hardness calculated from projected area.

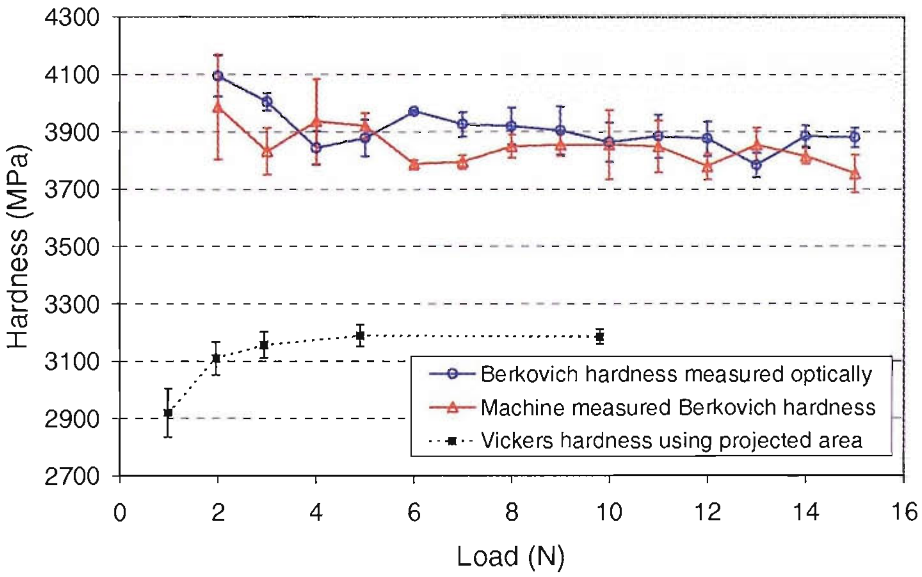

Fig. 3-16 Berkovich hardness of REF-303 measured by the instrumented hardness tester compared with the corresponding optically measured values and Vickers hardness calculated from projected area.

As can be noticed, Berkovich hardness values obtained by the instrumented tester agree well with those obtained from optical measurement of the corresponding indents. This suggests that the prediction of the contact area from the analysis of indentation data is valid. On the other hand, the Berkovich hardness is noticed to be 20% larger than Vickers hardness on both reference samples, which casts doubt on the measurement of the load applied by the instrumented tester. Referring to Section 3.2.1, load calibration is done automatically by the built-in software, which is set-up by the manufacturer and the operator has no control over this software. Hence, the only way to assess the accuracy of the instrument measurement of the applied load is by using independent means.

3.6.2 Assessing the measurement of the load applied by the instrumented hardness tester

In order to obtain indents from a known applied load, the Berkovich indenter was attached to the Vickers micro hardness tester by an adapter specially machined for this purpose. To measure the actual load applied by the Vickers micro hardness tester an electronic balance was positioned on its stage and the balance surface was levelled by means of a spirit level. The reference sample was then placed on the balance and indentation using the Berkovich indenter was performed at loads of 300, 500, and 1000g. By measuring the projected area of the indents the hardness values were obtained, and were found to be very close to the Vickers hardness values proving that the load measured by the instrumented hardness tester was incorrect. After referring to the manufacturer, they ascertained that the pendulum constant had been incorrectly entered in the software. This was then corrected by them. This was unfortunately ascertained after approximately 30 months of research.

Having corrected the manufacturer's error of load measurement, it was necessary to verify the load applied by the instrument using an independent method. For this purpose, a strain gauge attached to a ceramic cantilever was used. The strain gauge is oriented on the cantilever parallel to its longitudinal axis. In order to hold the cantilever, an aluminium stub with a cap of a rectangular cross section was machined. Using the two screws on the cap, the cantilever can be attached to the stub as illustrated in Fig. 3-17.

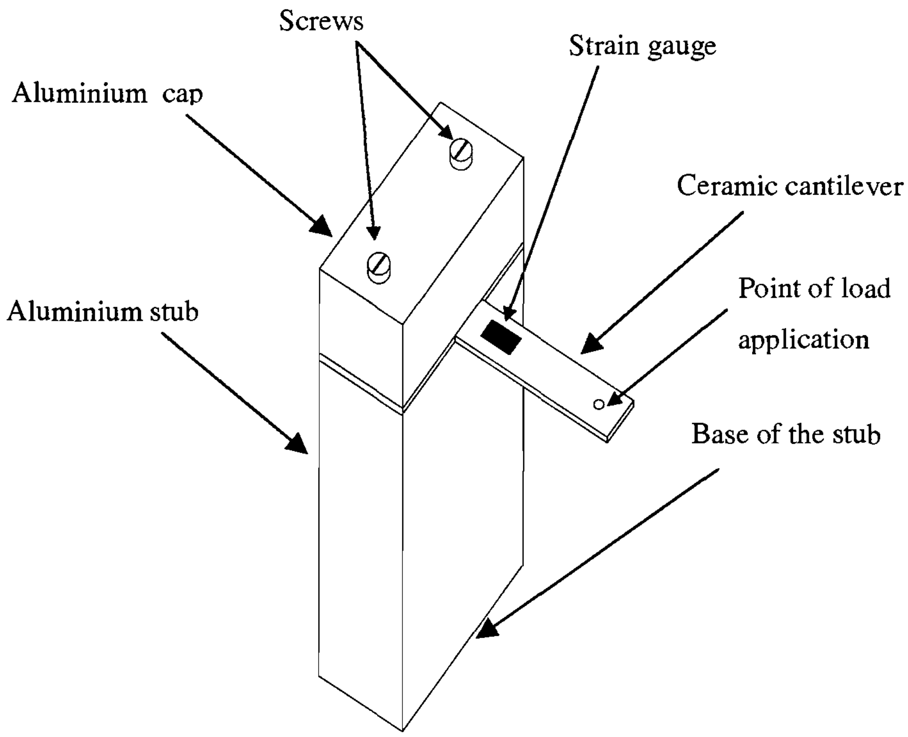

Fig. 3-17 Strain gauge fixed to ceramic cantilever clamped to an aluminium stub.

When load is applied to the cantilever, the cantilever will bend elastically and the resistance of the strain gauge changes in proportion to this deformation. Based on this principle, the strain gauge can be used to measure the load applied by the instrument provided it is calibrated beforehand. This calibration was performed as follows:
The stub with the cantilever anchored to it was fixed at its base to a horizontal plate. Three calibrating weights of masses 100.4, 125.3, and 150.6 g were hung from their hooks, one at a time, at a pre-defined point on the cantilever as shown in Fig. 3-17. Using a multi-metre, the gauge resistance was measured for each mass. Fig. 3-18 shows the results of plotting the resistance measured for the three applied masses.

Following calibration the load applied by the instrumented hardness tester was measured. The stub with its cantilever is fastened to the moving stage of the Microtest-200 and indentation testing was performed using a Berkovich indenter. The indenter was pressed against the same loading point at which the masses were hung. Because of the compliance of the cantilever and the high hardness of the ceramic, the indenter did not indent the ceramic, rather it caused that cantilever to bend elastically in the same way as when the cantilever was calibrated. At peak load the resistance of the strain gauge was measured. A dwell time of 60 seconds at peak load was taken to give enough time for taking measurements.

Three different load values were measured and plotted versus the corresponding resistance. The trend is shown to be linear, as would be expected from beam theory. The resulting line and that obtained from calibrating the strain gauge are compared in Fig. 3-18.

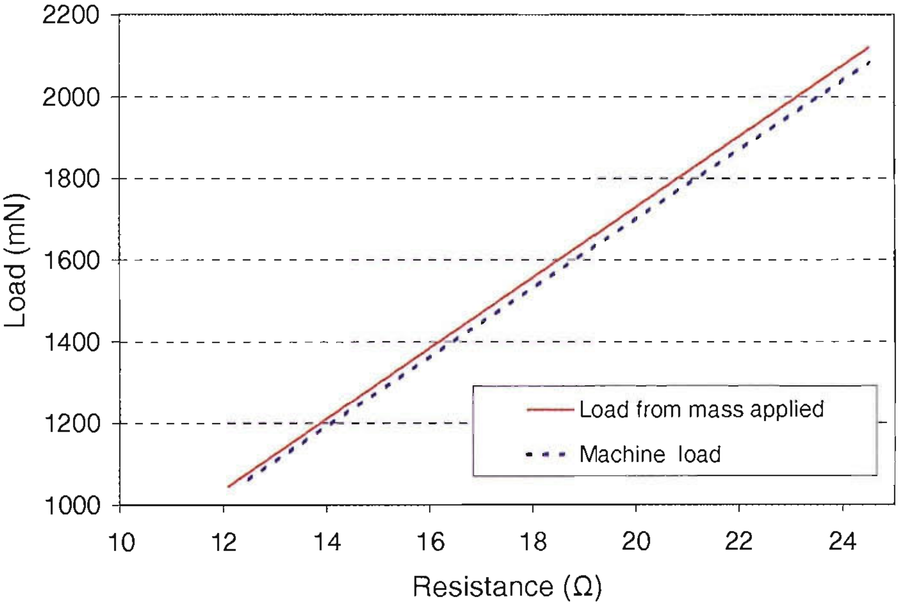

Fig. 3-18 Relationship between load applied and gauge resistance.

The two lines in Fig. 3-18 agree very well with a difference of less than 1.60%. Hence, the load measured by the instrument can be considered accurate.

3.6.3 Validity of the instrument derived hardness

Having validated the performance and measurement accuracy of the instrumented hardness tester, indentation testing using the Berkovich indenter was carried out on reference samples REF-700 and REF-303 using the same experiment setting and procedure described in Section 3.4. The Berkovich hardness values obtained by the instrument and by optical measurement of the indents are compared with the Vickers hardness in Fig. 3-19 and Fig. 3-20.

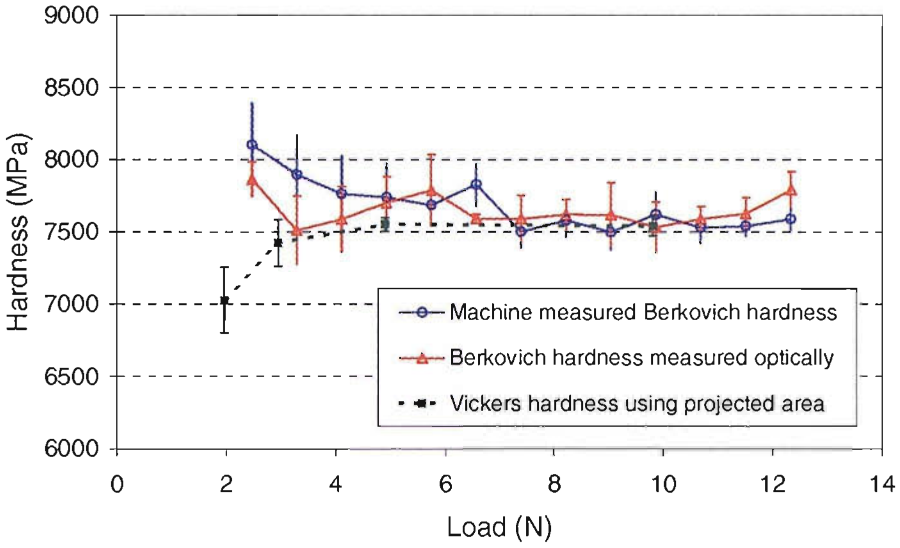

Fig. 3-19 Berkovich hardness of REF-700 measured by the instrumented hardness tester compared with the corresponding optically measured values and Vickers hardness calculated from projected area.

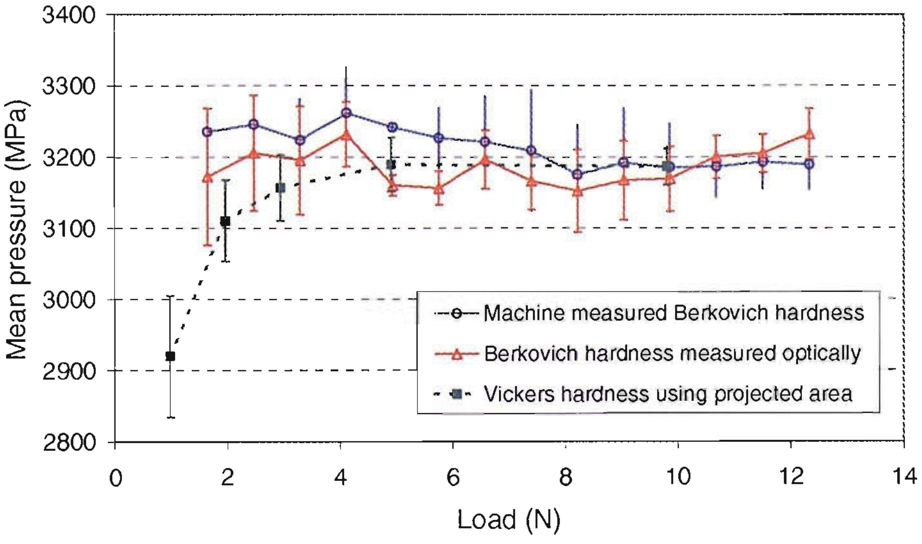

Fig. 3-20 Berkovich hardness of REF-303 measured by the instrumented hardness tester compared with the corresponding optically measured values and Vickers hardness calculated from projected area.

As can be observed the Berkovich hardness values derived by the instrumented tester at different loads agree with the Berkovich hardness obtained from optical measurement. Over the range of load from 4 to 12 N, the average difference is about 0.8% for REF-700 and 3.5% for REF-303. Also over the same range of load, the Berkovich hardness values derived by the instrument agree with the Vickers hardness based on projected area within an average difference of 1.8% for REF-700 and 4% for REF-303. This can be considered adequate validation of the performance and reliability of the instrumented microhardness tester.

3.7 Effect of frame compliance and depth calibration factor on hardness and reduced modulus measurements

It is obvious that the calibration factors of the instrumented indentation tester, described in Section 3.3, have an important effect on the accuracy of the indentation data, hence on the analytical results. A parametric study has been carried out to investigate the sensitivity of the analysis results to the effect of depth calibration and frame compliance especially when they vary within their range of fluctuation during the relevant calibration procedure.

Indentation testing was performed on the reference specimen REF 700 at various load levels to establish the sensitivity of the determined reduced modulus and Berkovich hardness to the frame compliance and depth calibration parameters of the instrument. It was found that the uncertainty in the value of the depth calibration factor can be up to 5%, which will incur a change of about 5% in hardness and 10-15% in reduced modulus; this change is inversely proportional to the change in the depth calibration factor. However, the frame compliance was found to be of greater significance as the frame deformation, $C_f P$, can constitute a considerable fraction of the raw depth measurement, h_{raw} included in Eq. 3-1. It was noticed that the variation in the frame compliance could be in the range of 7-10%, which will incur a change of 10-12% in hardness and 30% in reduced modulus, these changes being directly proportional to the change in frame compliance factor. Not only does the value of the frame compliance obtained from calibration depend on the load but also on the indenter tip imperfection. For shallow indents, the rounding of the tip, which is assumed perfectly sharp, has a worse detrimental effect on the results than in the case of deep indents. This was also reported by Oliver [43]. Values of frame compliance were obtained at different loads, and plotted in Fig. 3-21. For each of these values, hardness and modulus are obtained for all load values, and plotted in Fig. 3-22 and Fig. 3-23, respectively.

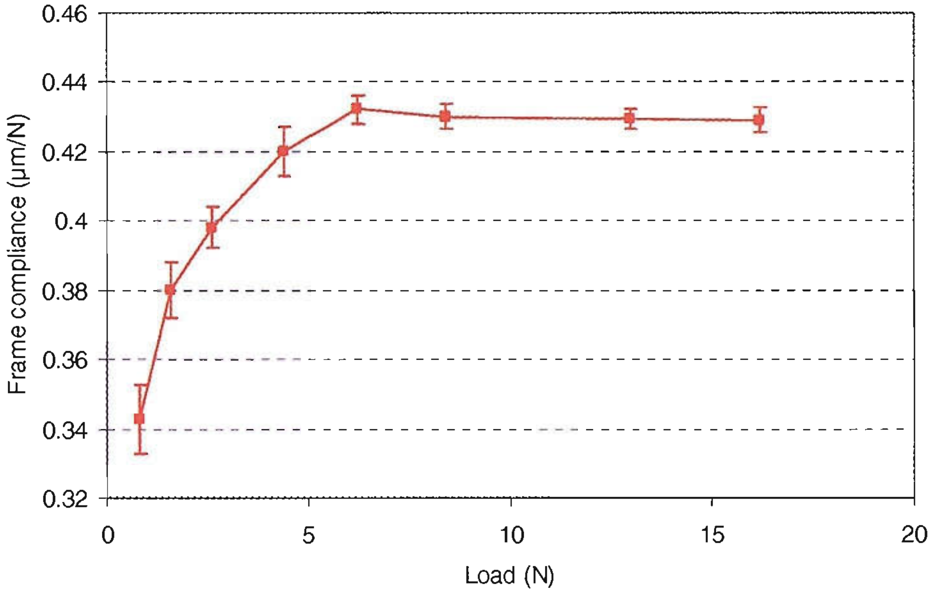

Fig. 3-21 Variation of frame compliance with load.

As can be observed, the frame compliance takes its smallest value at a small load and then increases with load until it reaches a constant value at high loads. This might be a direct consequence of the tip rounding effect, although this might not be the only reason. In fact, the frame might not deform linearly with load, especially at low loads.

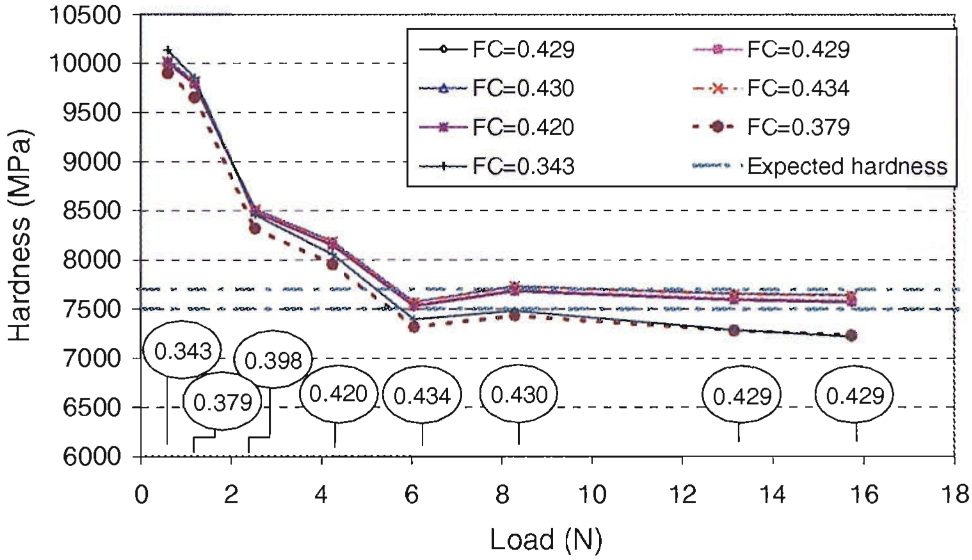

Fig. 3-22 Hardness of REF-700 calculated at a range of loads considering different frame compliance values, each obtained at different load.

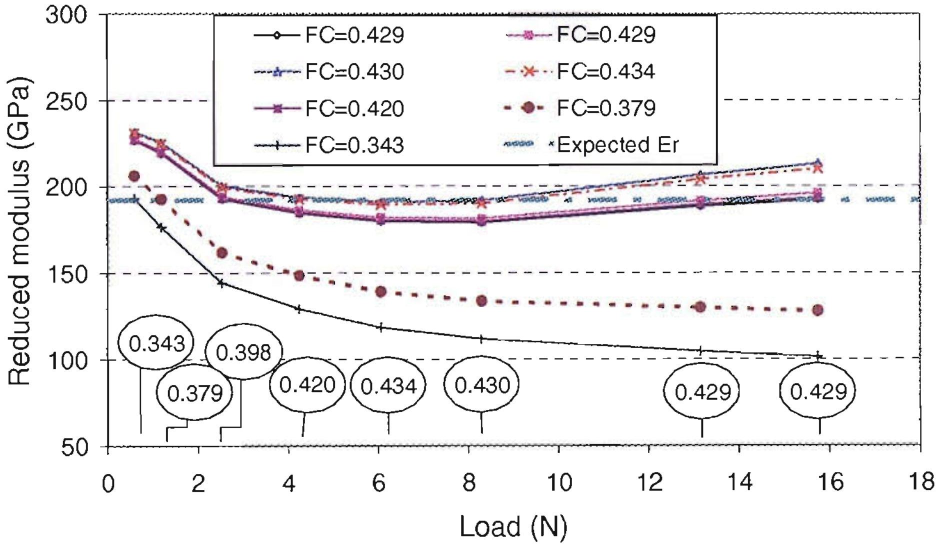

Fig. 3-23 Reduced modulus of REF-700 calculated at a range of loads considering different frame compliance values, each obtained at different load.

In Fig. 3-22 and Fig. 3-23 hardness and reduced modulus as a function of load are given for various values of frame compliance. Also included in the figures are the values of frame compliance at given loads. These figures show a pronounced sensitivity of modulus to the frame compliance, whilst hardness seems to be less sensitive. This suggests that great care should be taken in selecting a frame compliance value bearing in mind it varies with load. Hence, a curve for the frame compliance, as in Fig. 3-21, was obtained and used rather than a single value. For subsequent experiments performed at certain peak loads, the corresponding frame compliance value (using interpolation) should be used from Fig. 3-21.

3.8 Effect of fitting function to the unloading curve on hardness and reduced modulus measurements

The approach of Pharr *et al.* [15] and Oliver and Pharr [37] for analysing the indentation data obtained using the Berkovich indenter requires the determination of the contact stiffness in order to estimate the contact area, hence hardness and reduced modulus. Measurement of the contact stiffness is suggested to be taken as the first derivate of a simple power law function, at peak load, that fits the unloading curve. It is essential to assess the accuracy of determining this quantity, as this will affect the subsequent calculations of hardness and reduced modulus. Factors determining the measurement of the contact stiffness include the type of function that gives the best fit to the unloading curve and the portion of the unloading curve considered for fitting. To investigate these two factors, different functions were considered, namely 1st, 2nd , and 3rd order polynomials and a simple power law function according to Eq. 2-28 which was adopted in the built-in analysis software of the instrumented hardness tester. In addition, the effect of the unloading portion considered for fitting was assessed. The portions of 2.5%, 5%, 10%, 20%, and 30% of the unloading curve measured from peak load were considered for polynomial fitting. For power law fitting, the portions 30%, 40%, 50%, 60%, 70%, 75%, and 80% of the unloading curve were investigated. Indentation experiments at different loads were performed using the Berkovich indenter on the reference sample REF-700, and various portions of the unloading curve were fitted to the functions above with the aid of a program developed in Matlab. For every fitting function, the hardness was calculated and compared with the instrument derived values that were calculated from power law fitting. Fig. 3-24 to Fig. 3-26 show plots of the hardness of REF-700 calculated from 1st, 2nd and 3rd order polynomial fitting to various portions of the unloading curve measured from peak load. The instrument derived hardness values are also included in these figures.

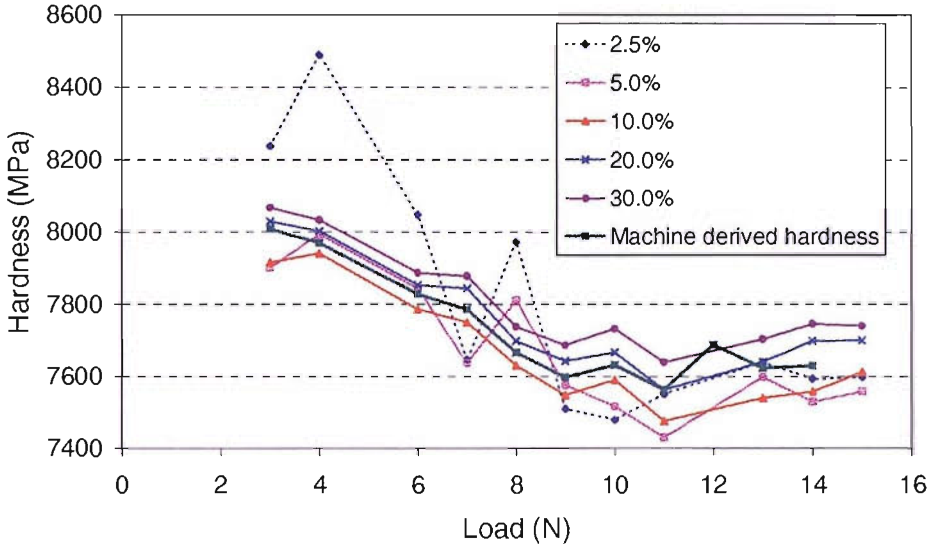

Fig. 3-24 Hardness of REF-700 from 1^{st} order polynomial fitting to various portions of the unloading curve measured from peak load compared with the instrument derived values.

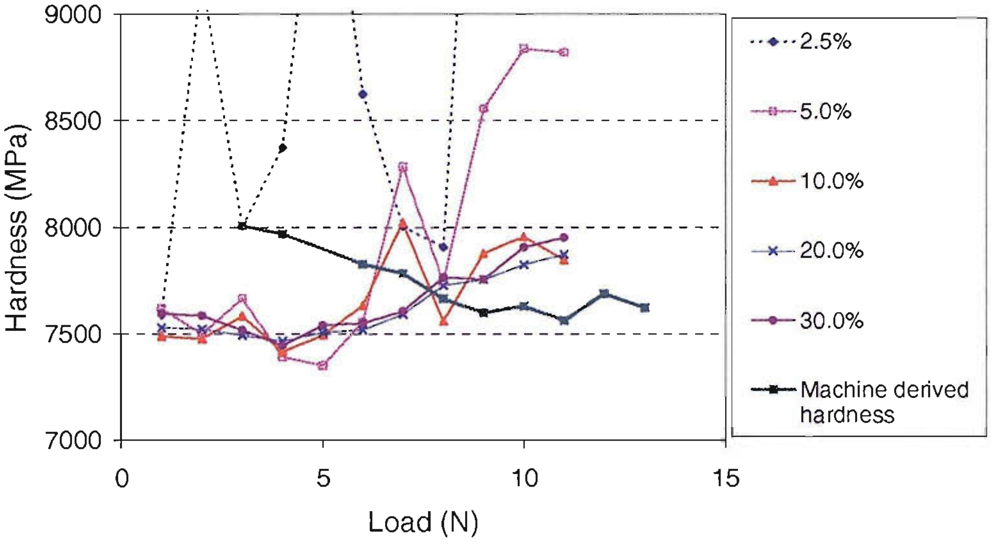

Fig. 3-25 Hardness of REF-700 from 2nd order polynomial fitting to various portions of the unloading curve measured from peak load compared with the instrument derived values.

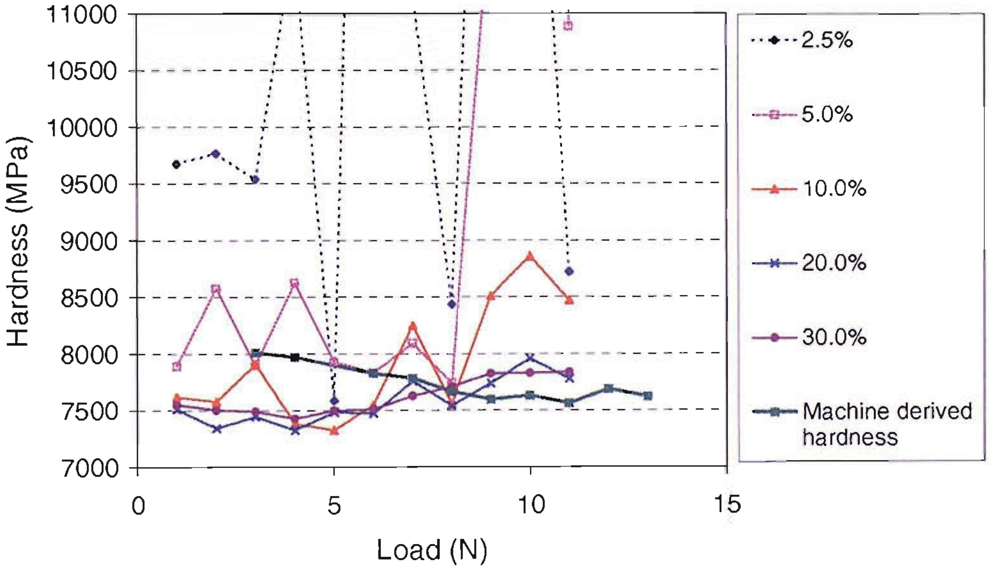

Fig. 3-26 Hardness of REF-700 from 3rd order polynomial fitting to various portions of the unloading curve measured from peak load compared with the instrument derived values.

As can be seen, the results are very dependent on the order of the polynomial used as a fitting function and the portion of the unloading curve considered for fitting. This results from the noise of the acquired data within a small range of the unloading curve which would have a big impact on the coefficients of the fitting function. The results for modulus have the same trend and so they are not plotted. On the other hand, power law fitting showed a much better performance. It was observed to be insensitive to the portion of the unloading curve considered for fitting. Hence, a large portion can be used for fitting which will be more representative of the material behaviour. Unlike the polynomial fitting function, the power law function is beneficial in estimating the residual depth from fitting since unloading is not complete in the loading cycles except for the final one.

CHAPTER 4

FINITE ELEMENT SIMULATION OF INDENTATION EXPERIMENTS

4.1 Introduction

The response of linear elastic materials during indentation can be predicted by elastic solutions as long as the indenter is described as a solid of revolution. However, modelling the indentation process in the elastic-plastic region is a more complex problem. Since the constitutive equations are non-linear and a number of plastic properties must be included to describe material behaviour, an analytical solution is not easily obtained. As a result, understanding of indentation behaviour in the elastic-plastic region can only be achieved through finite element simulation.

In this chapter, a finite element model is described which was developed and validated to simulate the indentation behaviour of elasto-plastic materials usually encountered in steel welded joints. Indentation experiments were performed on stainless steel and carbon steel samples, whose stress-strain curves were obtained from tensile testing. These curves were used as FE input to simulate the indentation process of a spherical indenter, R=150 μm, on these materials. The load-penetration depth curves predicted from the finite element simulations and those obtained from spherical indentation tests were compared.

4.2 Material selection

Three weldable steels were used for this research. They are mild steel and stainless steel supplied in plates of 8 mm thickness. Different grades of steel were considered in order to cover a range of hardness. The mild steel grades were 43A and 50A. The grade for stainless steel was 316L. Steel chemical composition is detailed in Table 4-1

Table 4-1 Details of chemical composition of the steel used

Plate No	Grade	C	Si	Mn	P&S	Nb	V	Cr	Mo	Ni
3,4	43A	0.25	0.50	1.60	0.05	-	-	-	-	-
5,6,7	50A	0.23	0.50	1.60	0.05	$\frac{0.003}{0.10}$	$\frac{0.003}{0.10}$	-	-	-
Stainless steel	316L	0.03	1.0	2.0	-	-	-	$\frac{16.5}{18.5}$	$\frac{2.0}{2.5}$	$\frac{11.0}{14.0}$

Sections were taken from the plates supplied and metallographically prepared and examined by optical microscopy. The rolling direction was determined by observing the orientation of inclusions. The grain size was determined as 10 to 15 μm. This is suitable as several grains would be included within an indent which typically might be 70-120 μm in diameter. Thus, the indentation data will reflect the average behaviour of the bulk metal determined in a tensile test, rather than the behaviour of a single grain.

4.3 Tensile testing

Tensile tests provide reliable and realistic information on elasto-plastic characteristics, which is essential input to the planned FE analysis. Tensile test samples were machined from the as-received plates according to the ASTM specifications with a circular cross-section. They were cut in the rolling direction of the plates with a gauge length of 25 mm. Tensile testing was carried out in the Engineering Materials Department laboratory using an Instron tensile testing machine. Machine crosshead speed was set up at 1mm/minute. Elongation was measured using an extensometer that can cover up to 40% strain. Elongation beyond this value is measured from the crosshead motion.

For a more accurate measurement of load and elongation and to reduce the experimental error, a digital data logger was connected to the Instron tensile tester for calibration and the test itself. The data logger acquires signals produced by the Instron, corresponding to force and elongation values, which are converted into the engineering stress-strain points. Up to 40% strain, elongation is measured directly from the extensometer rather than from the motion of the chart recorder.

Having determined the engineering stress-strain curve, the true stress-logarithmic strain (σ–ε) relation, which is the final information sought from tensile testing, can then be calculated using the equations

$$\varepsilon = \ln(e+1) \qquad \text{Eq. 4-1}$$

$$\sigma = \sigma_o(e+1) \qquad \text{Eq. 4-2}$$

where σ_0 and e are the engineering stress and strain values, respectively. The material true stress-logarithmic strain curve obtained from the tensile testing is then used as the material input data into the finite element simulation of indentation even though the normal stress applied by an indenter is compressive. It is worth noting that higher strains are exhibited in the compression test than the fracture strain in the tensile test. This requires extrapolating the (σ–ε) curve for higher strain values since the plastic strains induced by indentation far exceed the fracture strain from tensile test. It is assumed that the (σ–ε) curve obtained from a compression test would be the same as the extrapolated tensile (σ–ε) curve.

The maximum calculated logarithmic strain is at the engineering strain corresponding to maximum load where necking commences. The strain up to this point is considered uniform but beyond that, the strain becomes localised around the neck region hence its measured value depends on the considered gauge length, in which case Eq. 4-1 and Eq. 4-2 are not valid. To determine the (σ–ε) curve at higher strain values and also to determine the strain hardening exponent and strength coefficient, the (σ–ε) curve is fitted to a power law function in the form of Eq. 2-5. It was noticed that it was not possible to fit the whole plastic region of the curve by a single function. Hence the plastic part of the curve was broken into two parts, each of which was fitted separately to a power law function. The fitting function obtained for the larger strain values was used to extrapolate the curve.

The engineering and the true stress-logarithmic strain curves with the extrapolated part are all plotted in Fig. 4-1 to Fig. 4-6 and the values of all material parameters are summarised in Table 4-2. The strength coefficient, K, and the strain hardening exponent, n, resulting from power law fitting to the two parts of the true stress-logarithmic strain curve beyond yielding are also indicated on Fig. 4-1 to Fig. 4-6.

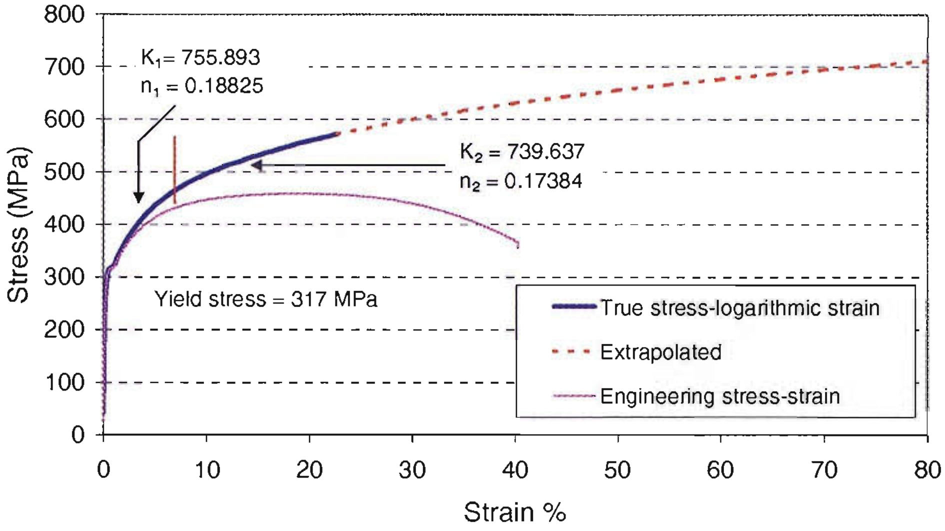

Fig. 4-1 Stress- strain curves for the steel plate number 3 Grade 43A.

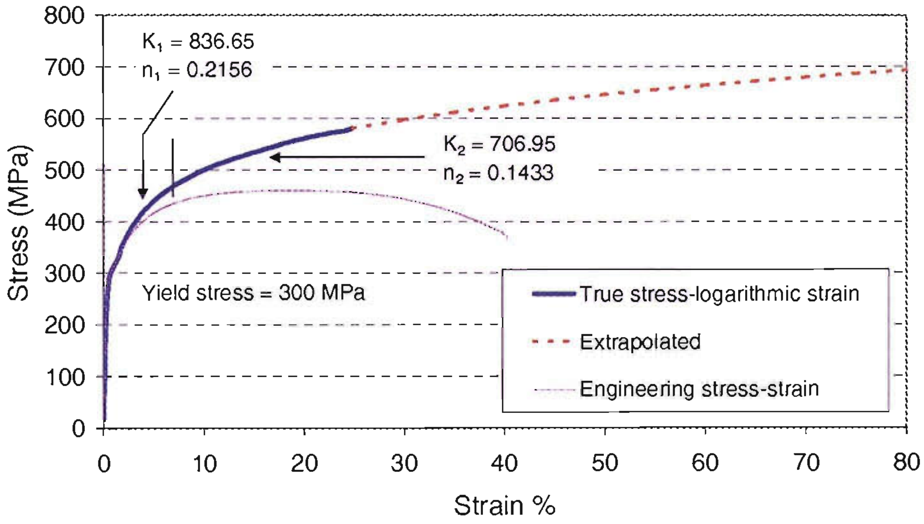

Fig. 4-2 Stress- strain curves for the steel plate number 4 Grade 43A.

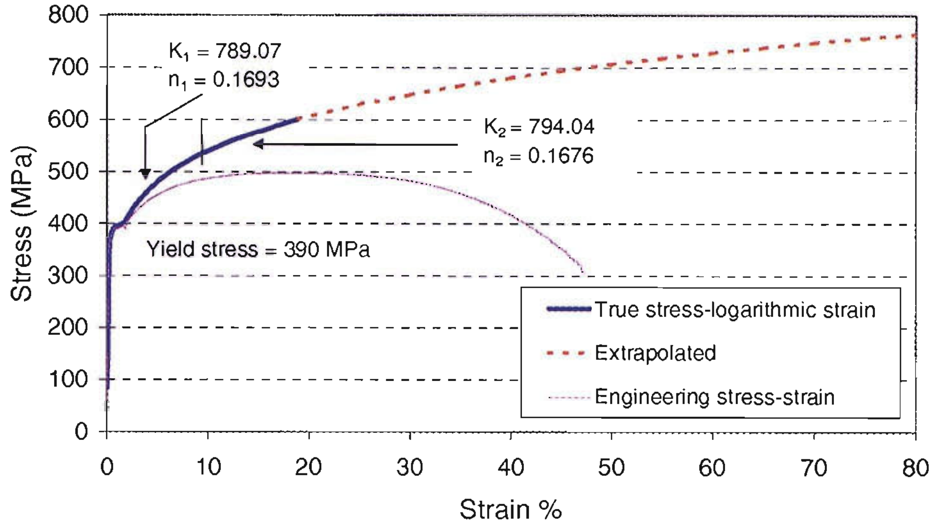

Fig. 4-3 Stress- strain curves for the steel plate number 5. Grade 50A.

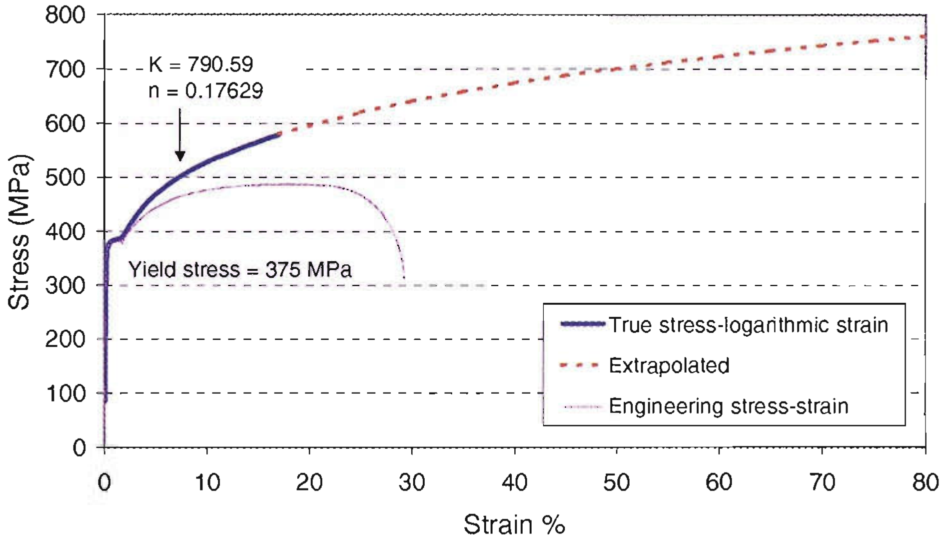

Fig. 4-4 Stress- strain curves for the steel plate number 6. Grade 50A.

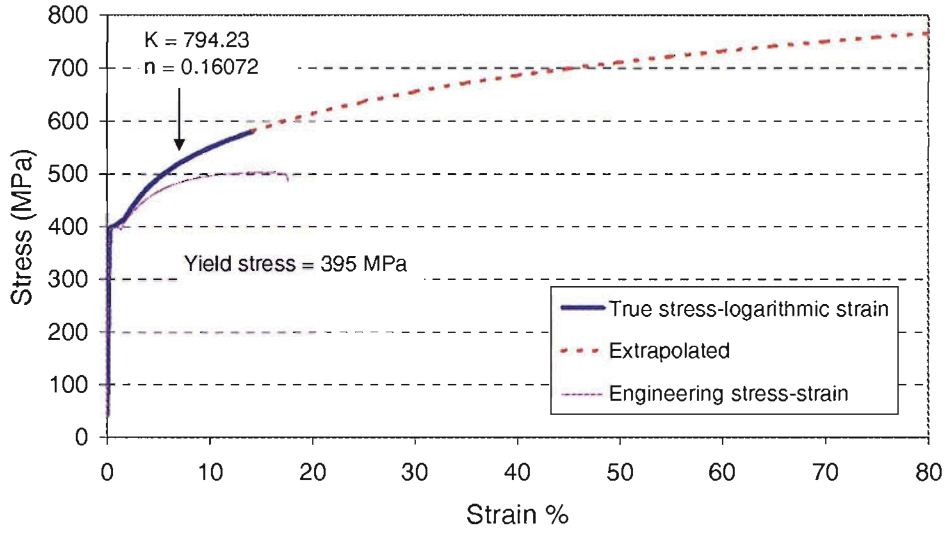

Fig. 4-5 Stress- strain curves for the steel plate number 7. Grade 50A.

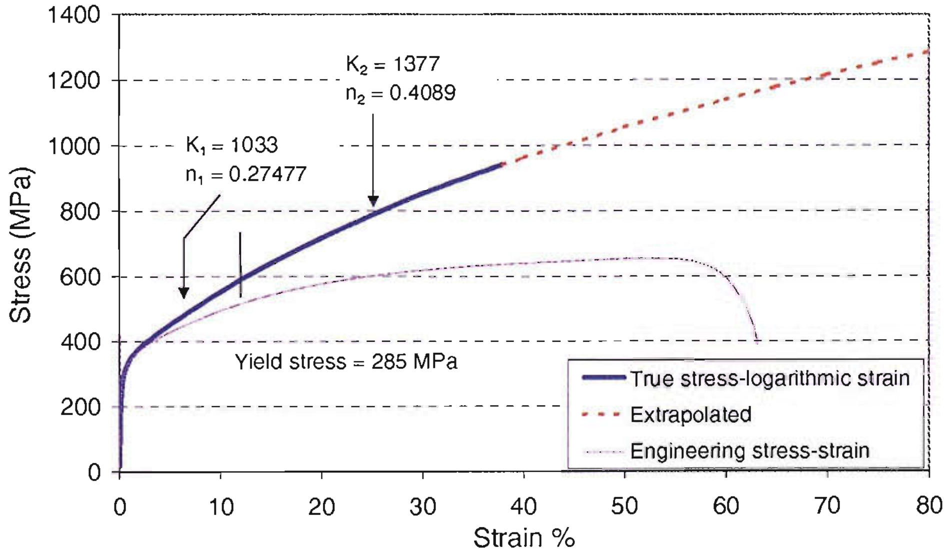

Fig. 4-6 Stress- strain curves for the stainless steel plate. Grade 316L.

Table 4-2 Summary of the material parameters obtained by tensile testing.

Plate number	Steel grade	Yield stress (MPa)	UTS (MPa)	Strain at UTS (%)	Failure strain (%)	Strength coefficient (MPa)		Strain hardening exponent	
						K_1	K_2	n_1	n_2
S3	43A	317	460	21	40	756	740	0.19	0.17
S4	43A	300	460	20.7	40	837	707	0.22	0.14
S5	50A	391	500	20.8	48	789	794	0.17	0.17
S6	50A	375	487	18.5	30	791	791	0.18	0.18
S7	50A	395	503	15.3	35	794	794	0.16	0.16
Stainless steel	316L	286	655	51.8	63.2	1033	1377	0.28	0.40

The moduli of elasticity are equal to 210 and 185.1 GPa for mild steel and stainless steel, respectively.

Although the stress-strain curves for plates S6 and S7 are well fitted by a single power law function and are close to each other, other plates showed different plastic properties despite being of the same grade. Hence, obtaining the stress-strain curve for each plate is beneficial for a more precise information on materials properties for finite element simulation.

4.4 Finite element simulation

An elastic-plastic finite element model was built using ANSYS 5.7 [100] to simulate the indentation process. Isotropic hardening plasticity and the von Mises yield criterion were assumed. Large strain and other non-linear features of ANSYS 5.7 were incorporated in the model. The material data input for the sample was the true stress-logarithmic strain curve. The diamond spherical indenter tip was modelled both as rigid and deformable with only linear elastic material properties, that is, no yield allowed and its modulus of elasticity and Poisson's ratio were taken equal to 1140 GPa and 0.07, respectively. These values were provided by the instrument manufacturer MicroMaterials [101], and were found to agree with those reported by Field [102].

The simulation of indentation process is a 3D axisymmetric problem. It assumes a spherical indenter tip pressed into a cylinder of material that should be representative of a homogenous infinite half space. Loading the indenter is prescribed as applied displacement on the top surface. Running a 3D problem is expensive and requires large memory and disk space. Advantage can be taken of the axisymmetry of the problem, so that it can be simplified to a 2D problem instead, and only half of the indenter and the material cylinder section by a plane through the axis of symmetry are modelled. This reduces the number of elements and the number of degrees of freedom per node, thus the running time and disk space required.

4.4.1 Element characteristics

Element PLANE42, which is a four-noded quadrilateral element, is used to mesh the deformable indenter and the sample. Each node of this element has two degrees of freedom. More details can be found in the online ANSYS 5.7 help [100].

The free mesh option in ANSYS was initially used to mesh both the indenter and the sample. Over the region where the two bodies are expected to be in contact, a regular mesh size was mapped on both bodies for generating elements of the same length in both bodies. This mesh regularity over that region is intended to help achieve better numerical performance and enhance the accuracy of stress and strain distribution over this region of interest, especially when results are averaged at nodes. However, the indentation process involves high geometrical non-linearity. With increasing penetration depth, the induced strains increase and element distortion increases excessively and reaches a stage where the solution fails to converge even at shallow indentation due to violating element geometry limits.

The automatic free and mapped mesh options in ANSYS create a large number of elements with less control on their shape and interior angles that deviate from 90° as shown in Fig. 4-7. The steeper the transition from a fine mesh, in the contact region, to a coarse one, at the far edges, the more irregularity in element shape.

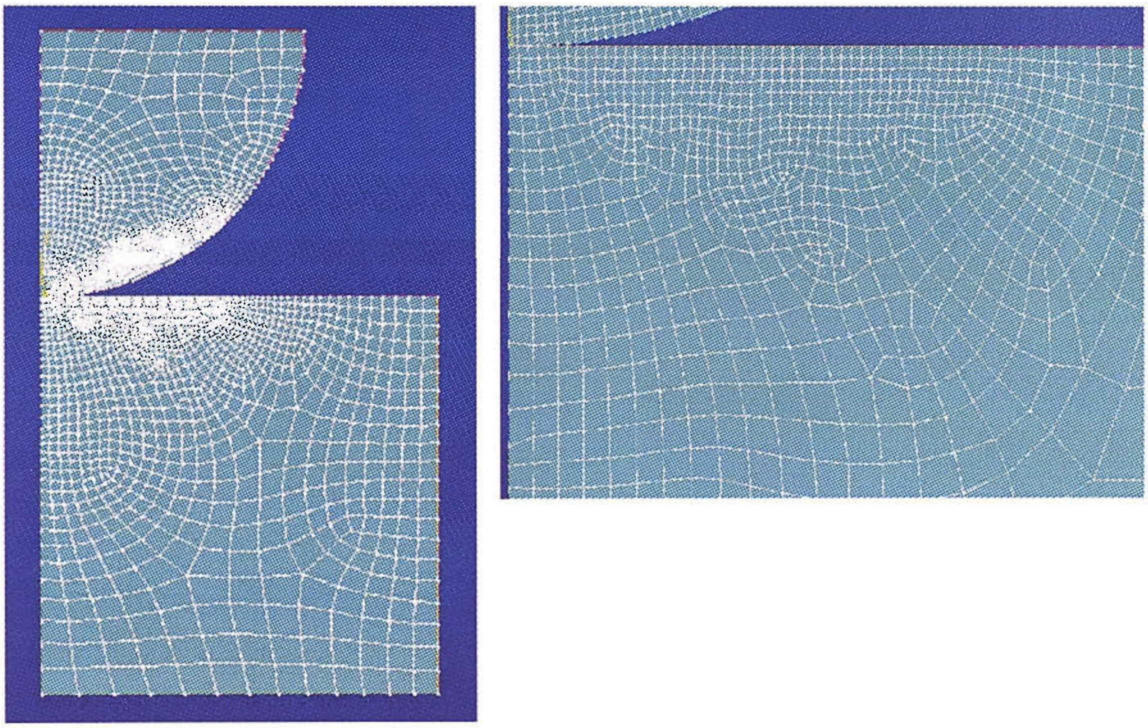

Fig. 4-7 The mesh generated using ANSYS showing the irregularity in the element geometry, which contributes to high element distortion when loading.

Decreasing the element geometric irregularity by introducing a smooth variation of mesh density will produce a mesh with larger number of elements, hence longer running time and convergence problems. This necessitates the imposition of more control on all elements of the mesh which can only be achieved by manually generating the mesh. Whilst this job is very complicated and tedious to do using ANSYS, PATRAN offers a powerful facility of manual mesh generation with full control on all elements size and shape. In addition, it has the capability of doubling element size in adjacent element layers during the transition in element size from the fine zone to the coarse zone without violating any element geometry limits. This is done by using trapezoidal elements as an interlink between the two-size zones as illustrated in Fig. 4-8. As a result, fewer elements will be created for the whole mesh compared with that of ANSYS.

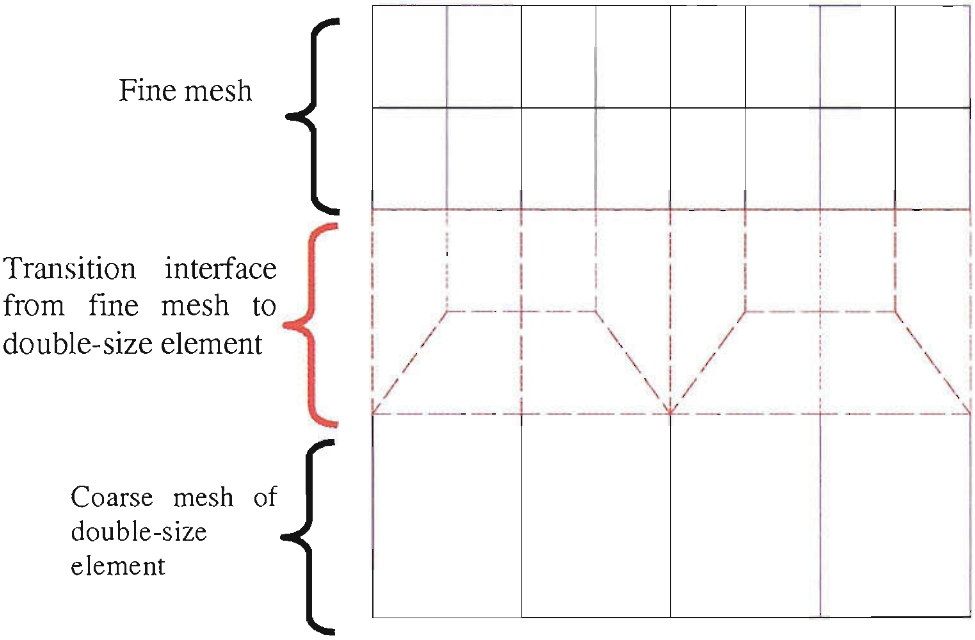

Fig. 4-8 Schematic drawing showing the transition in element size from fine mesh to a coarse one of double-sized elements.

Although this mesh decreased the running time for every load step, convergence difficulties persisted at deep penetration. This is owing to the high strains imposed on the elements within the indentation zone of the material, especially those closer to the contact centre, which undergo excessive deformation and almost get squashed as a result. To counteract this excessive change in the aspect ratio, the initial element geometry of the specimen was modelled as a rectangle instead of a square. The aspect ratio was taken equal to 2.0 with the length in the direction of indentation. This helped the model reach the sought penetration depth without any convergence problems, and thus was adopted for all subsequent FE simulations.

4.4.2 Contact modelling

Contact between the specimen and the indenter was modelled using contact elements generated over the region of possible contact between the two surfaces. Initially the contact element CONTA48 was used to present node-to-surface contact. The element geometry is a triangle with the base being the target line between two nodes on one of the surfaces (called the target surface) and the opposing vertex being the contact node on the other surface (called the contact surface), as illustrated in Fig. 4-9. The indenter surface, which should be convex, is considered 'contact' and the flat sample surface is the 'target'.

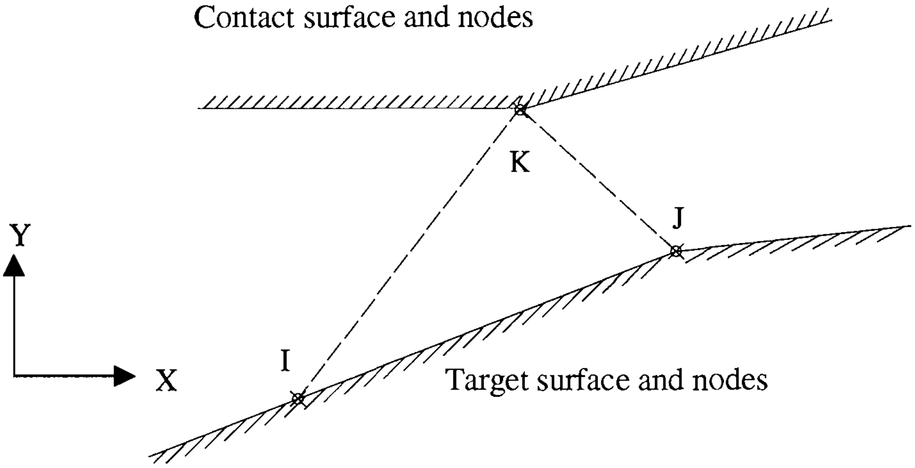

Fig. 4-9 2-D Node-to-Surface contact element *CONTA48*.

In reality during indentation, there is no penetration between the two bodies in contact, whilst numerically this is impossible. In fact, contact between two bodies is detected only when virtual penetration occurs within a certain limit. A compatibility control method is used to ensure that one surface does not penetrate into another surface by more than an acceptable tolerance. The method adopted in this model was the penalty method. This method is controlled by the normal contact stiffness, KN, which has units of force/length. KN should be large enough so that it reasonably restrains the model from over-penetration, yet it should not be so large that it causes ill conditioning and leads to convergence failure. A parametric study was carried out to ascertain the optimum value for KN. The analysis started with a low value for KN which was gradually increased until convergence difficulties began. A value of 10^6 N/m was selected as it showed a smooth convergence. When simulation reaches a few micrometres of penetration, the solution struggles to converge and the number of iterations per load step increases considerably. The conversion problem became even worse when sliding friction was included between the two surfaces. The difficulties with convergence prompted the transition to alternative contact modelling, which was adopted in all subsequent simulations and produced all the results presented in this study. Contact was modelled as a pair of contact elements, the contact CONTA171 and the target TARGE169 [100]. CONTA171 was used to represent contact and sliding between the target surface, the indenter, and a deformable surface, the specimen. The geometric description of the two elements is illustrated in the diagram shown in Fig. 4-10.

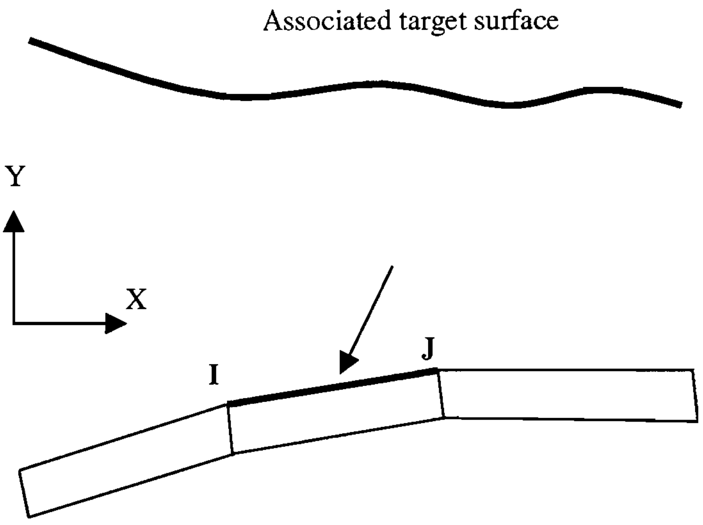

Fig. 4-10 *CONTA171* 2-D Surface-to-Surface Contact Element (2 nodes).

The specimen top surface was overlaid with contact element CONTA171 and the indenter surface was meshed with the target element TARGE169. The penalty method with Lagrange multiplier was used to ensure that the penetration compatibility is satisfied. The normal contact stiffness factor, FKN, was taken equal to the default value which is 1.0, and the tolerance FTOLN, the maximum penetration allowed as a fraction of the underlying element depth, was taken equal to the default value of 0.1.

4.4.3 Characteristics of the specimen mesh

Initially, the mesh of the indented specimen was generated with its refined zone in the indentation zone made up of element size (1.0×2.0) μm, as illustrated in Fig. 4-11. The area of the indenter was meshed using the free mesh option in ANSYS. Mesh dimensions that covers the modelled half of the cylinder are 672×448 μm. Details of the mesh are summarised in Table 4-3

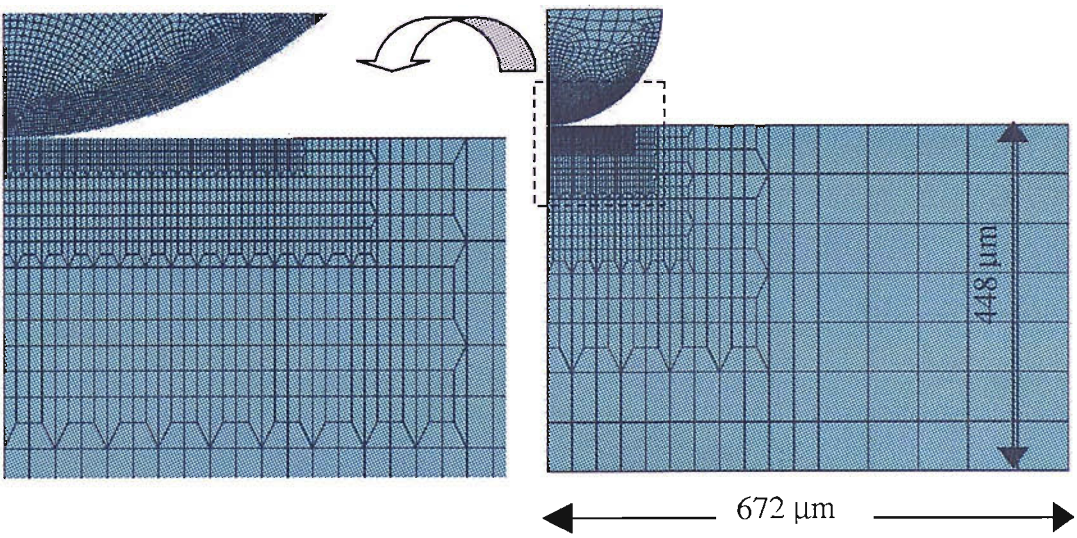

Fig. 4-11 Mesh (A) of the specimen. The indenter is meshed using ANSYS whilst the sample is meshed manually using PATRAN. Element size in the contact region is (1.0×2.0) μm.

To investigate mesh sensitivity, two other meshes were generated by enlarging the specimen dimensions and the refined zone covering the indentation region, as illustrated in Fig. 4-12 and Fig. 4-13. The characteristics of these meshes are summarised in Table 4-3. In all three meshes, the indenter is meshed using the free mesh option in ANSYS. Elements on the indenter perimeter from the tip up to the height that covers indentation depth are taken to be 1.0 μm wide, which is the same width as that of the corresponding elements of the specimen over the contact region.

Table 4-3 Details of the meshes considered

Mesh	Specimen dimensions (μm)		Number of Nodes	Number of Elements	Dimension of the finest zone covering the contact region (μm)	
	Width	Height			Width	Height
A	672	448	1602	1510	92	8
B	960	1600	4200	4046	112	16
C	1472	1568	8665	8470	127	96

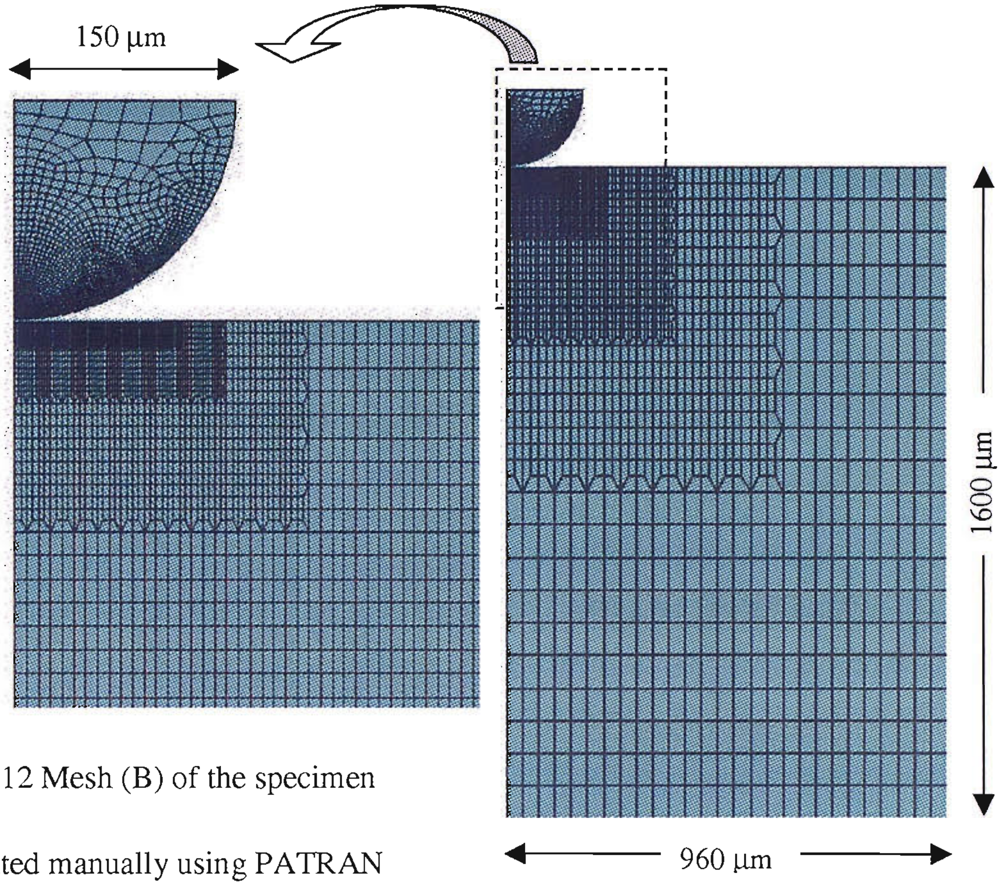

Fig. 4-12 Mesh (B) of the specimen generated manually using PATRAN

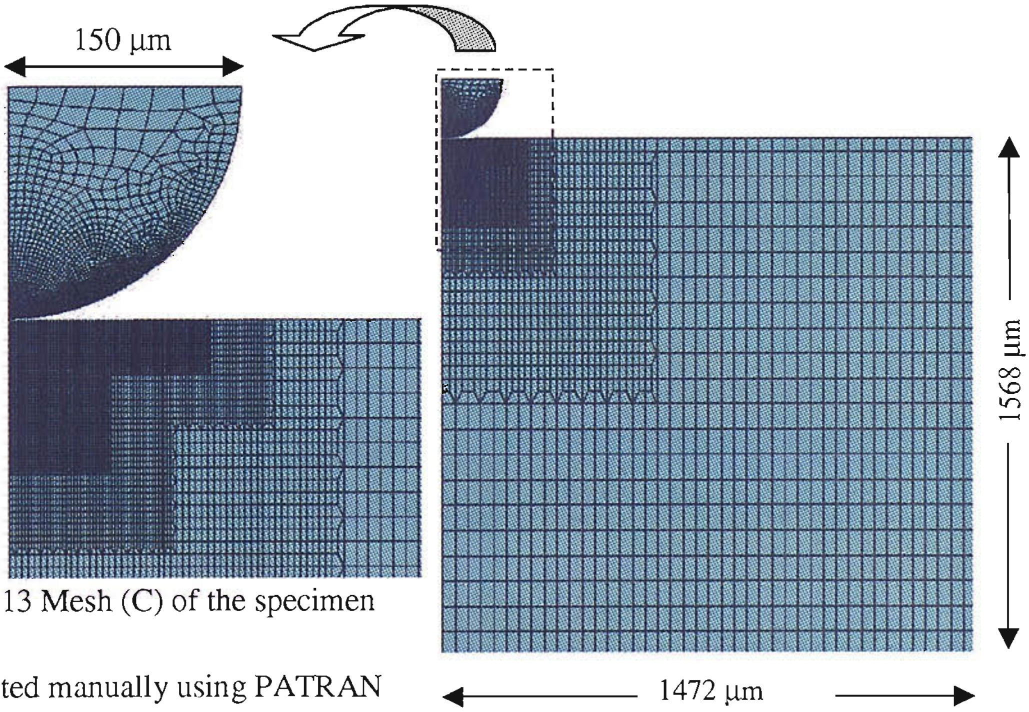

Fig. 4-13 Mesh (C) of the specimen generated manually using PATRAN

4.4.4 Validation against the elastic solution

The FE model developed was applied to simulate the indentation process of a perfect sphere with a radius of 150μm on a linear elastic material. Mesh sensitivity of the model is investigated by testing the three different meshes (A, B, and C) whose specifications are summarised in Table 4-3.

The first stage was to validate the model against Sneddon's elastic solution of a sphere on an elastic flat surface, [13]. The contact was modelled as frictionless. Loading is prescribed as displacement controlled and increased by 0.1 μm at every load step. Peak load is attained when the maximum depth reaches 20 μm. At every load step the indent profile geometry, contact radius and depth, was directly measured and compared with the prediction of Sneddon's solution. Comparison of the predicted load-indentation depth curve by FE and Sneddon's solution is shown in Fig. 4-14. Likewise, Fig. 4-15 shows the ratio of contact depth, h_c, to indentation depth, h_t, which should be equal to 0.5 according to Sneddon's solution.

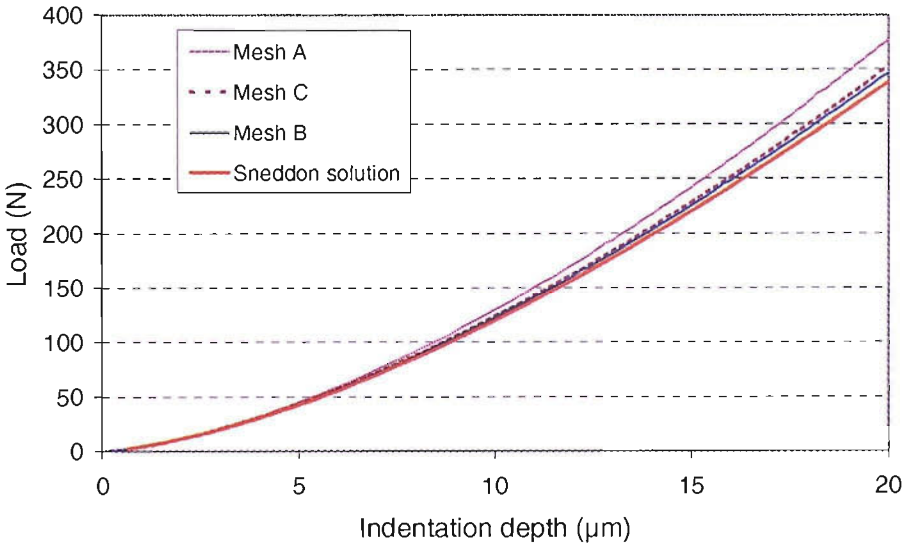

Fig. 4-14 FE-generated load-indentation curves for three different meshes

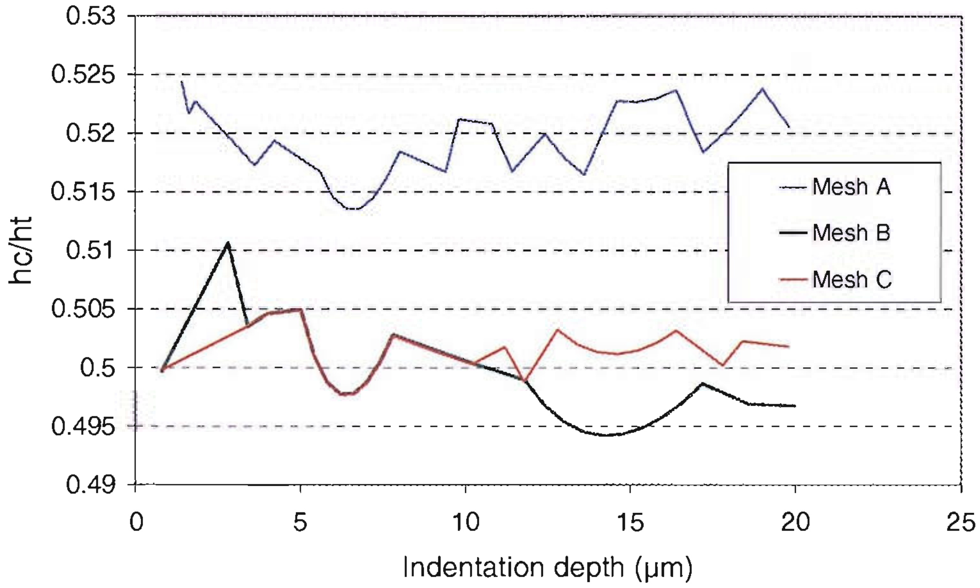

Fig. 4-15 Comparison of the ratio of contact depth to the indentation depth for the three meshes, which should equal to 0.5 according to Sneddon's solution.

The step-wise behaviour of the contact depth curve predicted by FE is a consequence of discretisation as the contact edge is only detected at the surface nodes. As observed from the plots above, Fig. 4-14 to Fig. 4-15 no significant difference can be noticed between results produced by meshes B and C and the resulting measurement of the contact depth and material response during indentation agree with the elastic solution of Sneddon for the elastic solution. Since mesh B has less than half the number of elements in mesh C, mesh B has been adopted for the FE simulation of the elastic contact carried out in this study.

4.4.5 Extension of the FE model in the elasto-plastic region

The second stage of validating the FE model developed is in the region of elasto-plastic deformation. The indentation simulation was initially carried out with idealised material properties and a perfect spherical indenter with a radius of 150 μm. A stress-strain curve produced by tensile testing was modified to an ideal curve with a single value for the strain hardening exponent and the strength coefficient. The modified stress-strain curve was based on the true curve for steel plate number 5, more details of which can be found in Section 4.3. The modified stress-strain curve, plotted in Fig. 4-16 together with the original true curve is characterised by three different regions:

Elastic properties are described by E=210 GPa, σ_e=340 MPa. The post-yield part is modelled using $\sigma_{0.2}$=375 MPa, n = 0.132, and K = 782.91 MPa, satisfying the continuity condition at yield point where

$$\varepsilon_{0.2} = 0.002 + \frac{\sigma_{0.2}}{E} \qquad \text{Eq. 4-3}$$

The part on the stress-strain curve joining the elastic limit to the yield stress is created using a quadratic function.

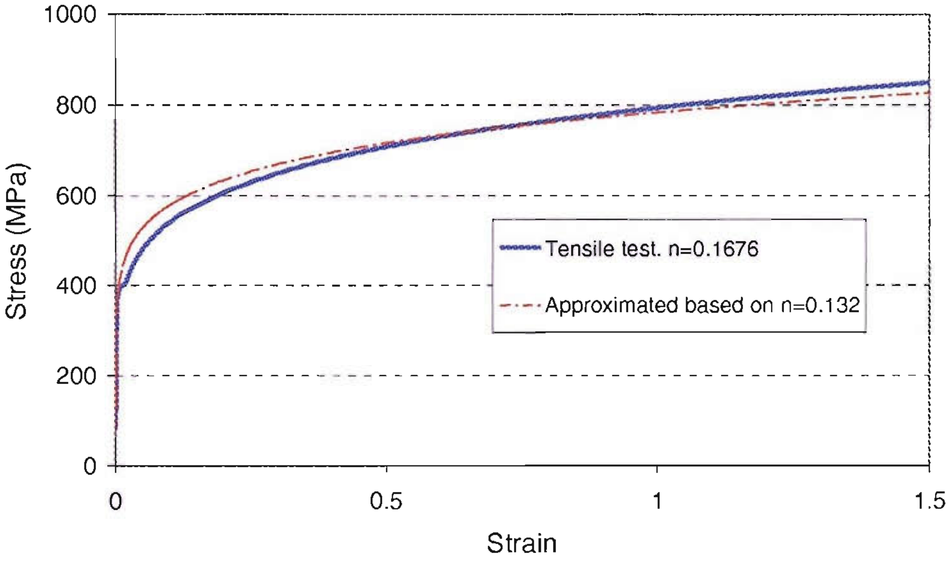

Fig. 4-16 Stress-strain curve of steel No 5 compared with its approximation.

Mesh sensitivity was investigated for the three meshes detailed in Table 4-3 in the elasto-plastic region. It was noticed that the resulting load-indentation curves almost overlap each other. Even though this suggests that mesh A is adequate, mesh B has been used for elasto-plastic FE simulation. A parametric study has been carried out to test the effect of contact tolerance and contact stiffness input to the model. The contact tolerance was reduced by half and the contact stiffness was increased 100-fold. No noticeable effect was observed on the indentation data. Finally, the effect of friction between indenter and specimen was examined. Five different values of the friction coefficient of contact were tried, namely 0, 0.05, 0.1, 0.2, and 0.5. The resulting *P-h* curves can be compared by reference to Fig. 4-17

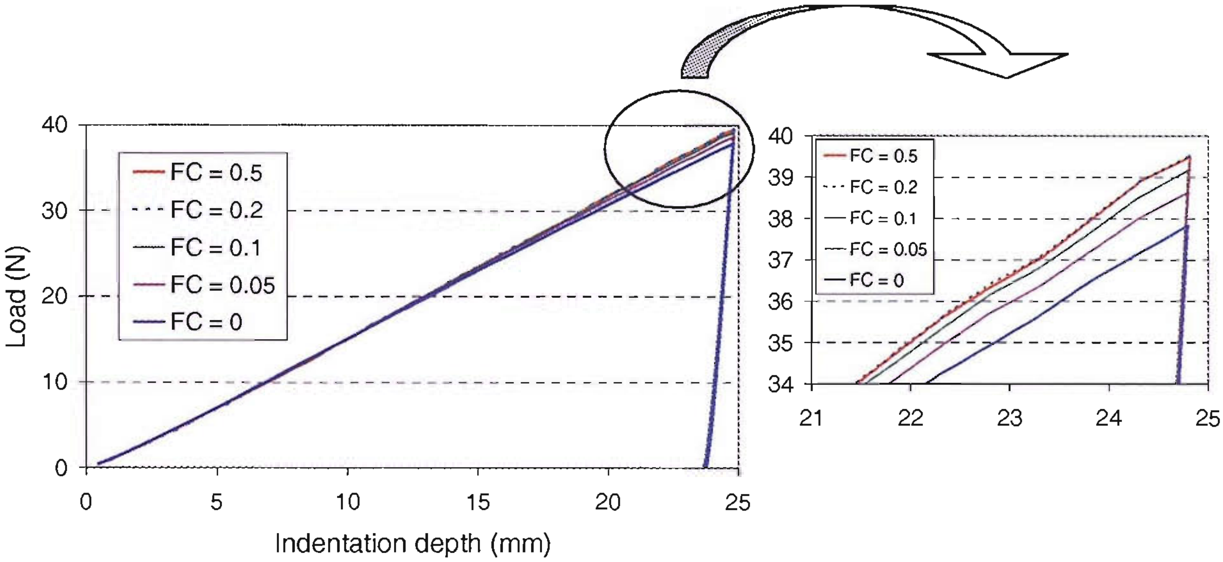

Fig. 4-17 FE-generated load-indentation curves for different assumed friction coefficients.

As noticed in Fig. 4-17, the curves start to deviate at around two-thirds of the maximum depth, and the difference at the peak load is less than 4%. However, when the pile-up is assessed, the effect of friction is more pronounced as shown in Fig. 4-18

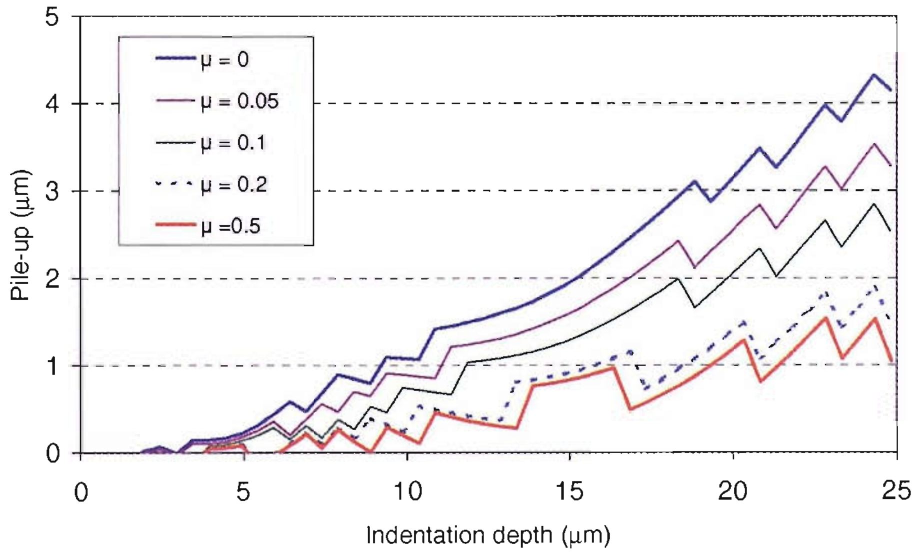

Fig. 4-18 Pile-up of the contact edges resulting from different friction coefficients.

The profiles of the indent for the five friction coefficients are compared in Fig. 4-19

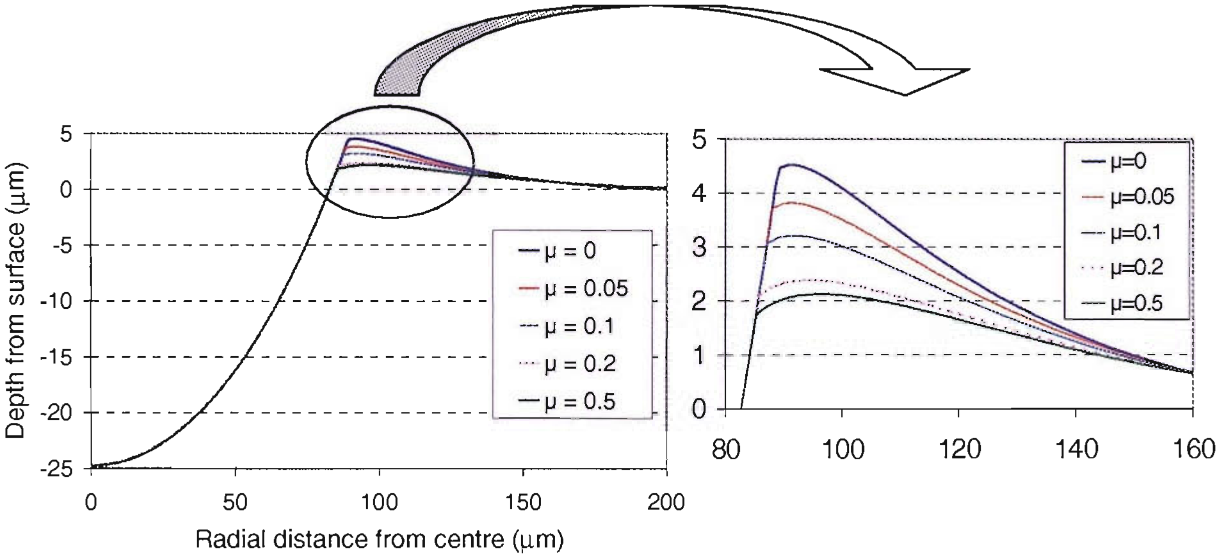

Fig. 4-19 Indentation profiles at peak load using five different friction coefficients.

The effect of friction on the resulting *P-h* curves appears to be insignificant. On the other hand, its influence on the contact depth, thus contact area is more marked, which agrees with the findings reported recently by Cao and Lu [96]. The height of the pile-up above the original specimen surface was shown to drop by over 50% when the friction coefficient rises from 0 to 0.5. It is, therefore, essential to consider frictional contact, with a realistic friction coefficient, for a more accurate indentation modelling.

4.4.6 The effect of the elastic modulus of the indenter

The indenters used for indentation testing are made of diamond, whose modulus of elasticity, E_i , is considered equal to 1140 GPa. However, due to the anisotropy of diamond the Young modulus varies with crystal orientation. The Young modulus can be measured in diamond with indirect methods. One way measures the speed of sound or compression waves in a diamond crystal. An approximate value of 1050 GPa is given by Wilks and Wilks [103], who reported that this value could vary with the crystal orientation by approximately 10%. This given value is very close to the adopted value of 1140 GPa. To assess the effect of E_i variation on the *P-h* curves resulting from FE simulation, a range of values for the diamond modulus including extreme limits was considered. These values were 800, 1000, 1500, and 2000 GPa in addition to the case of an infinitely rigid indenter. The FE simulation of indentation by a perfect spherical indenter, R=150 μm, on idealised *S5* with the properties described in Section 4.4.5 was carried out for the adopted range of values for the diamond modulus. The resulting load-depth curve from each case is plotted in Fig. 4-20.

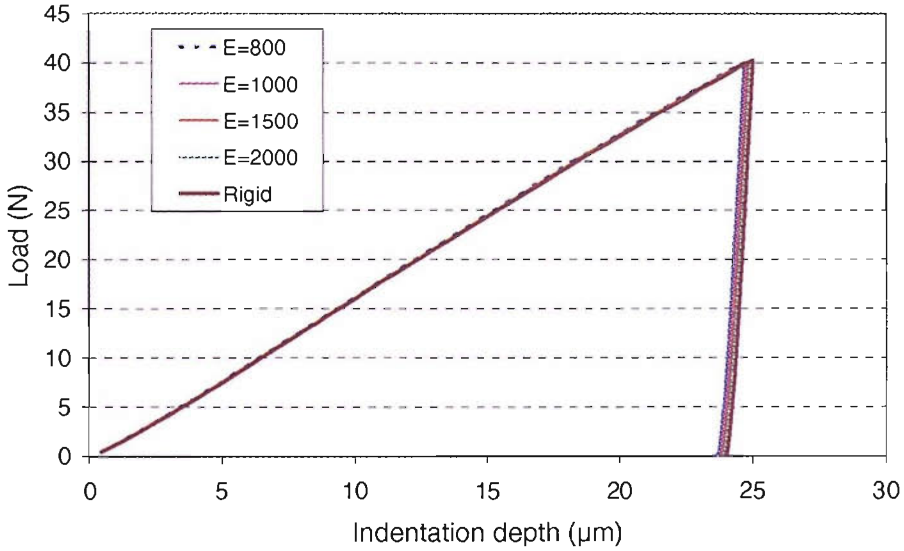

Fig. 4-20 Effect of a range of diamond modulus of elasticity on *P-h* curve.

As can be noticed, there is no significant difference in the *P-h* curves for the extreme cases for the Young modulus, and the difference is even more negligible for the more likely range between 800 and 1500 GPa. As a result, the adopted value 1140 GPa was proved to be acceptable.

4.4.7 Validation versus experimental results

FE simulation was performed on plates S5, S6, S7, and stainless steel considering 0.2 friction coefficient since the *P-h* curve is not affected by larger level of friction as shown in Fig. 4-17. The true properties were entered as material input to the elasto-plastic FEM. The indenter model was changed from perfect sphere to the real profile determined in Section 3.5. Both experimental and numerical results for each plate are shown in Fig. 4-21 to Fig. 4-24.

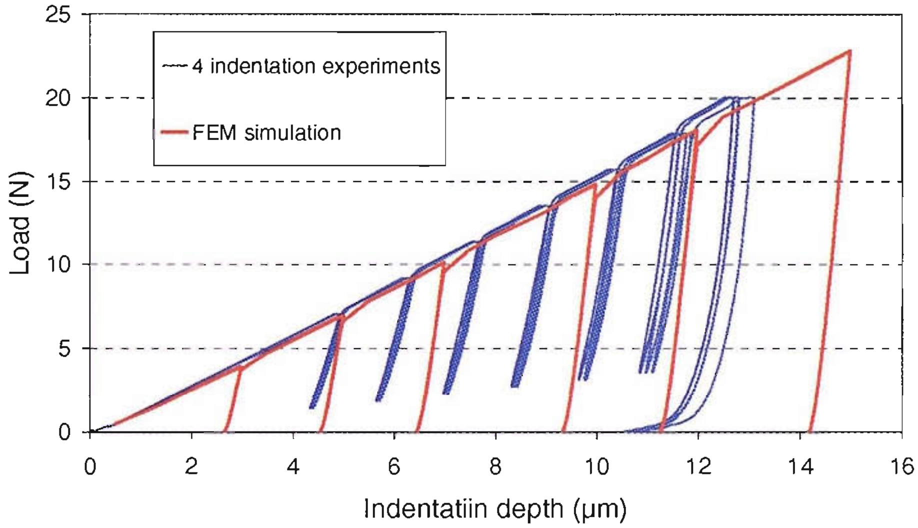

Fig. 4-21 Load-indentation obtained at 4 locations on S5 and the corresponding FE prediction.

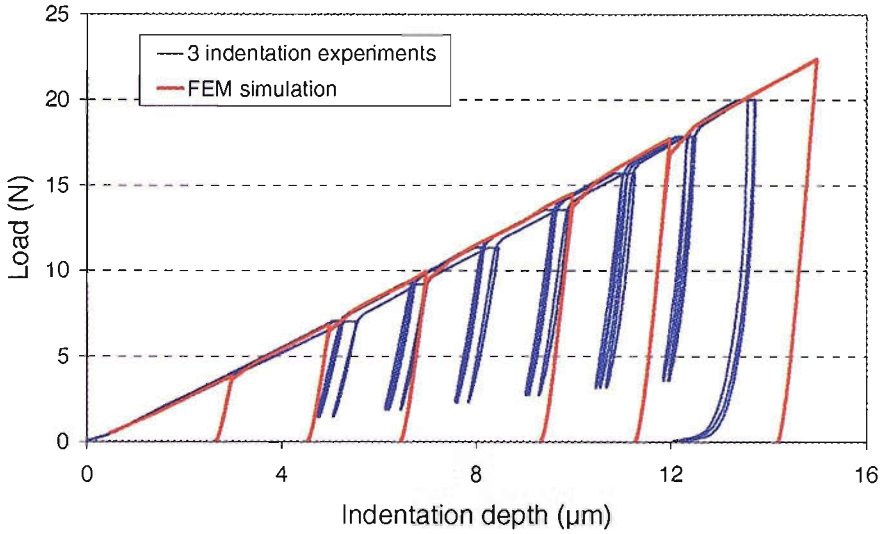

Fig. 4-22 Load-indentation obtained at 4 locations on S6 and the corresponding FE prediction.

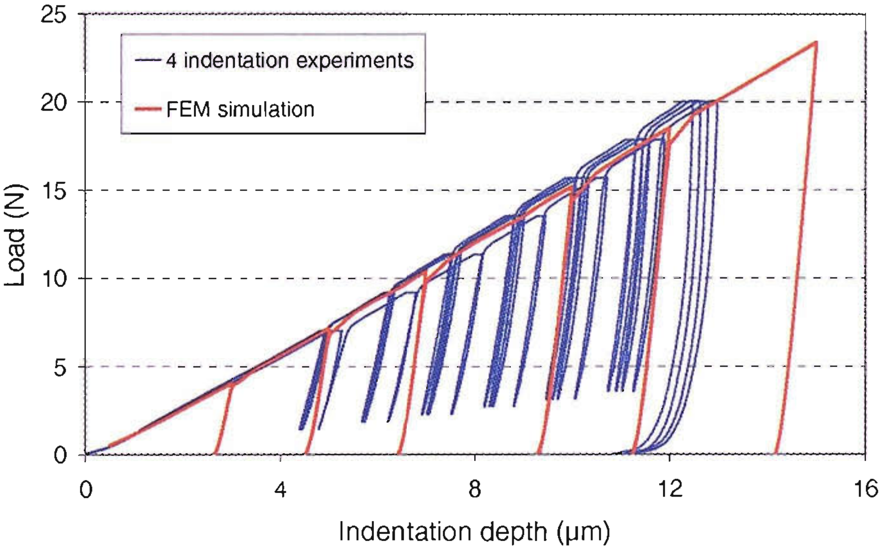

Fig. 4-23 Load-indentation obtained at 4 locations on S7 and the corresponding FE prediction.

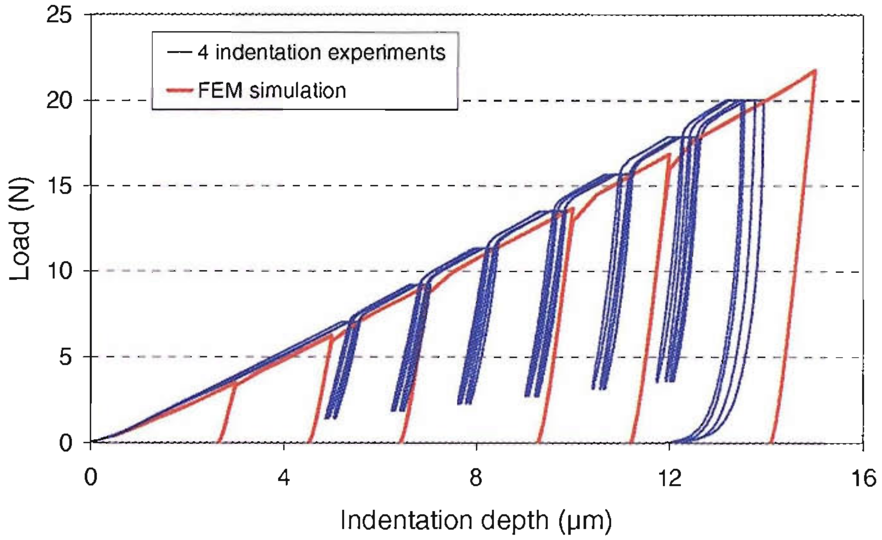

Fig. 4-24 Load-indentation obtained at 4 locations on stainless steel and the corresponding FE prediction.

The experimental results appear to indicate a stiffer material than that indicated by the predictions but it should be noted that the FE simulation does not consider the creep effect. Taking the effect of creep, discussed in Section 4.5, into consideration, the points at the end of creep on the loading curve, for each cycle, should be the points to compare with FE simulation, which are shown to be close to the FE prediction. The variation of the experimental curves observed seems to be acceptable and it can be understood as due to the variation of the material microstructure, surface finishes, equipment error, or other imperfections. Therefore, the agreement between experimental and modelling results is good proving the validity of the FE model and the characterisation of the spherical indenter.

4.5 Creep effect

The reliability of the indentation analysis results depends on ensuring the ideal conditions of measurement, which help eliminate undesired effects. Thus, the recorded indentation data will reflect the true material response during indentation. However, the effect of creep is observed in experimental data as a plateau in the load-indentation curve at peak load. Whilst creep depends on the material, it is also influenced by the loading rate and the hold/dwell time, which is the duration of the period at maximum load.

If creep is not considered, it can have a remarkable effect on the calculation of hardness and the reduced modulus from analysing the unloading curve. It was found by Chudoba and Richter [104] that creep not only affects the measured depth but also the slope of the unloading curve at peak load, which is a key quantity to calculate the reduced modulus. They reported that when creep was not allowed to take place, the resulting unloading curve showed bowing towards higher depth.

Pharr *et al.* [15], Oliver and Pharr [37], and Chudoba and Richter [104] reported a noticeable creep deformation in indentation on tungsten and aluminium using the Berkovich indenter. Hence it was seen essential to study the effect of creep in this study using a spherical indenter on mild steel so as to eliminate its influence on the analysis results. For this purpose, indentations were performed at 3 locations using the spherical indenter, R=150 μm, on steel plate S5. The peak load was chosen to be the maximum capacity of the instrument, which is 20 N. The effect of the loading time, which is the time required to reach the peak load, was studied by taking 3 values for the loading time, namely 8, 40, and 200 s. Furthermore, to remove any plastic-related behaviour, indentation was performed in 3 cycles reaching the same peak load. Having reached the peak load, it is held constant for a dwell time of 180 s then partial unloading by 80% follows at the same loading rate. The corresponding load-indentation curves for the three loading times can be compared with FE prediction by referring to Fig. 4-25, whilst Fig. 4-26 shows these curves at the peak of the first cycle.

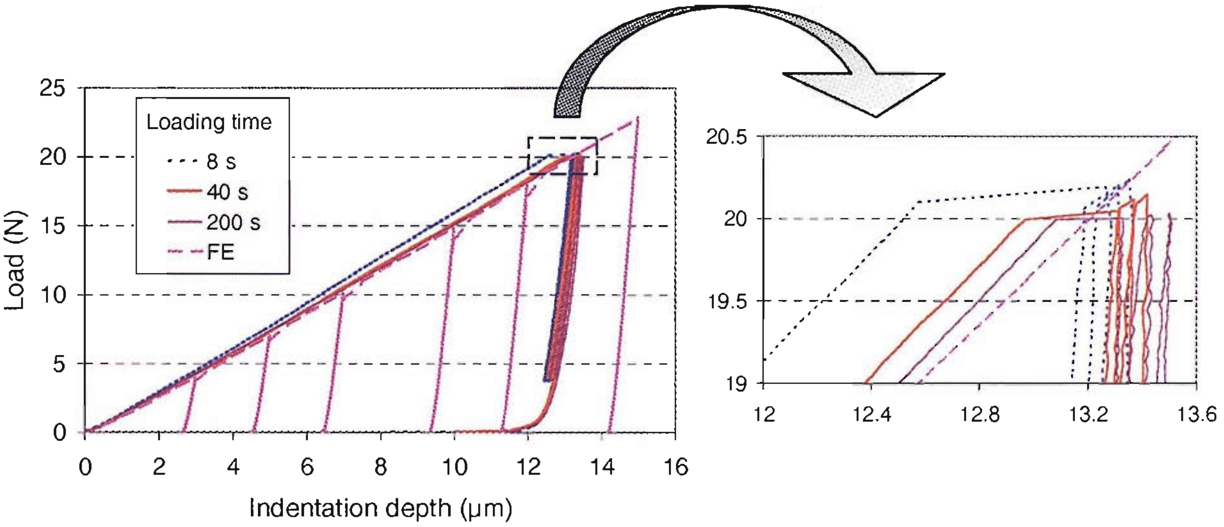

Fig. 4-25 Load-displacement curves for 3 loading time compared with FE prediction.

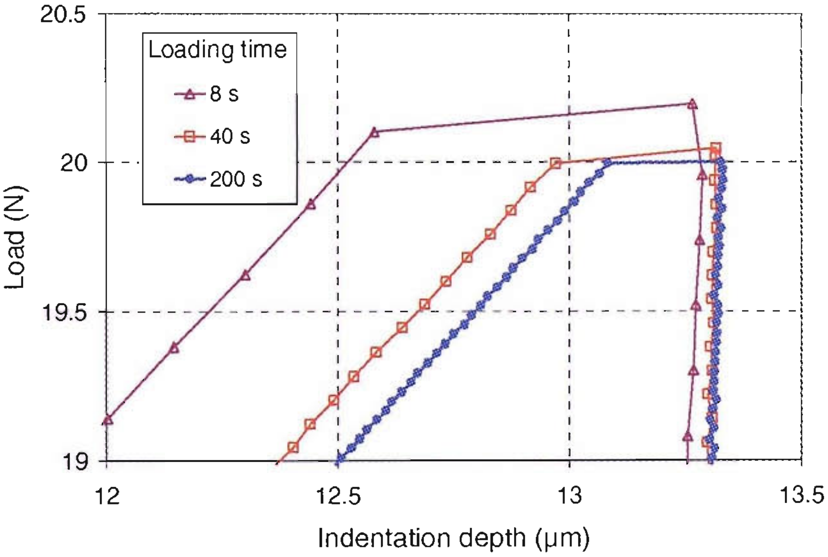

Fig. 4-26 Magnification of the-first-cycle indentation curves at peak load showing creep deformation

The capability of continuous recording the creep deformation with time facilitates monitoring the development of such deformation during the dwell time. This is applied to the first cycle for the various loading times adopted and shown in Fig. 4-27.

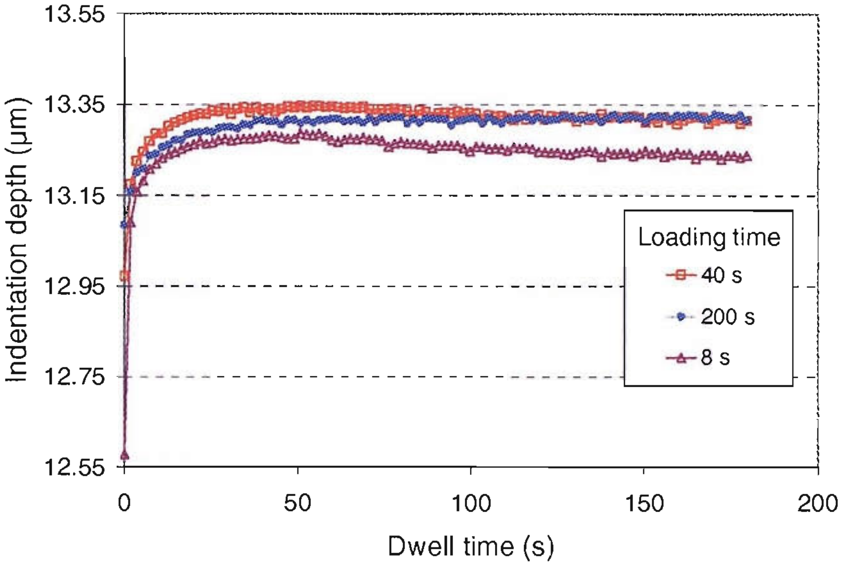

Fig. 4-27 Change of indentation depth during a dwell time of 180 s.

As can be clearly seen from Fig. 4-25 to Fig. 4-27, the creep effect can be removed by holding the peak load constant for a sufficiently long time. Creep deformation takes place at a high rate during the first few seconds then it diminishes within less than a minute. The creep rate reaches 150 nm/s in the first few second of the hold time and reduces to less than 3 nm/s after 15-20 s.

It can also be observed that the loading time has a noticeable effect on the 3 main segments of the load-displacement curve i.e. loading curve, hold time at peak load (amount of creep), and unloading curve. In the case of a loading time of 8 s, the loading curve appeared stiffer and the amount of creep deformation was large, that is, 1.387 μm. On the other hand, a more compliant loading curve and less creep were noticed when the loading time is longer. In the case of loading rates equal to 40 and 200 s, the corresponding creep measured was 0.6894 and 0.4983 μm, respectively.

Even though a long loading time results in less creep, allowing sufficient dwell time makes the depth at peak load reach the same value and the unloading curves almost overlap regardless of the loading time as long as it is not very short (40 s or more).

Applying the same dwell time in the case of the load time of 8 s, will bring the maximum depth close to the corresponding value of the other two cases. Nevertheless, the unloading curve shows bowing at peak load, which will incur an error in calculating the contact stiffness, thus the modulus. This indicates that short-time loading causes erroneous indentation data which seem to include undesired deformations. This explanation of bowing can be supported by the findings of Chudoba and Richter [104] who reported this bowing phenomenon when dwell time is zero and loading time is 92 s. The material behaviour in the case of short-time loading can be understood as a dynamic response to a high strain rate loading, in which the material seems stronger, compared with its response under static loading. Short time loading should thus be avoided during indentation to ensure more accurate results.

Referring to Fig. 4-21 through to Fig. 4-24, it can be observed that the creep value is not only dependent on the loading rate but also on the depth reached, which is in agreement with the results of Chudoba and Richter. Fig. 4-27 shows that a dwell time of 120 s is enough to allow creep deformation to take place in full and it can compensate for a smaller value for the loading time, as long as the latter has a value of 40 s or more. It also shows, together with Fig. 4-26, that a loading time of 200 s is adequate to produce reliable indentation data provided enough dwell time is allowed, and that increasing the loading time will not result in a noticeable change in the amount of creep. Therefore, a value of 120 s for the dwell time and a loading time of 200 s are adopted for the subsequent experiments in this study.

This creep effect clearly implies that since creep was not considered in the FE model, only those points corresponding to the end of the creep plateau of *P-h* curves should be considered when comparison with FE prediction is made, as the other points on the loading curve include creep, thus are expected to be stiffer. Furthermore, it can be seen that relying on the loading curve to derive material plastic properties, as adopted by a few authors [95, 96] can be misleading especially in the case of soft metals that exhibit creep deformation as the loading curve exaggerates the stiffness of the test material.

CHAPTER 5

MATERIAL CHARACTERISATION BASED ON FE SIMULATION

In this chapter, the finite element model described in Chapter 4 is used to simulate indentations by a perfect sphere, of 150 μm radius, on the idealised materials described in the same chapter. Loading, prescribed as controlled displacement, is applied in steps of 0.5 μm in size, whilst full unloading is performed in 200 load steps. For validation purposes, Tabor's relations for deriving the stress-strain curve from the indentation parameters., i.e. Meyer hardness and representative strain are initially applied to the FE results using direct measurements of the predicted indentation profile at every load step along the simulated loading curve.

Subsequently, *P-h* curves produced by FE simulation are analysed as experimental data, that is, without any further reference to other FE output. The effectiveness of Field and Swain's approach [45, 46], described in Section 2.4.2, for determining material properties from load-penetration data, is examined. Available correction formulae accounting for the pile-up effect are introduced into the material characterisation scheme and their effectiveness is investigated. A modification of this correction, improving significantly the accuracy of the plastic stress-strain relation, is proposed.

5.1 Assessing FE capability of linking the stress-strain curve to the indentation parameters

In order to verify that the FEM results are consistent with the fundamental principle linking true stress to strain, the contact area and indentation depth were determined by direct measurement from the simulated indentation profile at every load step during loading rather than at cycle peaks. The purpose of this was to monitor the gradual change in the predicted values of indentation parameters with load.

Due to the discrete nature of the FE solution, the contact edge, defining the contact area radius, can only be detected at the furthest specimen node in contact with the indenter; hence the contact radius obtained from the indentation profile is always an underestimate. With a small increase of the applied load, the observed contact radius stays unchanged until the adjacent node is detected in contact. This results in non-smooth variation of the estimated Meyer hardness manifested in the oscillatory plot of hardness vs. indentation strain, shown in Fig. 5-1.

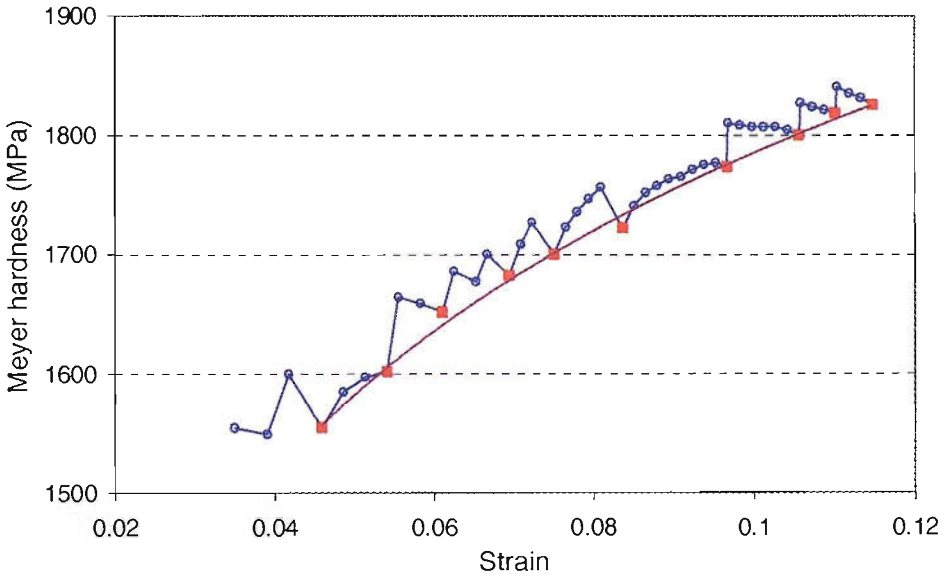

Fig. 5-1 Meyer hardness obtained from direct measurement of the indentation profile. The red line represents the lower bound points.

As a result, for a more reliable estimate of the contact radius a_c only the values corresponding to the lower bound points of the hardness-strain curve, forming the smooth red curve shown in Fig. 5-1, are considered in further analysis. The plastic part of the uni-axial stress-strain curve, described by Eq. 2-5, can be determined based on Tabor's findings in relating the stress-strain curve to the indentation parameters, which is achieved in two stages: First, uni-axial stress is related to Meyer hardness or mean pressure over the projected contact area through the constraint factor, C defined in Eq. 2-18. This factor was observed by Tabor to have the value of 3. Then the appropriate value of uni-axial strain, so called representative strain, is related to indentation geometry by Eq. 2-71.

Since all the idealised materials showed the same trend of behaviour, the results displayed in this section are for the idealised S5. For this test material, n and $\sigma_{0.2}$ are 0.132 and 375 MPa, respectively. It was pointed out in Section 4.4.5 that friction significantly affects the extent of the pipe-up and hence the size of contact radius. Having obtained FE-simulated P-h curves for a range of values for the friction coefficient μ (μ = 0.0, 0.05, 0.1, 0.13, 0.2, and 0.5), the stress-strain curves obtained by Tabor's method assuming C=3, for each μ value, can be compared with the FE input curve by referring to Fig. 5-2. Included in the plot are also the resulting values of n calculated as the gradient of the line fitted to the respective hardness vs. strain plots on a logarithmic scale. In addition, the resulting 0.2% yield stress for each of the stress-strain curve together with the corresponding strain hardening exponent and strength coefficient are presented in Table 5-1.

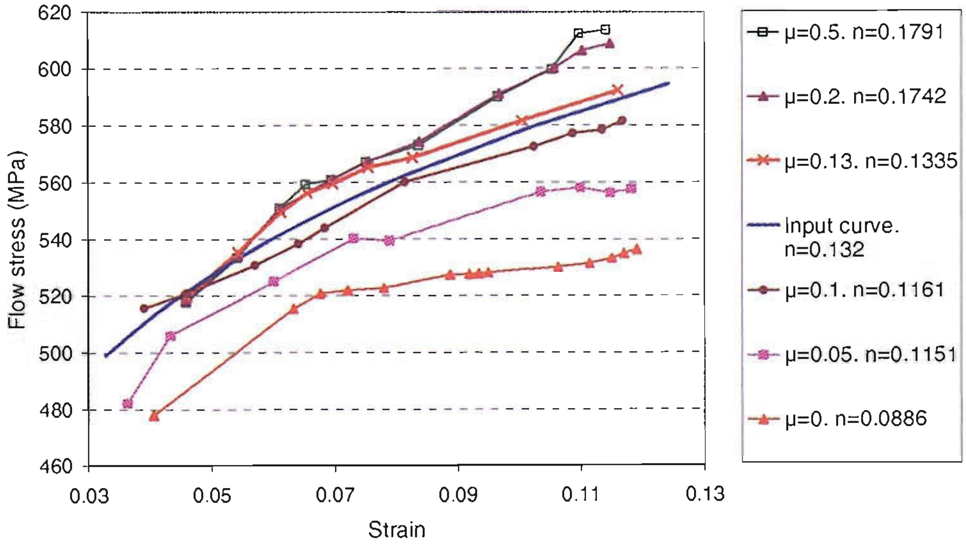

Fig. 5-2 Predicted stress-strain curves from simulated indentations compared with the corresponding input curve for the idealised S5 material.

Table 5-1 n, K and $\sigma_{0.2}$ of the curves resulting from FE direct measurement for various values of friction coefficients.

	μ=0.0	μ=0.05	μ=0.10	μ=0.13	μ=0.20	μ=0.50
n	0.09	0.12	0.12	0.13	0.17	0.18
K (MPa)	651	720	745	785	894	903
$\sigma_{0.2}$ (MPa)	398	379	391	373	335	329

It can be observed from Fig. 5-2 and Table 5-1 that the friction coefficient has a strong influence on the results. A value of μ around 0.13 appears to give the best agreement between the predicted and input curves for both the strain hardening exponents and the $\sigma_{0.2}$. This value also agrees with the experimental findings of Yurkov *et al.* [105] who reported that sliding friction of diamond on steel gave a range of friction coefficient values between 0.08 and 0.14, and it is close to the value of 0.1 which is considered the generally accepted value for friction between metal and diamond as reported in [96, 106, 107]. Thus, this value of μ is considered as best representing the real friction developing between the two bodies during indentation and will be adopted in further FE analysis in this study.

5.2 Application of Field and Swain's method to simulated indentation data

As pointed out in the Introduction the basis for almost all current approaches to obtaining the uni-axial stress-strain curve of a metal from indentation parameters is the work of Tabor [14, 28], outlined in Section 2.3.2 and Section 2.6.1 . This is also true for the method proposed by Field and Swain [45, 46] who adopted the value 3 for the constraint factor C.

5.2.1 Indentation data with spherical indenters

It is obvious that the application of the Tabor relations requires a reliable estimate of the contact area radius a_c so that both contact area, leading to Meyer hardness, and representative strain ε_r can be determined. Field and Swain [45, 46] proposed a model, discussed in Section 2.4.2, to extract the indentation geometry from analysing the unloading curve produced using a spherical indenter. This is without the need for any optical imaging or profilometry measurement. Their prediction of the residual depth described by Eq. 2-46 utilises only two points on the unloading curve. Whilst this gives consistent results in the case of FE-generated data, it loses stability when applied to experimentally produced data due to the unavoidable noise included in these data. In the latter case, a more rational way of describing the whole unloading curve passing through the two points previously mentioned is by means of fitting the non-linear relation in Eq. 2-28 with a power of 1.5 to the relevant portion of the unloading curve. This process automatically generates values for h_r. The non-linear fitting is here performed using Matlab, with its statistics toolbox, which requires the form of the fitted equation and initial values for the sought parameters as input. Fitting is then carried out iteratively based on the least squares method. When the solution is reached, the sought parameter values give the highest correlation factor of fitting.

5.2.2 Accounting for pile-up

As pointed out in Section 5.2.1, the approach adopted by Field and Swain assumes that at full load the indentation edges deform downwards, hence pile-up is not taken into account. However, soft metals, especially those with a low strain hardening exponent n, tend to pile up as the contact edges rise above the original surface. As a result, analysing the indentation data of such a material without accounting for the pile-up will result in underestimating the contact area and the representative strain, hence overestimating hardness. To account for the pile-up effect, the calculated contact radius can be corrected using a factor, c, defined in Eq. 2-57.

In an attempt to correlate the factor c to material properties, various authors have tried to derive an empirical formula for c as a function of n based on best fitting to the experimental work of Norbury and Samuel [56] who measured the true contact radius for materials with different n. Matthews [18] obtained an expression of the form

$$c^2 = \frac{a_c^2}{a_o^2} = \frac{1}{2}\left(\frac{2+n}{2}\right)^{2\left(\frac{1}{n}-1\right)} \qquad \text{Eq. 5-1}$$

Based on the work of Hill [17] on non-linear elastic theory, Hill *et al.*[58] suggested the following expression

$$c^2 = \frac{a_c^2}{a_o^2} = \frac{5}{2}\left(\frac{2-n}{4+n}\right) \qquad \text{Eq. 5-2}$$

which gives a better fit to Norbury and Samuel's data than Matthews' expression. Whilst Norbury and Samuel's data were based on measurement of residual indents, Taljat *et al.* [19] carried out FE simulations on many materials with different n and proposed two expressions for c for fully loaded and unloaded indents:

$$\text{Loaded: } \quad c^2 = \frac{h_c}{h_t} = \frac{1}{4}\left(5 - 3n^{0.7}\right) \qquad \text{Eq. 5-3}$$

$$\text{Unloaded: } \quad c^2 = \frac{h_c}{h_t} = \frac{1}{10}\left(13 - 8.5n^{0.8}\right) \qquad \text{Eq. 5-4}$$

As can be noticed, all the expressions above except Eq. 5-4 yield the value of 0.5 when n=1, which coincides with the case of perfectly elastic behaviour, whilst Eq. 5-4 gives the value of 0.45. A comparison of the various expressions given above can be made by referring to Fig. 5-3.

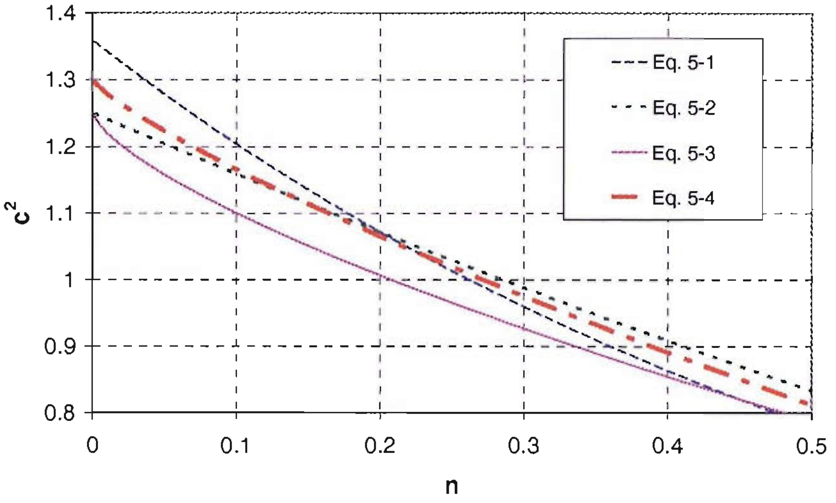

Fig. 5-3 Variation of correction factor c^2 with n. [18, 19, 58]

According to these expressions, if the strain hardening exponent n of the material is known a priori, the true contact area that accounts for pile-up can be determined from the measured h_t. However, till now, there is no way of finding n or even the yield stress solely from the indentation data by a spherical indenter.

5.3 Characterisation of an ideal material

The method described in the previous section was applied to the load-indentation output obtained from the FE simulation of a rigid spherical indenter of radius 150 μm, on the idealised S5 material described in Section 4.4.5. As noticed in that section, friction has a considerable effect on the contact radius and pile-up, hence friction contact is considered for a more accurate modelling of the problem. Loading was applied in a cyclic pattern, similar to that in an experiment, so that the peak loads are increased progressively. Typical P-h curves, treated as experimental data, can be seen in Fig. 5-4, which was obtained using a friction coefficient μ =0.13.

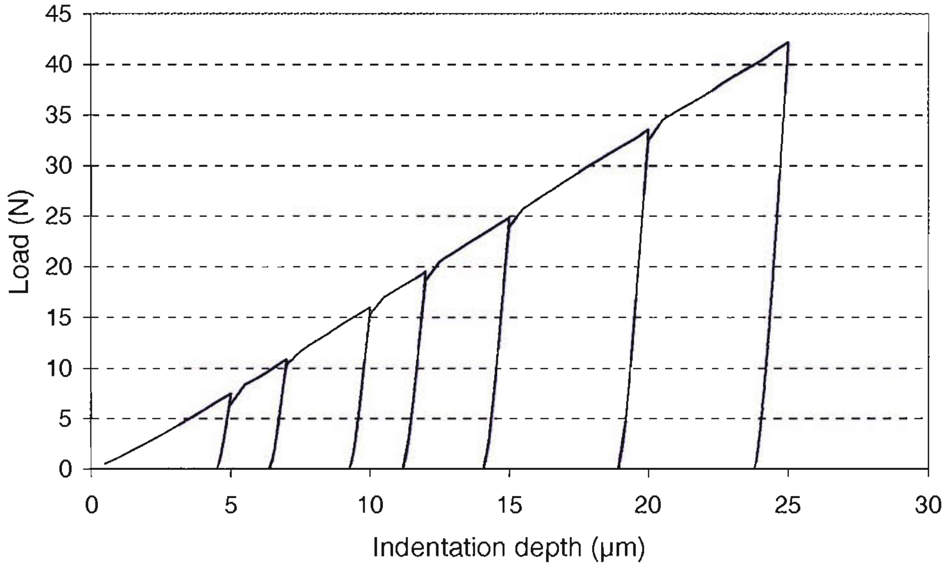

Fig. 5-4 FE simulated *P-h* curves for cyclic loading indentation by a rigid spherical indenter (R=150 μm).

The calculated values for n and $\sigma_{0.2}$ for various values of friction coefficients are summarised in Table 5-2. The predicted Meyer hardness vs. indentation depth and stress-strain curves for the same range of friction coefficient values compared with the input curve are shown in Fig. 5-5 and Fig. 5-6, respectively. According to the assumptions adopted, the flow stress, the strain hardening exponent and 0.2% yield stress predicted are larger than those of the input data, which are in this case, 0.132 and 375 MPa, respectively.

Table 5-2 n, K and $\sigma_{0.2}$ of the curves resulting from analysing the P-h curves for various values of friction coefficients.

	μ=0.0	μ=0.05	μ=0.10	μ=0.13	μ=0.20	μ=0.50
n	0.15	0.18	0.20	0.21	0.22	0.22
K (MPa)	887	978	1028	1054	1089	1089
$\sigma_{0.2}$ (MPa)	395	359	342	331	317	318

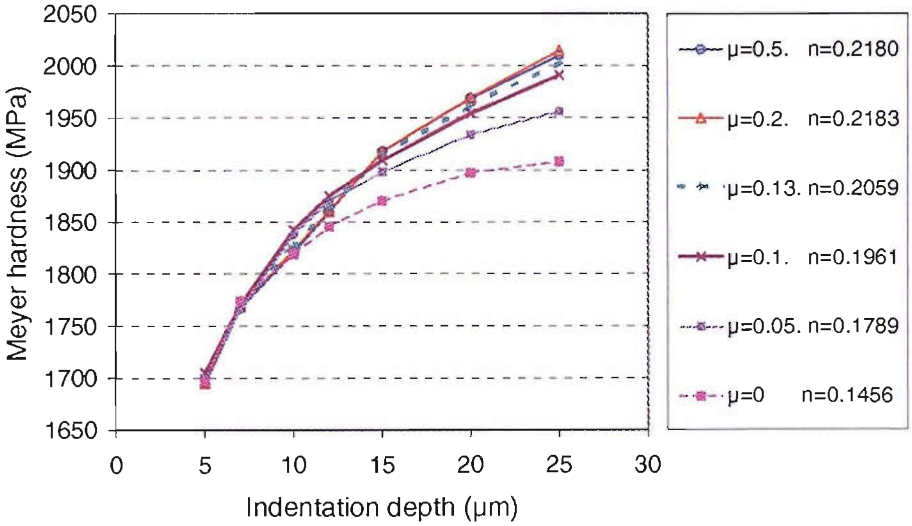

Fig. 5-5 Hardness and strain hardening predicted from simulated P-h curves. (Pile-up not accounted for)

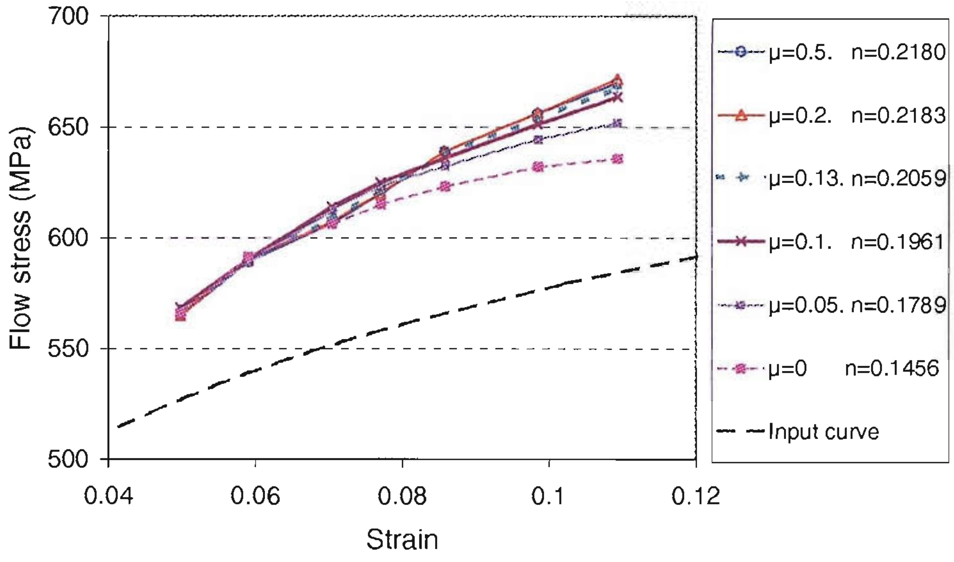

Fig. 5-6 Stress-strain curves predicted from simulated *P-h* curves compared to the corresponding part of the idealised FE input curve. (Pile-up not accounted for)

As observed, the predicted *n* appears to increase with the value of the friction coefficient, μ whilst $\sigma_{0.2}$ shows an opposite trend. The calculated stress is overestimated by 10%-17.5% compared with that of the input curve. Moreover, the effect of friction on the derived stress-strain curve is more noticeable when the friction coefficient is less than 0.13, beyond which any increase in its value will result in a negligible difference.

5.4 Performance of the pile-up correction formulae.

The various expressions for the correction factor c^2 mentioned in Section 5.2.2 can be applied to the indentation *P-h* data to account for the pile-up effect if *n* is known a priori. However, their capability of predicting the pile-up effect needs to be explored. To assess their accuracy, they were combined with the characterisation analysis based on the load indentation curves from the FEM analysis of the idealised S5 material, which were treated as experimental data. In addition, the contact area measured directly from the simulated profile during loading is also compared with the prediction of these expressions.

5.4.1 Known strain hardening exponent

For the idealised S5 material, whose *n* is assumed known, expressions given by Eq. 5-1 to Eq. 5-4 can therefore be applied to estimate the true contact area and thus correct the hardness predicted by the applied characterisation analysis. As such a material is expected to pile up, $c^2 > 1$, hence the area correction will result in lower flow stress and higher representative strain at any maximum indentation load. The correction was applied to the *P-h* curve obtained with a friction coefficient of 0.20. This value of friction coefficient was chosen as it is the value above which no significant difference will be noticed in indentation data [19], which is also confirmed in section 4.4.5.

Hardness values at cycle peaks resulting from the original characterisation analysis and those resulting from introducing the pile-up corrections using the known value of *n* (n = 0.132), can be compared by referring to Fig. 5-7. Comparison of the input, idealised σ-ε curve with that resulting from the original characterisation analysis, based on C=3, as well as those incorporating the various pile-up corrections can be made by referring to the plots of Fig. 5-8.

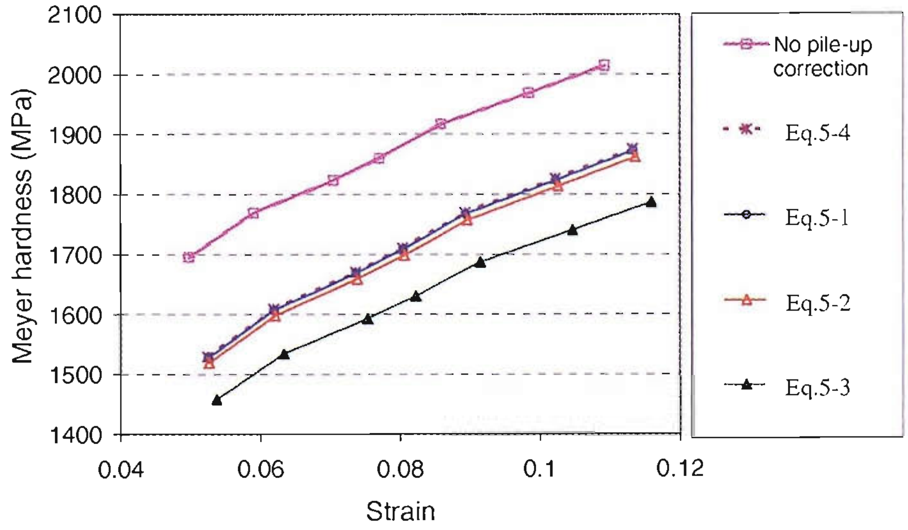

Fig. 5-7 Predicted hardness of idealised S5 accounting for pile-up through various correction formulae.

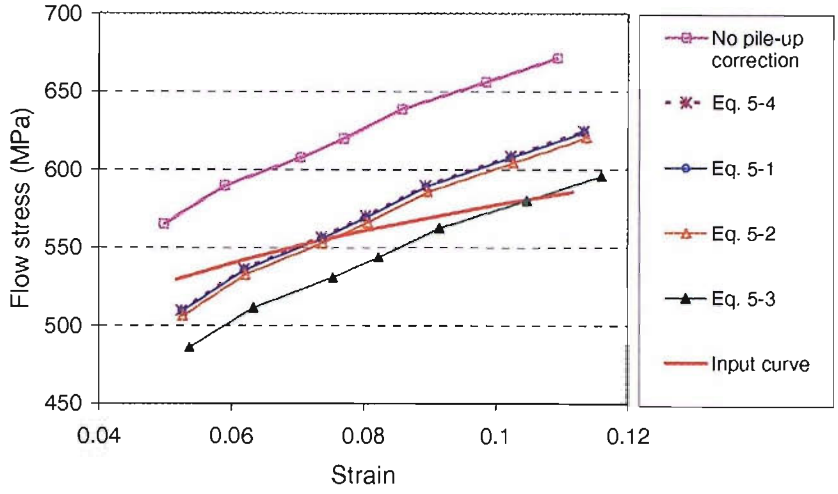

Fig. 5-8 Idealised and predicted stress-strain curves accounting for pile-up through various correction formulae.

The strain hardening exponent and 0.2% yield stress of the stress-strain curves resulting from the original characterisation analysis and the modified ones using the pile-up corrections are summarised in Table 5-3.

Table 5-3 Predictions of n, K and $\sigma_{0.2}$ accounting for pile-up corrections. μ=0.2

	Eq. 5-1	Eq. 5-2	Eq. 5-3	Eq. 5-4	No pile-up correction
n	0.26	0.26	0.26	0.26	0.22
K (MPa)	1170	1145	1231	1159	1089
$\sigma_{0.2}$ (MPa)	259	253	274	257	317

As can be observed from Fig. 5-7, Fig. 5-8, and Table 5-3, the characterisation analysis with various pile-up corrections brings the predicted stress-strain curves closer to the original input, but the resulting n is found equal to 0.2628, and $\sigma_{0.2}$ ranges from 256 to

274 MPa, that is, still less accurate than those values obtained from the original application of the characterisation analysis without any correction.

To examine the effect of friction coefficient on the performance of the various pile-up correction formulae, they have been likewise applied to *P-h* curves predicted for frictionless contact, that is, with $\mu=0$. Analysis results show the same trends as those mentioned above. Plots of corresponding hardness and flow stress predictions are shown in Fig. 5-9 and Fig. 5-10, respectively. The resulting values of n and $\sigma_{0.2}$ from direct application of the characterisation analysis and from the corrected stress strain curves are presented in Table 5-4.

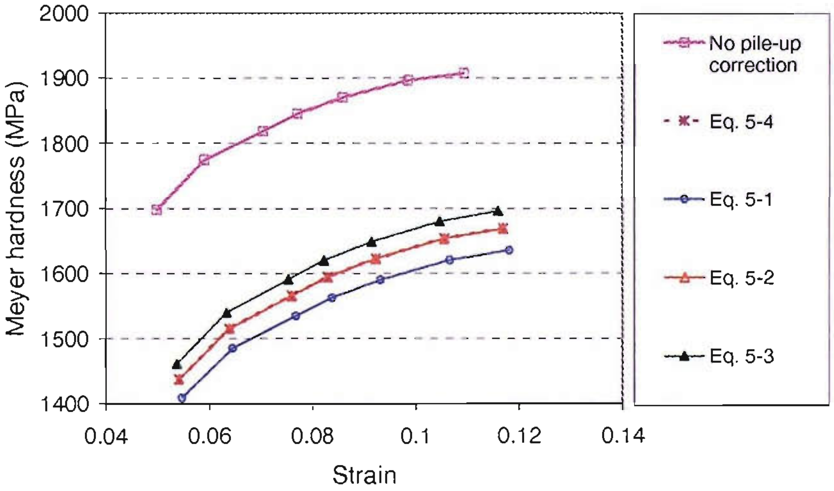

Fig. 5-9 Hardness comparison of idealised S5 after using the expressions in section 5.2.2 to account for pile-up using n from tensile test. $\mu=0$

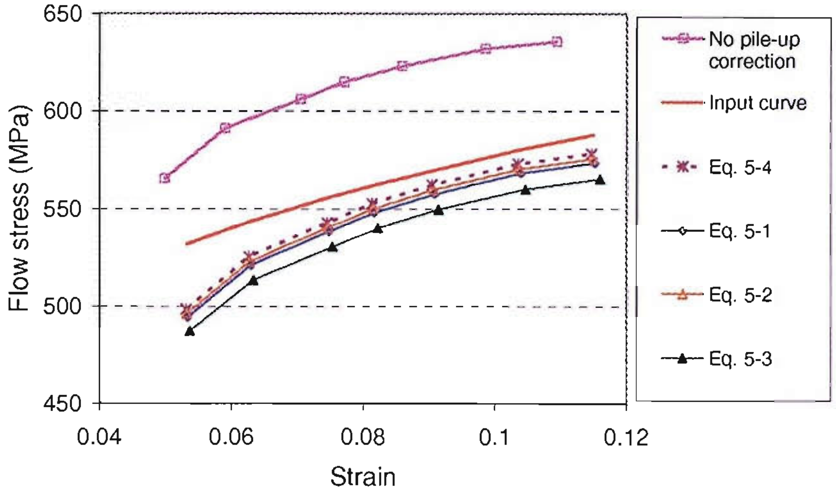

Fig. 5-10 Flow stress comparison of idealised S5 after using the expressions in section 5.2.2 to account for pile-up using n from tensile test. μ =0, C=3.

Table 5-4 n, K and $\sigma_{0.2}$ of the curves corresponding to the pile-up corrections and the characterisation analysis. μ =0.

	Eq. 5-1	Eq. 5-2	Eq. 5-3	Eq. 5-4	No pile-up correction
n	0.19	0.19	0.19	0.19	0.15
K (MPa)	875	878	940	883	887
$\sigma_{0.2}$ (MPa)	297	299	321	300	395

As observed from Fig. 5-9, Fig. 5-10, and Table 5-4, even though the final n and $\sigma_{0.2}$ are closer to the original input, compared to the case of μ =0.2, they are is still different from those of the input curve, and the predicted stress-strain curve does not agree with the input curve. It was also found that all corrected stress-strain curves give the same n.

It can be mathematically proved that this is the consequence of Eq. 2-57. Assuming that σ_0 and ε_0 are stress and strain corresponding to a_0, taking the logarithm of both sides in Eq. 2-5 and substituting Eq. 2-57 and Eq. 2-72, will yield

$$\log\left(\frac{P}{C\left(\pi c^2 a_0^2\right)}\right) = \log(K) + \log\left(0.2\frac{ca_0}{R}\right)^n \qquad \text{Eq. 5-5}$$

which can be re-arranged as

$$\log\left(\frac{P}{C\left(\pi a_0^2\right)}\right) = \log\left(c^2\right) + \log(K) + \log\left(c^n\right) + \log\left(0.2\frac{a_0}{R}\right)^n \qquad \text{Eq. 5-6}$$

Simplifying Eq. 5-6 gives

$$\sigma_0 = K_0\varepsilon_0^n \quad \text{where } K_0 = K\left(c^{n+2}\right) \qquad \text{Eq. 5-7}$$

This shows that since the factor c is constant, the resulting n from the corrected stress strain curve by any of the aforementioned expressions will remain unchanged, as it depends solely on P and h_t. The only difference between these expressions is the value of the coefficient K, which affects the position of the resulting flow stress vs. representative strain.

5.4.2 An iterative approach to account for pile-up

Applying any of the various pile-up correction formulae necessitates the prior knowledge of n, which is, of course, not known when the characterisation analysis is applied to a new material such as the HAZ in a weld. Based on the requirement that the input value of n should be equal to that obtained from the predicted stress-strain curve, an iterative process is suggested in this study. It starts with a valid arbitrary entry of n, say 0, to apply a correction formula for calculating a 'corrected' contact area and hence flow stress-strain relation. Then the new value of n obtained from this 'corrected' flow stress-strain relation is re-entered to the pile-up correction formula to re-calculate a new, 'corrected' contact area, thus generating an iterative process which terminates when two successive output values of n are equal within a pre-defined tolerance. The resulting flow stress strain plots for the expressions after iterations are plotted in Fig. 5-11 and Fig. 5-12 for a friction coefficient of 0.2 and 0, respectively.

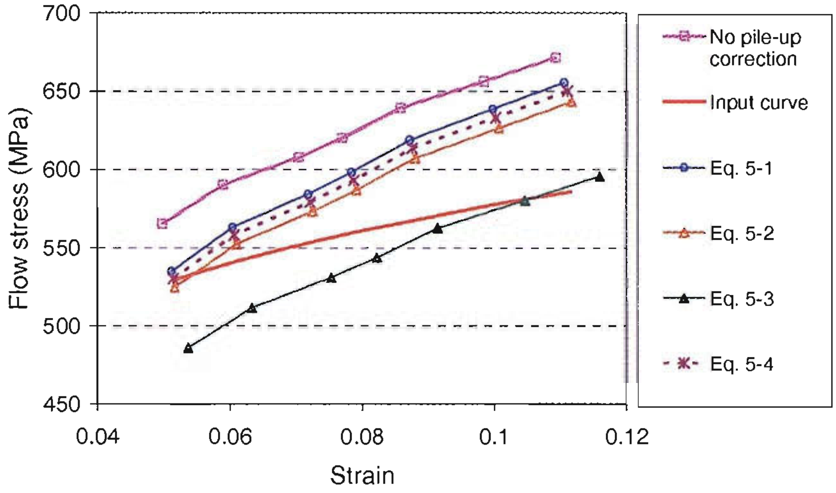

Fig. 5-11 Flow stress comparison of idealised S5 after an iterative use of the expressions in section 5.2.2 to account for pile-up using n from tensile test. μ =0.2, C=3.

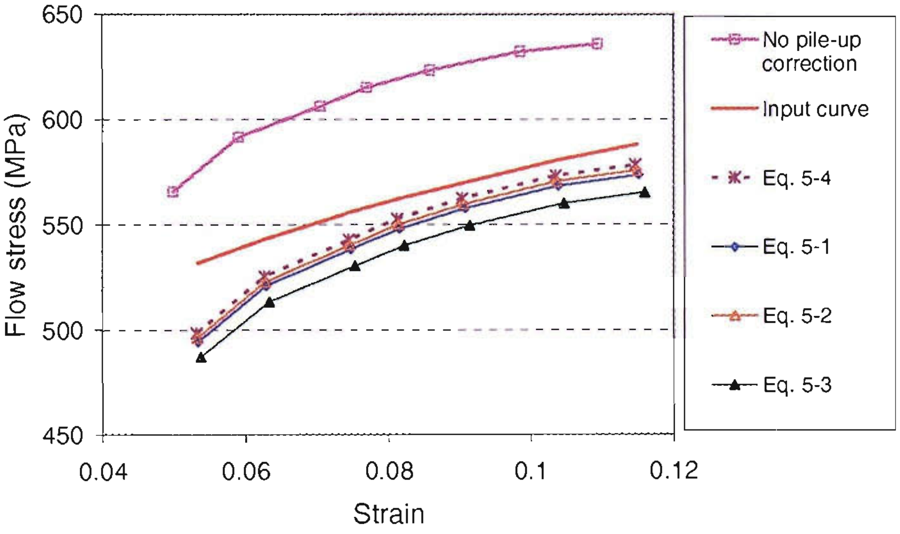

Fig. 5-12 Flow stress comparison of idealised S5 after an iterative use of the expressions in section 5.2.2 to account for pile-up using n from tensile test. μ =0, C=3.

It was noticed that only two iterations were needed to yield the same overestimated n regardless of the first input value. Although this method reproduces the same n as when entering the true n from tensile test curve, the values of the coefficient K are different. This accounts for the changed position of the flow stress curves compared with those produced in 5.4.1, as can be noticed by comparing Fig. 5-10 with Fig. 5-12 and Fig. 5-8 with Fig. 5-11

5.4.3 Assessment of pile-up formulae based on FE predictions

The conclusion drawn from the results above is that these expressions fail to give a good estimate of n although they bring the predicted stress-strain curves closer to the original input. This questions the accuracy of their pile-up prediction and the validity of their application in the case of spherical indentations.

FE-predicted data of the change of contact area during loading were employed to monitor the development of pile-up by calculating its parameter, c^2, directly from the simulated profile throughout the load steps of the loading curve. The resulting values for c^2 for each indentation depth were compared with those calculated from the original characterisation analysis without any pile-up correction in Fig. 5-13.

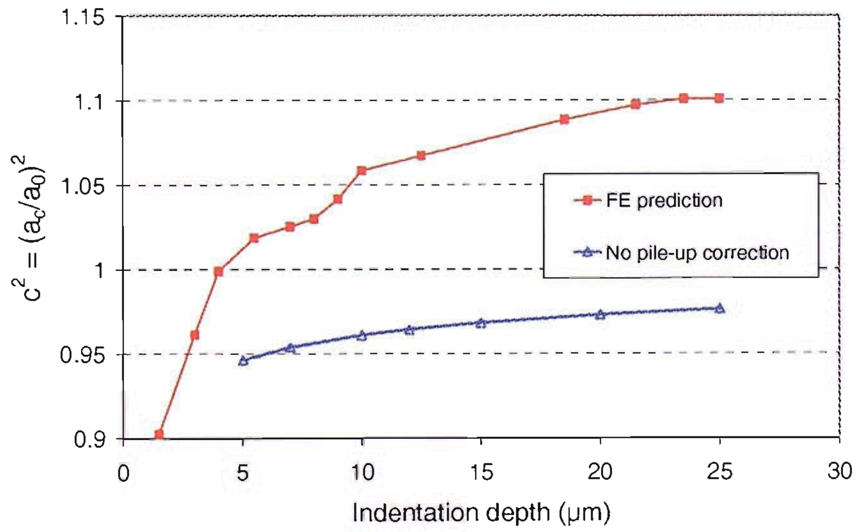

Fig. 5-13 Pile up correction factor c^2 from the FE-predicted indentation profile (μ =0.13).

As observed, the c^2 value from the indentation profile is not independent of the indentation depth as assumed by the expressions given by Eq. 5-1 to Eq. 5-4 . It starts with values less than unity for indentation less than 4 μm deep, as pile-up has not started forming yet. When indentation exceeds 5 μm in depth, pile-up starts building up but at a decreasing rate, and then stabilises when indentation exceeds 20 μm in depth. At this stage, the value of c^2 gets closer to those predicted by the expressions. In fact, it is 2.7 % lower than that given by Eq. 5-2 and Eq. 5-4, and almost equal to that obtained by Eq. 5-3. This agreement suggests that these expressions were obtained for indentations performed at similar rather high strain values, which range from 0.1 to 0.12. Furthermore, the original characterisation analysis by Field and Swain [45, 46] was shown to predict that c^2 depends on the indentation depth. While this result is not, of course, valid in this case because pile-up has been ignored and thus c^2 is always less than unity, it would be acceptable for hard materials that sink-in. As a result, this clearly proves that c^2 cannot always be considered constant and the expressions given by Eq. 5-1 to Eq. 5-4 are unable to accurately predict the effect of pile-up, for low and moderate indentations by a spherical indenter and hence predict the correct hardness and n from these indentations.

5.5 Modified modelling of the pile-up effect

FE simulations show that the ratio $(a_c / a_0)^2$ is not constant as assumed by the expressions given by Eq. 5-1 to Eq. 5-4. This suggests the need for modifying these expressions so that they account for the dependence of $(a_c / a_0)^2$ on indentation depth and thus provide a more accurate prediction of the contact area.

Based on the same FE output as that generating Fig. 5-13, the ratio of the residual depth (h_r) to the total (h_t) indentation depth was calculated and plotted versus the total indentation depth in Fig. 5-14. It can be noticed in that figure that the variation of h_r/h_t follows the same trend as that of FE-predicted c^2, which is shown in Fig. 5-13.

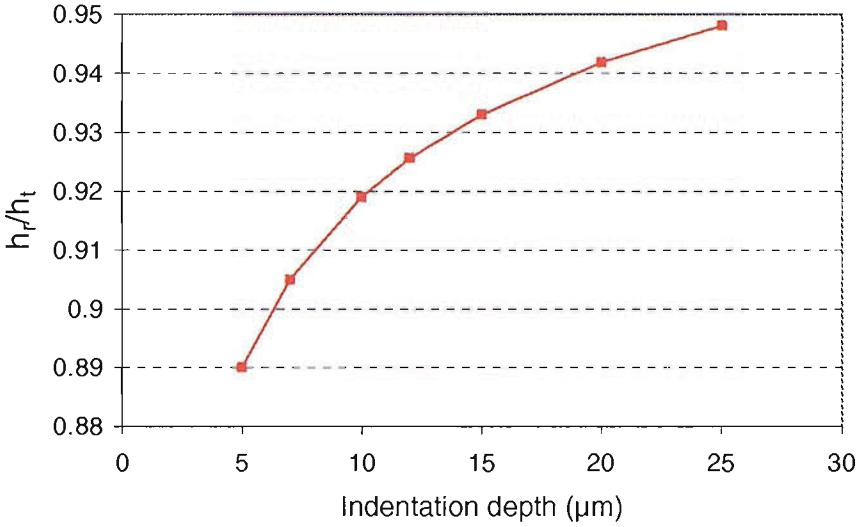

Fig. 5-14 Ratio of the residual to total indentation depth versus total indentation depth.

This observation suggests that the ratio h_r/h_t can be used in conjunction with one of the expressions given by Eq. 5-1 to Eq. 5-4 to correct the prediction of the pile-up effect. The physical reason for this suggestion is the dependence of pile-up on the extent of plastic deformation, which can be considered directly linked to the magnitude of residual indentation. By examining the FE indentation output for the three different idealised materials (corresponding to S3, S5, and stainless steel), whose properties are listed in Table 5-5, a statistical study was carried out to correlate $(a_c/a_0)^2$ with (h_r/h_t) and c^2 obtained from Eq. 5-2, proposed by Hill *et al.* [58]. This expression for the correction factor was chosen over those proposed by Taljat *et al.* [19] since it was based on measurement of real indentation profiles rather than FE modelling of indentation of metals with E_s/σ_y=500. However, for the idealised materials used in this study the ratio E_s/σ_y has the values, 840, 560, and 649, respectively. In addition, Eq. 5-2 gives a better fit to Norbury and Samuel's data than Eq. 5-1.

It was anticipated that the pile-up factor $(a_c/a_0)^2$ should be a product of c^2 and an expression which is a function of (h_r/h_t). This expression should be equal to unity for purely elastic indentation, that is when h_r=0, resulting in $(a_c / a_0) = 0.5$, which complies with the elastic contact solution. Hence, it should also include a term (h_e / h_t) which will equate to unity when (h_r / h_t)=0. Attempting various forms to correlate the pile-up with the indentation data, a relation of the form

$$\left(\frac{a_c}{a_0}\right)^2 = c^2 \sqrt{\gamma\left(\frac{h_r}{h_t}\right)^z + \left(\frac{h_e}{h_t}\right)^z} \qquad \text{Eq. 5-8}$$

showed to give better results in describing the FE prediction presented in Fig. 5-13, for the idealised materials. These materials were chosen to cover the commonly encountered properties of the weldable structural steel. The strain hardening exponent and 0.2% yield stress for these materials range from 0.132 to 0.25 and from 250 to 375 MPa, respectively. By fitting the non-linear Eq. 5-8 to the FE output for the three idealised steel specimens, the constants of this equation are determined as z=3 and γ=1.125. This empirical formula is thus proposed herein to estimate the true contact area, allowing for pile-up as a function of n, and (h_r / h_t), where the residual depth h_r is determined from non-linear fitting to the unloading curve.

The pile-up correction parameter for the three idealised materials, obtained from Eq. 5-8, can be compared with those extracted from the FE-simulated indentation profiles by referring to Fig. 5-15 and Fig. 5-16, which show, respectively, $(a_c / a_0)^2$ as a function of (h_r / h_t) and h_t.

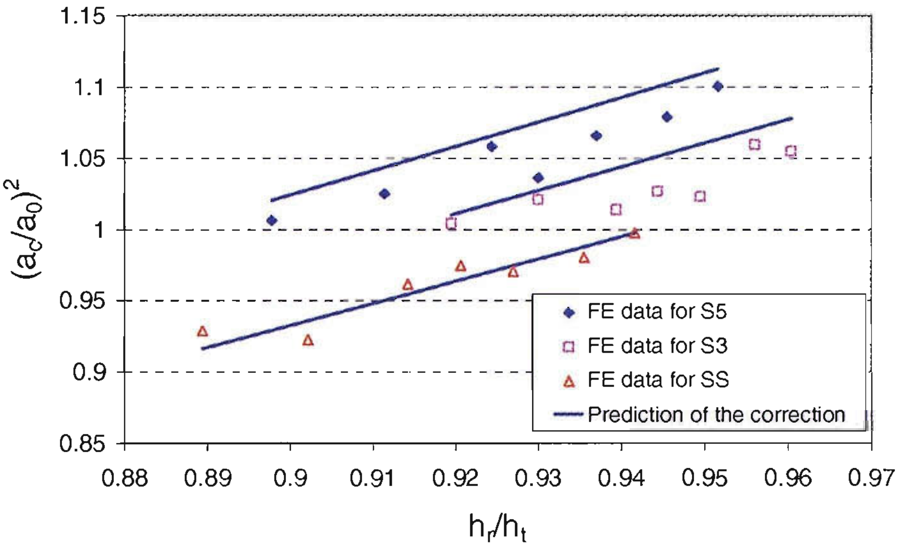

Fig. 5-15 Pile-up correction factor from Eq. 5-8 and simulated indentation profile versus (h_r / h_t).

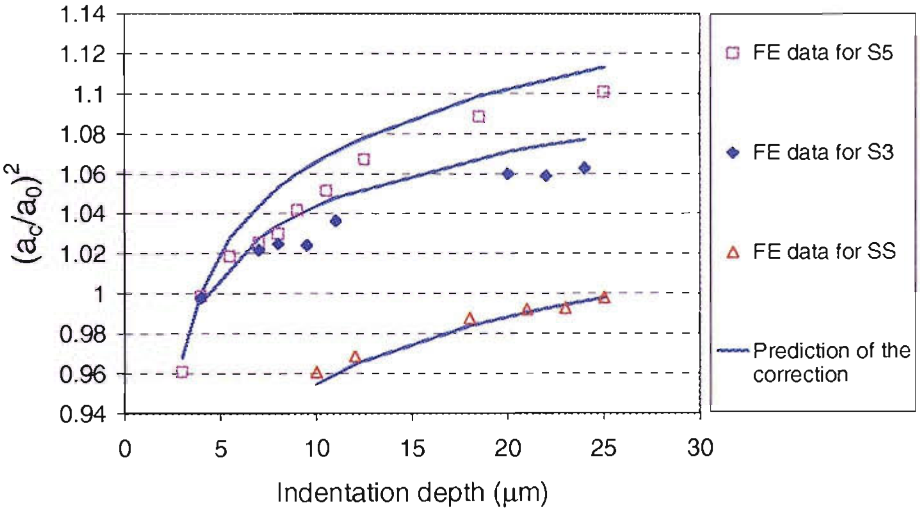

Fig. 5-16 Pile-up correction factor from Eq. 5-8 and simulated indentation profile versus h_t.

As seen in Fig. 5-15 and Fig. 5-16, the prediction of the proposed Eq. 5-8 is in good agreement, within 1% error, with that obtained from FE simulations of the indentation profile for the three idealised materials, which demonstrates the performance of the non-linear fitting used to determine the constants in Eq. 5-8. This small error actually is in favour of the accuracy of the proposed formula since the contact radius obtained from FE is always underestimated. Even though this correction is derived for three idealised materials, its application for other steels within the same range of *n* and $0.2\%\sigma_y$ is expected to be valid. Furthermore, Eq. 5-8 has the capability of predicting the true contact area even when it lies beneath the original plane of the specimen surface, which happens during shallow indentation before any formation of pile-up. This clearly shows its extended applicability not only for soft metals but also for hard metals whose elastic deformation predominates with no tendency for piling-up, and also for the case of purely elastic materials when $(a_c / a_0) = 0.5$.

The application of Eq. 5-8 to the indentation data, that is, the *P-h* curves, requires the evaluation of c^2, given by Eq. 5-2, which necessitates a prior knowledge of *n*. Since *n* is unknown for a given material, the proposed empirical relation is applied using the iterative process proposed in 5.4.2. This process consists of the following steps:

a) The unloading curve at every cycle is fitted with a non-linear function of the form $y = \varphi(h_t - h)^{1.5}$ so that it could be extrapolated to the zero load axis thus yielding the residual indentation depth, hence the ratio (h_r / h_t).

b) The projected area radius, a_0, corresponding to h_t is calculated for every cycle. Thus initial values of Meyer hardness and representative strain are obtained assuming a_0 is the contact area radius.

c) The strain hardening exponent *n* is determined by regression analysis of the hardness vs. representative strain plot on a logarithmic scale.

d) From the knowledge of the initial value of *n*, c^2 is calculated from Eq. 5-2 and substituted together with the ratio (h_r / h_t) into Eq. 5-8 to determine an initial value for the true contact area radius a_c, at every loading cycle. Thus Meyer hardness and representative strain corresponding to a_c are obtained.

e) Then *n* is determined in the same manner as in step (c), based on the new a_c, and is compared with the input value for *n* used to calculate a_c in step (d). If the difference between the two values is larger than a pre-defined tolerance, then steps (d) and (e) are repeated, otherwise the iteration process terminates.

Since the ratio (h_r / h_t) can only be obtained at every cycle, the data points at which hardness can be calculated are restricted to the number of loading cycles. However, when the number of cycles is relatively large, say five or more, then it is suggested in this study that the ratio (h_r / h_t) can be interpolated to all loading points lying between the first and the last cycle peaks on the loading curve. This will facilitate, within a reasonable accuracy, the use of more points at which the Meyer hardness can be determined, thus producing a smoother flow stress curve.

The proposed new empirical relation (Eq. 5-8) is applied to the *P-h* curves produced by FE simulation of indenting the idealised materials corresponding to S3, S5, and SS. The flow stress curve generated by this method, the one obtained using the contact radius from the simulated indentation profile as well as that produced by the conventional characterisation method that ignores the pile-up effect can be compared with the original input stress-strain curve for the three idealised materials by referring to Fig. 5-17 to Fig. 5-19. Included in the plots is also the resulting *n* value for every curve. These values for *n* together with the 0.2% yield stress are summarised in Table 5-5 for each curve.

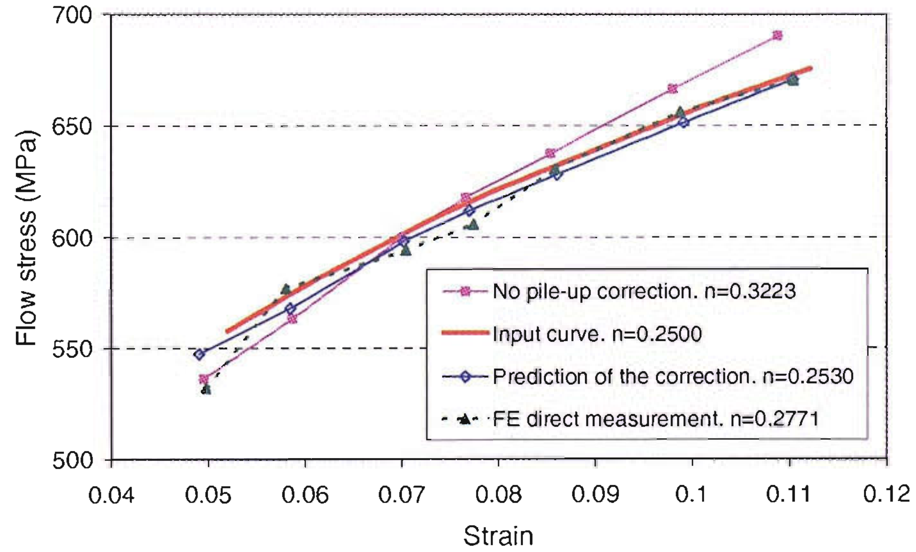

Fig. 5-17 Predicted and original flow stress curves for the idealised stainless steel.

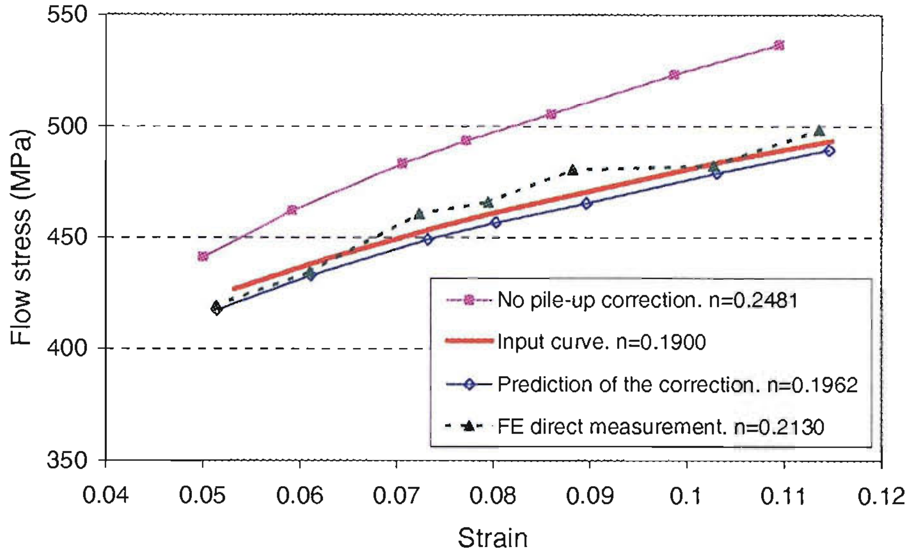

Fig. 5-18 Predicted and original stress-strain curves, for the idealised S3.

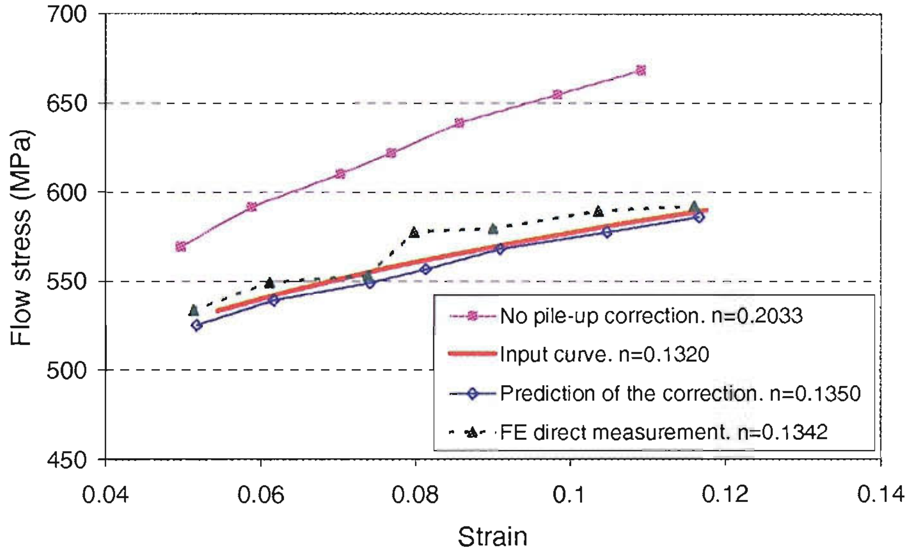

Fig. 5-19 Predicted and original flow stress curves for the idealised S5.

As observed in the figures above, the proposed method, based on Eq. 5-8 and an iterative procedure, has proved to be very effective in accounting for the pile-up effect through the determination of the true contact area, and thus the stress-strain curve. The strain hardening exponent and 0.2% yield stress is within 3% of the corresponding value of the input curve. Therefore, this method will be adopted, in the next chapter, to analyse the experimental indentation data from the test materials obtained using the available spherical indenter.

Table 5-5 Predicted and original values of strain hardening exponent and yield stress for the three materials studied.

Type of idealised material	n & $\sigma_{0.2}$	Input curve	Characterisation predictions		
			No pile-up correction	Contact radius from FE	Pile-up correction
S3	n	0.19	0.25	0.21	0.20
	$\sigma_{0.2}$ (MPa)	250	221	232	242
S5	n	0.13	0.20	0.13	0.13
	$\sigma_{0.2}$ (MPa)	375	334	377	369
Stainless steel	n	0.25	0.32	0.28	0.25
	$\sigma_{0.2}$ (MPa)	285	221	257	280

CHAPTER 6

APPLICATION OF THE PROPOSED CHARACTERISATION ANALYSIS TO EXPERIMENTAL DATA

The development of the new characterisation technique, that is, the modified pile-up correction combined with Tabor's original analysis presented in Section 5.5, was based on FE simulated indentations by a rigid perfect sphere. In this chapter, this new analysis technique is applied to the experimental *P-h* data produced using the available spherical indenter, whose geometrical characteristics are described in detail in Chapter 3. In the first part of this chapter, the effectiveness and accuracy of the proposed technique is assessed using experimental data from the test materials whose properties are described in Chapter 3. In the second part of the chapter, the new analysis technique is utilised to analyse the indentation data of a butt welded steel joint. Indentation testing was carried out to span the three distinct regions of the weld, which are the parent metal, weld heat affected zone, and weld fusion zone.

6.1 Effect of new analysis on frame compliance calibration

Applying the new analysis technique to estimate the true contact area necessitates the correct load-indentation data, that is, the indented material response only, so that the correct (h_r/h_t) ratio can be obtained. Whilst this condition can always be met in the case of FE generated data, the experimental data acquired by the instrument intrinsically include the effect of frame compliance, that is the amount of displacement that should be removed prior to the implementation of the new analysis technique. Conventionally, this is achieved through the frame compliance calibration described in Chapter 3, which is based on the use of the Berkovich indenter. The analysis adopted in the frame compliance software provided with the instrument can only be run with indentation data produced from that indenter. However, the holders for the Berkovich and spherical indenter are different in material and length, leading to a different frame compliance factor. This means that a different frame compliance factor must be obtained for the spherical indenter. For this reason, the contact stiffness of the unloading curves of the indentation data generated using a spherical indenter was determined and used according to Eq. 2-52. However, this calibration is based on the characterisation analysis that ignores the pile-up effect. Hence, for materials that pile-up, it underestimates the contact area, and thus the true frame compliance, leading to erroneous load-indentation data for the indented material.

In order to extract the true material deformation from the raw indentation data, the contact area should be accurately estimated. It is, therefore, suggested in this study that the new pile-up correction method should be incorporated into the frame compliance calculation through an iterative process. This starts with the load-indentation data produced by measuring the conventional frame compliance that is based on the characterisation analysis with no pile-up correction. The pile-up correction, represented by Eq. 5-8, is then applied, hence a new value of the contact area corresponding to each unloading curve is obtained, and compared with the previously calculated values. If the difference is within a predefined tolerance, the iteration process terminates and the resulting P-h curves are considered as the true material response. Otherwise the resulting P-h curves are re-entered into the conventional frame compliance routine with the new values for contact area predefined a priori in order to obtain a new set of P-h curves that satisfy the condition of correct E_r prediction based on the new values of contact area provided. Both the frame compliance calibration that is implemented through the original Matlab routine that ignores the pile-up effect, and the complementary routine that considers the pile-up correction are illustrated in the flow charts presented in Fig. 6-1 and Fig. 6-2, respectively.

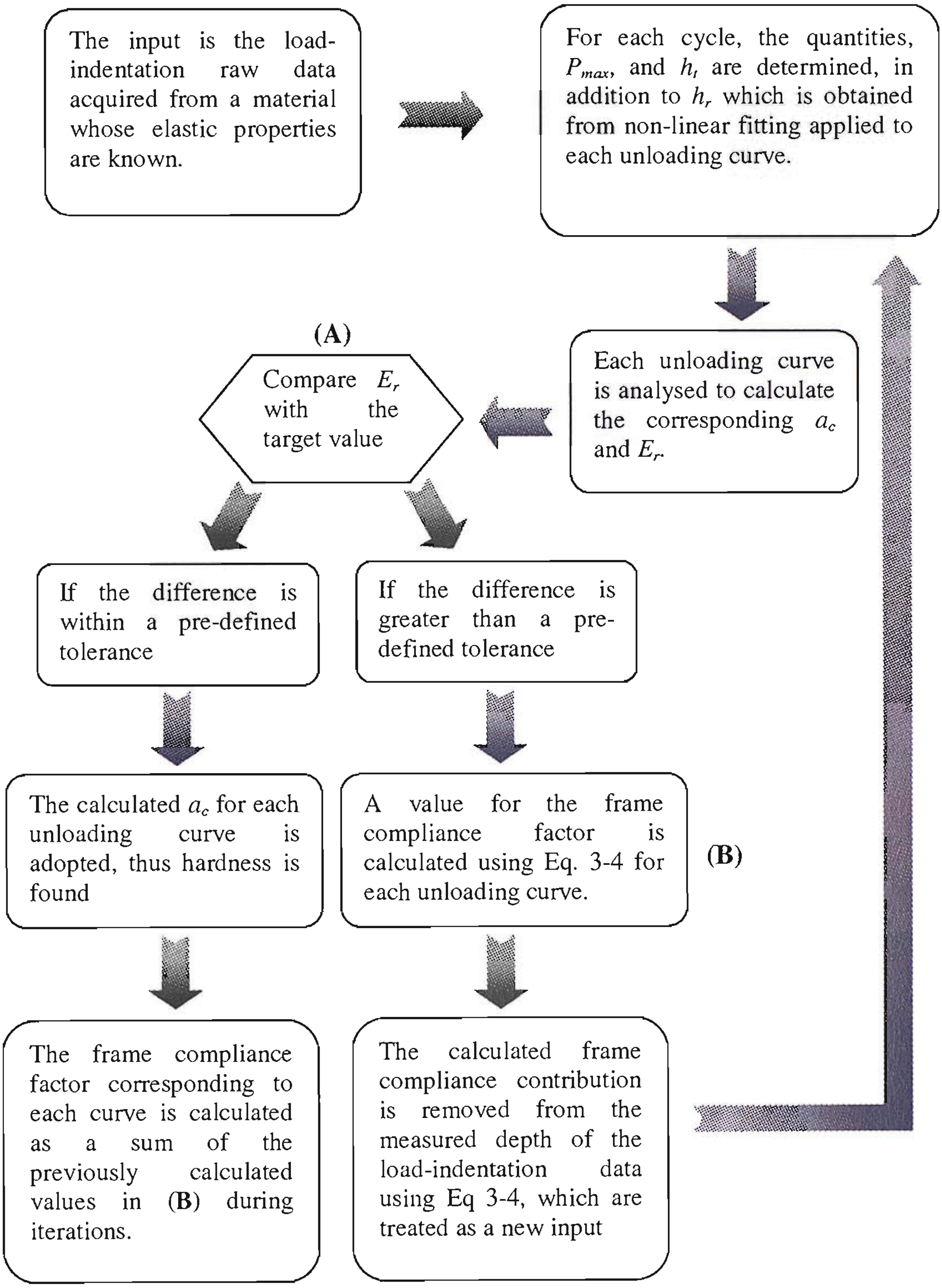

Fig. 6-1 A flow chart showing the steps used in performing the conventional frame compliance calibration that ignores any pile-up effect.

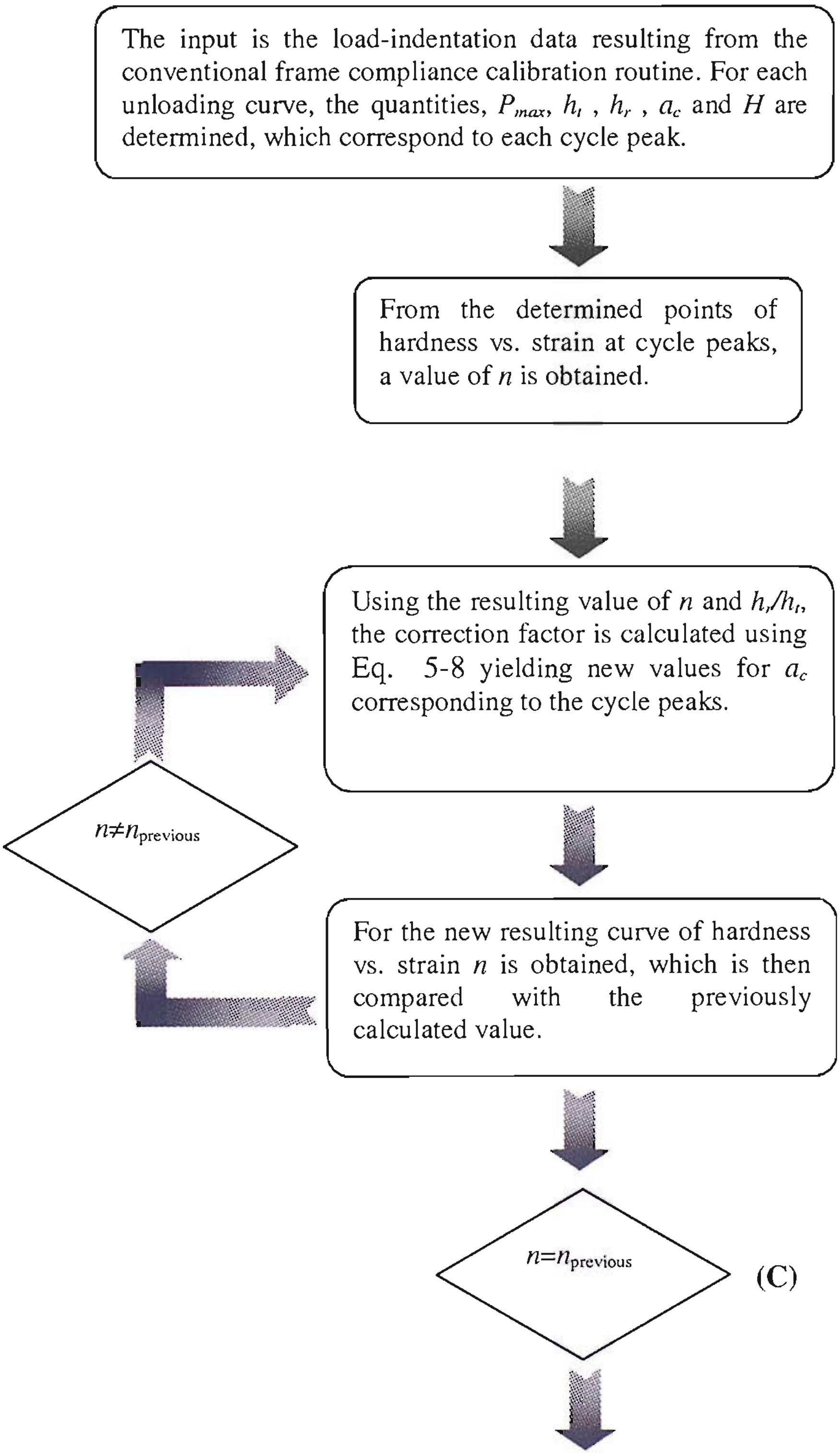

The input is the load-indentation data resulting from the conventional frame compliance calibration routine. For each unloading curve, the quantities, P_{max}, h_t , h_r , a_c and H are determined, which correspond to each cycle peak.

From the determined points of hardness vs. strain at cycle peaks, a value of n is obtained.

Using the resulting value of n and h_r/h_t, the correction factor is calculated using Eq. 5-8 yielding new values for a_c corresponding to the cycle peaks.

For the new resulting curve of hardness vs. strain n is obtained, which is then compared with the previously calculated value.

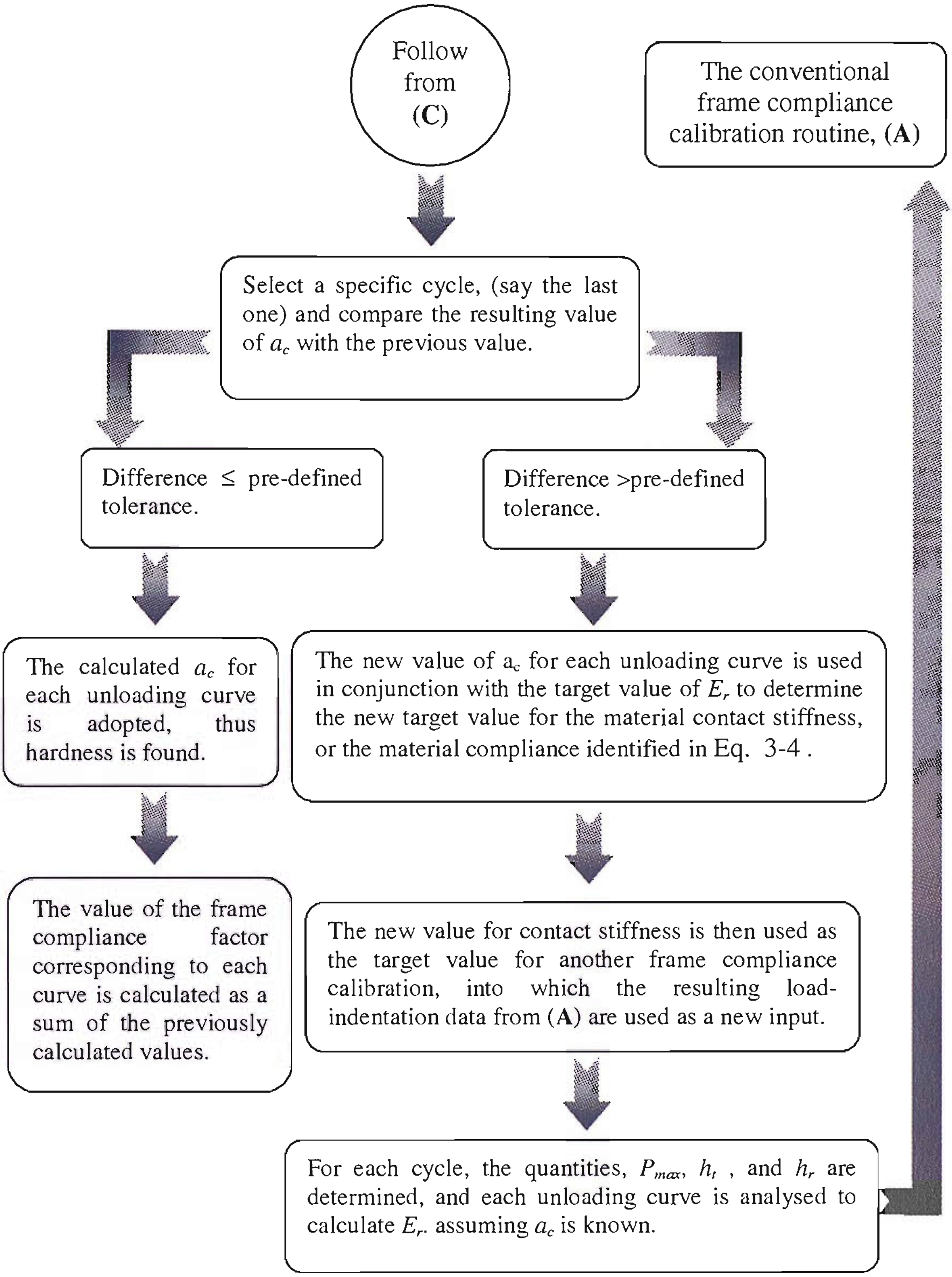

Fig. 6-2 A flow chart showing the steps of incorporating the pile-up correction into the frame compliance calibration.

The frame compliance calculations illustrated in Fig. 6-1 and Fig. 6-2 provide the load-indentation data for the indented material and the frame compliance factor corresponding to the cycle peaks. The variation of the frame compliance factor with peak loads can then be used in the analysis of the raw experimental data to eliminate from them the frame compliance. Although the values for this factor are obtained at certain load values, interpolation can be applied in the case of any subsequent experiment that includes a load cycle with a different peak load.

6.1.1 Experimental details

In order to assess the consistency of the frame compliance factor, that is, whether it is independent of the nature of the specimen, indentation testing was performed on the three steel specimens S3, S5, S7, and a stainless steel specimen. Details on the properties of these materials are given in Chapter 3. For every specimen, indentation experiments were performed at 5 different locations. Every experiment consisted of 7 loading cycles to a progressively higher peak load. All experiments had the same set-up. Peak loads were defined at the values: 7.04, 9.21, 11.39, 13.55, 15.72, 17.88, and 20.05 N. The loading and unloading rate was 100 mN/s. For every cycle, the peak load was held for 120 s to allow any time dependent deformation to take place. Unloading was terminated at 20% of the peak load. Indents were placed 500 μm apart, in order to avoid any deformation or residual stress interference between adjacent indents.

The raw data resulting from every experiment was then analysed to calculate the frame compliance factor for every load value. The average of the resulting values of this factor is plotted as a function of peak load in Fig. 6-3.

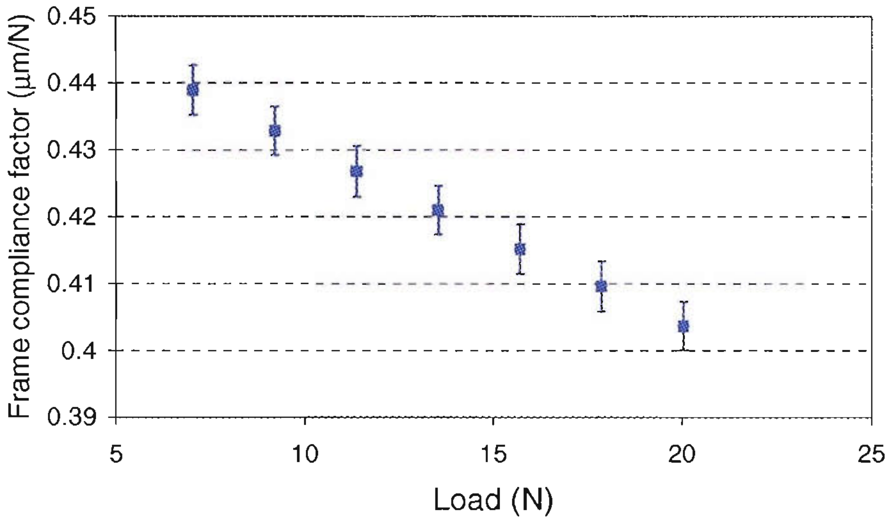

Fig. 6-3 Frame compliance factor variation with indentation load. The error bar is twice the standard deviation.

As can be observed from Fig. 6-3, the frame compliance factor decreases with load. It appears to be almost insensitive to the test material with a variation of less than 0.5%. This decrease in frame compliance factor can be attributed to the assumptions on which the formula given by Eq. 2-26 to calculate E_r from the unloading indentation curve is based. Eq. 2-26 describes the response of a flat surface of material indented elastically by a rigid parabola. However, the contact during unloading in the case of elasto-plastic indentation is not in accordance with that theory since the indent does not recover to a flat surface. Furthermore, the plastic deformation induced during indentation causes the surface of the residual impression to be different from a perfect parabola or even a perfect sphere. As a result, the calculated E_r from analysing the unloading indentation curve increases with load due to the extent of plastic deformation, when it should be constant since it is a material property. In order to maintain E_r constant with load the frame compliance factor thus must decrease with load as shown, while it should be a machine constant. Thus the decrease in frame compliance with load can be thought of as an artefact brought about by the method of analysing the unloading curve.

Since the frame compliance factor should be a machine characteristic, the curve connecting these data points in Fig. 6-3 can then be used as a machine compliance curve for obtaining the frame compliance in any subsequent experiment involving testing of an unknown material.

6.2 Characteristic strain for an imperfect spherical indenter

In linking the indentation parameters to the stress-strain curve, the characteristic strain, ε_r, for a perfect sphere was considered by Tabor as 20% of the ratio (a_c/R). The impossibility of having a perfectly spherical indenter, especially when the indenter is made from diamond on the micrometer scale, makes it necessary to determine an equivalent expression for the characteristic strain in the case of an imperfect indenter so that the stress-strain curve could be determined from the indentation data. Section 3.5 addressed the issue of characterisation of the geometry of the spherical indenter used in this study. Two distinct methods of characterising the geometric variation of the average indenter profile with vertical distance from the indenter tip were presented. In order to assess which of these two methods best describes the characteristic strain, both were implemented for the derivation of the stress-strain curve from the indentation data using the new analysis technique, that is, the pile-up correction integrated within the original characterisation analysis. The two methods are investigated in Sections 6.2.1 and 6.2.2.

6.2.1 Characteristic strain as a function of (a_c/R)

In this version of characterisation, the radius of curvature at a certain vertical distance from the indenter tip was identified as the radius of the fitted axi-symmetric arc to the relevant part of the average indenter profile, as explained in Section 3.5.2. This means that the value of the indenter radius at a certain location is influenced by the profile geometry lying in between this location and the indenter tip. On the other hand, the contact area radius is measured on the average profile as a function of the contact depth h_c.

The indentation data from three grades of steel specimens resulting from one of the experiments described in Section 6.1.1 were analysed using the new analysis technique to obtain the Meyer hardness at the cycle peak loads. The stress-strain curve was then calculated considering the characteristic strain ε_r to be 20% of (a_c/R), where a_c and R are determined from Fig. 3-10 and Fig. 3-14, respectively as functions of the vertical distance from the tip. By non-linear fitting a power law function to these data points, n and K were obtained and employed to calculate the $\sigma_{0.2}$ representing the yield stress. The resulting stress-strain curve through these points is compared with the corresponding curve obtained from the tensile tests in Fig. 6-4 and Table 6-1.

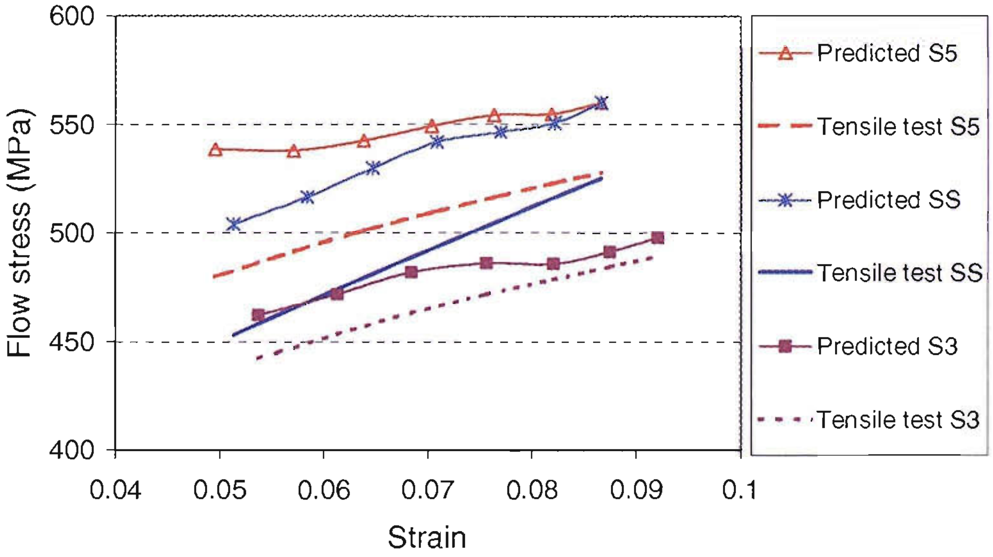

Fig. 6-4 Stress-strain points from indentation data compared with the corresponding stress-strain curve from tensile tests.

As observed in Fig. 6-4 and Table 6-1, the stress-strain curve resulting from the indentation data for each material appears to be close to that from the corresponding tensile test. However, the predicted n is considerably underestimated whilst $\sigma_{0.2}$ is overestimated. More importantly the shape of the predicted stress-strain curves manifests a noticeable plateau between strain values of 0.068 and 0.085, which may well be the reason for the underestimation of n. This suggests that the characteristic strain adopted over this region does not seem to best correspond to the indenter geometry.

6.2.2 Characteristic strain as a function of sin(β)

In this version of the characterisation analysis, the local gradient of the average indenter profile was taken as that of the line fitted to the relevant part of the profile. Unlike the method presented in Section 6.2.1, the characteristic strain at a certain location of the average indenter profile is independent of the rest of the profile. More details on this method can be found in Section 3.5.2. For calculating hardness, the contact area radius was again measured on the average profile as a function of the contact depth, h_c.

The indentation data from the three grades of steel specimens resulting from the experiments described in Section 6.1.1 were analysed in the same manner as in Section 6.2.1, and the points of the stress-strain curve determined at the cycle peaks by considering the characteristic strain ε_r to be 20% of sin(β). n and K were obtained from fitting a power law function to these data points, and the yield stress is presented as $\sigma_{0.2}$. The resulting predicted stresses and strains at those points can be compared with the corresponding curve obtained from the tensile tests in Fig. 6-5 and Table 6-1.

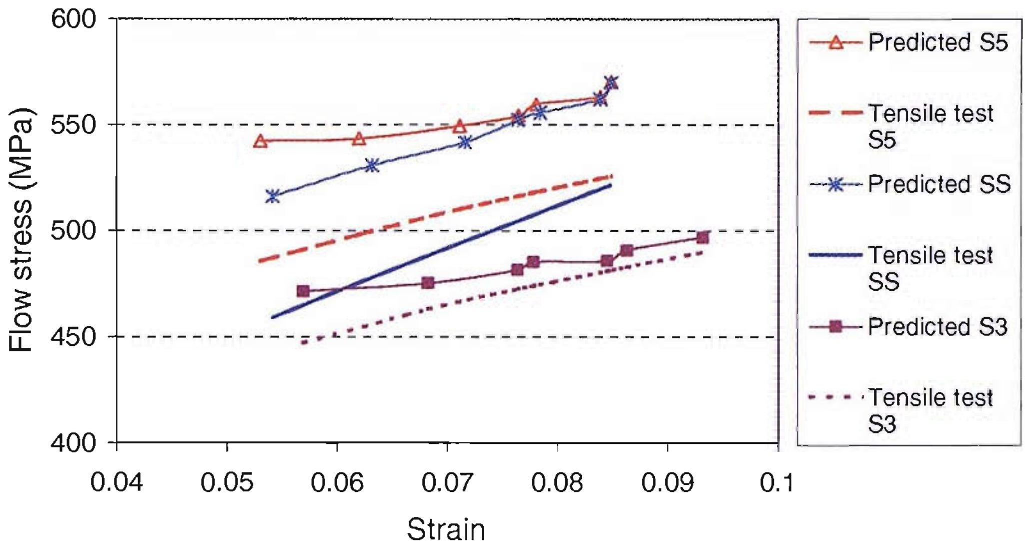

Fig. 6-5 Stress-strain data points from indentation data compared with the corresponding stress-strain curve obtained from tensile tests.

Table 6-1 Plastic properties from tensile tests compared with those calculated from indentation data based on two different expressions for characteristic strains.

	$\sigma-\varepsilon$ curve from tensile test		Calculated $\sigma-\varepsilon$ using $\varepsilon_r = 0.2a_c/R$		Calculated $\sigma-\varepsilon$ using ε_r=0.2sin(β)	
	n	σ_y (MPa)	n	σ_y (MPa)	n	σ_y (MPa)
Stainless steel	0.27	286	0.19	301	0.25	268
S5	0.17	391	0.10	416	0.14	362
S3	0.19	317	0.11	345	0.14	316

The resulting predicted stress-strain data points for each material shown in Fig. 6-5 exhibit a smoother variation with strain than that observed in Fig. 6-4. The predicted n and $\sigma_{0.2}$ are closer to the values from the tensile tests than those from the method presented in Section 6.2.1 although they are still smaller than the values from the tensile tests. Referring to Section 4.4.5, it was noticed that approximating the $\sigma-\varepsilon$ from the tensile test to an ideal curve with a single n and K and no yield plateau resulted in a reduced n. Hence, the $\sigma-\varepsilon$ curve derived from indentation data using the characteristic strain in terms of sin(β) can be considered as a representative approximation of that from the tensile test.

6.3 Assessment of the proposed analysis

The experimental indentation data produced, as described in Section 6.1.1, were obtained for all test materials, i.e. S3, S5, S6, S7, and stainless steel (SS), and analysed using the proposed analysis technique, that is, the new pile-up correction integrated within the characterisation method with 0.2sin(β) as a measure of the characteristic strain. The analysis results include the true contact area, Meyer hardness and characteristic strain at every cycle peak.

6.3.1 Prediction of the stress-strain curve from indentation data

The analysis results given in Section 6.1.1 from the 5 experiments for S3 are gathered in one group and used to derive the stress-strain data points that are then fitted with the power law curve, as shown in Fig. 6-6. This curve serves as an equivalent average to all data points. Its function parameters, n and K, are then used to generate the flow stress over a large range of strains. A comparison of this fitted curve with the original one generated from the tensile test is made in Fig. 6-7. This procedure of assessment has been followed and applied to the other test specimens, i.e. S5, S6, S7, and SS. Corresponding plots for these materials are presented in Fig. 6-8 to Fig. 6-15.

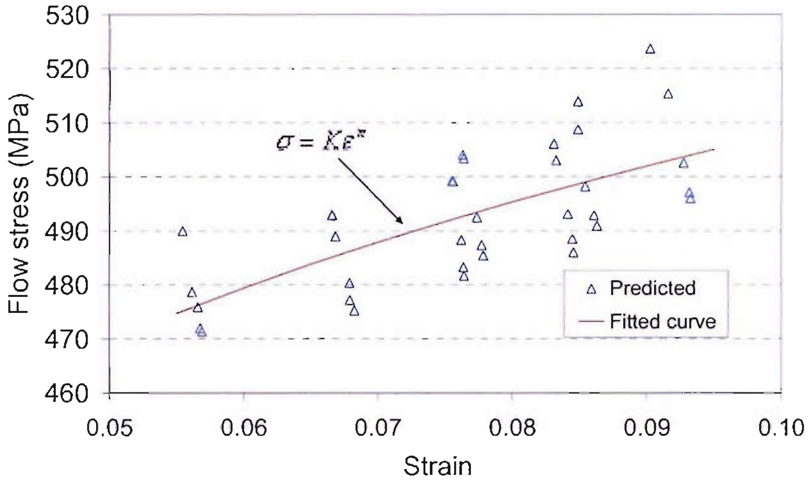

Fig. 6-6 Stress-strain data points resulting from 5 indentation experiments on specimen S3.

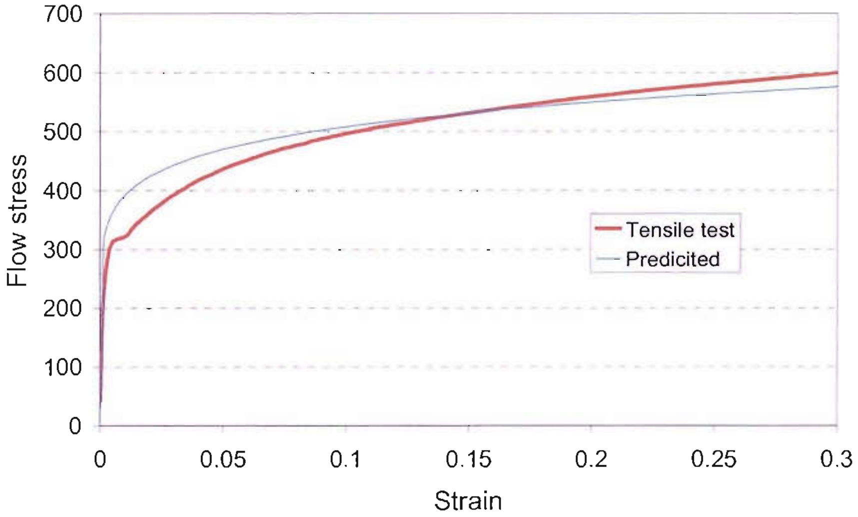

Fig. 6-7 Stress-strain curve predicted from indentations on specimen S3 compared with that obtained from the tensile test.

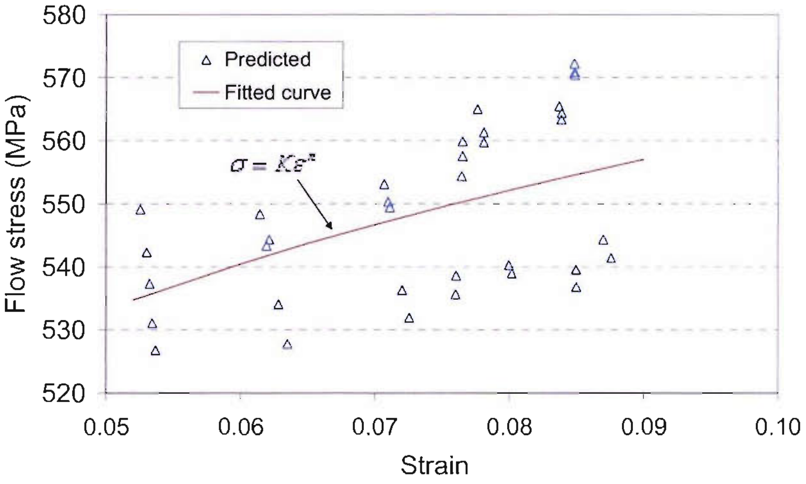

Fig. 6-8 Stress-strain data points resulting from 5 indentation experiments on specimen S5.

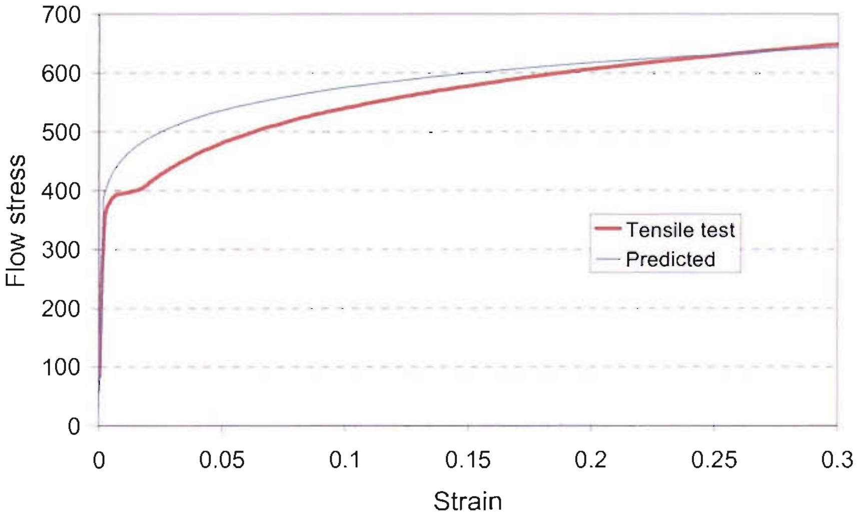

Fig. 6-9 The fitted stress-strain curve from the 5 indentation experiments on specimen S5 compared with that derived from the tensile test.

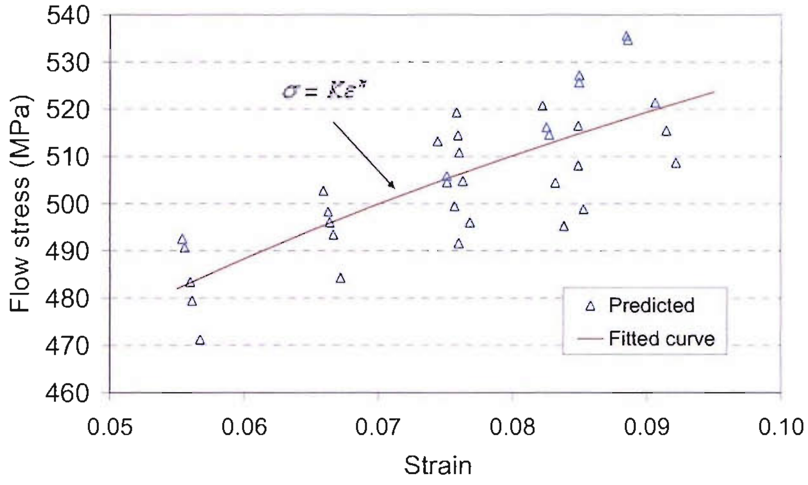

Fig. 6-10 Stress-strain data points resulting from 5 indentation experiments on specimen S6.

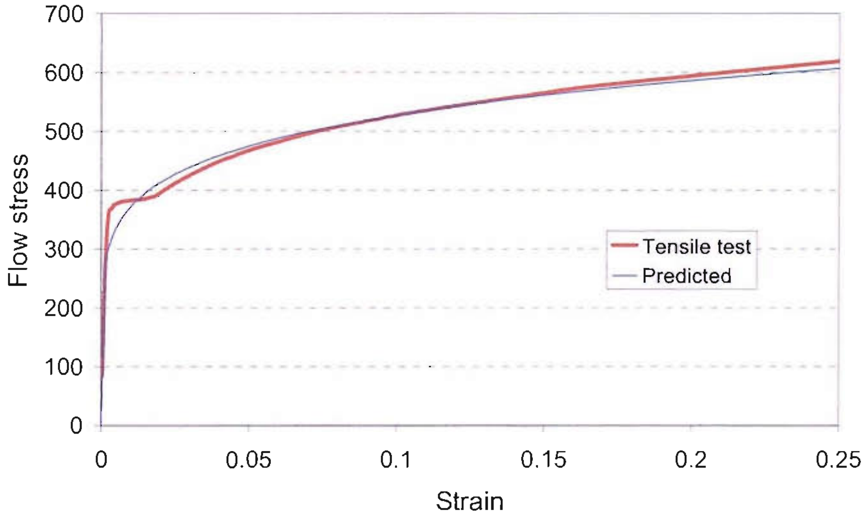

Fig. 6-11 The fitted stress-strain curve from the 5 indentation experiments on specimen S6 compared with that derived from the tensile test.

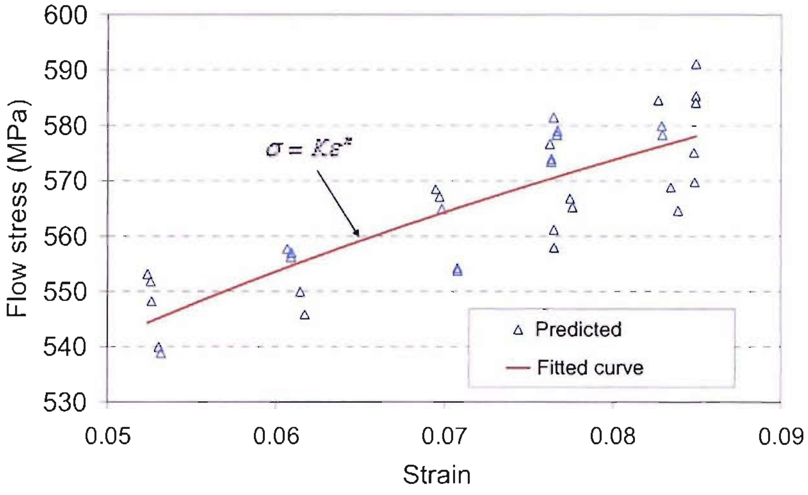

Fig. 6-12 Stress-strain data points resulting from 5 indentation experiments on specimen S7.

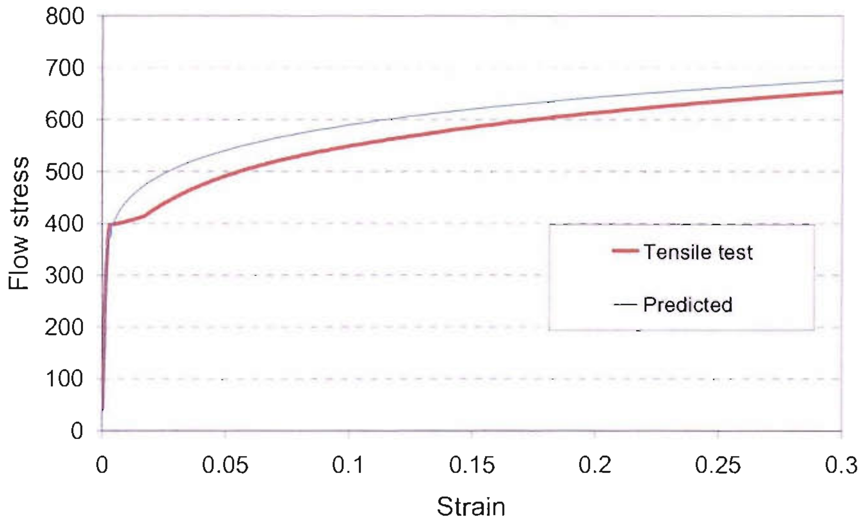

Fig. 6-13 The fitted stress-strain curve from the 5 indentation experiments on specimen S7 compared with that derived from the tensile test.

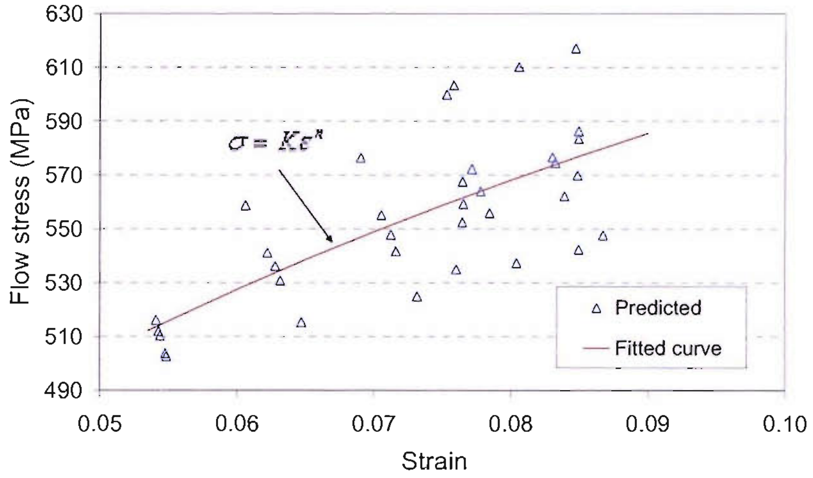

Fig. 6-14. Stress-strain data points resulting from 5 indentation experiments on specimen SS.

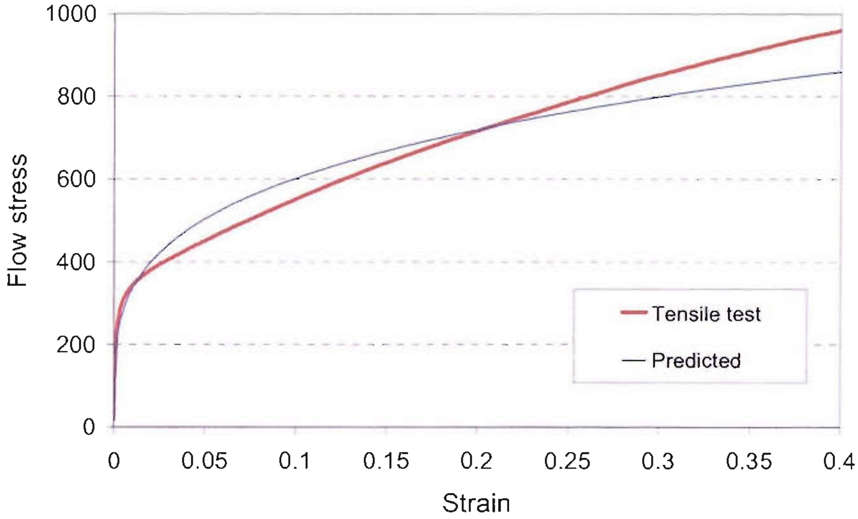

Fig. 6-15 The fitted stress-strain curve from the 5 indentation experiments on specimen SS compared with that derived from the tensile test.

The values of n and $\sigma_{0.2}$ from the curves fitted to the stress-strain points generated from the indentation data are compared with the corresponding values from the tensile test in Table 6-2. Included in that table is the extent of the yield plateau strain of each curve from the tensile test normalised with respect to yield strain.

Table 6-2 Comparison of the σ-ε curve parameters from the tensile test with those generated from indentation data.

	$\sigma - \varepsilon$ curve from tensile test			**Generated from indentation data**		**Extent of yield plateau strain/yield strain)**
	n	**σ_y (MPa)**	**Extent of yield plateau strain (%)**	**n**	**$\sigma_{0.2}$ (MPa)**	
S3	0.19	317	0.8	0.11	349	228
S5	0.17	391	1.35	0.07	415	350
S6	0.18	375	0.80	0.15	317	211
S7	0.16	395	0.88	0.12	374	227
Stainless steel	0.27	286	0	0.26	250	0

As can be observed in Fig. 6-6 to Fig. 6-15 and Table 6-2, the predicted stress-strain curves have lower n values compared with those from the tensile test whilst $\sigma_{0.2}$ is within 10% of the respective values from the tensile test except for S6, where the error is about 15%. Even though the difference in the values of n seems large, the stress-strain curve derived is similar to that from the tensile test. The first post-yield part of the predicted relation appears to slightly overestimate the stress whilst at greater strains the stresses are slightly underestimated. However, the curve as a whole appears to represent material behaviour equivalent to that corresponding to the curve from the tensile test.

The stress-strain curves of the idealised materials, discussed in chapter 4, also had a value of n considerably less than the true one. This can be understood as a consequence of the presence of the yield plateau, which is expected to cause a drop in n if it is to be averaged over the post-yield part of the curve. Furthermore, the magnitude of this yield plateau strain is expected to influence the underestimation of n. Referring to Table 6-2, it can be appreciated that the underestimation in n is proportional to the magnitude of this yield plateau strain except for $S3$ which does not seem to follow this trend. This can be clearly thought of as an influence of yield strain based on the averaging argument, leading to the influence of the yield plateau being more significant at small values of yield strain. Normalising the extent of the yield plateau strain with respect to yield strain seems to give a value that is consistent with the underestimation of n.

Even though the characteristic strain cannot exceed a value of 0.2 for a perfect sphere, the maximum equivalent strain induced within the indentation zone beneath the indenter could, according to the FE results, reach larger values depending on the depth of indentation. Consequently, the resulting P-h curve is a reflection of the specimen material undergoing high equivalent strains which are not limited by the characteristic strain. It is also worth bearing in mind that the stress-strain field of the indented material is different from that developing in the specimen of a tensile test. In the tensile test the strain is uniform along the gauge length until the tensile strength is reached after which the strain concentrates in the necked region. However, in the case of indentation, the situation is different. At a very small load, the material reaches its yield stress in a very localised region directly beneath the contact centre, which is enclosed by elastically deformed material. As the indenter is pressed into the specimen, the elastic material bounding the plastic zone will reach its yield stress causing the plastic zone to enlarge while the material around this region is still elastic. Hence, at every increase in load, the strain field across the region of indentation spans from the elastic to high plastic strain values in the stress-strain curve. The P-h curves resulting from indentation thus reflect this as they are affected by values of strain considerably greater than that given by the characteristic strain.

Hence, the resulting stress-strain curve obtained from the analysis of *P-h* data is strongly influenced by the complete stress-strain curve of the material especially at high strain values, rather than by its behaviour up to the characteristic strain limit.

The hypothesis that the derived stress-strain curve, which has no yield plateau, is equivalent to the original curve determined by the tensile test although its value of n is smaller due to the absence of yield plateau is verified in Section 6.3.2.

6.3.2 FE regeneration of the *P-h* curve from the predicted σ-ε curve

At this stage of assessment, the stress-strain data points resulting from analysing the experimental load-indentation curve of a material were fitted to a power law function. Its parameters, n and K, are then used to generate the flow stress-strain curve, which is then used as the material input into an FE model to simulate indentation in a cyclic loading pattern reaching peak loads almost the same as, or close to those in the experimental data. The load-indentation data produced by this FE simulation is compared with that from the corresponding experiment used to derive the input stress-strain curve to this FE model. This comparison is made for all test materials, and presented in Fig. 6-16 to Fig. 6-20. It should be noted that as FE is displacement controlled while the indentation experiments are load controlled, the unloading data will not always coincide for both results.

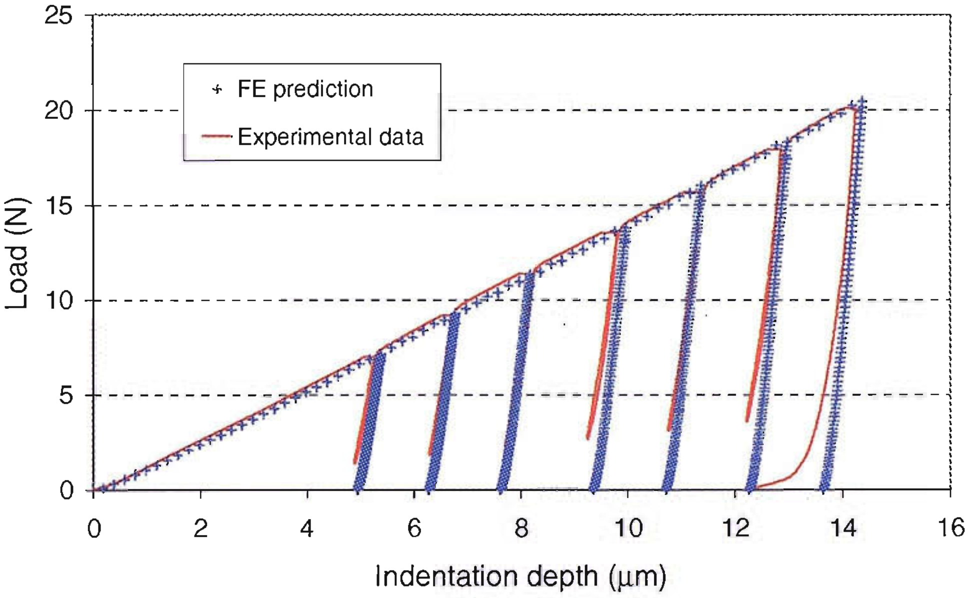

Fig. 6-16 Comparison of the experimental data from S3 with the FE prediction based on the stress-strain curve derived from the same experimental data.

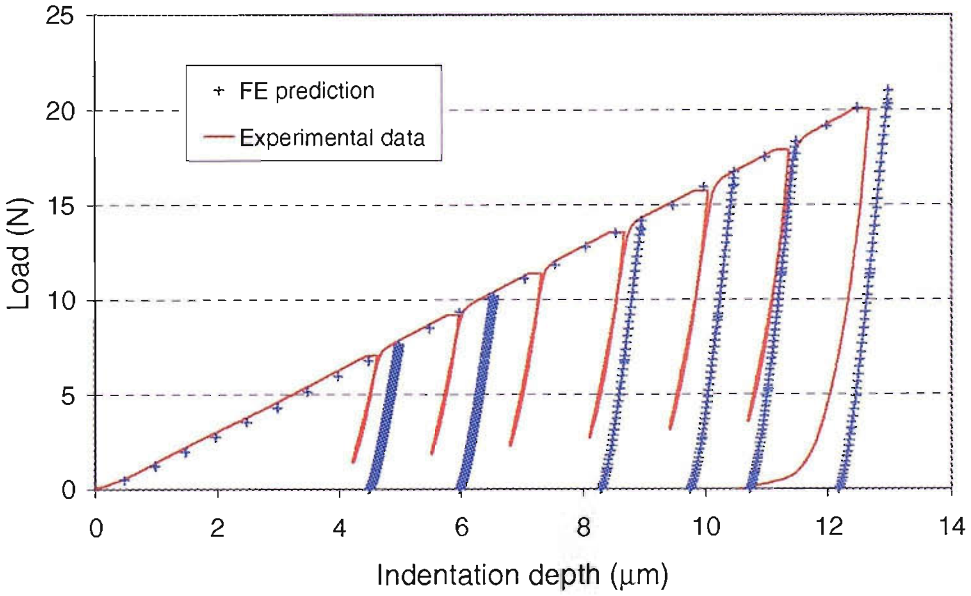

Fig. 6-17 Comparison of the experimental data of S5 with the FE prediction based on the stress-strain curve derived from analysing the same experimental data.

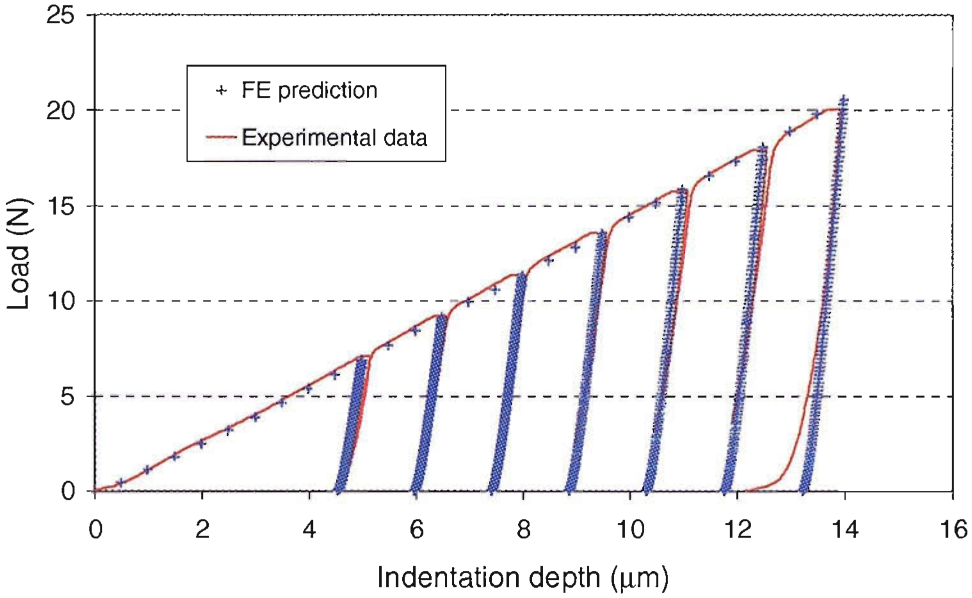

Fig. 6-18 Comparison of the experimental data of S6 with the FE prediction based on the stress-strain curve derived from analysing the same experimental data.

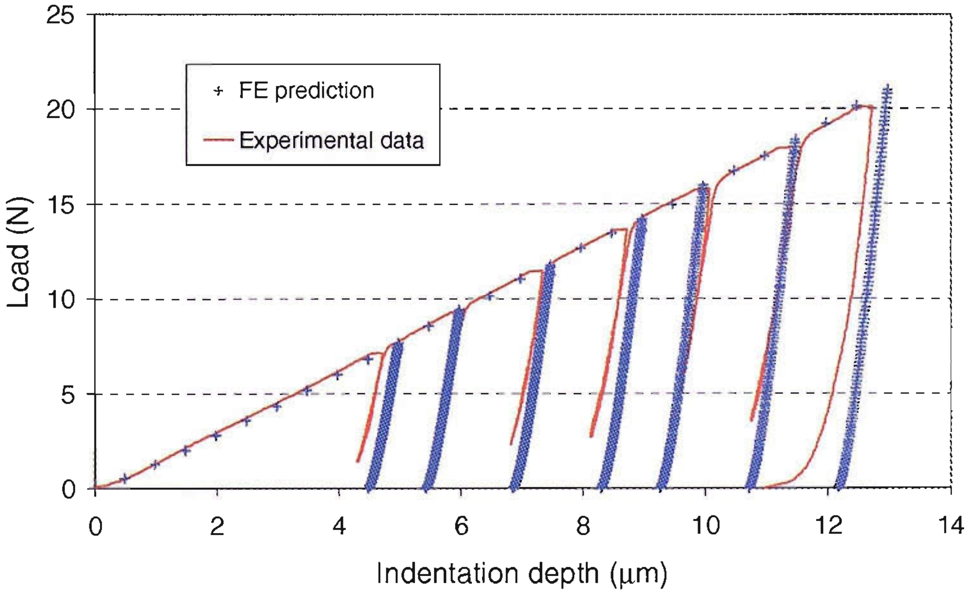

Fig. 6-19 Comparison of the experimental data of S7 with the FE prediction based on the stress-strain curve derived from analysing the same experimental data.

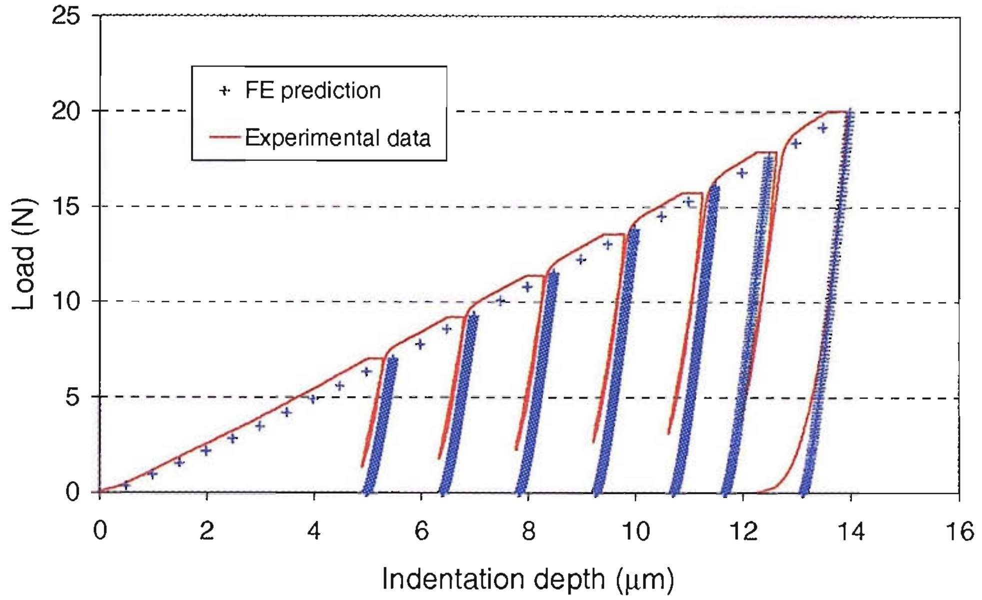

Fig. 6-20 Comparison of the experimental data of SS with the FE prediction based on the stress-strain curve derived from analysing the same experimental data.

In Fig. 6-16 to Fig. 6-20 good agreement can be observed between the experimental *P-h* curve, for each test material, and that predicted by FE simulation based on the stress-strain curve derived from the same experimental indentation data. This clearly proves that even though the derived stress-strain curve, which has no yield plateau, has a much smaller value of *n* compared with that of the tensile test, it behaves in an equivalent manner to that obtained from the tensile test as it can lead to an accurate prediction of material response. In addition, it can be seen that the absence of the yield plateau in the derived stress-strain curve compensates for the underestimation of the value of *n* making this curve equivalent to that obtained from the tensile test.

6.4 Experimental variability

The test materials are modelled as homogeneous and perfectly isotropic. However, they are not homogeneous on the micro scale since the microstructure consists of small grains. Depending on the number of grains included in every indent and the density of the grain boundaries, the resulting *P-h* curve will vary from one location to another. In order to evaluate this variation and to investigate its effect on the results, the 5 experiments on stainless steel were treated individually. The five *P*-*h* curves from these experiments are presented in Fig. 6-21.

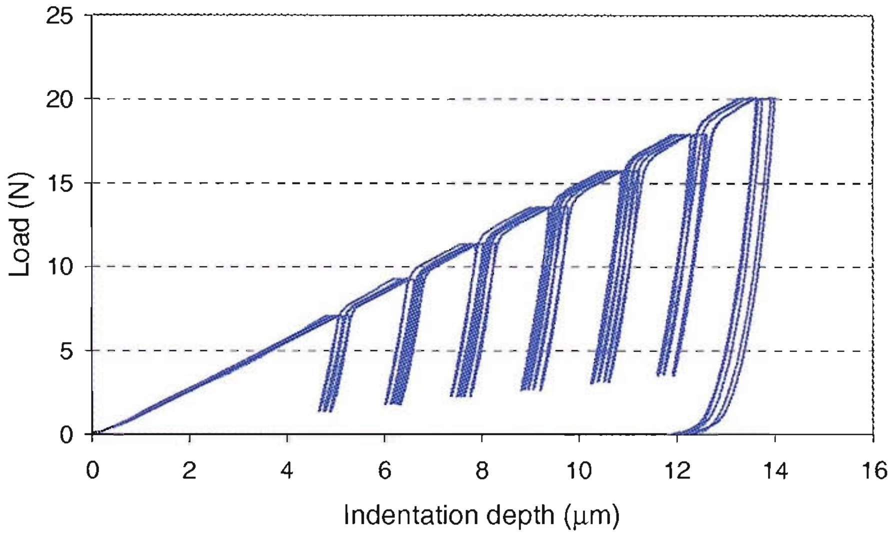

Fig. 6-21 Load-indentation data resulting from the 5 experiments on the stainless steel.

The stress-strain curves resulting from analysing the indentation data from the 5 experiments are compared to the stress-strain curve from the tensile test in Fig. 6-22. The values of *n* and *K* for these predicted curves in addition to the values of Meyer hardness corresponding to the last cycle peak are summarised in Table 6-3.

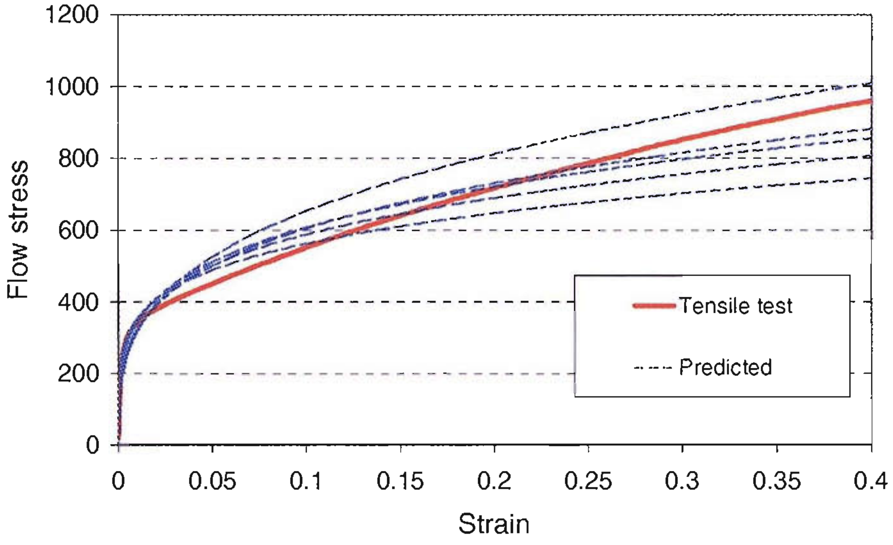

Fig. 6-22 Predicted stress-strain curves from the 5 experiments on the stainless steel sample compared with the stress-strain curve from the tensile test.

Table 6-3 Characterisation results from the 5 indentations on stainless steel.

Experiment	*n*	σ_y **(MPa)**	*H* **(MPa)**
1	0.20	282	1643
2	0.23	268	1710
3	0.25	260	1759
4	0.31	218	1851
5	0.27	235	1751

It should be noted that even though the *P-h* curves seem very similar, the characteristics of the predicted stress-strain curves vary. The average of these curves represents the overall material behaviour in a similar way as the results from a tensile test reflect the average behaviour of many grains of the material.

6.5 Welded joint details

A steel plate of 8 mm thickness was cut and joined again using a single pass submerged arc weld to form a butt-welded joint. The joint was then sectioned transverse to the weld line, and this cross section was metallographically prepared and polished using 1 μm diamond paste. Indentation testing was carried out on the cross section to span the three distinct regions of the weld, which are the parent metal, weld heat affected zone, HAZ, and weld fusion zone. Six rows of indents were made. The second and the fifth rows were obtained using the conventional Vickers micro-indentation tester, whilst the rest were made using the spherical indenter on the instrumented micro-indentation tester.

The indented surface was then etched in 2% nital to reveal the variation of the microstructure across the various material boundaries as shown in Fig. 6-23. The location of each indent relative to the three regions of weld is also shown in the same figure.

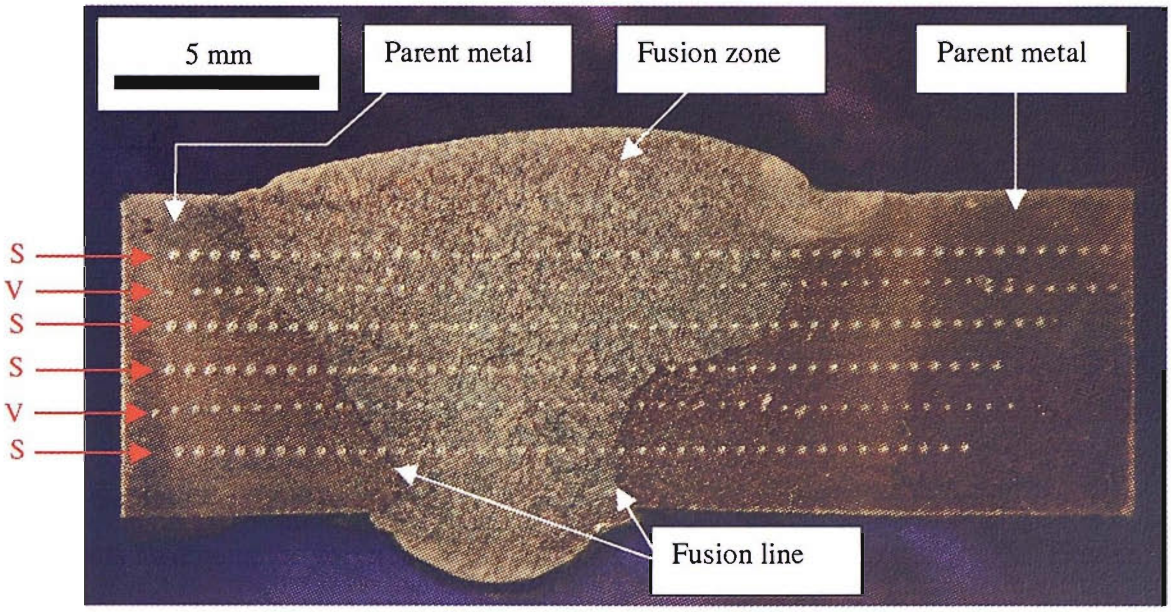

Fig. 6-23 Etched surface of the cross section of the butt-welded steel joint showing the indents traversing the parent metal, heat affected zone and fusion zone. S and V denote spherical and Vickers indentations, respectively. The HAZ is adjacent to the fusion line in the parent metal.

A micrograph showing a detail of the microstructural variation from the parent metal towards the fusion zone of the weld is presented in Fig. 6-24. The micrograph shows the top left corner of Figure 6-23 with some indents from the first three rows.

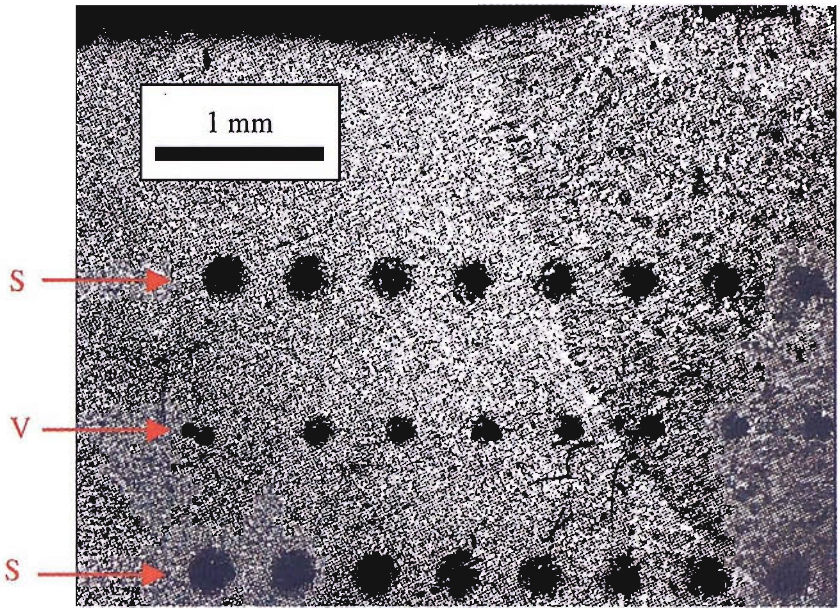

Fig. 6-24 Etched surface showing the microstructural variation in the top left corner of the weld specimen shown in Figure 6-23.

A detailed micrograph showing the variation of the crystal structure from the heat affected zone to the fusion zone is presented in Fig. 6-25. Included in that micrograph is the fourth and the fifth indents of the first row.

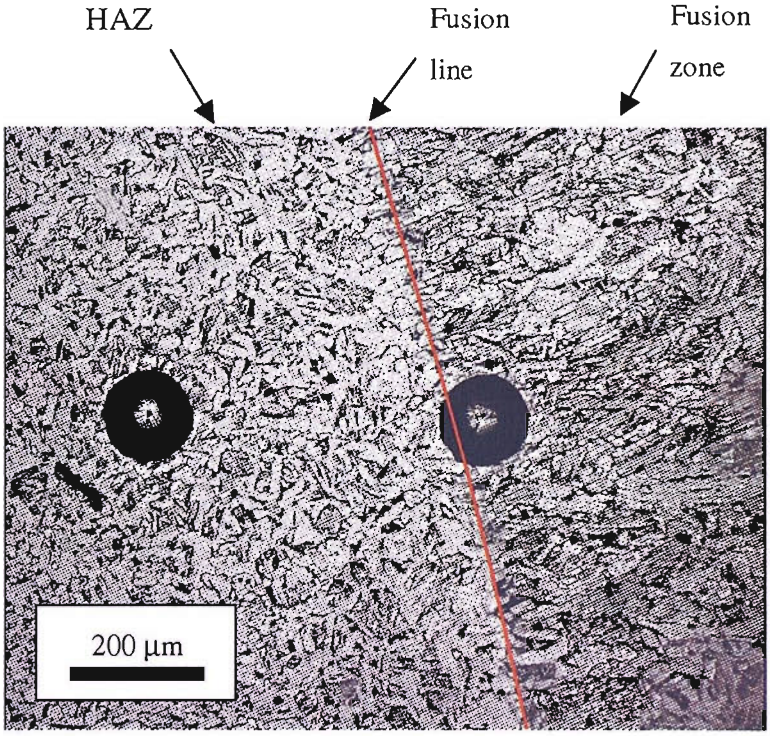

Fig. 6-25 Microstructural variation across the boundary between the weld heat affected zone and the fusion zone.

As can be observed from Fig. 6-24 and Fig. 6-25, welding has caused a noticeable change in the microstructure of the metal in the vicinity of the weld fusion zone making this area inhomogeneous. The change in microstructure between the HAZ and fusion zone can be observed on either side of the fusion line separating the two zones, as shown in Fig. 6-25. A more detailed comparison of the microstructure in the various weld regions, i.e. parent metal, HAZ, and fusion zone can be made by referring to Fig. 6-26, Fig. 6-27 and Fig. 6-28

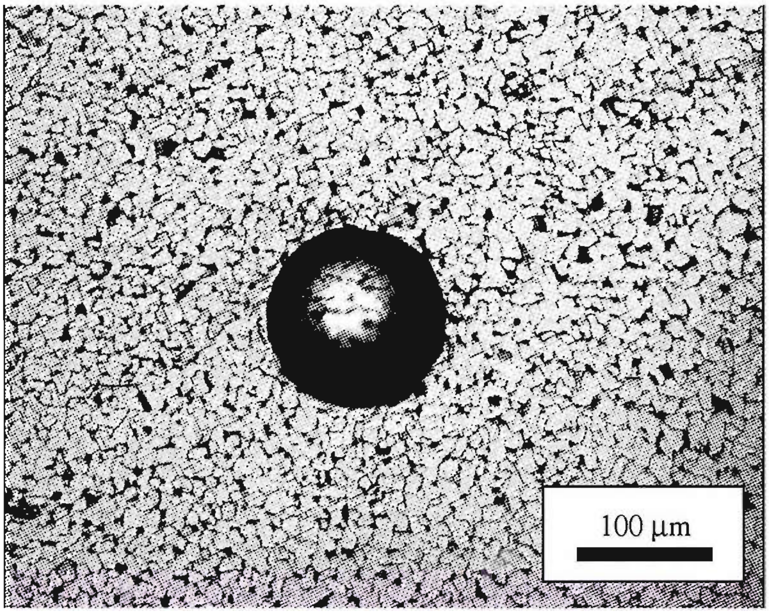

Fig. 6-26 Microstructure of the parent metal, showing a residual indent.

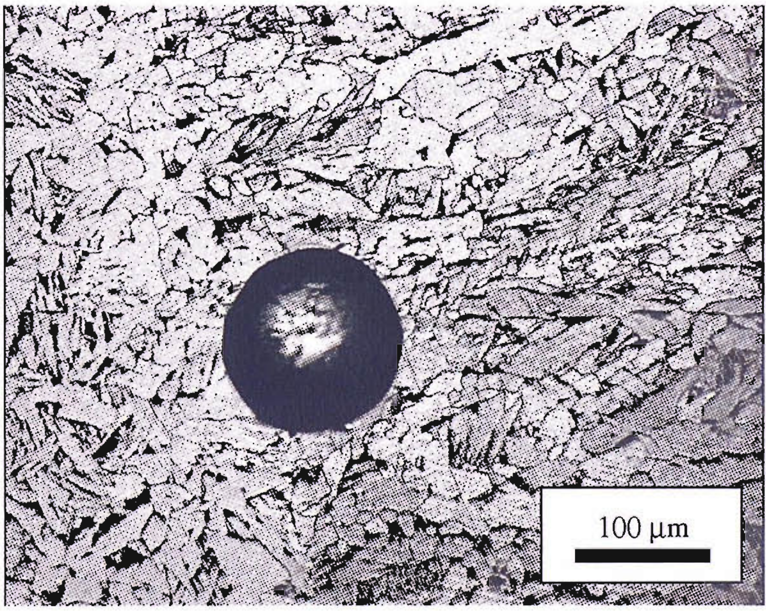

Fig. 6-27 Microstructure of the heat affected zone, showing a residual indent (the fifth indent of the first row).

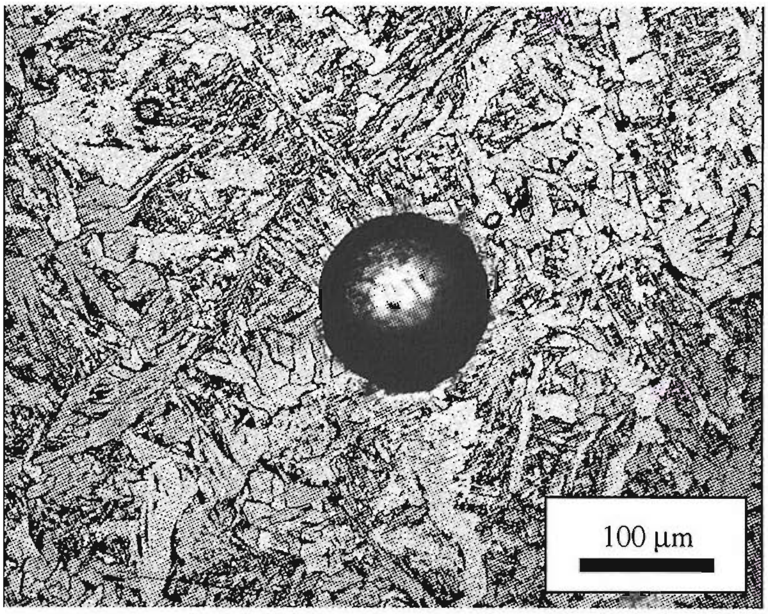

Fig. 6-28 Microstructure of the fusion zone, showing a residual indent.

The micrographs shown in Fig. 6-26 to Fig. 6-28 illustrate the distinct features of the microstructure across the weld regions. In the parent metal, the grains are small, rounded and equiaxed whilst in the fusion zone the grains have a columnar nature and acicular ferrite is present. A gradual change between the two structures is observed in the heat-affected zone. The nature of the carbides also varies across the weldment.

This variation in the microstructure will affect the mechanical properties of the relevant regions. Such properties can be measured locally from the load indentation data obtained from an indent located at a given position. Hence, carrying out indentation testing across the weld regions is utilised as the means of providing information on variation of material mechanical properties. Whilst conventional hardness testing using the Vickers indenter only provides a value of hardness, other properties that describe the strain-strain curve, i.e. $\sigma_{0.2}$, n, and K, in addition to Meyer hardness, can be obtained from analysing the load-indentation data obtained by the instrumented microhardness tester using a spherical indenter. These material properties are plotted, for the indents lying on the 1st, 3rd, 4th, and 6th rows as a function of the distance from the left edge of the welded specimen in Fig. 6-31 to Fig. 6-46 to show their variation across the weld regions. In addition, the variation of Vickers hardness across the weld regions for the indents lying on the 2nd and 5th rows is presented in Fig. 6-29 and Fig. 6-30, respectively. The parent metal and the fusion zones are labelled in the graphs as *P* and *F*, respectively. The HAZ is a 1.0 mm region adjacent to the fusion line in the parent metal.

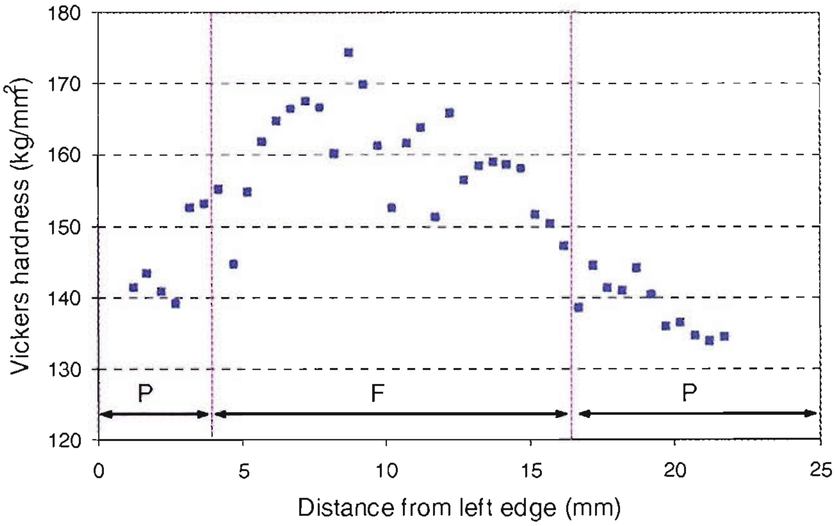

Fig. 6-29 Vickers hardness from the 2nd row of indentations.

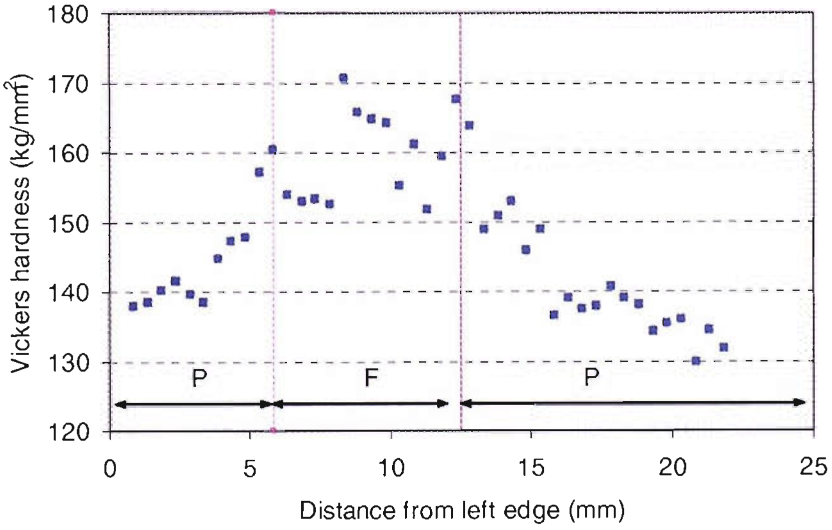

Fig. 6-30 Vickers hardness from the 5th row of indentations.

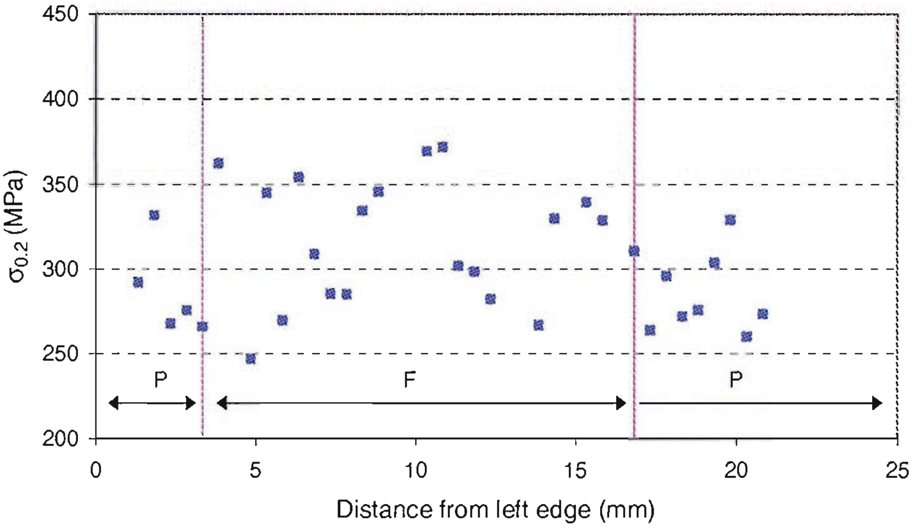

Fig. 6-31 The value of 0.2 % yield stress from the 1st row of the spherical indentations.

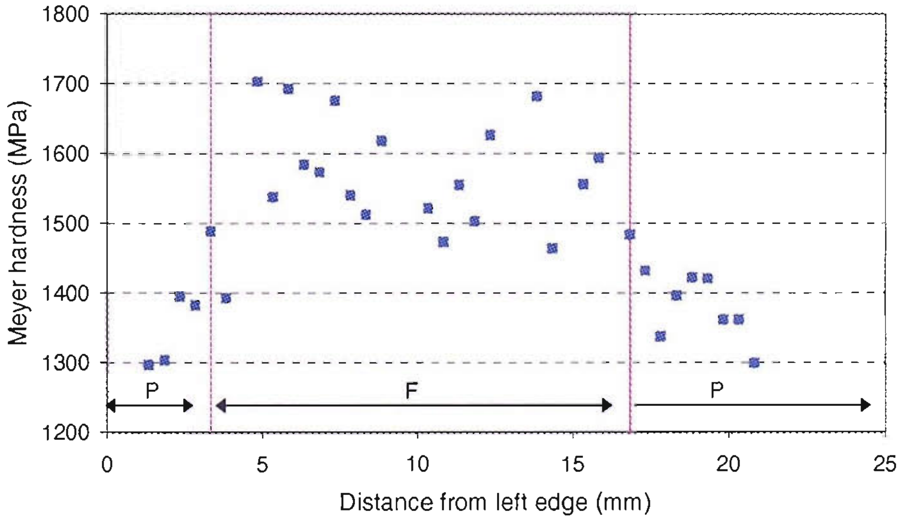

Fig. 6-32 Meyer hardness from the last loading cycle and the 1st row of the spherical indentations.

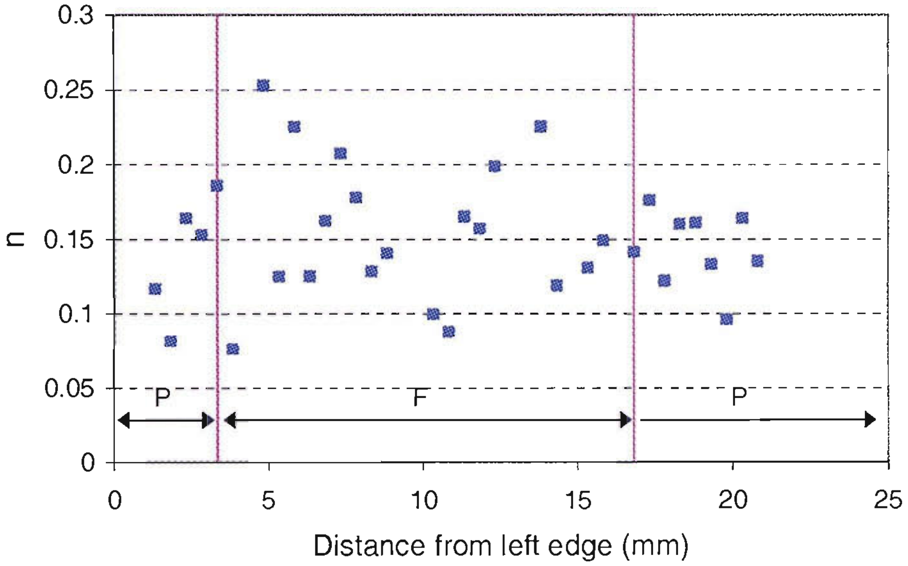

Fig. 6-33 The value of n from the 1st row of the spherical indentations.

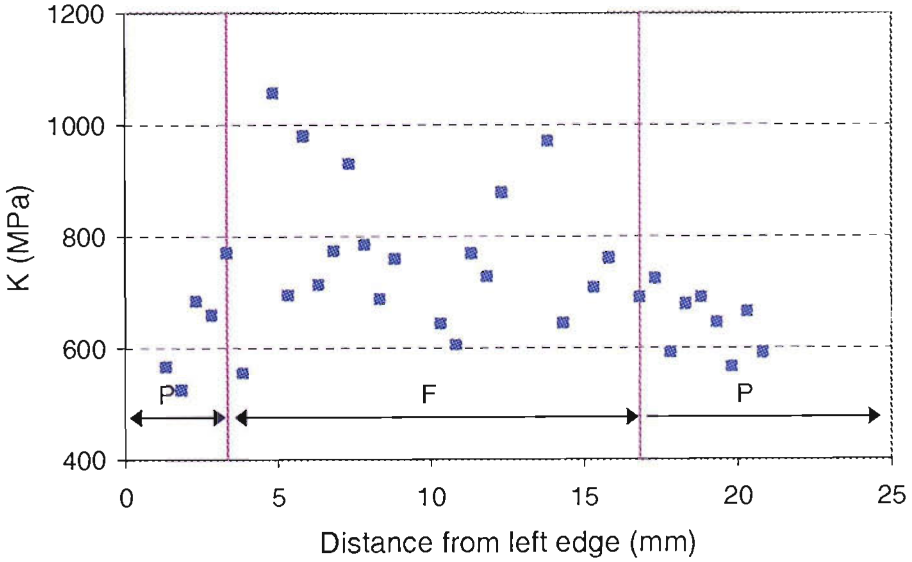

Fig. 6-34 The value of K from the 1st row of the spherical indentations.

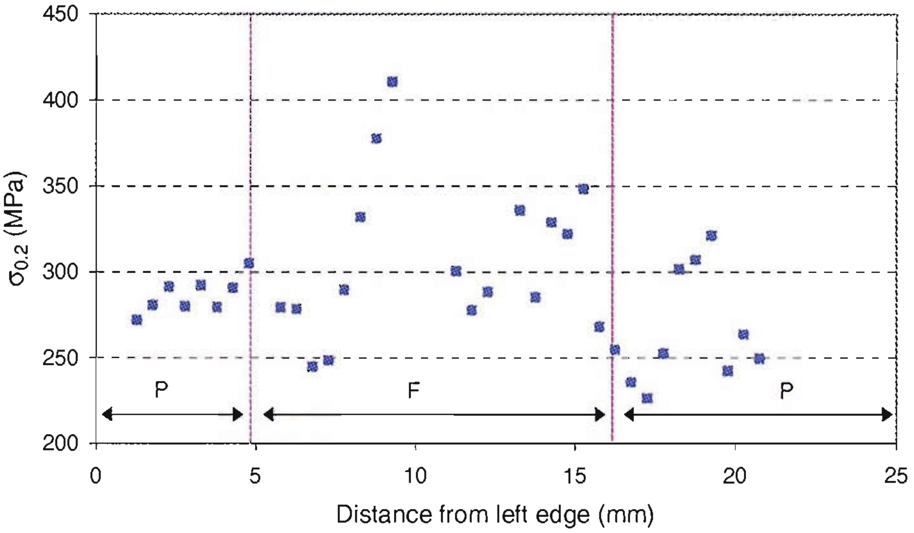

Fig. 6-35 The value of 0.2 % yield stress from the 2nd row of the spherical indentations.

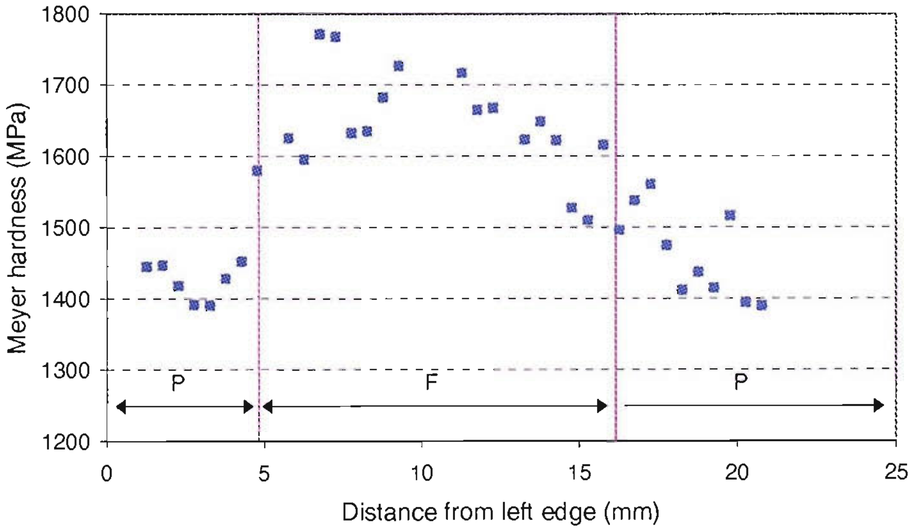

Fig. 6-36 Meyer hardness from the last loading cycle and the 2nd row of the spherical indentations.

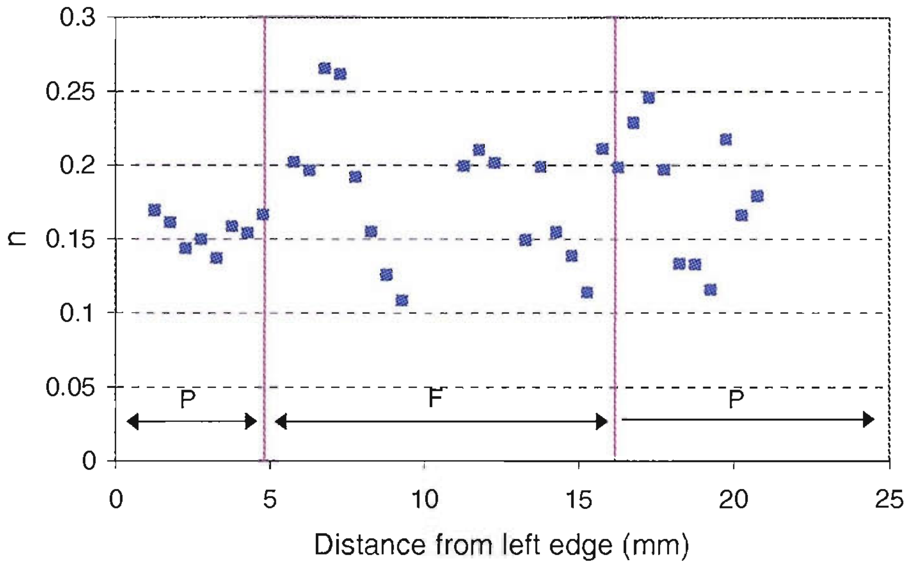

Fig. 6-37 The value of n from the 2nd row of the spherical indentations.

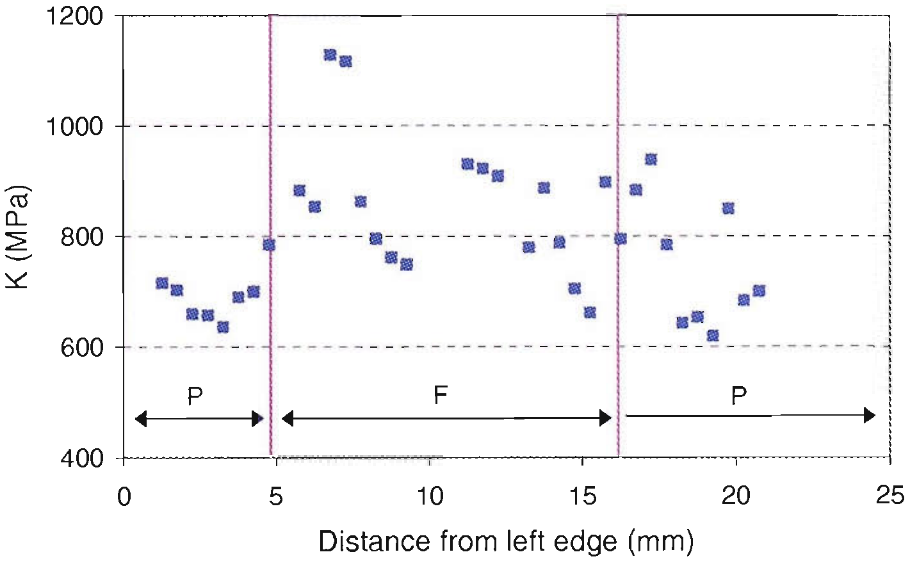

Fig. 6-38 The value of K from the 2nd row of the spherical indentations.

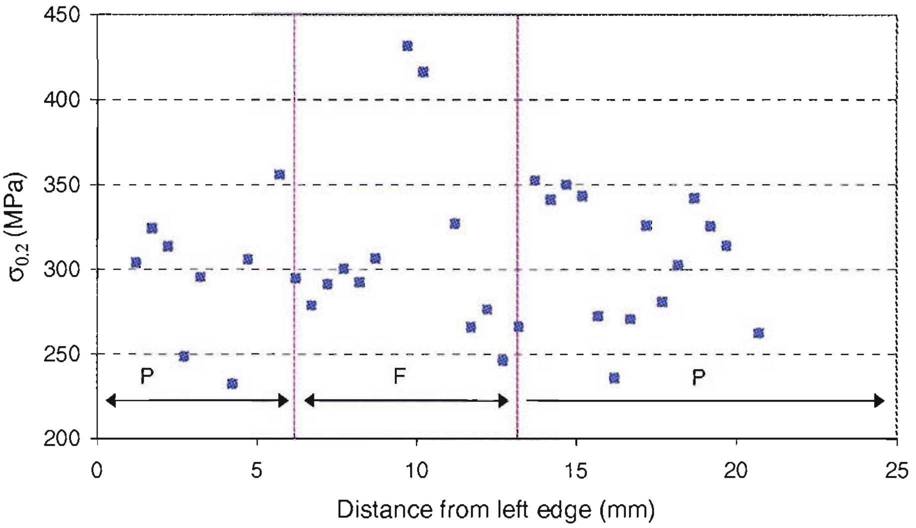

Fig. 6-39 The value of 0.2 % yield stress from the 3rd row of the spherical indentations.

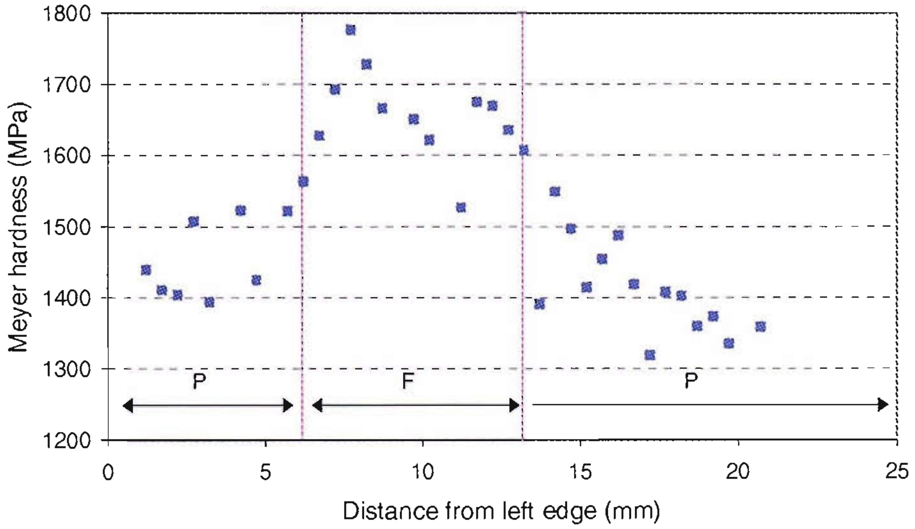

Fig. 6-40 Meyer hardness from the last loading cycle and the 3rd row of the spherical indentations.

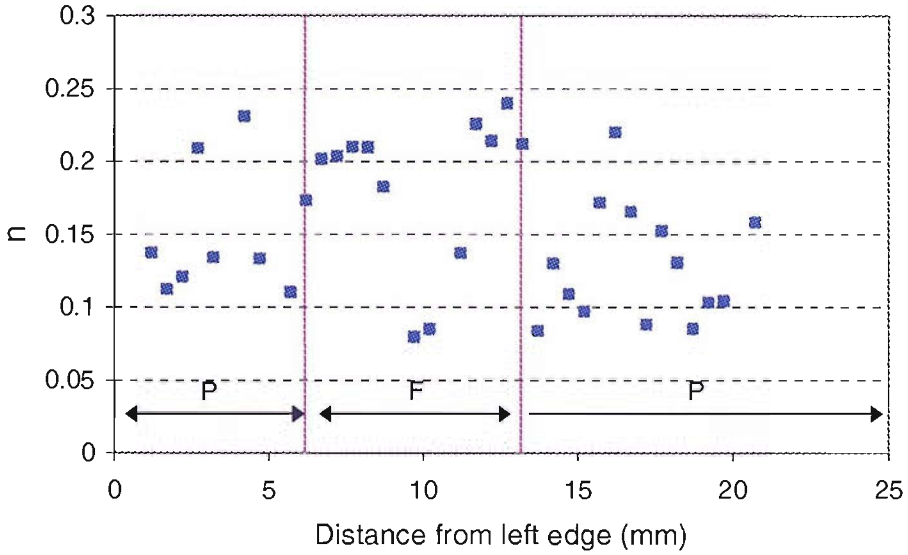

Fig. 6-41 The value of *n* from the 3rd row of the spherical indentations.

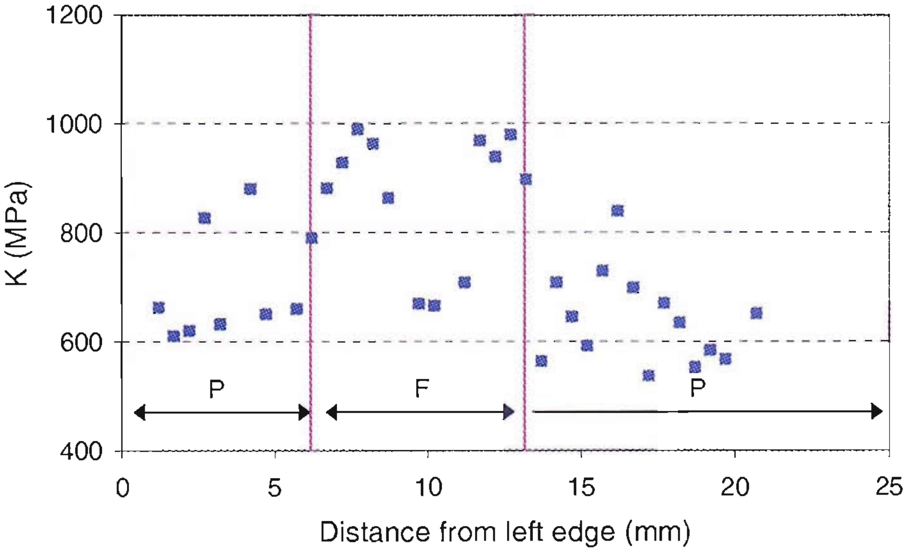

Fig. 6-42 The value of *K* from the 3rd row of the spherical indentations.

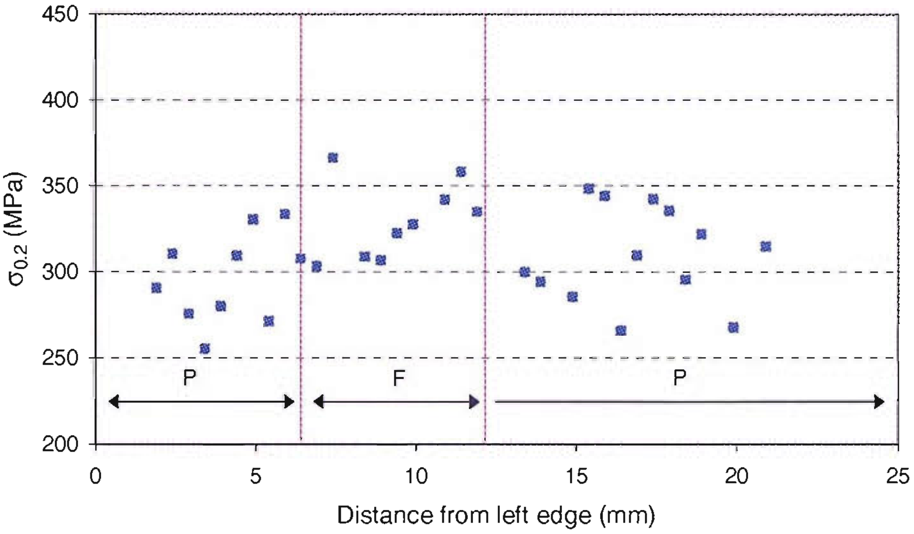

Fig. 6-43 The value of 0.2 % yield stress from the 4th row of the spherical indentations

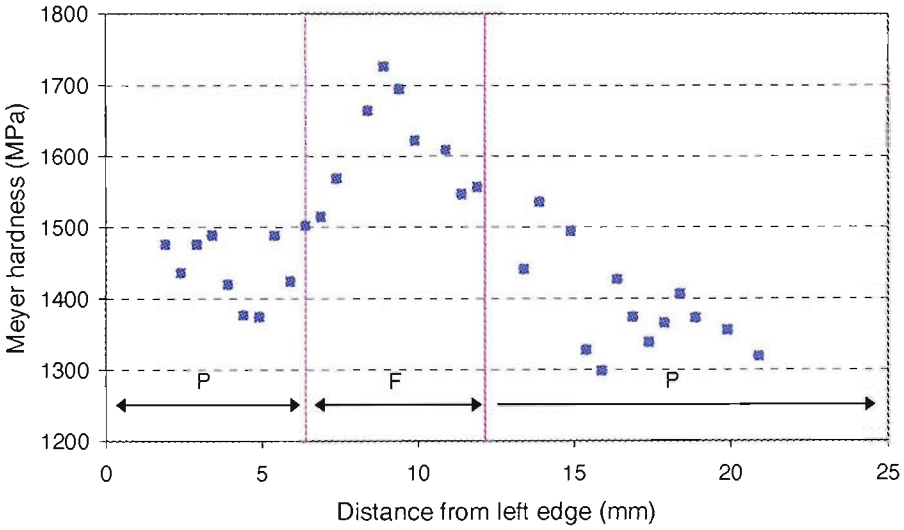

Fig. 6-44 Meyer hardness from the last loading cycle and the 4th row of the spherical indentations.

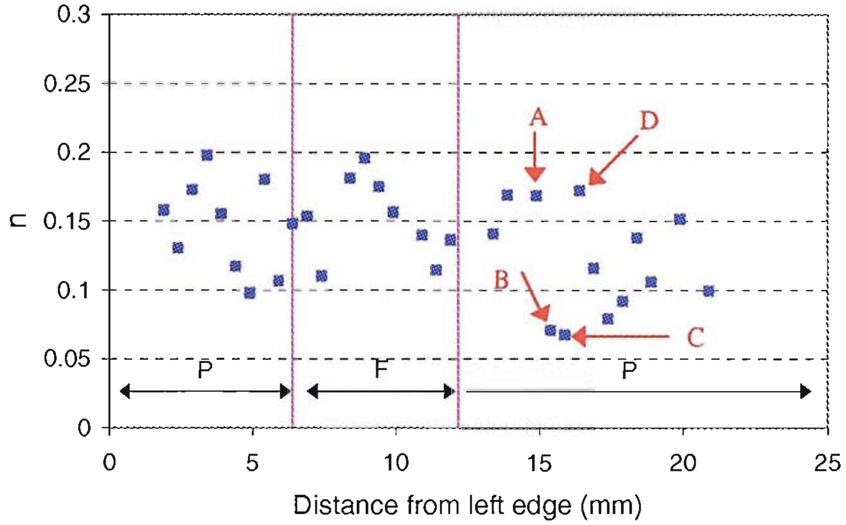

Fig. 6-45 The value of n from the 4th row of the spherical indentations.

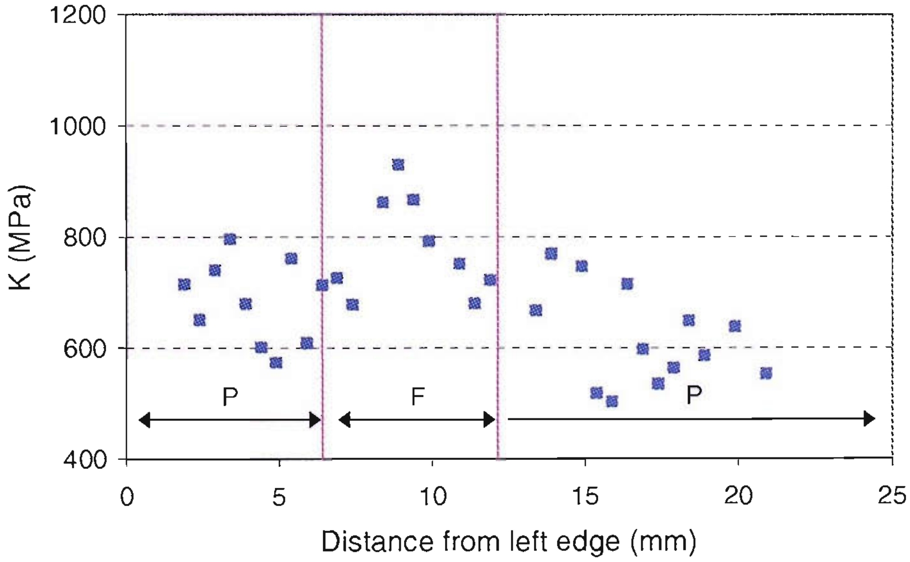

Fig. 6-46 The value of K from the 4th row of the spherical indentations.

As can be observed from Fig. 6-29 and Fig. 6-30, Vickers hardness has an average value of about 135 $H_V1.0$ in the parent metal and increases towards the weld fusion zone until it reaches its maximum value of about 170$H_V1.0$ in the centre of the fusion zone. A similar trend is exhibited for Meyer hardness obtained by the instrumented microhardness tester, which can be seen in Fig. 6-32, Fig. 6-36, Fig. 6-40, and Fig. 6-44. As shown in these figures, Meyer hardness starts at an average value of about 1350 MPa in the parent metal and then increases towards the weld fusion zone and reaches an average value of 1700 MPa at its centre. This observation clearly indicates that the hardness of the weld is greater than that of the parent metal. However, the other elasto-plastic properties characterising the stress-strain curve seem to behave in a rather random manner. The 0.2% yield stress is noticed to range between 250 and 350 MPa. Its variation does not manifest the same pattern as that for hardness, nevertheless most of the low values appear to fall within the parent metal region whilst the larger values are reached within the weld fusion zone. For n and K, the analysis results exhibit a larger scatter than that of $\sigma_{0.2}$ with no noticeable distinct trend, although $_{[o]}K$ seems to be higher in the fusion zone than in the parent material. The values of n range between 0.1 and 0.25, and those of K range between 500 and 1000 MPa. On the other hand, the trend of these two parameters appears to relate inversely to that of $\sigma_{0.2}$, that is, the difference in $\sigma_{0.2}$ for two adjacent indents is opposite in sign to that for the values of n and K.

Due to the scatter associated with the material properties obtained from indentation analysis, the values of H, n, K, and $\sigma_{0.2}$ are averaged across the weld regions in order to show more clearly the trend of their variation. The results are summarised in Table 6-4 and the corresponding graphs are shown in Fig. 6-47 to Fig. 6-50. In addition the corresponding stress-strain curves for each region are compared in Fig. 6-51.

Table 6-4 Average values of H, n, K, $\sigma_{0.2}$ across the weld regions.

Zone	H [MPa]	n	K [MPa]	$\sigma_{0.2}$ [MPa]
Parent metal	1406	0.14	659	292
HAZ	1482	0.16	721	295
Fusion zone	1619	0.17	818	315

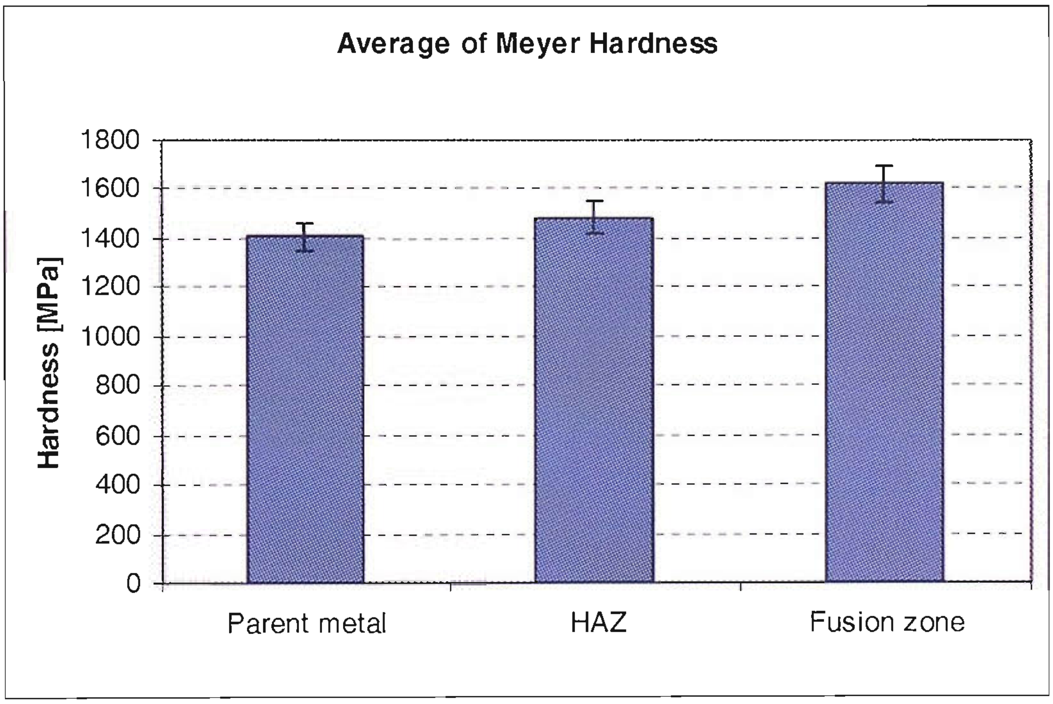

Fig. 6-47 Average values of Meyer hardness over the three weld regions.

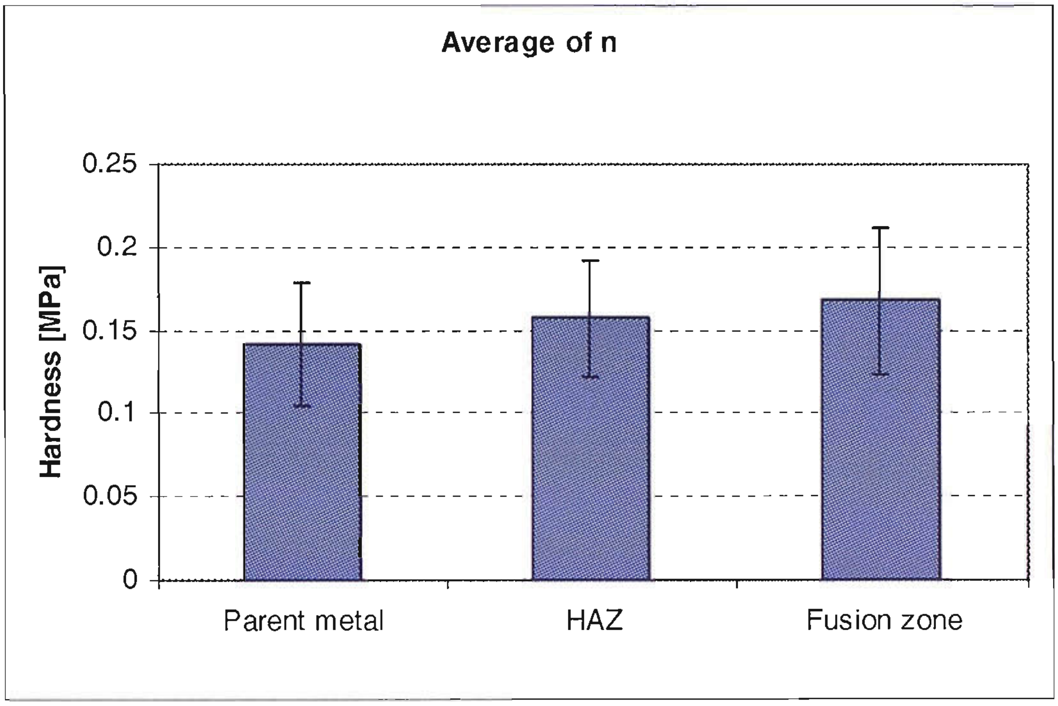

Fig. 6-48 Average values of the strain hardening exponent over the three weld regions.

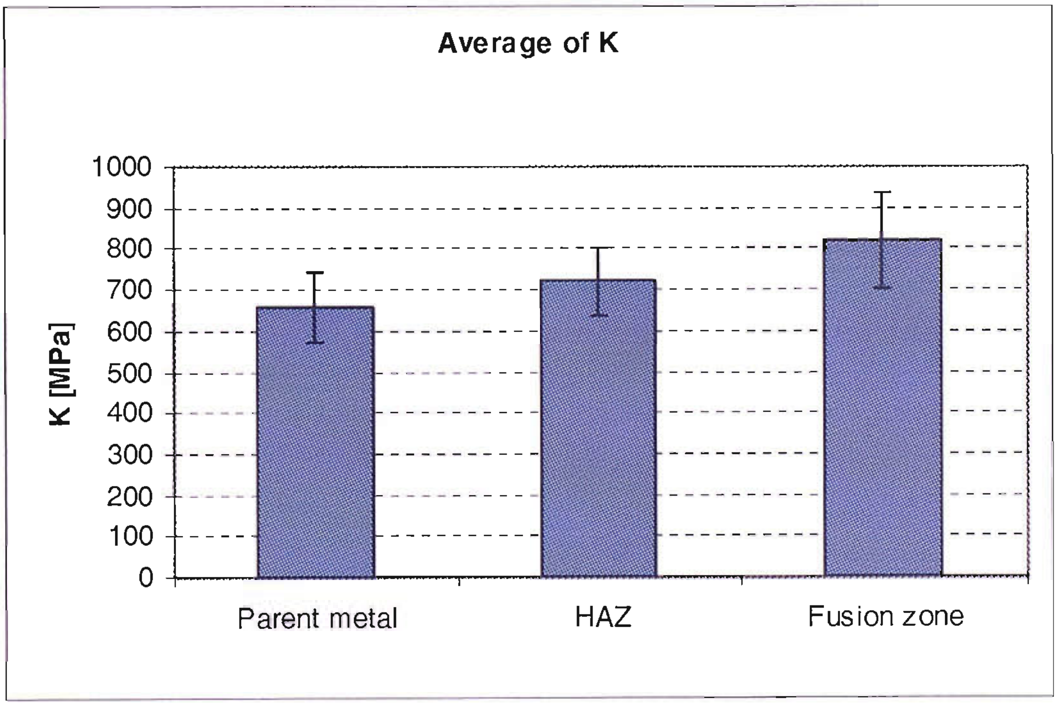

Fig. 6-49 Average values of the strength coefficient over the three weld regions.

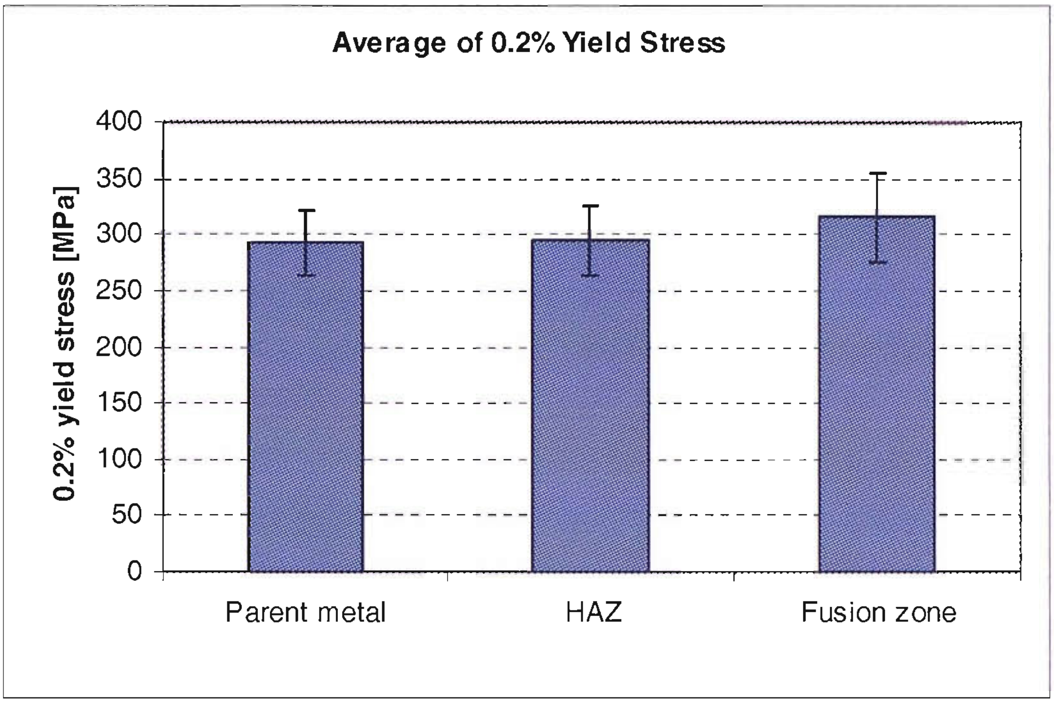

Fig. 6-50 Average values of the 0.2% yield stress over the three weld regions.

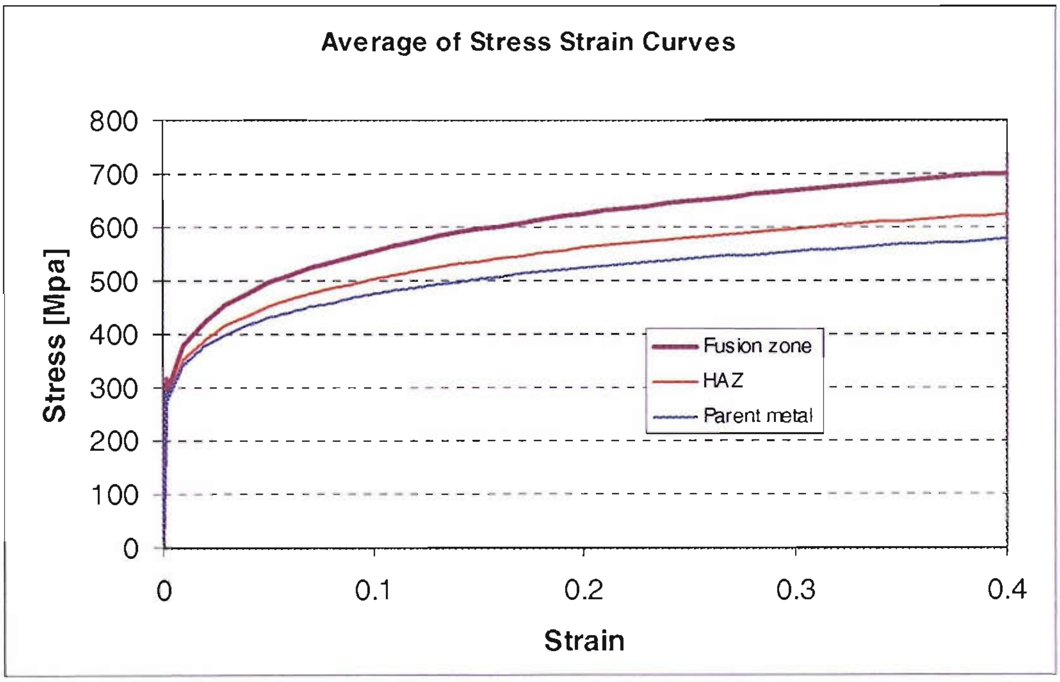

Fig. 6-51 Corresponding stress-strain curve for each region.

It can be observed from Table 6-4 and Fig. 6-47 to Fig. 6-50 that the trend in material properties variation across the various weld regions becomes clearer when the average values of the properties over each area (parent metal, HAZ and fusion zone) are calculated. These figures show that all properties follow a similar trend, that is, they increase from the parent metal towards the weld fusion zone. On average, hardness and strength coefficient show a more pronounced variation across the weld regions, whilst least variation was manifested for 0.2% yield stress and the strain hardening exponent. Interestingly, the average value of the 0.2% yield stress calculated for the parent metal was found to be 292 MPa with a standard deviation of 29.3 MPa, which tie up with the yield stress of 43A-grade steel plate, presented in Table 4-2, which ranges between 300 and 317 MPa as calculated from tensile testing.

Since the scatter in the individual results of n and K at every indent appears to be large, it was felt important to investigate the cause of such scatter in order to assess the sensitivity of these parameters. Two arbitrary pairs of adjacent points, which correspond to an abrupt change in the values of n and K were chosen, labelled (A and B) and (C and D) in Fig. 6-45. The percentage of the change in the values of H, $\sigma_{0.2}$, K, and n between the two adjacent points in each pair amounts to 12%, 20%, 30%, and 59% , respectively. Amongst the four parameters, the results for n and K appear to exhibit the higher scatter.

As a means of investigating the cause of such an effect, the raw load indentation data for the two points in a pair are compared, and so are the corresponding data after frame compliance calibration. This comparison can be made by referring to the graphs in Fig. 6-52 to Fig. 6-55

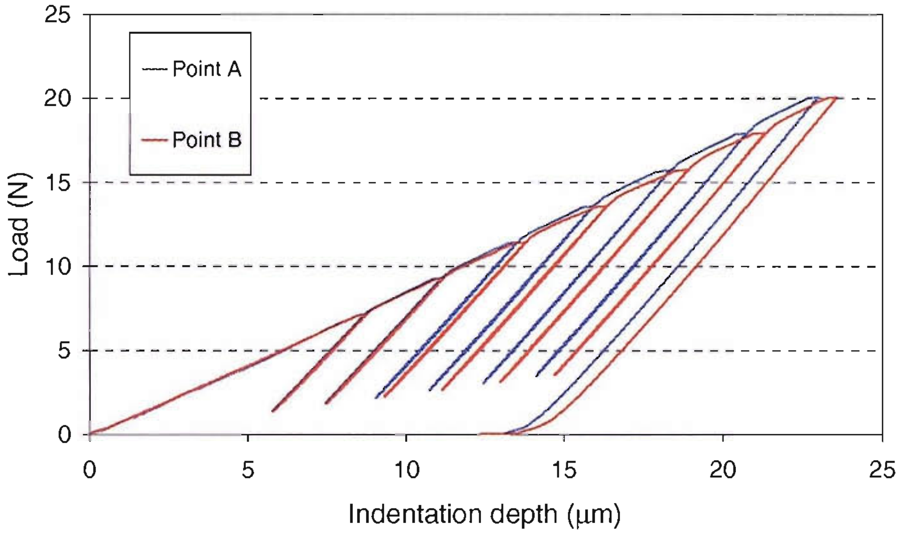

Fig. 6-52 Raw instrumented microhardness P-h data corresponding to locations identified by referring to Fig. 6-45 and Fig. 6-23.

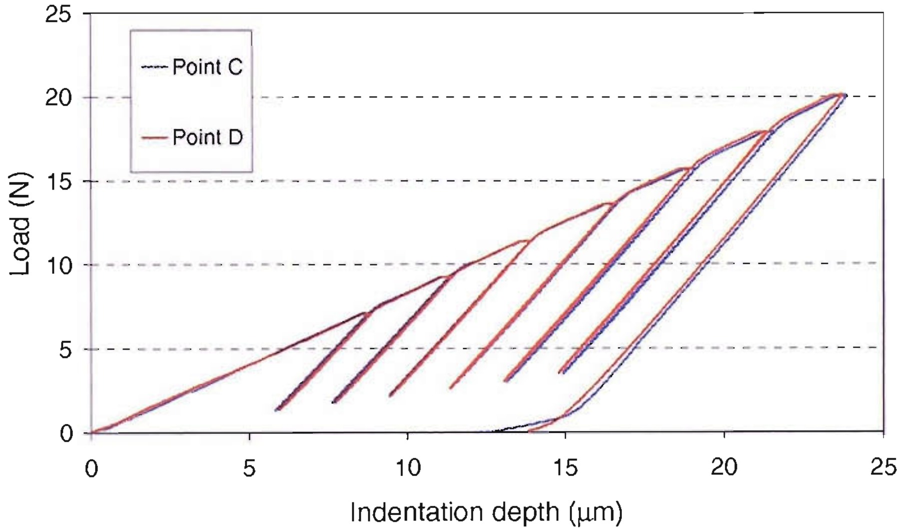

Fig. 6-53 Raw instrumented microhardness P-h data corresponding to locations identified by referring to Fig. 6-45 and Fig. 6-23.

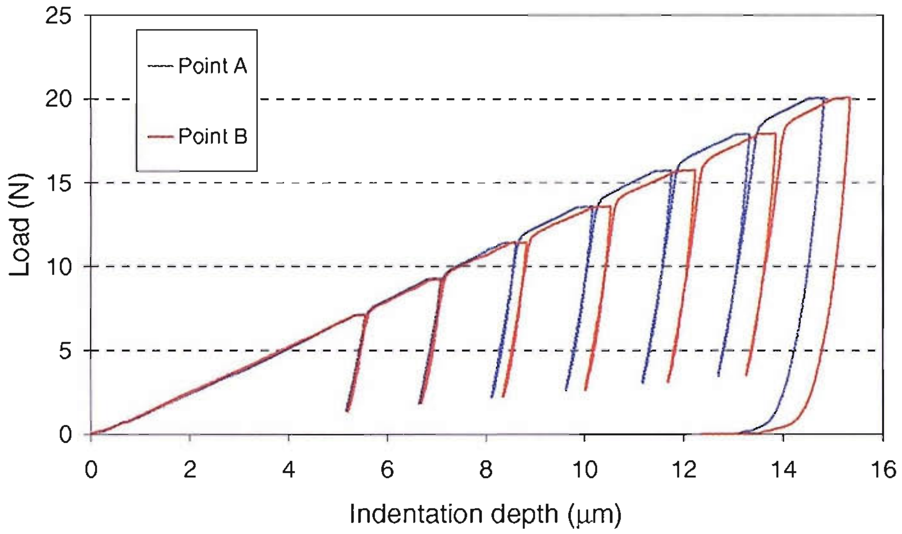

Fig. 6-54 *P-h* curves of Fig. 6-52 after frame compliance calibration.

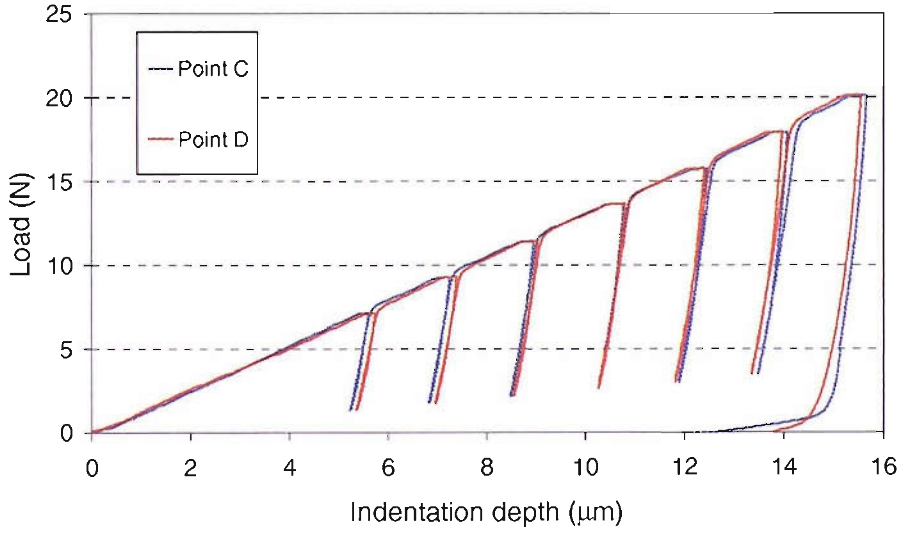

Fig. 6-55 *P-h* curves of Fig. 6-53 after frame compliance calibration.

As can be noted in Fig. 6-52 and Fig. 6-54, the *P-h* curves for points *A* and *B* are almost overlapping over the first two loading cycles, then they diverge with a difference in h_t of about 0.6 μm at the last cycle peak. The *P-h* curves in Fig. 6-53 and Fig. 6-55 look closer to each other over all the loading cycles. However, the curve corresponding to point *D* starts below that of point *C* over the first three cycles then it rises above it for the rest of the cycles. Comparing the hardness results from the two points of the pairs , the difference in the maximum total depth achieved at the last cycle of the two curves is the cause of different hardness measurement for points *A* and *B*. However, for points *C* and *D*, the difference in h_t for the last cycle is not of the same order as that for points *A* and *B* but there is a similar difference in hardness measurement. This is due to the indenter geometry deviating from the perfect sphere. Examining the resulting contact area considering the indenter average profile demonstrates a difference of the same order of magnitude as that for hardness. The corresponding true contact radii for the four points are plotted in Fig. 6-56.

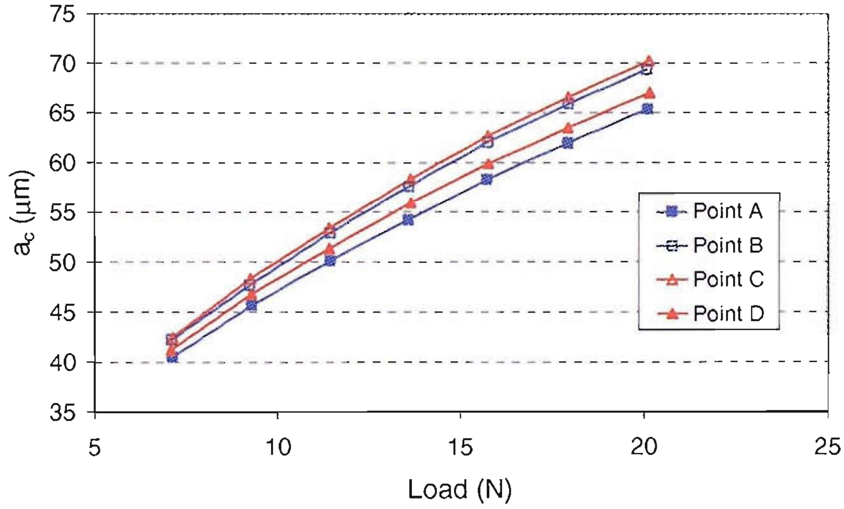

Fig. 6-56 Calculated contact radius vs. load corresponding to Points A, B, C and D.

Fig. 6-56 shows that there is a noticeable difference in the corresponding contact area values at the cycle peaks for the indentations at the four points even though the difference in h_t appears to be small.

The difference in hardness measurement, which amounts to 12%, is associated with only the last cycle peak. However, the estimate of *n* and *K* is dependent on the fitting of hardness vs. strain for all cycle peaks in an experiment, which are plotted for the four points in Fig. 6-57.

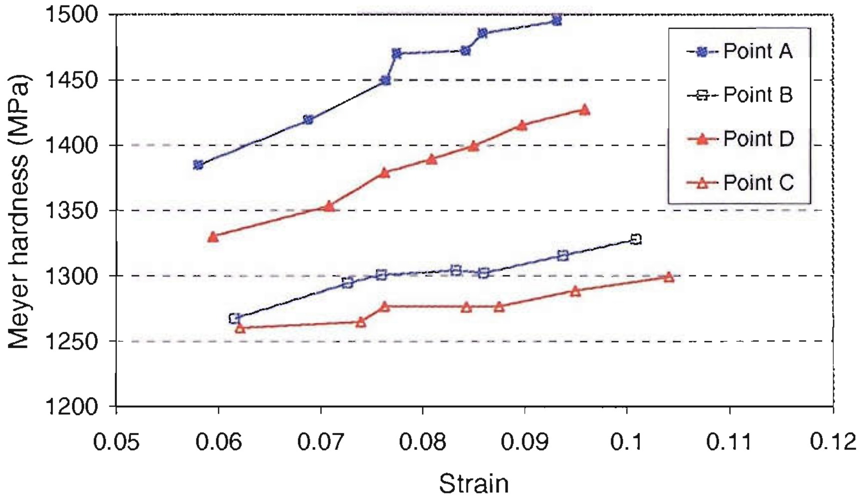

Fig. 6-57 Calculated Meyer hardness vs. strain corresponding to points A, B, C and *D*.

As can be seen in Fig. 6-57, hardness and strain values appear to be sensitive to the indenter profile. In fact, the indenter profile has an effect on both hardness and the characteristic strain when calculating *n* and *K*, that is, an increase in the contact area results in a decrease in the calculated hardness and an increase in the corresponding strain. Both of these effects work together in decreasing the resulting slope of the curve. This accounts for the large difference in the values of *n* and *K* for the two points in each pair even though the corresponding *P-h* curves look close to each other.

To show the effect of the indenter profile on the calculated strain, the characteristic strain is plotted vs. load for the four points in Fig. 6-58.

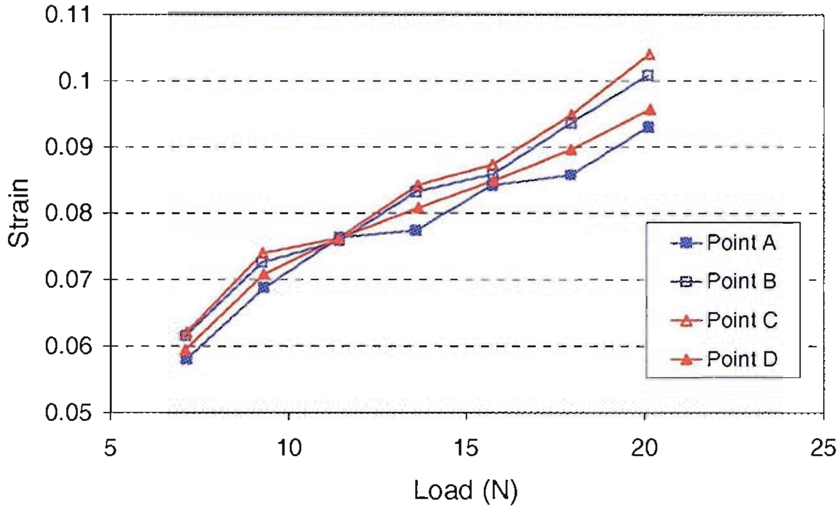

Fig. 6-58 Calculated strain vs. load corresponding to Points A, B, C and D.

Fig. 6-58 shows that the relative changes in the calculated strain values at the cycle peaks for the four points result in different slopes for the curves even though the positioning of these points on the *P-h* curves appears to be close.

The graphs in Fig. 6-56 to Fig. 6-58 show the marked sensitivity of the calculated values of *n* and *K* to the analysis results at the cycle peaks, which are in turn largely dependent on the description of the indenter profile. Hence, this key parameter should be determined as accurately as possible for a more realistic estimate of the material properties.

To eliminate any effects that could be caused by the proposed pile-up correction of the analysis technique for estimating *n* and *K*, the load indentation data were analysed using the characterisation method with the pile-up effect ignored. The resulting values for *n* from analysing the 4th row of spherical indents are plotted in Fig. 6-59. This row is the same row for which *n* measurements are shown in Fig. 6-45. The indents corresponding to the points *A*, *B* , *C* and *D* are also indicated in Fig. 6-59.

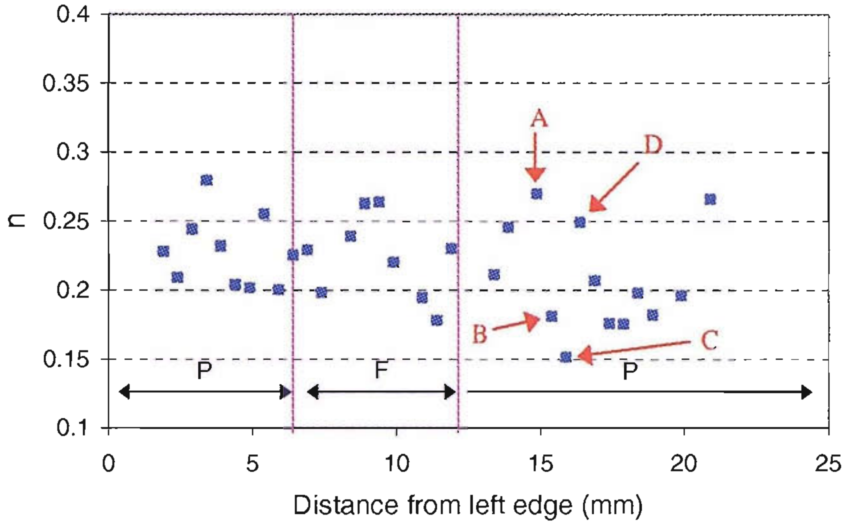

Fig. 6-59 The value of n corresponding to each indent in the fourth row of spherical indentations calculated using no pile-up correction.

As can be seen in Fig. 6-59, the calculated values for *n* even though they appear to increase as a result of ignoring the pile-up effect on the contact area, still manifest the same degree of scatter. Referring to the points *A*, *B* , *C* and *D* in Fig. 6-45 and Fig. 6-59, it is evident that the adjacent points in a pair still maintain almost the same difference in value. Thus, it is evident that such scatter is due to the characterisation of the indenter profile and the assumption of it being axi-symmetric.

CHAPTER 7

DISCUSSION AND FUTURE WORK

7.1 Summary

The idea of correlating the indentation pressure and geometry with the tensile stress-strain curve for the tested material was first proposed by Tabor [14]. The salient parameter in this correlation is the actual contact area. Several analytical approaches have been proposed to deduce the contact area from analysing the indentation data, which obviates the need for direct imaging of the residual indents and thus enables performing cyclic loading indentation with progressively higher peak load at one location, so as to obtain the stress-strain curve from these load cycles. Whilst the performance of these approaches was found reliable for hard materials, a large error arises for soft metals where pile-up dominates the behaviour of the material. This error is due to the nature of the basic assumptions of the analytical approaches. Correction expressions [18, 19, 58] have been proposed as a function of the strain hardening exponent, n, to predict pile-up. Hence, a prior knowledge of n is a prerequisite for these correction expressions to be incorporated in an analysis. In addition their applicability is valid only for relatively deep indentation when pile-up becomes steady with depth. Some approaches [95, 96] attempted, through empirical relations, to link the loading curve to the material plastic properties. Their functionality was limited by a prior knowledge of n. Furthermore, the loading curve could well include a strain rate effect especially in the case of soft metals which exhibit creep when the peak load is held constant for an adequate dwell time. Thus, the results obtained from this correlation could possibly be misleading.

In Chapter 3, the reliability of the instrument performance and analysis technique were assessed. In addition, a geometrical characterisation of the spherical indenter tip was introduced based on averaging the profiles of the indenter SEM micrographs. Since the indenter tip appeared to deviate from its intended spherical geometry, the variation of the effective radius on the average profile and gradient leading to the characteristic strain were defined. Three methods were followed in this characterisation process, namely local arc fitting, local linear fitting, and axi-symmetric circle fitting. The first method exhibited a large scatter and sensitivity to the fitted portion of the profile, whilst the latter two showed a rather smooth variation with negligible sensitivity to the fitted portion of the profile.

The instrument depth measurement and analysis capability were verified by comparing the Berkovich hardness values on a hard material derived by the instrument with those obtained from optical measurement of the same indents, and with the hardness values obtained using a conventional Vickers tester on the same sample. Good agreement was observed.

The effect of depth calibration and frame compliance factor on the analysis results were investigated. The reduced elasticity modulus was found to be noticeably more influenced by both calibration factors than hardness. The frame compliance, however, manifested a stronger effect on the analysis results than the depth calibration factor. In addition, the frame compliance was found to vary with load. It started at small values for shallow indentations, and then stabilised for deep indentations. This was believed to be a consequence of the tip rounding of the Berkovich indenter, which was assumed to be perfectly sharp in the analysis. This effect was also reported by Oliver and Pharr [37]. The function fitted to the unloading curve of indentation data by the Berkovich indenter and the effect of the unloading portion considered for fitting were investigated. Polynomial of 1st, 2nd , and 3rd order and a simple power law function were fitted and their performance was assessed. The power law function showed a much better and robust performance, and was insensitive to the portion of the unloading curve considered for fitting. It was also preferable over the polynomial in that it enables the estimate of the residual depth.

In chapter 4 an axisymmetric 2-D finite element model was developed, using ANSYS, and validated to simulate the elasto-plastic indentation behaviour of a spherical indenter, radius R=150 μm, on the test materials whose stress-strain curves were obtained from tensile testing. Due to high geometrical nonlinearity induced by deep indentation, the sample mesh was generated manually using PATRAN as it proved to be optimal to those produced by ANSYS, namely free mesh and mapped mesh. Mesh sensitivity was then carried out to ensure the capability of the adopted mesh with regards to accuracy and efficiency.

The FE model was first validated against the Sneddon's elastic solution of a sphere onto a flat surface. Then it was used to simulate the elasto-plastic response of indented idealised materials, that is, materials with similar stress-strain relations as those of the test materials, but whose post-yield curve can be described by a single power law function. The effects of various physical parameters and FE numerical controls were investigated. These included: the contact tolerance and contact stiffness, friction coefficient between indenter and specimen, and the elastic modulus of the diamond indenter. It was found that none of these parameters, within their range of variability and load range of application, had a noticeable effect on the simulated P-h curves. However, friction revealed a small difference on the P-h curves for loads of 40 N, which is double the limit of the instrument, whilst it showed a pronounced influence on the predicted pile-up, thus the contact area.

Time-dependent deformation, so-called creep, was also investigated. The experiment conditions influencing the creep were examined. It was found that loading rate and the hold/dwell time at peak load govern not only the extent of creep but also the initial contact stiffness, which agreed with the findings by Chudoba and Richter [104]. It was also noticed that the higher the loading rate, the larger the creep, thus a longer dwell time will be required to allow for this deformation to take place as long as the full load is not applied abruptly, i.e. in less than 10 s, which can affect the initial contact stiffness. Based on the experimental observations on the test materials, it was advised for practical purposes that a loading time of not less than 40 s followed by a dwell time of not less than 100 s should be adequate to account for the plastic-related deformation.

The FE model was finally validated versus the experimental data. The simulated P-h curves were compared with those obtained from indentation experiments using the spherical indenter, as characterised in Chapter 3, on the test materials. Indentation experiments were performed in progressively cyclic loading patterns and the peak load was held for a specified time to account for the effect of plastic-related behaviour. The points corresponding to the end of the creep plateau of the experimental *P-h* curves were compared with the FE prediction. Good agreement was observed.

In Chapter 5, the adopted FE model was used to simulate indentations by a perfect sphere, of 150 μm radius, on the idealised materials, whose stress-strain behaviour approximates that of the test materials. The FE capability was first assessed by verifying Tabor's relations between the stress-strain curve and the indentation parameters.

The friction coefficient proved to have a strong influence on the pile-up. A value of μ around 0.13 was considered best representing the real friction between the diamond indenter and the steel samples, and was adopted in subsequent FE analysis in this study. This value for μ falls within the range of values reported by Yurkov *et al* [105].

The FE simulated *P-h* data were treated as experiment data and analysed using initially Field and Swain's approach [45, 46]. The predicted n was noticeably overestimated whilst $\sigma_{0.2}$ was underestimated. The effectiveness of existing correction formulae accounting for the pile-up effect was examined. The assumption of these expressions that the pile-up parameter $c = a_c / a_0$ is constant throughout loading, was proved invalid by the FE simulation. These correction formulae failed to give a good estimate of n although they brought the predicted stress-strain curves closer to the original input. In addition, they require previous knowledge of n, which is clearly not known when the analysis is applied to unknown material. The corrected σ-ε curves by these expressions have the same value for n, but they differ on the K value thus $\sigma_{0.2}$.

An iterative process was proposed in this study to enable the application of any of the various pile-up correction formulae without the need for previous knowledge of n. This was based on the requirement that the input value of n should be equal to that obtained from the predicted stress-strain curve.

A modification to Hill's expression [58] presented in Eq. 5-2, which accounts for the development of the pile-up throughout loading, was proposed in this study. It has the form of multiplying the pile-up parameter c given by Hill's expression, by a factor. This factor was determined based on the observation of the dependence of the pile-up on the extent of plastic deformation, which can be considered directly linked to the ratio of the residual indentation to the total depth. The proposed empirical expression, based on the FE simulations, allowed a significant improvement to the accuracy of the predicted contact area, thus the true stress-strain curve.

In chapter 6, the proposed pile-up correction, derived from FE simulation, was integrated with characterisation analysis and employed in a complex iteration process to perform the frame compliance calibration on the raw load indentation data. It was then assessed on the experimental data of the test materials considering the indenter geometry characterisation in Chapter 3. The resulting σ–ε curve, which has no yield plateau, showed a good agreement with that from the tensile test. Although the predicted n was underestimated, the predicted curve was shown to behave as equivalent to that from the tensile test, and the accuracy of the prediction appeared to exceed that predicted by Herbert *et al.* [84], which is presented in Fig. 7-1.

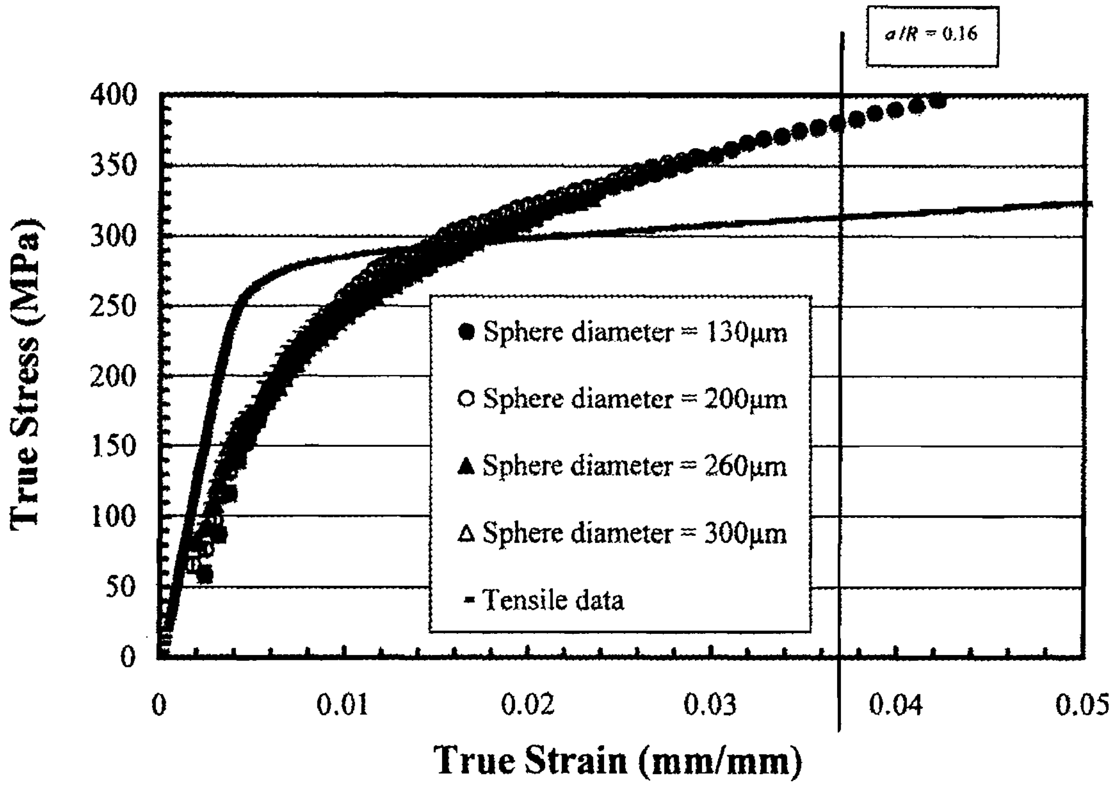

Fig. 7-1 Stress-strain curve of 6061-T6 as determined by uniaxial tension and spherical indentation analysis by Herbert *et al.* [84]

The characterisation of the indenter geometry and the characteristic strain were shown to have a noticeable influence on the analysis results. The characteristic strain defined as 20% of sin(β) was found to give a representative approximation of the $\sigma - \varepsilon$ curve.

The characterisation analysis modified with the correction technique proposed in this study was applied to indentations performed on a butt-welded joint. The indents were made on a micrometer scale to span various weld regions in order to obtain the variation of the elasto-plastic material properties across these regions. It was revealed that a trend of increasing value of H, $\sigma_{0.2}$, n, and K was noticed from the parent metal towards the weld fusion zone.

7.2 Contributions of this study

A geometrical characterisation model was proposed for an imperfect spherical indenter so that the indenter geometry could be incorporated in the indentation analysis formulae. It models the variation of curvature of the indenter at various vertical depths from the indenter tip, through defining the effective radius at these depths. This definition allows the analysis to represent the indenter response by an equivalent perfect spherical indenter at a certain depth. It was proposed that the effective radius should be obtained from axisymmetric arc fitting to the part of the indenter average profile bounded by the relevant depth. This was integrated by using the area function calculated from the indenter average profile and by defining the characteristic strain corresponding to the contact depth. It was proposed that the characteristic strain at a certain depth should be calculated as the sine of the slope angle obtained from local linear fitting to the relevant part of the indenter average profile.

A modification to Hill's expression [58] presented in Eq. 5-2, was proposed in this study to account for the development of pile-up at various load levels. This leads to a more accurate prediction of the actual contact area at various indentation depths and thus a better estimate of the true stress-strain curve. The modification was in the form of multiplying the pile-up parameter c given by Hill's expression by the correction expression proposed. This factor is a function of the residual indentation to the total depth ratio which is directly linked to the extent of plastic deformation imposed. The proposed empirical expression was based on FE simulations of three materials whose properties span a wide range of those encountered in structural steels. An important aspect of operating the correction proposed was the iterative algorithm, also developed in this study which obviates the need of prior knowledge of n, and thus it can be applied to any material whose true stress-strain curve can be described by a simple power law function. This algorithm was based on the requirement that the input value of n should be equal to that obtained from the predicted stress-strain curve.

In this study it proved essential, through numerical analysis, to consider the friction between the surfaces in contact in order to achieve more accurate modelling of the material response with regard to pile-up. A value of μ around 0.13 was considered best to represent the real friction coefficient between the diamond indenter and steel.

It was suggested that the frame compliance of the instrument does not have a constant value, rather it varies with load level. This could be due to the instrument configuration, experimental conditions, indenter imperfection and analysis approximations. Hence, its variation over a wide range of loads should be determined and incorporated in the analysis accordingly.

The resulting $\sigma - \varepsilon$ curve from an experiment has no yield plateau, thus its n could be underestimated depending on the extent of yield plateau exhibited in the curve from the tensile test. However, the predicted $\sigma - \varepsilon$ curve was shown to behave as equivalent to that from the tensile test.

7.3 Discussion

The precision of the analysis results depends largely on the accuracy of the indentation data produced by the instrument. This, in turn, is highly dependent on the reliability of the calibrations performed which then allow the time response of the material to be determined. Whilst load calibration is a straight forward and a reliable routine, material depth measurement is subject to more uncertainty. The depth calibration factor is calculated by indenting elastically a quartz sample by a relatively large hard ball, and is thus subject to experimental errors. More importantly, the frame compliance routine, which allows the true material deformation response to be extracted, is the most important calibration that can noticeable affect the material measurements recorded, and hence the analysis results. It is governed by the instrument configuration and the experimental conditions. For example, different indenter holders might well result in different values for the frame compliance. In addition, the resin, e.g. Bakelite, the specimen is embedded within will contribute to the frame compliance value. Therefore, the experiment conditions should be consistent with those present when the frame compliance calibration was performed. Furthermore, it was found that due to the instrument configuration, indenter imperfection and analysis approximations, the frame compliance does not have a constant value. Rather, it varies with load level. Hence, its variation over a wide range of loads should be incorporated into data analysis when testing unknown materials. The reference sample used for calibration should demonstrate an acceptable level of purity, homogeneity and isotropy. It is recommended that long experiments be avoided as the electronics calibration, i.e. the bridge box balance was noticed to drift over a long time (in excess of 8-12 hrs), which in return affects the accuracy of the acquired data. A bridge box test should be performed after each experiment to ensure its proper performance.

The geometry of the indenter is a key parameter in interpreting the load indentation data, and in the determination of frame compliance factor. An adequate level of accuracy in the determination of the effective radius of curvature and the characteristic strain at various vertical distances from the tip should be ensured in order to achieve a more accurate analysis. Due to the interdependent nature of the relationship between the indenter geometry and the analysis of the indentation data, it is necessary to characterise the indenter geometry of an imperfect sphere using other means independent of the indentation data. Relying solely on indentation testing to determine the geometric characterisation of an imperfect spherical indenter is more likely to be misleading since other factors relating to the analysis method, numerical fitting, and the specimen crystal structure will interfere. As far as perfect spherical geometry is concerned, making a spherical indenter from diamond leads to inevitable geometrical imperfection due to the crystal structure of diamond, whilst other materials such as sapphire can be a better option, and should be considered.

The most important objective of analysing the load-indentation data is the estimate of the true contact area since it is the key quantity in hardness and modulus determination. Whilst this quantity is intrinsically underestimated by the available analysis approaches for piling-up metals, the proposed formula in this study accounts not only for the pile-up effect but also for its development during loading unlike the other existing correction expressions [18, 19, 58] discussed in Section 5.2.2, leading to a good estimate of the stress-strain curve that serves as an equivalent to that from the tensile test. The reason for the inaccurate prediction of n and $\sigma_{0.2}$ by the existing correction expressions [18, 19, 58] can be attributed to the fact that they were fitted to indentation data corresponding to fairly large depth values (large characteristic strains) at which the simulated pile-up parameter c was shown, by FE simulation, to stabilise towards a constant value. On the other hand, the correction proposed in this study accounts for the variability of c for various indentation depths. The basis, assumptions, and limitation of the proposed formula are explained as follows:

The empirical relation Eq. 5-8 was derived based on only three idealised materials. However, these materials were chosen to cover the commonly encountered properties of the weldable structural steel. The strain hardening exponent was equal to 0.132, 0.19 and 0.25, whilst the corresponding values of 0.2% proof stress were 375, 250, 285 MPa. The applicability of Eq. 5-8 is valid only during the full plastic stage when plastic strains enclose the indentation perimeter, as it assumes a constant value for the constraint factor C. This results in limiting the smallest value of the predicted strain, which is larger than the yield strain. The derived stress-strain curve is defined by the determination of both n and K which are obtained from logarithmic fitting to the Meyer hardness vs. characteristic strain curve. The 0.2% proof stress, $\sigma_{0.2}$, is determined from extrapolating the predicted σ-ε curve to the yield strain, Eq. 2-81. This proposed formula, together with all other existing approaches, cannot predict the yield plateau in the $\sigma - \varepsilon$ curve.

On testing the various regions of a butt-welded joint, the Meyer hardness showed a relatively smooth variation across the weld regions agreeing with that determined by the conventional Vickers hardness test. Its values increased from the parent metal towards the centre of the fusion zone. The other plastic parameters of the derived σ-ε curve, which are $\sigma_{0.2}$, K, and n exhibited a larger scatter, the value of which increased in the same order (the scatter in the values of n was larger than that of K). The scatter, especially for the values of n was proved to be not a direct consequence of the performance of the new analysis technique. Other factors thought to be the reason for such scatter are:

- Weakness in the characterisation of the indenter profile and the definition of the characteristic strain for an imperfect spherical indenter.

- The assumption that the indenter is axisymmetric while it is clearly not, especially when it is made from diamond.
- The variation in material properties which reflect the change in the material crystal structure, in addition to the material inhomogeneity and anisotropy on the micro scale.
- Material imperfections such as the density of the grain boundaries and dislocations confined in the plastic indentation zone beneath the indenter. At different cycle peak levels, different volumes of material are included in this zone, thus different densities of grain boundaries, dislocations, and variation in the crystal structure will influence the results.

Hardness testing involves local measurement of material properties, hence variation in the structures on the material surface is expected to result in different properties. In addition, this variation is more likely to exist with depth as well, especially in the HAZ and fusion zone where more irregularity in the crystal structure may occur due to the welding process, impurities, and imperfection of the weld. Thus, a larger scatter in this region is thought to arise as a result.

When comparison is made between the derived stress-strain curve and that obtained from the tensile test, the fundamental differences of these two testing methods should be borne in mind. This can justify the differences in shape whilst both can be equivalent to each other. Tensile testing is a displacement controlled static test through which the material undergoes a uniform stress field that gradually increases with load in a smooth transition from linear elastic to the elasto-plastic stage. The resulting curve represents the average behaviour of the whole material in the specimen. On the other hand, indentation testing, as previously stated elsewhere, is load controlled and implies the application of a high strain rate. The strain field beneath the indenter changes in a steep gradient in both directions, the plane of the surface and the indentation depth, hence the response of the material under such conditions can differ from that in a tensile test. Indentation testing also reflects an average response of the crystals enclosed within the indentation zone, hence the more crystals enclosed beneath the indenter, the more representative the indentation data of that localised region of the material.

The stress-strain curve determined for every indent as a result of analysing the corresponding *P-h* curves is considered to model the material at that location whose representative area is taken proportional to the spacing between indents. These locally measured data at the indent positions across the weld regions are considered to reflect the variation in the crystal structure. Consequently, for a more realistic FE simulation of the behaviour of a welded joint, these data can be input into the model as different materials comprising the joint. Through meshing procedure, the area of the welded joint is divided into as many sub-areas as the number of indents. Each of these areas is assigned material properties obtained from indentation performed at that area.

Averaging the material properties across the various weld regions showed a clear trend, that is the average values increase from the parent metal towards the fusion zone. The variation was more pronounced for hardness and strength coefficient measurements than for the 0.2%yield stress and strain hardening exponent.

7.4 Conclusions

The extent of meeting the objectives set in this study is summarised below:

- The performance of the instrumented micro indentation tester was confirmed as reliable.
- An FE model was developed and validated to accurately simulate the material response during indentation, which was then employed to link the pile-up to the *P-h* curves through an empirical relation.
- An iterative procedure is suggested in this study to enable the application of a correction expression as a function of n when n is not known.
- Established analysis approaches and their limitation to hard materials that do not pileup were highlighted. In addition, assessing the existing corrections for the pile-up effect showed their inability to account for the development of pile-up in the case of indentation with a spherical indenter.
- The correction proposed in this study to account for pile-up, which was derived from FE simulation, was assessed through application to experimental data from the

provided test materials. Satisfactory agreement was observed between the predicted $\sigma - \varepsilon$ curve and that from the tensile test.

- Indentation testing was carried out on the cross sectional area of a butt-welded joint. Indentation data were analysed for every indent resulting in a stress-strain curve corresponding to the location of the indent. Variation in the measured material properties was noticed across the weld regions. These data can be used as material input into an FE model of the whole welded joint to simulate its behaviour under different loading conditions. By this provision of a more realistic description of the material comprising the joint, a more accurate response of the joint can be predicted.

7.5 Future work

- Manufacturing stiffer indentation instruments with small frame compliance so as to decrease the contribution of the frame deformation to indentation depth measured. This can be attained by using more rigid holders for specimen and indenter with stiffer material, and also by placing the depth measurement mechanism as close to the indenter tip as possible to minimise the effect of the indenter holder deformation on the depth measured.
- Devising other means for determining the frame compliance and depth calibrations that do not rely on indentation experiments of reference specimens. The method currently used for calibration makes the accuracy of the obtained calibration factors sensitive to the correctness of the indentation analysis adopted and the perfectness of the indenter geometry. Depth measurement calibration can be achieved by making the indenter slide on a plane normal to the indentation direction with a step of a pre-specified depth so as to perform depth calibration against the step depth. Although this has recently been applied by MicroMaterials for calibrating the nanoindentation instrument, it has not been extended yet to the microindentation instrument as the indenter is unable to move sideways. Laser capabilities can be utilised to measure the indenter tip movement into the test specimen relative to its surface, which should provide a more accurate means of indentation depth measurement and would obviate the need for the frame compliance calibration. Although employing such technology will add to the instrument cost, on the other hand, indentation data obtained will be

more accurate since their measurement is independent of both the analysis of the indentation data and the indenter geometry.

- Machining the spherical indenters from materials other than diamond. The crystal structure of diamond in addition to its great hardness makes it impossible to obtain a perfect sphere for an indenter on a micro-scale. Other materials such as sapphire can be a better option than diamond and should be considered.
- More research is required on cost-effective methods for a more representative geometrical characterisation of imperfect spherical indenters, especially as it is erroneous to describe the available indenter by an equivalent sphere as the indenter deviates noticeably from its intended geometry. This can be achieved using high-resolution optical scanning (non-contacting) measurement or by direct contacting means that scan the indenter surface with a stylus. The geometrical characterisation model should describe the indenter as a function of the vertical depth from its tip.
- Verifying the proposed formula in this study by applying it to indentation data from other test materials of various properties and tendencies for piling up, and at different depth levels within the full plastic regime.
- More research is required to describe the material behaviour during the transition stage of indentation (from elastic to full plastic), and extend the proposed correction formula to predict the material stress-strain curve over this region (small strains) so as to capture the yield stress. This will necessitate elaborate study on the determination of the constraint factor *C* which is no longer constant during this stage, as it is a function of various material properties and indenter geometry.
- More research is required on relating the yield plateau of a material to the load indentation data in a scheme to predict the extent of the yield plateau. This will allow a more accurate stress-strain curve to be deduced which will be closer to that derived from a tensile test. FE analysis can be a useful tool to model the indentation of various isotropic materials whose properties cover a wide range.

REFERENCES

1. Butler, L.J. and G.L. Kulak, *Strength of fillet welds as a function of direction of load.* Weld J (NY), 1971. **50**(5): p. 231s-4s.
2. Kato, B. and K. Morita, *Strength of transverse fillet welded joints.* Weld J (Fla), 1974. **53**(2): p. 59-s - 64-s.
3. Kamtekar, A.G., *New analysis of the strength of some simple fillet welded connections.* Journal of Constructional Steel Research, 1982. **2**(2): p. 33-45.
4. Kennedy, D.J.L. and G.J. Kriviak, *The strength of fillet welds under longitudinal and transverse- shear - a paradox.* Canadian Journal of Civil Engineering, 1985. **12**(1): p. 226-231.
5. Kamtekar, A.G., *The strength of inclined fillet welds.* Journal of Constructional Steel Research, 1987. **7**(1): p. 43-54.
6. Kamtekar, A.G., *Strength of planar fillet weld groups subjected to an eccentric shearing force in their planes.* Journal of Constructional Steel Research, 1987. **7**(3): p. 155-187.
7. Miazga, G.S. and D.J.L. Kennedy, *Behavior of Fillet Welds as a Function of the Angle of Loading.* Canadian Journal of Civil Engineering, 1989. **16**(4): p. 583-599.
8. Mellor, B.G., R.C.T. Rainey, and N.E. Kirk, *The static strength of end and T fillet weld connections.* Materials & Design, 1999. **20**(4): p. 193-205.
9. Hou, K.H. and W.A. Baeslack, III, *Characterization of the heat-affected zone in gas tungsten arc welded aluminium alloy 2195-T8.* Journal of Materials Science Letters, 1996. **15**(3): p. 239-244.
10. Zhu, Y.H., *Microstructural changes in welded Zn-Al alloy.* Journal of Materials Research, 1996. **11**(3): p. 593-598.
11. Lancaster, J.F., *Metallurgy of Welding.* 1980, London: George Allen and Unwin.
12. Doerner, M.F. and W.D. Nix, *A method for interpreting the data from depth-sensing indentation instruments.* Journal of Materials Research, 1986. **1**(4): p. 601-609.
13. Sneddon, I.N., *The relation between load penetration in the axisymmetric Boussinesq problem for a punch of arbitrary profile.* International Journal of Engineering Science, 1965. **3**(47): p. 47-57.
14. Tabor, D., *A simple theory of static and dynamic hardness.* Proceedings, Royal Society of London, Series A: Mathematical and Physical Sciences, 1948. **192**: p. 247-274.
15. Pharr, G.M., W.C. Oliver, and F.R. Brotzen, *On the Generality of the Relationship among Contact Stiffness, Contact Area, and Elastic-Modulus During Indentation.* Journal of Materials Research, 1992. **7**(3): p. 613-617.
16. Bolshakov, A., W.C. Oliver, and G.M. Pharr, *Influences of stress on the measurement of mechanical properties using nanoindentation .2. Finite element simulations.* Journal of Materials Research, 1996. **11**(3): p. 760-768.
17. Hill, R., *On a class of constitutive relations for nonlinear infinitesimal elasticity.* Journal of the Mechanics and Physics of Solids, 1987. **35**(5): p. 565-576.

18. Matthews, J.R., *Indentation Hardness and Hot Pressing.* Acta Metallurgica, 1980. **28**(3): p. 311-318.
19. Taljat, B., T. Zacharia, and F. Kosel, *New analytical procedure to determine stress-strain curve from spherical indentation data.* International Journal of Solids and Structures, 1998. **35**(33): p. 4411-4426.
20. Meyer, E., Zeits. d. Vereines Deutsch. Ingenieure, 1908. **52**(645): p. 740.
21. Bulychev, S.I., V.P. Alekhin, M.K. Shorshorov, A.P. Ternovskii, and G.D. Shnyrev, *Determining Young's Modulus from the Indentor Penetration Diagram.* Ind Lab (USSR), 1975. **41**(9): p. 1409-1412.
22. Blau, P.J., J.R. Keiser, and R.L. Jackson, *A Comparison of 3 Microindentation Hardness Scales at Low and Ultralow Loads.* Materials Characterization, 1993. **30**(4): p. 287-293.
23. Berkovich, E.S., *Three-faceted diamond pyramid for micro-hardness testing.* International Diamond Review, 1951. **11**: p. 129-132.
24. Hertz, H., *Uber die Beruhrung fester elastischer Korper (On the contact of elastic solids).* J. reine und angewandte Mathematik, 1882. **92**: p. 156-171.
25. Boussinesq, *Application des Potentiels a l'etude de equilibre et du mouvement des solides eslastique.* 1885, Paris: Gauthier-Villars.
26. Johnson, K.L., *Contact mechanics.* 1985, Cambridge: Cambridge University Press.
27. Ishlinsky, A.J., *Axisymmetric plastic flow in the Brinell test.* Journal of Applied Mathematics and Mechanics, 1944. **8**(233).
28. Tabor, D., *The Hardness of Metals.* 1951, Oxford: Clarendon Press.
29. Johnson, K.L., *The correlation of the indentation experiments.* Journal of the Mechanics and Physics of Solids, 1970. **v 18**(2): p. 115-126.
30. Prandtl, L., *Über die Härte plastischer Körper.* Nachr. d. Gesellschaft d. Wissensch. zu Gottingen, Math. Phys. Klass, 1920. **74-85**.
31. Hencky, H., *Concerning a few statically determinant cases in plastic bodies.* Zeitschrift Fur Angewandte Mathematik Und Mechanik, 1923. **3**.
32. Hill, R., E.H. Lee, and S.J. Tupper, *Theory of Wedge Indentation.* Proceedings, Royal Society of London, Series A: Mathematical and Physical Sciences, 1947. **188**: p. 273.
33. Hill, R., *The mathematical theory of plasticity.* 1950, Oxford: Clarendon Press.
34. Hirst, W. and M.G.J.W. Howse, *Indentation of Materials by Wedges.* Proceedings, Royal Society of London, Series A: Mathematical and Physical Sciences, 1969. **311**: p. 429-444.
35. Marsh, D.M., *Plastic flow in glass.* Proceedings of the Royal Society of London Series A: Mathematical Physical and Engineering Sciences, 1964. **279**(420).
36. Stilwell, N.A. and D. Tabor, *Elastic recovery of conical indentation.* Proceedings of the Physical Society of London, 1961. **78**(2): p. 169-179.
37. Oliver, W.C. and G.M. Pharr, *An Improved Technique for Determining Hardness and Elastic- Modulus Using Load and Displacement Sensing Indentation Experiments.* Journal of Materials Research, 1992. **7**(6): p. 1564-1583.
38. King, R.B., *Elastic analysis of some punch problems for a layered medium.* Int. J. Solids Structures, 1987. **23**(12): p. 1657-1664.
39. Fischer-Cripps, A.C., *A review of analysis methods for sub-micron indentation testing.* Vacuum, 2000. **58**(4): p. 569-585.

---

40. Fischer-Cripps, A.C., A. Bendeli, T.J. Bell, J.S. Field, and A.K. Jamting, *Methods of correction for analysis of depth-sensing indentation test data for spherical indenters.* Journal of Materials Research, 2001. **16**(8): p. 2244-2250.
41. Fischer-Cripps, A.C., *Simulation of sub-micron indentation tests with spherical and Berkovich indenters.* Journal of Materials Research, 2001. **16**(7): p. 2149-2157.
42. Hay, J.C., A. Bolshakov, and G.M. Pharr, *A critical examination of the fundamental relations used in the analysis of nanoindentation data.* Journal of Materials Research, 1999. **14**(6): p. 2296-2305.
43. Oliver, W.C., *Alternative technique for analyzing instrumented indentation data.* Journal of Materials Research, 2001. **16**(11): p. 3202-3206.
44. Malzbender, J., G. de With, and J. den Toonder, *The P-h(2) relationship in indentation.* Journal of Materials Research, 2000. **15**(5): p. 1209-1212.
45. Field, J.S. and M.V. Swain, *A Simple Predictive Model for Spherical Indentation.* Journal of Materials Research, 1993. **8**(2): p. 297-306.
46. Field, J.S. and M.V. Swain, *Determining the Mechanical-Properties of Small Volumes of Material from Submicrometer Spherical Indentations.* Journal of Materials Research, 1995. **10**(1): p. 101-112.
47. Goodman, L.E. and L.M. Keer, *The contact stress problem for an elastic sphere indenting an elastic cavity.* International Journal of Solids and Structures, 1965. **1**: p. 407-415.
48. Fischer-Cripps, A.C., *The hertzian contact surface.* Journal of Materials Science, 1999. **34**(1): p. 129-137.
49. Fischer-Cripps, A.C., *Use of combined elastic modulus in the analysis of depth-sensing indentation data.* Journal of Materials Research, 2001. **16**(11): p. 3050-3052.
50. Fischer-Cripps, A.C., *Elastic-plastic behaviour in materials loaded with a spherical indenter.* Journal of Materials Science, 1997. **32**(3): p. 727-736.
51. Fischer-Cripps, A.C., *Study of analysis methods of depth-sensing indentation test data for spherical indenters.* Journal of Materials Research, 2001. **16**(6): p. 1579-1584.
52. Hay, J.L. and P.J. Wolff, *Small correction required when applying the Hertzian contact model to instrumented indentation data.* Journal of Materials Research, 2001. **16**(5): p. 1280-1286.
53. Cheng, Y.T. and C.M. Cheng, *Effects of 'sinking in' and 'piling up' on estimating the contact area under load in indentation.* Philosophical Magazine Letters, 1998. **78**(2): p. 115-120.
54. Bolshakov, A., W.C. Oliver, and G.M. Pharr, *Finite element studies of the influence of pile-up on the analysis of nanoindentation data.* Materials Research Society Symposium Proceedings, 1996. **436**.
55. Pharr, G.M., *Measurement of mechanical properties by ultra-low load indentation.* Materials Science and Engineering a-Structural Materials Properties Microstructure and Processing, 1998. **253**(1-2): p. 151-159.
56. Norbury, A.L. and T. Samuel, *The recovery and sinking-in or piling-up of material in the Brinell test, and the effects of these factors on the correlation of the Brinell with certain other hardness tests.* Journal of the Iron and Steel Institute, 1928. **17**: p. 673-678.

57. Richmond, O., H.L. Morrison, and M.L. Devenpeck, *Sphere Indentation with Application to the Brinell Hardness Test.* Int J Mech Sci, 1974. **16**(1): p. 75-82.
58. Hill, R., B. Storakers, and A.B. Zdunek, *A Theoretical-Study of the Brinell Hardness Test.* Proceedings of the Royal Society of London Series A: Mathematical Physical and Engineering Sciences, 1989. **423**(1865): p. 301-330.
59. Alcala, J., A.C. Barone, and M. Anglada, *The influence of plastic hardening on surface deformation modes around vickers and spherical indents.* Acta Materialia, 2000. **48**(13): p. 3451-3464.
60. Dieter, J., *Mechanical Metallurgy.* 1961, London: McGraw-Hill. 245.
61. Atkins, A.G. and D. Tabor, *Plastic indentation in metals with cones.* Journal of the Mechanics and Physics of Solids, 1965. **13**: p. 149-164.
62. Devenpeck M.l. and Weinstein A.S., *Experimental Investigation of Workhardening Effects in Wedge Flattening with Relation to Nonhardening Theory.* Journal of the Mechanics and Physics of Solids, 1970. **18**(3): p. 213-232.
63. Cahoon, J.R., W.H. Broughton, and A.R. Kutzak, *The Determination of Yield Strength From Hardness Measurements.* Metallurgical Transactions, 1971. **2**(7): p. 1979-1983.
64. George, R.A., S. Dinda, and A.S. Kasper, *Estimating yield strength from hardness data.* Metal Progress, 1976. **109**(5): p. 30-33.
65. Haggag, F.M., J.A. Wang, M.A. Sokolov, and K.L. Murty, *Use of portable/in situ Stress-Strain Microprobe system to measure stress-strain behavior and damage in metallic materials and structures.* ASTM Special Technical Publication, 1997. **1318**: p. 85-98.
66. Haggag, F.M. and K.L. Murty, *Novel stress-strain microprobe for nondestructive evaluation of mechanical properties of materials.* Proceedings of the TMS Fall Meeting, 1996: p. 101-106.
67. Haggag, F.M. and G.E.C. Bell, *Measurement of yield strength and flow properties in spot welds and their HAZs at various strain rates.* International Trends In Welding Science And Technology, 1993: p. 629-635.
68. Byun, T.S., J.H. Hong, F.M. Haggag, K. Farrell, and E.H. Lee, *Measurement of through-the-thickness variations of mechanical properties in SA508 Gr.3 pressure vessel steels using ball indentation test technique.* International Journal of Pressure Vessels and Piping, 1997. **74**(3): p. 231-238.
69. Murty, K.L., M.D. Mathew, Y. Wang, V.N. Shah, and F.M. Haggag, *Nondestructive determination of tensile properties and fracture toughness of cold worked A36 steel.* International Journal of Pressure Vessels and Piping, 1998. **75**(11): p. 831-840.
70. Murty, K.L., M.D. Mathew, Y. Wang, and F.M. Haggag, *Deformation characteristics of Sn5%Sb solder alloy.* TMS Annual Meeting, 1998: p. 145-152.
71. Murty, K.L., P.Q. Miraglia, M.D. Mathew, V.N. Shah, and F.M. Haggag, *Characterization of gradients in mechanical properties of SA- 533B steel welds using ball indentation.* International Journal of Pressure Vessels and Piping, 1999. **76**(6): p. 361-369.
72. Murty, K.L., F.M. Haggag, and R.K. Mahidhara, *Tensile, creep, and ABI tests on Sn5%Sb solder for mechanical property evaluation.* Journal of Electronic Materials, 1997. **26**(7): p. 839-846.

---

73. Sinclair, G.B., P.S. Follansbee, and K.L. Johnson, *Quasi-Static Normal Indentation of an Elasto-Plastic Half-Space by a Rigid Sphere .2. Results.* International Journal of Solids and Structures, 1985. **21**(8): p. 865-888.
74. Au, P., G.E. Lucas, J.W. Sheckherd, and G.R. Odette, *Flow property measurements from instrumented hardness tests.* Nondestructive Evaluation In The Nuclear Industry, 1981: p. 597-610.
75. Francis, H.A., *Phenomenological Analysis of Plastic Spherical Indentation.* Trans. ASME, 1976. **98**: p. 272-281.
76. Lucas, G.E. and F.M. Haggag, *Determination of Luders Strains and Flow Properties in Steels from Hardness/Microhardness Tests.* Metallurgical Transactions A (Physical Metallurgy and Materials Science), 1983. **14A**(8): p. 1607-1613.
77. Haggag, F.M., *Application of flow properties to evaluate gradients in weldment properties.* International Trends In Welding Science And Technology., 1993: p. 629-635.
78. Haggag, F.M., *In-situ measurements of mechanical properties using novel automated ball indentation system.* ASTM Special Technical Publication, 1993. **1204**: p. 27-44.
79. Haggag, F.M., R.K. Nanstad, and D.N. Braski, *Structural integrity evaluation based on an innovative field indentation microprobe.* American Society of Mechanical Engineers, Pressure Vessels and Piping Division (Publication) PVP, 1989. **170**: p. 101-107.
80. Haggag, F.M., W.L. Server, G.E. Lucas, G.R. Odette, and J.W. Sheckherd, *Use of minaturized tests to predict flow properties and estimate fracture toughness in deformed steel plates.* Journal of Testing & Evaluation, 1990. **18**(1): p. 62-69.
81. Haggag, F.M., R.K. Nanstad, J.T. Hutton, D.L. Thomas, and R.L. Swain, *Use of automated ball indentation testing to measure flow properties and estimate fracture toughness in metallic materials.* ASTM Special Technical Publication, 1990. **1092**: p. 188-208.
82. Haggag, F.M., H. Wong, D.J. Alexander, and R.K. Nanstad, *The Use of Field Indentation Microprobe in Measuring Mechanical Properties of Welds.* Proceedings of the 2nd International Conference on Trends in Welding Research, 1990: p. 843-849.
83. Tirupataiah, Y. and G. Sundararajan, *On the Constraint Factor Associated with the Indentation of Work-Hardening Materials with a Spherical Ball.* Metallurgical Transactions a-Physical Metallurgy and Materials Science, 1991. **22**(10): p. 2375-2384.
84. Herbert, E.G., G.M. Pharr, W.C. Oliver, B.N. Lucas, and J.L. Hay, *On the measurement of stress-strain curves by spherical indentation.* Thin Solid Films, 2001. **398-399**: p. 331-335.
85. Mesarovic, S.D. and N.A. Fleck, *Spherical indentation of elastic-plastic solids.* Proceedings of the Royal Society of London Series a- Mathematical Physical and Engineering Sciences, 1999. **455**: p. 2707-2728.
86. Jayaraman, S., G.T. Hahn, W.C. Oliver, and P.C. Bastias, *Determination of monotonic stress-strain curve of hard materials from ultra-low-load indentation tests.* International Journal of Solids and Structures, 1998. **35**(5-6): p. 365-381.

87. Giannakopoulos, A.E. and P.L. Larsson, *Analysis of pyramid indentation of pressure-sensitive hard metals and ceramics.* Mechanics of Materials, 1997. **25**(1): p. 1-35.
88. Giannakopoulos, A.E., *Total deformation, plane-strain contact analysis of macroscopically homogeneous, compositionally graded materials with constant power-law strain hardening.* Journal of Applied Mechanics-Transactions of the Asme, 1997. **64**(4): p. 853-860.
89. Suresh, S., M. Olsson, A.E. Giannakopoulos, N.P. Padture, and J. Jitcharoen, *Engineering the resistance to sliding-contact damage through controlled gradients in elastic properties at contact surfaces.* Acta Materialia, 1999. **47**(14): p. 3915-3926.
90. Venkatesh, T.A., K.J. Van Vliet, A.E. Giannakopoulos, and S. Suresh, *Determination of elasto-plastic properties by instrumented sharp indentation: Guidelines for property extraction.* Scripta Materialia, 2000. **42**(9): p. 833-839.
91. Vaidyanathan, R., M. Dao, G. Ravichandran, and S. Suresh, *Study of mechanical deformation in bulk metallic glass through instrumented indentation.* Acta Materialia, 2001. **49**(18): p. 3781-3789.
92. Chollacoop, N., M. Dao, and S. Suresh, *Depth-sensing instrumented indentation with dual sharp indenters.* Acta Materialia, 2003. **51**(13): p. 3713-3729.
93. Xu, Z.H. and D. Rowcliffe, *Method to determine the plastic properties of bulk materials by nanoindentation.* Philosophical Magazine a-Physics of Condensed Matter Structure Defects and Mechanical Properties, 2002. **82**(10): p. 1893-1901.
94. Taljat, B., *Determining Stress-Strain Curves of Metals by Nondestructive continous Ball-Indentation methods*, in *Ph.D thesis*. 1996, University of Ljubljana: Slovenia.
95. Nayebi, A., R. El Abdi, O. Bartier, and G. Mauvoisin, *New procedure to determine steel mechanical parameters from the spherical indentation technique.* Mechanics of Materials, 2002. **34**(4): p. 243-254.
96. Cao, Y.P. and J. Lu, *A new method to extract the plastic properties of metal materials from an instrumented spherical indentation loading curve.* Acta Materialia, 2004. **52**(13): p. 4023-4032.
97. Dao, M., N. Chollacoop, K.J. Van Vliet, T.A. Venkatesh, and S. Suresh, *Computational modeling of the forward and reverse problems in instrumented sharp indentation.* Acta Materialia, 2001. **49**(19): p. 3899-3918.
98. Taljat, B. and G.M. Pharr, *Development of pile-up during spherical indentation of elastic- plastic solids.* International Journal of Solids and Structures, 2004. **41**(14): p. 3891-3904.
99. *Manual of Microtest-200 and Nanotest-600*, Wrexham: MicroMaterials Ltd.
100. *ANSYS 5.7*, ANSYS, Inc: USA.
101. Ltd, M., *Manual of Microtest-200 and Nanotest-600.* 1999, MicroMaterials Ltd: Wrexham.
102. Field, J.E., *The properties of natural and synthetic diamond.* 1992: Academic Press.
103. Wilks, J.W.a.E., *Properties and Applications of Diamond.* 1991: Butterworth-Heineman Oxford.

104. Chudoba, T. and F. Richter, *Investigation of creep behaviour under load during indentation experiments and its influence on hardness and modulus results.* Surface & Coatings Technology, 2001. **148**(2-3): p. 191-198.
105. Yurkov, A.L., V.N. Skvortsov, I.A. Buyanovsky, and R.M. Matvievsky, *Sliding friction of diamond on steel, sapphire, alumina and fused silica with and without lubricants.* Journal of Materials Science Letters, 1997. **16**(16): p. 1370-1374.
106. Bucaille, J.L., S. Stauss, P. Schwaller, and J. Michler, *A new technique to determine the elastoplastic properties of thin metallic films using sharp indenters.* Thin Solid Films, 2004. **447**: p. 239-245.
107. Lide, D.R., *Handbook of chemistry and physics*, ed. 76. 1995, Boca Raton: CRC Press.

APPENDIX A

BACKGROUND ON WELDING PROCESS AND METALLURGY

The variation of microstructures in a weld results from the reaction of the alloy to the various welding variables. During solidification most grains grow epitaxially from the fusion line but some can form from nucleation events in the fusion zone. However not all of the grains undergo extensive growth, some are pinched off during the growth process. This produces fewer but larger grains in the weld metal. The weld metal often exhibits a columnar structure where the grains are relatively long and parallel to the direction of heat flow. Not all weld metal is coarse grained and columnar. The grain structure varies with different alloys, and can be modified by process variables, which alter the pattern of turbulence in the liquid metal. In general, nearly pure metals, and alloys which solidify over a narrow range of temperatures develop the most columnar and coarse-grained weld metal.

Fusion welding is the interest of this study. Fig. A-1 shows the composition of a fusion weld and weld regions during the welding process. The heat input and the temperature gradients around the heat source have a direct effect on the determination of the width and depth of penetration, microstructure changes in the heat affected zone, and residual stresses.

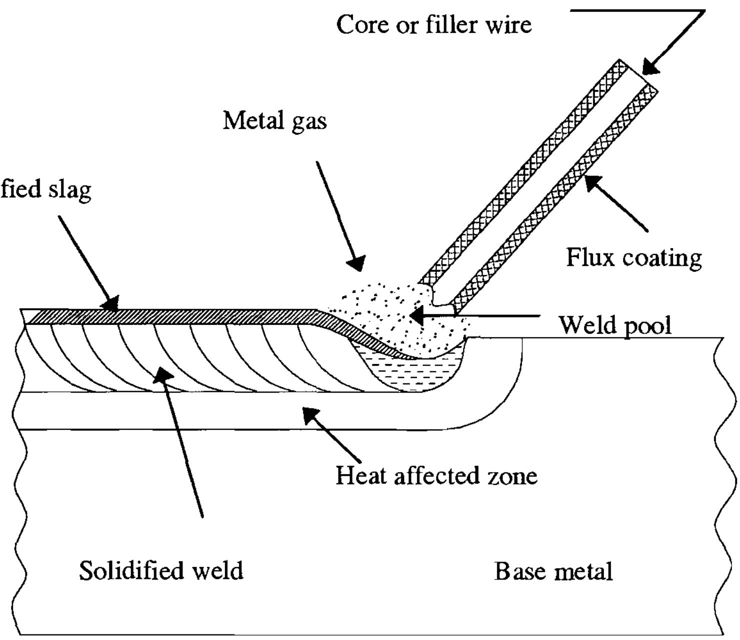

Fig. A-1 Schematic drawing illustrating various contributions to the composition of a fusion weld

The weld metal is the welding pool after solidification. It consists of a mixture of several materials, obtained from the filler rod, the base metal and the flux material, and it is less homogeneous than the base metal. The heat-affected zone, HAZ, is the part of the base metal close to the weld and because of its proximity to the fused metal, its microstructure is influenced by the heat generated in the welding process. As the melting is very local, a full range of temperatures will take place across the heat-affected zone. The zone may be small in size if the heat is intense. On the other hand, it may be quite large, as in the case of a high heat input fusion weld.

APPENDIX B

PROGRAM INTERFACE AND FILES CONNECTIVITY

The analysis program reads the raw indentation data produced by the instrument from an experiment and performs the frame compliance calibration and the indentation analysis simultaneously in an iterative manner as both are interdependent. The program analyses each unloading curve individually and the user has the option of choosing between the power law function and the Hertzian equation form for fitting to the unloading curve as well as the portion of the unloading curve required for fitting. The user has also the preference to choose whether the indentation data are to be analysed based solely on the conventional analysis methods that is, with the pile-up effect not accounted for, or implementing the correction expression proposed in this study. The analysis results for each unloading curve are arranged in columns in the output files.

The analysis program is composed of four individual files written in Matlab programming language in the M-files format. These are "*fccal_cor_main.m, fccal_cor_1.m, fccal_cor_2.m, fccal_cor_3.m*".

These files should be placed in a directory included in the specified path of Matlab or in the working directory. Operating the analysis program starts with the main file "*fccal_cor_main*", simply by typing its name without any extension in the command window, and each file calls the next one in the aforementioned order. The program also calls a built-in function, "*nlinfit.m*" available in the statistics toolbox of Matlab, which performs non-linear fitting iteratively to the unloading curve to a predefined function by the user. It should be saved as an M-file in a directory included in the defined path or in the working directory. Two forms are defined and saved in two files: "*sph.m*" and "*ff.m*" . The first file contains the Hertzian equation whilst the latter contains the simple power law function form. Below are the inputs, outputs and the connectivity of the four files:

File 1: *fccal_cor_main.m*

This file reads the files produced by the instrument and extracts the raw indentation data. The program passes these data to ***fccal_cor_1.m*** from which it receives the analysis and frame compliance calibration results. It then prints out the output files.

Inputs:

All data included in the input files should be comma-separated without headings unless otherwise stated.

1. *filename.LDD* and *filename.SYS*. The user is requested to enter the filename which is common for these two files. These files are produced by the instrument at the end of an experiment. The *LDD* file contains load depth indentation data of all indents performed in an experiment. The *SYS* file contains calibration parameters including the initial frame compliance entered in the instrument. In each data set, the first column is the load applied whilst the second column is the raw indentation depth. Preceding each data set for every indent is information about the data set such as the index of the peak load applied and size of the indentation data array.
2. Name of steel plate used in this study which is one of: s3, s4, s5, s6, s7, or ss. Each file contains the stress-strain data points. If the stress-strain curve is unknown, then the user should press the enter button.
3. Type of fitting function to the unloading curve whether it is the Hertz equation or a power law function
4. Portion of the unloading curve considered for fitting. A value should be selected among to 30%, 50%, 70%, or 80%.
5. Young's modulus and Poisson ratio of the specimen.
6. Whether or not to analyse the indentation data using the correction proposed in this study.
7. Type of spherical indenter geometry, whether the user wishes to assume a perfect sphere, R=150 μm, or use the real profile of the indenter. If the real profile option is selected then the following files are requested:
   A. *Aver-Prof.txt*: It contains the data points of half the axisymmetric indenter profile arranged in two columns. The first column includes the radial

distance of each data point whilst the second one is the vertical distance from the indenter tip.

B. *R-TIP.txt*: It includes the variation of the effective radius of curvature, at various vertical depths from the indenter tip, which results from axisymmetric arc fitting to the indenter profile. Included in this file are also the corresponding gradient and *sin* resulting from this fitting. Data are arranged in six columns. The first two columns are the coordinate data as in the profile file mentioned above. The third column includes the evaluation of the vertical distance from the indenter tip resulting from the axisymmetric arc fitting. The fourth column contains the effective radius of curvature. In the last two columns are the resulting gradient and *sin* resulting from the fitting procedures. The first row is a heading of the variables of the corresponding columns.

C. Whether the user wishes to use the gradient and *sin* resulting from the local linear fitting, in which case the user should provide the file *Linears.txt*. This file starts with a heading row, and is composed of three columns. The first column includes the vertical distance from the indenter tip corresponding to the indenter profile data points, whilst the last two columns are the gradient and *sin* at these data points.

Outputs:

The output files are grouped into two categories:

A. Results from implementing the conventional analysis approach with no pile-up effect accounted for. These results are arranged in four files:

1. *FC-DATA-filename .txt*: It contains the analysis results for every load cycle, and is given in an array whose number of rows are equal to the number of load cycles in the experiment. In every row the following information is provided: initial frame compliance pre-entered into the machine prior to the experiment, total frame compliance, maximum indentation depth, peak load, contact stiffness, contact depth, contact radius, residual depth, characteristic strain, Meyer hardness, reduced modulus, corresponding stress from input stress-strain curve, strain hardening exponent of the input stress-strain curve, strain hardening exponent from indentation calculations, calculated strength coefficient, calculated 0.2 yield stress.

2. *FC-filename.txt*: It is a short form of the file above with two columns for the peak loads and total frame compliance calculated for each load cycle.
3. *L_Ph-filename.txt*: This file contains all data points lying on the loading curves from all cycles in an experiment. Indentation data are modified by the frame compliance calculated.
4. *Ph-filename.txt*: This file includes all data points lying on the loading curves from all cycles in an experiment

B. Results from incorporating the correction technique proposed in this study accounting for the pile-up effect in calculating the contact area are outputted to files similar to those mentioned above. Likewise the output files are:
   1. *FC-DATA-COR-filename.txt*: Similarly, this file contains the analysis results for every load cycle from implementing the correction proposed in this study in addition to the original contents of the file *FC-DATA-filename .txt.*
   2. *FC-COR-filename.txt*: Similar to *FC-filename.txt*
   3. *L_Ph-cor-filename.txt.*
   4. *Ph-cor-filename.txt.*

File 2: ***fccal_cor_1.m***

This file serves as a function to *fccal_cor_main.m* from which it receives the recorded raw load indentation data arranged in one array. It then performs some operations to separate the set data for each load cycle. It passes these sets one at a time to *fccal_cor_2.m*. Thus, it calls *fccal_cor_2.m* as many times as the number of load cycles.

File 3: ***fccal_cor_2.m***

This file serves as a function to *fccal_cor_2.m* from which it receives the load indentation of one load cycle arranged in sets. Each set is passed at a time, from which the unloading indentation data are extracted and modified by the frame compliance. Its value is calculated iteratively between *fccal_cor_2.m* and *fccal_cor_3.m*. Each set of unloading indentation data is then passed to *fccal_cor_3*.

File 4: ***fccal_cor_3.m***

This file serves as a function to *fccal_cor_2.m* from which it receives the unloading data corresponding to one load cycle modified by a selected value for the frame compliance.

The resulting reduced modulus is passed back to *fccal_cor_2.m* and compared with the target value. Unless a pre-specified tolerance is satisfied, a new value for the frame compliance is applied to the unloading data and passed again to *fccal_cor_3.m*. An iterative procedure is followed until a the pre-specified tolerance is satisfied. Analysis results, those comprising the content of *FC-DATA- filename .txt* are passed to *fccal_cor_2.m*, *fccal_cor_1.m*, and finally to *fccal_cor_main.m*.

APPENDIX C

APDL SCRIPT TO EXTRACT VARIOUS QUANTITIES OF THE FE MODEL

ANSYS PROGRAMMING LANGUAGE (APDL) was utilised to build a script in order to extract various output quantities of the FE model, such as

- The number of load steps in addition to the number of substeps and iterations in each load step.
- The coordinates of the surface nodes and their radial and vertical displacements in order to obtain the deformed shape of the surface at peak loads and at full unloading. If indentation is performed in a single load cycle then the deformed shape of the surface is determined over 20 steps of the loading curve including the peak load.

At every load step, the following information is also extracted:

- Applied force on the indenter.
- Indentation depth, which is determined as the vertical displacement of the specimen node at the contact area centre, which is the node of first initial contact with the indenter.
- The node number at the contact edge that is defined as the furthest node in contact. The knowledge of its radial and vertical displacement in addition to its original coordinates leads to the calculation of the contact radius and pile-up.